The Dissertation Committee for Joseph Anthony Hashem Certifies that this is the approved version of the following dissertation:

Automating X-Ray and Neutron Imaging Applications with Flexible Automation

Committee:

Sheldon Landsberger, Supervisor

Mitchell Pryor, Co-Supervisor

Steven Biegalski

Erich Schneider

David Janecky

Automating X-Ray and Neutron Imaging Applications with Flexible Automation

by

Joseph Anthony Hashem, B.S.M.E; M.S.E

Dissertation

Presented to the Faculty of the Graduate School of

The University of Texas at Austin

in Partial Fulfillment

of the Requirements

for the Degree of

Doctor of Philosophy

The University of Texas at Austin

December 2015

Dedicated to my entire family

Acknowledgements

Automating X-Ray and Neutron Imaging Applications with Flexible Automation

Joseph Anthony Hashem. Ph.D.

The University of Texas at Austin, 2015

Supervisor: Sheldon Landsberger

Co-supervisor: Mitchell Pryor

This dissertation advances the capability of autonomous manipulation systems for non-destructive testing applications, specifically computed tomography and radiography. Non-destructive testing is the inspection of a part that does not affect its future usefulness. Radiography and tomography technologies are used to detect material faults inaccessible to direct observation. An industrial 7 degree-of-freedom manipulator has been installed in various x-ray and neutron imaging facilities, including the Nuclear Engineering Teaching Laboratory and Los Alamos National Laboratory, for imaging purposes.

Inspection of numerous components manually is laborious and time consuming, and there is the risk of high radiation dose to the operator. As Low As Reasonably Achievable exposure can be significantly reduced by installing a robot in an x-ray or neutron imaging facility to perform part placement in the beam for radioactive parts and nuclear facilities. Automation has the additional potential benefit of improving part throughput by obviating the need for human personnel to move or exchange parts to be imaged and allowing for flexible orientation of the imaged object with respect to the x-

ray or neutron beam. When the process is fully automated, it eliminates the need for a human to enter the beam area.

The robot needs to meet certain performance requirements, including high repeatability, precision, stability, and accuracy. The robotic system must be able to precisely position and align parts, and parts need to be held still while the image is taken. Any movement of the specimen during exposure causes image blurring.

Robotics and remote systems are an integral part of the ALARA approach to radiation safety. Robots increase the distance between workers and hazards and reduce time that workers must be exposed. Research performed aims to expand the role of automation at nuclear facilities by reducing the burden on human operators. The robot's control system must manage collision detection, grasping, and motion planning to reduce the amount of time that an operator spends micro-managing such a system via tele-operation.

The subject of this work includes modeling (in MCNP) and measuring flux, dose rates, and DPA rates of neutron imaging facilities to develop predictions of radiation flux, dose profiles, and radiation damage by examining neutron and gamma fields during operation. Dose and flux predictions provide users the means to simulate geometrical and material changes and additions to a facility, thus saving time, money, and energy in determining the optimal setup for the robotic system.

Table of Contents

List of Tables

List of Figures

Chapter 1: Introduction

Penetrating radiation has been used throughout history for imaging purposes dating back to 1895 when Roentgen discovered x-rays. Emerging threats to national security from cargo containers and improvised explosive devices have reinvigorated efforts using tomography and compact radiography. Additionally, unusual environmental threats, like those from underwater oil spills and nuclear power plant accidents, have caused renewed interest in fielding radiography in severe operating conditions. Today any particle type can be combined with an increasingly wide range of digital detectors to image almost any conceivable object in extreme environments. These severe operating conditions pave the way for remote handling systems, such as robots. While most non-destructive testing (NDT) is conducted manually or with purpose built motion stages, there has recently been a growing interest in the development of robotic systems for NDT. [Laux, 2013] [Bosserman, 2007] Even more so, having a flexible robotic system allows for a single system to be used to image various sizes and shapes of parts for radiography and Computed Tomography (CT) purposes. [Hashem, 2013] CT is a method to produce 3D representations of the scanned object both internally and externally by using many radiographic images taken from different angles to produce cross-sectional tomographic images.

NDT encompasses a wide range of techniques aimed at evaluation of material properties and detection of defects, both surface and internal, without object disassembly and affecting the object's integrity or future usefulness. [Prakash, 2009] The NDT system is required to be capable of finding and characterizing component and structural defects to a high probability of detection thereby decreasing the probability of failure. NDT is necessary because all parts are not made perfectly and to ensure that the part is within

design specifications. Compared to manual NDT for inspection of components, automated robotic deployment of the same NDT techniques enables increases in accuracy, precision, and speed of inspection while reducing radiation doses to workers (when working with radioactive parts) and associated labor costs. This work will focus on digital radiography and CT NDT applications. The radiography of parts is a manually intensive process. Operators must manually change out each part and manually fine-tune the orientation of the part. The geometric complexity of larger parts inhibits many radiographic results when conducting static exposures. Typically, coverage of larger film sizes is only possible by using increased source-to-detector distances. Even with longer source-to-detector distances (approximately 1.5 to 3 m) and minimal magnification (less than 1.5 magnification), only a small area of interest may be discernible. Increasing the source-to-detector distance increases the exposure time required since the beam intensity decreases with distance. This "manual" radiographic analysis leads to significant time loss, manpower usage, and monetary expenditure. The use of robots can provide additional flexibility and autonomy to automated NDT. The term "imaging" in this work applies to both radiography and CT. An application of a seven Degrees-of-Freedom (DoF) robotic manipulator (Yaskawa SIA5) for automated x-ray and neutron radiography and CT is presented. [Yaskawa, 2012] DoF for a mechanical system is the number of independent parameters that define its configuration. For each DoF in a robot, a joint is required.

1.1 COMPUTED TOMOGRAPHY & RADIOGRAPHY PRINCIPLES

CT is a method to acquire three-dimensional information about the structure inside a sample and is based on the integral of attenuation. [Prakash, 2009] The basic principles of radiography and CT are as follows:

1. X-rays or neutrons from the radiation source pass through the object. In both cases, collimation is used to guide the x-rays or neutrons from the source to the object.

2. The detector behind the object converts the transmitted radiation into another physical quantity, e.g. light, which is then measured and recorded.

3. Each area detector element records the intensity of the transmission in a pixel, an element of the image plane. The spatially varying transmission through the object is thereby mapped into a plane radiograph, i.e. projection image.

4. For tomographic imaging, the object is rotated in small angular steps through either 180° or 360°. Images of plane sections, perpendicular to the objects rotation axis, can then be mathematically reconstructed from all projections and merged as a stack of slice images. Then a volumetric, tomographic representation of its neutron or x-ray attenuation characteristics is reconstructed and can be visualized using three-dimensional rendering graphics software.

CT typically requires one view per pixel of maximum region of interest width. In tomography, a variety of artifacts may be present in projection sets that propagate errors back into the reconstructed image. If fewer projections of the object are captured, the image will have more reconstruction artifacts and poorer resolution, boundary definition, and uniform voxel (the 3D analog of the pixel in a 2D image) spacing. Thus, it is typical to have uniformly spaced view angles. An illustration of a CT application is shown in Figure 1-1.
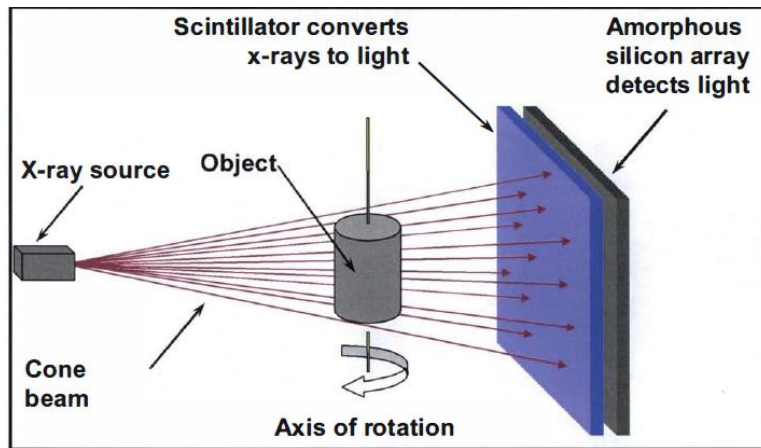
Figure 1-1. Simple CT or radiography layout. [Hunter, 2012]

1.1.1 NDT Radiography

Radiography relies on radiation transmission measurements to provide a 2D projection of a 3D part. Wilhelm Roentgen [1896] discovered x-rays and invented x-ray radiography. In Roentgen's original paper he demonstrated that high-energy photons could penetrate opaque objects and reveal their internal structure. In follow up work he established that x-rays produced at higher voltages were more penetrating. Scattered x-rays add a diffuse background to the radiographed image that obscures the details of the transmission, especially in the regions of low transmission. Accurate measurements depend on the x-rays that are transported through an object with no interaction. As some x-rays are absorbed by matter, many more are scattered. Bucky [1915] discovered that by placing a collimator made of sheets of lead spaced by layers of balsa wood in front of the detector, with the sheets parallel to the x-ray beam, much of the scatter background could be removed, resulting in higher scene contrast and much cleaner images.

Radiography is a non-destructive technique that typically requires several images with long exposure times taken for each part. Longer exposure times increase the fidelity of the image. A low energy, high intensity source allows for shorter exposure times. Therefore, vibrations must be minimized. LANL radiography applications include NDT

4

on parts and components to find material defects, Department of Energy (DOE) stockpile maintenance, science-based stockpile stewardship programs, research and development, and industrial applications. Source parameters to take into account for radiography applications are the initial beam width, shielding requirements, and collimation. [Morris et al., 2013] An example radiography application is shown in Figure 1-2.
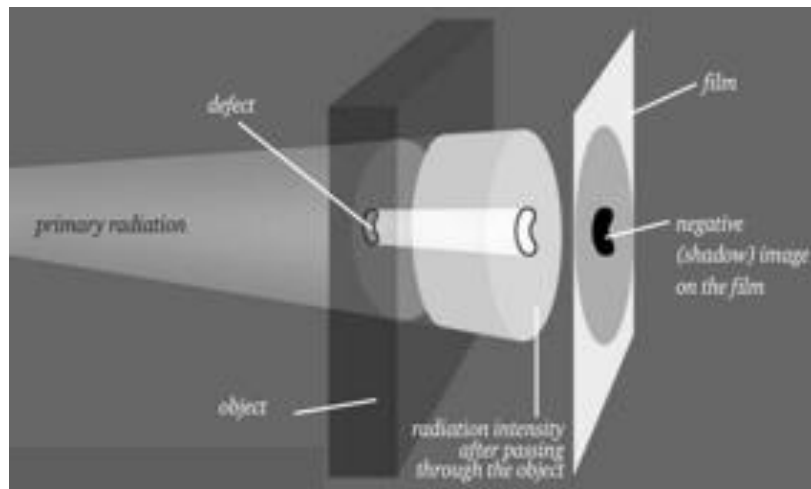
Figure 1-2. A negative radiograph image. [General Electric, 2007]

1.1.2 Comparison of Medical and Industrial X-Ray CT

Medical x-ray is the application familiar to most people, due to its frequent use by physicians and dentists. In the hospital, x-ray CT provides volumetric information about inner organs, bone fractures, cancer, etc. In industrial CT, the object is typically rotated using a turntable. In contrast, the beamline and detection systems are typically rotated around the patient in a medical CT, or CAT scan.

To maximize their effectiveness in differentiating tissues while minimizing patient exposure, medical CT systems use a limited dose of relatively low energy x-rays (<140 keV). They must also acquire their data rapidly to minimize patient movement during scanning. In order to obtain optimal data given these requirements, they use relatively

large (mm-scale), high efficiency detectors, and x-ray sources with a high output, requiring relatively large (mm-scale) focal spots.

Because industrial CT systems image non-living objects, they can be designed to employ the following optimizations: use of higher-energy x-rays which are more effective at penetrating dense materials; use of smaller x-ray focal spots which provides increased resolution at a cost of x-ray output; use of finer, more densely packed x-ray detectors which also increases resolution at a cost in detection efficiency; use of longer exposure times which increases the signal-to-noise ratio to compensate for the loss in signal from the diminished output and efficiency of the source and detectors; and a broader range of x-ray source/energy systems (including *bremsstrahlung*, synchrotron, etc.).

1.2   X-RAY VS. NEUTRON TOMOGRAPHY AND RADIOGRAPHY

Neutron tomography and radiography (i.e. imaging) have evolved over the past decades and are now routinely used with dedicated beam lines at many neutron facilities in the world. [Lehmann et al., 2011] Neutron imaging provides a complement to conventional x-ray investigations. In comparison to established x-ray radiography and tomography, neutrons do not attenuate in the same manner, being sensitive to properties of the atomic nucleus rather than the atomic electrons. This sensitivity results in radically different attenuation coefficients and creates the potential for measuring physical quantities other than x-ray attenuation due to atomic properties. X-ray radiography and tomography utilize the attenuation depending on the number of electrons per atom in the beam, while neutron radiography and tomography depend on nuclear scattering and absorption cross-sections. X-rays are electromagnetic radiation that interacts with the electrons in the atomic shell of a nucleus. Their interaction probability correlates strongly

with the number of electrons of an element, i.e. the atomic number Z. Therefore, heavy materials induce strong x-ray attenuation, whereas light materials, like water and plastics, attenuate weakly. Since x-rays are sensitive to atomic electrons, they serve best to image heavier elements inside lighter elements; for example, steel pins in bones. X-ray absorption (photoelectric effect) is the dominant reaction at low photon energies, whereas x-ray scattering (Rayleigh scattering and Compton scattering) prevails at higher energies. [Hunter, 2012]

There is no such Z dependence that exists for low energy neutron matter interaction since the interaction of a free neutron with atoms is not influenced by their electron cloud, so neutrons penetrate many heavy elements much more than x-rays. The neutron reacts with the atomic nucleus in a manner that varies greatly with isotopic composition and neutron energy. Neutrons, sensitive to scattering from nuclei, are able to image lightweight, hydrogen-containing objects inside dense, high atomic number materials. A classic example is an image of a flower inside a steel or lead box, an imaging condition that is intractable with x-rays. The high penetration of epithermal neutrons through most materials is very useful for studies where samples consist of heavy-Z elements opaque to x-rays and sometimes to thermal neutrons as well. The ability to image the distribution of hydrogen atoms is virtually impossible with x-rays. This ability is an advantage in specific applications, for example, in evaluating items like solder on circuit boards or plastic parts embedded in heavy metal containers. Due to typically lower source intensities and lower detection efficiencies for neutrons compared to x-rays, longer scans are typically required to obtain good images. Due to flux limitations and thus imaging statistics, neutrons do not provide the resolution possible with x-ray radiography. Neutrons also allow for isotopic imaging and the use of isotopic tracers without changing the chemical composition.

Generally, high intensity neutron sources are not transportable; therefore most neutron imaging investigations have to be performed on the site of the neutron source. Neutron imaging is not yet widely used for NDT, because it is available only at a few places. On the other hand, x-ray imaging is much more common and it is not uncommon for portable x-ray sources to be used for imaging.

Figure 1-3 presents complementary images derived from x-ray and neutron radiography of a concrete sample embedded with steel fibers. The rendering of the neutron tomography volume in green shows clearly all components containing hydrogen (cement and sand), but the embedded steel fibers are invisible. Displayed in blue, the x-ray CT of the same sample shows the embedded steel fibers. On the left in Figure 1-3, the x-ray and neutron radiograph of the concrete sample are shown in gray, illustrating that not as much detail about the sample composition can be derived from the ordinary radiographs as from three-dimensional tomography.
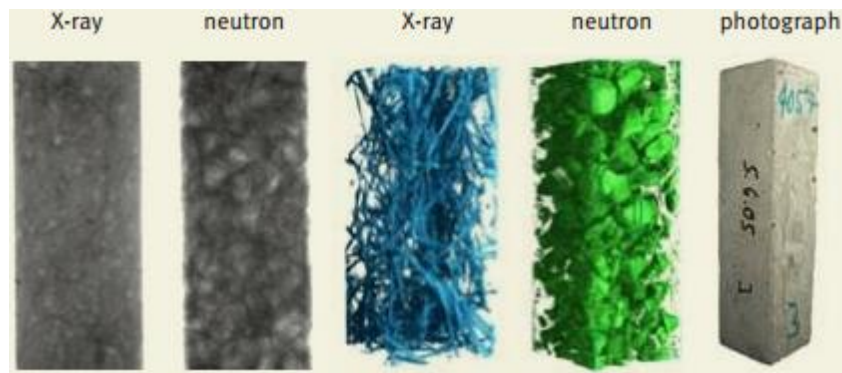
Figure 1-3. X-ray and neutron transmission radiographs (left) and tomographic views (middle) made from a concrete sample embedded with steel fibers. [Lehmann et al., 2011]

1.2.1   Image Detection

In a neutron imaging detector, the amount of electric charge produced by nuclear reactions is most often converted into another more observable physical entity such as light. In neutron scintillation screens, the charged particles stimulate light emission that is

detected by a camera or a flat panel detector. An alternative method is via neutron imaging plates known as storage phosphors. The charged particles create electron-hole pairs that produce light when de-excited by laser stimulation via photo-stimulated luminescence. If there are a lot of x-rays, it is important to use a neutron specific scintillator because it reduces secondary gamma rays and eliminates the need to filter them out. In x-ray films, the electromagnetic radiation produced by charged particles creates a latent image in the photo-emulsion, which results in selective film blackening during chemical film-development. [Lehmann et al., 2011]

1.2.2   X-ray Film vs. Digital Imaging

In the past, neutron imaging relied exclusively on x-ray films, used together with a screen converting neutrons to x-rays or light. During the last several years, digital neutron detectors have gradually replaced film-based detection. The main advantages of digital systems include: "real-time" imaging, chemical development is unnecessary, the digital images can easily be stored or copied and transferred over long distances, and they can be more easily/directly post-processed. Additional important advantages of digital detectors in neutron imaging are: the reduced activation risk and the possibility of quantitative evaluation. The shorter the neutron exposure is, the smaller the induced activity. Digital neutron detectors allow for CT and can achieve shorter exposure times due to their higher sensitivity than x-ray films by orders of magnitude. [Lehmann et al., 2010] Statistical or systematic image distortions can be eliminated by methods of digital image analysis, such as noise filtering and contrast enhancement. This elimination of image distortions is possible for film radiographs as well.

9

1.3 RADIOGRAPHY EXAMPLE AT LOS ALAMOS NATIONAL LABORATORY

One potential for Special Nuclear Material (SNM) container failure is over-pressurization from a loading error or from an unrecognized gas-generation mechanism. Assemblies that consist of a minimum of two individually welded, nested containers, makes it impossible to directly measure gas pressure in the inner container. To overcome this, radiography is used to detect changes in a pressure-indicating inner container lid. As a can pressurizes the lid will deflect outward and thus provide an indication of the internal pressure. Possibility of corrosion of a container and breach of the container is a technical issue that remains under intensive study at LANL (see Figure 1-4). Both the outer and interior containers allow for non-destructive verification, inspection, and surveillance of the contents. The introduction of flexible automation manipulation of these SNM containers is useful to reduce operator handling and the resulting dosage to operators. A robot also allows for rotation of the object in six DoF that makes for easy viewing of a region of interest.
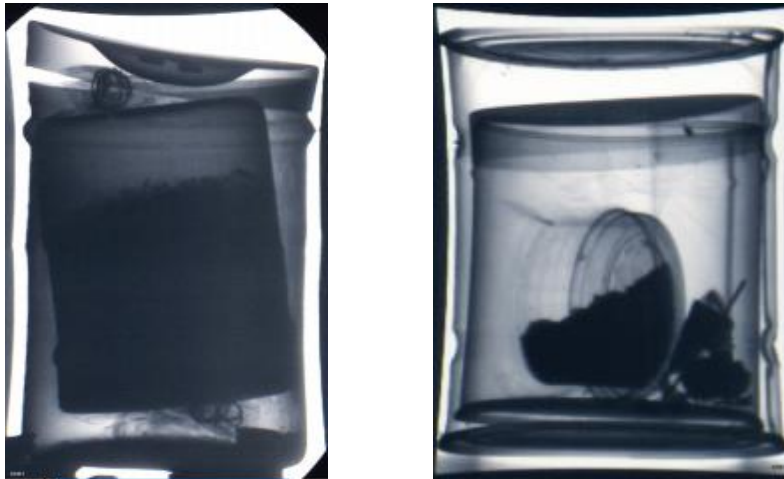
Figure 1-4. Radiographs of non-3013-packaged solids showing a breach of an outer container (left) and a partial vacuum created in an outer container (right) following the reaction of plutonium-bearing material with atmosphere in the sealed containers. The DOE 3013 Standard describes how plutonium-bearing solids and oxides containing at least 30 wt % plutonium plus uranium must be processed, packaged, and stored. The overall intent of the 3013 Standard is to stabilize excess plutonium-bearing solids and ensure they are secure for up to fifty years. [Paffett, 2004]

1.4 ROBOTS IN HAZARDOUS ENVIRONMENTS

Robots are increasingly deployed in remote and hazardous environments such as in nuclear waste cleanup and other radioactive environments. The DOE has in particular targeted robotic handling of hazardous waste to be an essential element in its efforts of environmental restoration and waste management. [Department of Energy, 1990] Within the DOE complex, the primary purpose of robots are to replace (or augment) human operators to increase safety without adversely impacting process efficiency. Increasing use of robots for applications in hazardous and/or inaccessible environments such as those in which waste management operations and radioactive material handling take place has created a need for safe, intelligent, flexible, and reliable robots. Successful performance of hazardous material handling operations will require a robot to perform tasks involving accurate positioning of its end-effector (EEF) and will demand that these tasks be completed in uncertain surroundings. The rationales for using manipulators in these hazardous environments are many, and include the desire to remove humans from hazardous environments, to reduce the cost of the operations, and to increase the speed with which the repeatable operations can be performed. Robots are not just used for individual operations, but repeated sequences of detailed operations that are potentially unattended if the tasks are completely automated.

Many of the robots in operation today are used in highly structured environments, performing repetitive tasks. This is in contrast to the robots performing tasks in hazardous environments that can be remote, harsh, and contain uncertain surroundings. A robot designed to work in hazardous environments often includes at least 7 DoF (i.e. a redundant manipulator) in order to negotiate around obstacles that present in these types of environments. A redundant manipulator has more than 6 DoF which means that it has additional parameters that allow the configuration of the robot to change while it holds its

EEF in a fixed position and orientation. [Patel and Shadpey, 2005] Kinematic redundancy greatly enhances a robot's capability to operate in unstructured and cluttered environments with incomplete information.

One of the most challenging aspects of robotic material handling is the problem of defining the robot's location with respect to its surrounding environment. Contributing to the difficulty of this problem is the harsh and unstructured nature of the operating environment and the demand for high reliability and safety. Reliability and safety take into account both the robot's hardware and software failure rates as reviewed in detail by Dhillon, Fashandi, and Liu [2002]. Harsh environments could include high radiation areas, space applications, extremely forward environments such as battlefields, etc. This type of environment is relevant for many DOE applications, however any type of dynamic environment presents a challenge for robotic material handling, which makes the obtainment of reliable results more difficult. A set of guidelines for calibration of industrial manipulator in hazardous environments are listed:

- What is the required accuracy/precision of the task?

- What is the required speed/velocity of the task?

- How quickly does the task need to be completed?

- Are the locations of the task fully defined, or not?

- What is the length of stay of the manipulator in the hazardous environment?

These guidelines were specified by the author through interviews with persons from LANL, Mitch Pryor from U.T. Austin, as well as from his personal experience with working with robots in hazardous environments. The robot used for the applications described in this work is the industrial Yaskawa SIA5 manipulator. The SIA5 has 7 DoF and a 5 kg maximum payload at maximum velocity and acceleration. Figure 1-5 shows

12

the SIA5 with a 3-fingered aluminum Robotiq gripper. The robotic manipulator provides the following potential capabilities and advantages over ordinary motion stages with regards to motion control integrated with imaging: computed tomography and helical scanning without the need for multiple systems, infinitely flexible orientation of the sample in 3D space, reduced radiation dose to workers, increased sample throughput, and better process control. Evaluation of these capabilities and applications to industrial radiographic applications are the thrust of this thesis. The robotic system described in this thesis is capable of autonomously imaging multiple samples, but this requires more than just the robotic manipulator, including automation of image acquisition, coordination of the robot, detector and radiation source, as well as the human operator to initially transport the samples into the radiography bay and position them next to the robot. The operator is kept in-the-loop throughout the process as the overseer and can safely cancel the robotic motion at any time throughout the process. Even if motion stages are capable of performing one of these tasks, the control of motion stages is not as intuitive as the control of a robot. With robotic software capable of inverse kinematic calculations, the operator only needs to specify the final location and orientation of the robot to hold the part whereas the operator would have to specify the position of each of the motion stage axes independently. Because occupational doses are considered in the As Low As Reasonably Achievable (ALARA) approach [Washington University in St. Louis, 2014], even for very low levels, remote operation can be useful in helping achieve this since it increases the distance between the worker and the radiation. LANL has safety structures and procedures in place to keep radiation exposure of personnel as low as reasonably achievable. ALARA exposure has the potential to be significantly reduced depending on the application by installing a robot in an x-ray or neutron imaging facility to perform part placement in the beam. For example, if there is a highly radioactive part imaged with

a dose of 100 rads/min at 1 meter from the source, and if the part requires a total of 10 views where it takes approximately 1 min for an human operator to manipulate the part to the correct angle, a total of about 1,000 rads received by the operator could be eliminated or reduced by having the robot handle the parts instead. Automation has the additional potential benefit of improving part throughput by obviating the need for human personnel to move or exchange parts to be imaged and allowing for flexible orientation of the imaged object with respect to the x-ray or neutron beam. A majority of Chapter 6 evaluates and demonstrates this benefit of robotics to NDT imaging and how it can improve image quality and imaging techniques.

Figure 1-5. Yaskawa SIA5 manipulator with attached Robotiq 3-finger gripper.

1.4.1 Robots in X-Ray and Neutron Imaging Applications

Using a robot for radiography allows the sample to be specifically oriented with respect to the beam by either teleoperation methods or by programmed motions. Manual adjustments can achieve similar results but will generally take a longer amount of time

since the operator has to turn the radiation source off, manually adjust the object, turn the source back on, and check the resulting radiograph. This manual process may even have to be repeated until the required view angle is achieved. Radiography applications often require several images taken from different angles, which requires that the parts be repositioned and held in various and precise orientations relative to the beam. Thus a robotic system capable of recognizing and tracking multiple part orientations has the potential for imaging in dramatically shorter periods with less operator interaction since they would not have to repeatedly cycle the beam source or close the shutter to replace/reposition parts when performing digital radiography. For example, in a worst case scenario, a robot could save 3 minutes per view. If there are 1,000 parts a year, 50 hours would be saved plus labor costs. This does not take into account the time it takes for re-entry into radiation areas and any small motion adjustments. A robot would also allow operational extension and the potential to have multiple shifts. Currently, in order to switch or re-position parts in LANL facilities, the x-ray source must be shut down, which takes several minutes for the beam and x-ray source to minimize to a level that permits personnel in the beam port area. Depending on the part composition, it may need additional cooling time. After the operator enters and the part is properly positioned manually, the beam/x-ray source is restarted and brought back to power to capture the next image. Current detailed radiography inspection applications at LANL involve the manual positioning of items and assemblies with film and/or digital panel detectors. This time-consuming process also presents the possibility of an increased integrated or even acute accidental exposure. For these reasons, a robotic part positioning system has been proposed to perform these tasks while the beam is at power when digital detection is used.

Robots are an ideal candidate for the manipulation of nuclear fuel rods and single fuel pellets in neutron imaging applications. Since nuclear fuel is highly radioactive, they must be transported and manipulated within heavily shielded containers, making remote handling necessary.

1.4.2 Robotic Imaging System for Radiography

The robotic manipulator was implemented as the motion control and manipulation system for neutron/x-ray imaging tasks. It provides advanced motion capabilities for imaging techniques to compare and evaluate in comparison with linear and rotary stages, including identification of motions that are presently difficult to achieve. Typically, motion stages have three motion axes: translations along the x and y axes, and rotation along the z-axis (see Figure 1-6). Also, having a robotic system allows for a single system for various types of imaging applications instead of having dedicated machines for different imaging purposes. A robot can freely produce almost any movement pattern required; hence the system is expected to be less restricted to what imaging geometry it can produce. In depth repeatability tests presented in this thesis have been performed on the Yaskawa SIA5 robot [Hashem, 2013] and are evaluated below to demonstrate that the robot's repeatability is sufficient for these types of imaging tasks.
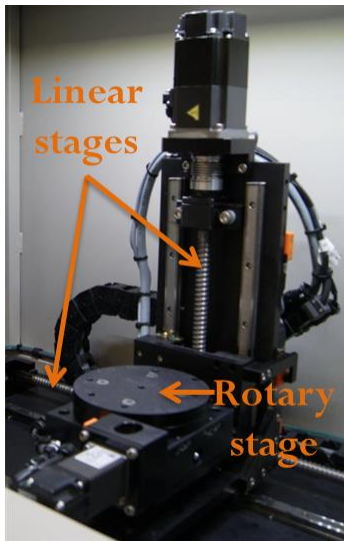
Figure 1-6. Typical motion stage system for CT applications.

Robots can also achieve high resolution. For example, a robot can conduct a CT scan with less than 0.1 degree increments, which is greater than 3600 images per CT scan. It can also achieve Cartesian movement commands on the order of tens of microns resolution movements. [Hashem, 2013] Radioactive objects can be imaged, reducing dose to workers. Having a robotic system can replace or reposition the need for the human operator to change out samples for inspections. The time it takes to change out samples is significant in some cases. For example, at the Nevada test site, the radiography room has to be surveyed after every sample has been imaged before the sample can be changed out due to dose rates. A radiation protection technician has to enter the area to measure radiation levels to ensure they are low enough for personnel to enter. It takes about half an hour to back out of the radiography room. This time becomes significant if multiple samples need to be imaged. This information was gathered through personal communications with David Janecky of LANL.

1.4.3 Disadvantages of Robotic Imaging Systems

Disadvantages of a flexible imaging system include the investment in an industrial robotic arm, including initial purchase (approximately $60,000 for the manipulator and controller), training, and maintenance. In comparison, motion stages require purchase and maintenance of multiple systems in order to provide for similar imaging capabilities to that proposed for a single robotic manipulator. Both motion stages and robots include electronics that can fail due to radiation damage. However, this can be mitigated by introducing radiation tolerant components, adding shielding to the robot directly, and/or removing the electronics from the robot itself, moving them to a shielded location. General maintenance of robotic components are generally more expensive and complex than standard rotary or linear stages as well. Operators must also be trained to use the robot effectively, automate tasks, and evaluate teleoperation to reduce the levels of operator training required. Safety and controls must also be taken into account, whether it is the robot running into a human or the robot dropping a radioactive or fragile part. Cultural reluctance, or the resistance to and opportunity for change in practices, is another hurdle that must be taken into account when looking to implement robotics for NDT imaging.

1.5 REPEATABILITY, ACCURACY, AND RESOLUTION OF A ROBOT

In order to unambiguously discuss system requirements, certain terms that are often used loosely and (incorrectly) interchangeably used in literature and commercial documents are formalized for this report. These include accuracy, and resolution, precision, and repeatability.

Accuracy is the ability of the robot to go to a specified location within the prescribed tolerance. It is impossible to position a machine exactly. Accuracy is therefore defined as the difference (i.e. the error) between the requested task and the obtained task

(i.e. the task actually achieved by the robot). It is the difference in position between a point called for by a robot's control system and the point actually achieved by the robot.

Resolution, a function of a robot's control system, specifies the smallest increment of motion by which the system and parts of the system can divide the work envelope. Since resolution is limited for the motion of each joint, the resolution possible for the EEF is not only a function of the joint resolution, but also the configuration of the robot since the geometrical relationship between the joint and EEF spaces will deterministically scale the joint resolution errors. This is either a function of the smallest increment in position that the controller can command or the smallest incremental change in position that the controller can distinguish. Resolution is determined by the design of the control unit and also by integrated positioning and is dependent on the position feedback sensor.

The accuracy and repeatability of most industrial robots is typically around 20-80 µm as shown in Table 2-1. Robots can achieve superior position accuracy and repeatability to that of a human without compromising the flexibility as is the case with fixed automation or single DoF servo systems. This allows robots to achieve tasks more precisely, with more uniform results, with smaller standard deviations, in less time, and for more applications and tasks. Typically, industrial robots attain higher repeatability levels than positioning accuracy. Maier-Hein et al. [2009] demonstrated that the accuracy and repeatability of a robot was 10-20 µm while that of a human was on the order of a magnitude greater. EEF resolution will vary depending on the kinematic configuration of the system since the fixed joint resolutions are perceived at the EEF as a highly variable and nonlinear kinematic transformation.

Precision is a systems ability to meet the positioning requirements for a given task whether they are formally defined in terms of repeatability, accuracy, resolution or a combination of all three.

Repeatability is the ability to consistently duplicate an action or a result. For example, repeatability would be the ability of a robot to position itself in the same orientation and position at a defined level of measurement when asked to perform a task multiple times. It is normally defined as a tolerance about a position and is a relative concept. In robotics, it includes the positional error of the EEF when it returns to a previously designated location, but also may require repeatability of the overall supporting structure, in addition to the EEF's positional error. Cartesian and rotation repeatability are of importance. Repeatability is affected by resolution, hysteresis, and inaccuracies in components such as linkages, gears, and beam deflections due to the payload or the weight of the robot itself. Repeatability can be further complicated for redundant systems since there is commonly manifold(s) of solutions for a given EEF location.

According to LANL radiographers, product specifications call out 0.05 mm (0.002 inch), 0.08 mm (0.003 inch), and 0.15 mm (0.006 inch) maximum feature requirements to be measured for radiography inspection in the LANL Plutonium Facility. These features are measured to 0.001 inch (0.025 mm). Vibrations cannot exceed 6 μm (i.e. one quarter of the maximum requirement) while the part is held in order to allow accurate measurements. Also, the tilt of the part relative to the x-ray beam needs to be known to within 0.1 degrees. These requirements were acquired through personal communications from David Fry and James Hunter from LANL.

1.6   OBJECTIVES

This thesis describes results from a collaborative project between University of Texas at Austin (U.T. Austin), Nuclear Robotics Group, and Los Alamos National Laboratory (LANL) to characterize, evaluate, and implement a robotic manipulator as the motion control system for neutron and x-ray imaging tasks. This effort includes taking state-of-the-art robotic technologies out of the realm of pure research and using them to automate non-destructive imaging tasks in nuclear facilities.

The ultimate goal of this research and development work is to implement robotics for automation in non-destructive imaging applications. These imaging tasks required high precision, stability, resolution, and repeatability as well as flexibility in order to perform more advanced imaging applications such as computed tomography and helical scanning.

To complete the high level objective, four key research objectives must be addressed as a part of this effort:

Validate the feasibility of the robotic system. The robot needs to meet certain performance requirements, including quantitatively measured demonstration of high repeatability, stability, accuracy, survivability, safety, and programmability. The accuracy of the robot needs to be better than x-ray system resolution. If positioning accuracy is equivalent to x-ray detection precision, then the integrated detection precision is decreased due to the sum of uncertainties. For example, if a resulting radiograph measurement, x, has two sources of uncertainty, the robot's positioning accuracy and the x-ray detection precision for which the two standard uncertainties $u_1(x)$ and $u_2(x)$ have been determined, then the combined standard uncertainty $u_c(x)$ for the measurement is given by:

$$u_c(x) = \sqrt{(u_1(x))^2 + (u_2(x))^2} \qquad (1\text{-}1)$$

Survivability of the hardware in the environment where NDT is performed needs to be evaluated with the help of MCNP[1]. Once the robot has been deployed in radioactive environments, the degradation of the robot's performance, if any, has to be experimentally tested. It is necessary for the software used for commanding the robot to integrate capabilities such as motion planning, collision detection, obstacle avoidance, grasping, etc. while still meeting the NDT performance requirements. The motion-planner and inverse kinematic solver need to be precise and robust. The software must allow the NDT engineer to easily and safely command the robot. Additionally the developed software must simplify the integration of the robot with other NDT hardware components.

Design the robotic and supporting systems. There are inherent design trade-offs that must be considered when developing, implementing, and evaluating an automation system for NDT applications. For example, it may be desirable to extend the tool/grasping point away from the robot to keep the robot away from the beam. Extending the tool point of the robot without adding an additional rotary joint in the robot would reduce the robot's dexterity. However, the extended tool point may reduce EEF accuracy by magnifying joint resolution limits. The system will be configured/designed to accommodate this apparent conflict between precision (i.e. unrestricting the robot's workspace and motion planning) and survivability (i.e. restricting the robot's workspace and motion planning abilities to increase distance between the robot and beam). Additional design considerations such as shielding, payload, deflection, user-interface, parts storage/retrieval, etc. will be considered when/if necessary in order to complete the design and meet the following objectives.

---

[1] MCNP is a general-purpose Monte Carlo N-Particle code that can be used for neutron, photon, electron, or coupled neutron/photon/electron transport. [Pelowitz, 2011]

Evaluated constraints on robot survivability in radiation environments using MCNP simulation and real-life applications. MCNP provides a powerful tool for determining radiation fields in a defined environment. Experimental validation of these simulations using dosimetry, dose rate meters, shielding, etc. provide the ability to make the MCNP simulation as extensive as possible for the actual system. High enough levels of neutrons or photons will eventually affect the reliability of electronic components. Thus radiation tolerance is critical to the reliability of the imaging process. Therefore, the radiation damage to the robot and its electronics must be quantitatively evaluated.

Implementation of an automated NDT system and performance comparison to manual operations on relevant DOE applications. Manual NDT inspections, with regards to repeatability and throughput, are constrained by the operator and equipment. Quantitative data on the performance, time, and cost-saving advantages of using a robotic system over a human operator will provide justification for the implementation of the proposed NDT robotic system. The performance of the proposed system will be quantitatively evaluated in the following sections through simulations and experimentally to ensure that the robotic system can perform NDT imaging tasks safely and effectively.

Additional operational and experimental capabilities made possible given the existence of an automated NDT system will then be identified. Once the proposed system is in place, it may be possible to propose new techniques that advance the state-of-the-art in NDT. Implementing yet to be identified techniques is beyond the scope of this effort, but suggestions for such techniques will be listed for future researchers to consider pursuing.

1.7 MAIN CONTRIBUTIONS

Although many kinds of experiments will need to be performed in the future to further optimize the automation of NDT imaging tasks, the main objectives of this work were accomplished (described in detail throughout the following chapters) and significantly advance the state of NDT automation. Furthermore, the results of this effort provides the capability and flexibility to further optimize NDT imaging tasks without the need to continually redesign and upgrade more traditional automation components. To complete this task, it was necessary to address design issues spanning multiple and disparate research areas including robotics control, radiation assessments, metrology and system design optimization. This thesis effort was directed toward automating neutron and x-ray radiography at the Nuclear Engineering Teaching Laboratory (NETL) and Los Alamos National Laboratory (LANL).

1.8 OUTLINE OF SUBSEQUENT CHAPTERS

This chapter discussed the motivating application behind the current research. The following chapters are summarized as follows:

- Chapter 2: *Related Work/Literature Review* provides background on NDT imaging techniques, radiation damage to robots, and a review of published literature on NDT automation. Its main purpose is to introduce some of the concepts and terminology found in the remaining chapters and the frame the activities performed in this work within the current understanding of automating radiography and CT applications.

- Chapter 3: *Evaluation of Hardware Feasibility* overviews the techniques performed to characterize the NDT imaging facilities, including calibration, metrology, and Monte Carlo modeling techniques that ensured the feasibility of the robotic systems for imaging purposes. Also described are repeatability and accuracy experiments for validation of automating imaging applications at LANL.

- Chapter 4: *Evaluation of Operational Software Feasibility* overviews the techniques performed to characterize the NDT imaging facilities, focusing on if existing software can provide the necessary control capability for NDT applications. The simulation techniques that ensured the feasibility of the robotic systems for imaging purposes are also discussed. Failure modes and recovery techniques in the event of breakdown are looked at.

- Chapter 5: *Radiation Damage* describes the implications of radiation effects on the reliable and safe operation of robotic and manipulator systems in nuclear environments. Experimental radiation readings as well as simulated radiation tests (using MCNP) are used to analyze the radiation damage to the robot. Areas of the robot that receive the highest amount of radiation damage will be discussed.

- Chapter 6: *System Implementation/Experimental Results/Application Demonstrations* show the validation of the methods presented in previous chapters. The implementation of the system is described, showing how the methods presented in Chapter 3 are used in conjunction with other hardware and software tools to provide a functional autonomous radiography and/or CT system.

- Chapter 7: *Conclusions and Further Work* presents a summary of the work and the central conclusions drawn from it. Questions remaining about the robot imaging system are outlined here and recommendations for further modeling, experimental, and application areas are suggested.

Chapter 2: Related Work and Literature Review

2.1 IMAGING WITH ROBOTICS

Robotic systems have been often considered and occasionally used for a wide variety of imaging purposes, from medical imaging to tomography using dual-arm robotic systems. [Laux, 2013] This chapter broadly reviews literature relevant to different types of robotic imaging applications, the different types of software used in the current work, and also describes possible radiation effects to the robotic system.

2.1.1 Radiography

For at least 80 years, the industry standard in radiography has been the use of images on film, first used extensively in controlling the process of fusion welds in 1927. The last 30 years have seen rapid growth in digital radiography, which generates radiographs using electrical detectors that store the image information on a computer. The image is electronically transferred to a viewer, allowing for the image to be inspected virtually in real time. Digital radiography eliminates the wait for processing time required by film. Manufacturing companies have been moving towards the deployment of robotics in their radiography operations to increase productivity (see Figure 2-1). [Bosserman, 2007]

Burdea et al. [1999] describe a proof-of-concept system developed for robot-based dental subtraction radiography. The system is used to automate dental x-ray imaging processing, and it replaces mechanical or 'free hand' attempts to standardize exposure geometry with a non-contact approach using a 3-D position sensor. This resulted in less variation in the x-ray images and in a smaller standard deviation in the intensities of subtracted images overall. This work shows that robotic systems can be superior to mechanical alignment approaches, due to their accuracy and repeatability.

26

The use of robotics poses both challenges and opportunities to industries that employ computerized digital robotic radiography. A simple robotic radiograph inspection involves a conveyor belt moving engine blocks past an x-ray source on one side and a detector on the other as an operator inspects the image as the objects pass by. A more complex robotic radiograph inspection involves a manipulator holding the radiographed part and another for the x-ray source and detector. These more complex robotic systems require computer programs to maintain the correct locations and levels of energy and intensity to create the required image. For example, a large jet-engine component can be rotated on its axis at any angle desired with it positioned between a radiographic source on one manipulator and a digital detector on another manipulator. This entire process can be programmed.

Figure 2-1. Robotic radiography inspection of a turbine case for a jet aircraft engine. The radiographic source is on one robotic arm and a digital detector on another. [Bosserman, 2007]

The cumulative effects of combining digital radiography and robotics can lead to an overall increase in efficiency of producing high-quality radiographs. Using flexible automation as opposed to fixed automation allows for new tasks to be reprogrammed when work orders change. The differences between fixed and flexible automation is discussed by Hashem et al. [2011]. If multiple robots are used, productivity per man-hour can be multiplied.

2.1.2   Neutron Radiography Radiological Safety

Neutron radiography is non-destructive; however, many materials placed in a flux of neutrons can absorb neutrons and become radioactive. Depending on the energy and amount of radioactivity, this can be harmful to the experimenter. It is important to understand the resulting radioactivity of samples placed in the neutron beam so measures can be taken to limit this exposure as much as possible.

For example, if an aluminum sample is placed in the neutron beam, ^{27}Al has a sufficient capture cross section (i.e. 203 mb) to produce an appreciable amount of radiation, due to neutron capture and creation of the radioactive isotope, ^{28}Al. ^{28}Al subsequently decays via a 4.6 MeV beta particle with a half-life of 2.24 minutes to the stable isotope of ^{28}Si. The rate of ^{28}Al production in the sample can be calculated from

$$R = \Sigma\gamma\varphi V \tag{2-1}$$

where R is the production rate [1/s], $\Sigma\gamma$ is the radiative capture cross section [cm^2], φ is the neutron flux at the sample [n/cm^2/s], and V is the volume of aluminum in the sample [cm^3]. From this information, the activity of the sample can be calculated as a function of time by

$$\alpha(t) = R\left(1 - e^{-\lambda t}\right) \tag{2-2}$$

where $\alpha(t)$ is the activity [decays/s], λ is the decay constant [1/s], and t is the time, beginning at the inception of the incident flux. After the beam shuts off, the sample activity exponentially decays according to

$$\alpha(t) = \alpha_0 e^{-\lambda t} \tag{2-3}$$

where α_0 is the initial activity. Figure 2-2 shows how the activity of the ^{28}Al sample asymptotically approaching a maximum value and then subsequently decaying after the beam is shut-off. After the sample is irradiated, it must be allowed to decay for a certain period of time before the operator approaches the sample. This is necessary to reduce dose to the operator from radioactivity from the sample.
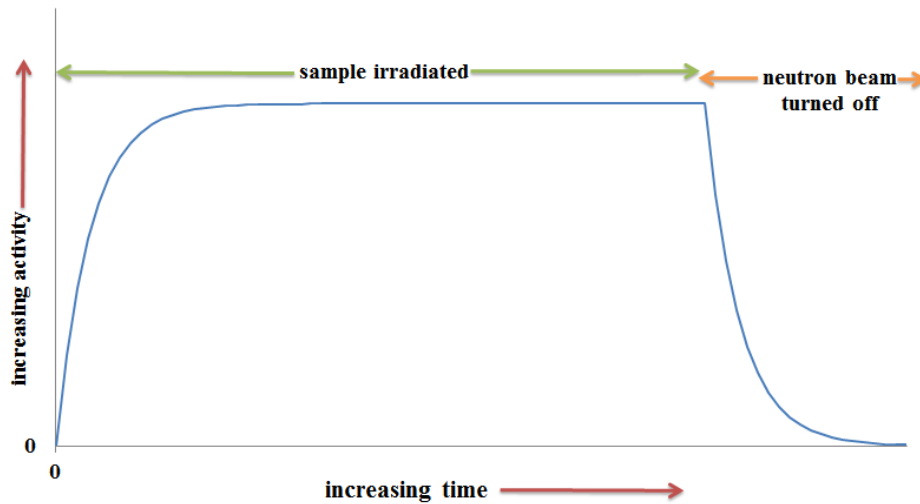
Figure 2-2. Activity of ^{28}Al sample as a function of time in a neutron beam and subsequent beam shut-down.

2.1.3   Tomography

Tomography is a technique where structures above and below a given point in the cross section of a structure are purposely blurred to reveal a specific area of interest. Tomography has been used to delineate suspect conditions of materials since it was first suggested in 1914 by Karol Mayer, a Polish radiologist. The advent of CT has taken the forefront in many ways, putting aside standard tomography. With the use of a dual-arm robotic system, with one arm holding the source and the other the detector, Laux [2013] proposes that tomography should be reconsidered as a NDT technique, since many NDT facilities do not have the capital expenditure necessary to buy and install the necessary

equipment for CT. The application of dual-arm robotic systems may be able to simulate tomographic techniques and create radiographic sectional data. When radiographing large, complex parts, such as aerospace structures, the part's geometric complexity presents a myriad of problems and inhibits many radiographic results. One key problem is that only a small area of interest may be discernible while conducting static exposures, even with long source-to-part distances. Presently, without the use of robotics, tomography of a large, complex part with suspect discontinuities or anomalies may lead to sectioning the part, significant time loss, manpower usage, and monetary expenditure.

Fundamentally, tomography can be improved with the use of robotics. In the medical field and other tomography applications, a static object and mobile source/detector system is used. This is in contrast to a typical industrial CT system, which consists of a static source/detector with rotating object. Typically, the x-ray tube is connected to the radiographic film by a mechanical linkage, which is usually a solid rod connecting the film to the x-ray source. As the x-ray moves in one direction, the film moves in the opposite direction. This is achieved by a fulcrum between the x-ray tube and film. The fulcrum angle decides the thickness of the imaged section and is inversely comparative; that is, as the fulcrum angle decreases, the sectional thickness increases. The exposure initiation can be established with the x-ray tube at the left or right side and moving at a predetermined arc while the film moves in the opposite direction, as shown in Figure 2-3.
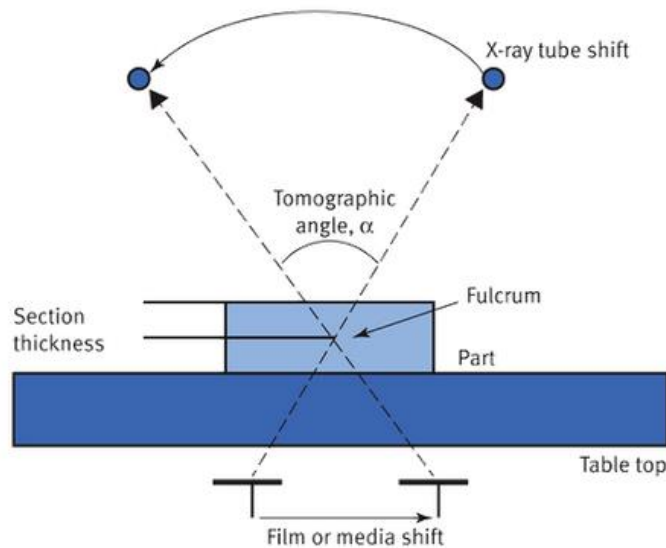
Figure 2-3. **The fundamental tomographic principle. [Laux, 2013]**

With an adjustable fulcrum, magnification becomes an issue, whereas a fixed fulcrum does not pose much of a magnification problem. With the use of a robotic system, mechanical linkages are not used between the source and film, therefore magnification would not be a problem. Two aspects of existing scanning systems are machine vibrations and loosening of mechanical linkages. Machine vibrations, which must be kept at a minimum, should not be a remarkable consideration depending on the robotic system used. In addition, as mechanical linkages loosen the prescribed motion deteriorates. With the application of robotic systems, these issues can be reduced and made self-correcting. Another significant source of inaccuracy in motion is variable part weight on the same system (e.g. grams to tens of kilograms) with no correction.

The theoretical application of tomography as applied to a dual-arm robotic system by [Laux, 2013] is shown in Figure 2-4. This system has not been built or tested. When utilizing a dual-arm robotic system in 3D space, the use of a fixed mechanical linkage is not necessary. Instead, the robotic system should be able to isolate a fixed tomographic

31

point in 3D space and identify this point as the fulcrum. The robots will then execute predetermined motions about this fixed point.
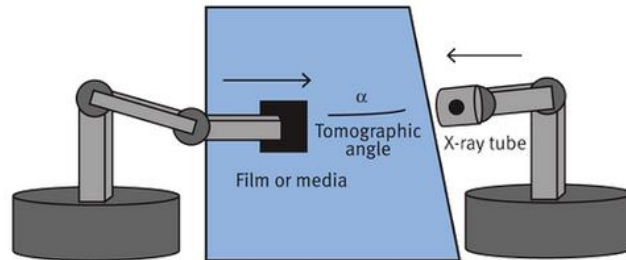
Figure 2-4. The fundamental tomographic principle as applied to a dual-arm robotic system in a 3D space. [Laux, 2013]

2.2 ROBOTICS FOR EDDY-CURRENT INSPECTION

Eddy-current techniques are commonly used for NDT of metallic objects. They use the principal of electromagnetism as the basis for conducting examinations. Eddy-current inspection procedures have been implemented using robotics with high precision to accelerate product verification without interrupting work flow. Uni-West developed the Univ-Versal test machine (shown in Figure 2-5), a flexible test platform that offers dual-arm robotic testing of metal bearing and spindles using eddy-current testing for cracks. [UniWest, 2011] For operation, an operator selects a part number and a 3D image of the part appears on the screen. One manipulator lifts the part from the conveyer and brings it into the test machine where it is placed on a rotating chuck. The other manipulator manipulates the eddy-current probe, while ensuring that it remains precisely the same distance from the part's surface to ensure accuracy. Separate probes robotically test inside and outside diameters for flaws. The system is relatively compact, measuring 37 in. deep and 44 in. long. The ability of the system to be reprogrammed to accommodate new part designs prevents it from becoming obsolete. This application demonstrates successful robot use in NDT, just not for radiography.

32

Figure 2-5. Operation of Univ-Versal dual-arm robotic eddy-current system. [UniWest, 2011]

2.3 ROBOTIC ASTRONOMICAL TELESCOPES

Monitoring the night sky for transient events, such as supernovae, gamma-ray bursts, active galactic nuclei, comets, and satellites, requires a robotic observatory that can be tasked autonomously to observe and analyze these events with no human in the loop. A closed-loop robotic telescope has the capability to evaluate its operations to ensure it is operating properly. An example of a closed-loop system is the capability of evaluating the system's exposed images to ensure it was pointed at the correct field of view. This type of system is important, because to capture a transient optical event, a telescope must center the event in its field of view before the event disappears. The ability of the telescope to autonomously capture images and safely operate without operator intervention demonstrates that the technology and software is available for NDT automation.

In 2002, the RAPid Telescopes for Optical Response (RAPTOR) project, shown in Figure 2-6, became the first fully autonomous closed-loop robotic telescope, with the project headed by Vestrand [2002]. It is a fully autonomous robotic telescope with 0.4 m aperture and typical operating focal ratio f/5. It is equipped with a 1K x 1K pixel CCD camera employing a back-illuminated Marconi CCD47-10 chip with 13 μm pixels. The observatory consists of a wide-field telescope and a narrow-field telescope mounted on a platform that can swivel to any point in the sky in less than 3 seconds. RAPTOR

33

monitors the sky for optical transients, with the core of the system composed of two telescope arrays, separated by 38 km. Each telescope array has a real-time data analysis pipeline that is designed to identify interesting transients on timescales of seconds and, when a celestial transient is identified, to command the rapidly slewing robotic mounts to point the narrow-field "fovea" images at the transient, similar to how the cones in the fovea of the human eye sharply images a region of interest. RAPTOR distinguishes between transient optical events and nearby space junk, such as asteroids, with its stereovision.
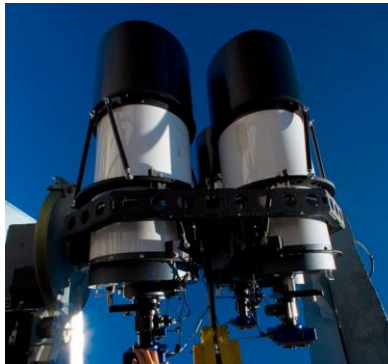
Figure 2-6. The RAPTOR telescope array. [Vestrand, 2002]

RAPTOR makes use of a real-time pipeline with a feedback loop (shown in Figure 2-7) that uses a collection of components and algorithms, ranging from data acquisition to source extraction, astrometry, relative photometry corrections and the actual smarts of transient detection. A feedback loop can be utilized in NDT automation to autonomously orient a sample based on the transmission histogram of a recorded radiograph. To detect a new object, RAPTOR compares the position and brightness of each object in the image with those of known objects identified in previous scans. After completion of each exposure, the raw images are combined with flat-field and dark frames to form corrected images, and sources are then extracted to form a source-object

file for each corrected image. The entire process of calibrated list extraction takes less than 10 seconds and runs in parallel for all of the stereoscopic array cameras. Astrometric and photometrics are then performed for forming the calibrated object list. The next component of the real-time analysis pipeline is the transient detection software, with the key for a real-time sky monitoring system being the elimination of false triggers.
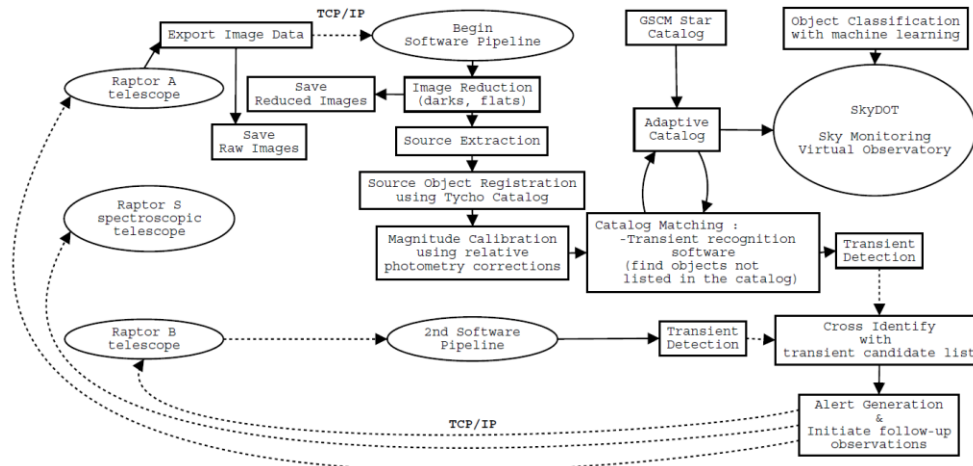
Figure 2-7. Flow chart of the basic components of the RAPTOR real-time pipeline and feedback loop. [Vestrand, 2002]

2.4 ROBOTIC NDT POSITIONING AND SAMPLE-EXCHANGE SYSTEMS

One of the major bottlenecks in the data collection process at beamlines is the constant need to change and realign a sample. This is a very time- and manpower-consuming task. The time it takes to change and realign the sample, together with the time it takes to go in and out of the experimental area often exceeds the time of actual data acquisition. Shu et al. [2002] at Argonne National Laboratory's Advanced Photon Source (APS) employs a high-precision robotic positioning system. APS has developed this system, an industrial Mitsubishi 6 DoF robot-based sample-exchange automation system with high positioning repeatability, for x-ray cryo-biocrystallography (shown in Figure 2-8). Samples are mounted to or retrieved from the x-ray diffractometer by the

robotic arm with programmable sequences. More than 100 samples can be run through the system without operator intervention. This system is fixed however, meaning that the motions are pre-programmed and hard-coded to complete the same tasks every time. Because crystallography studies involve repeated measurements of the same kind, it is especially well-suited for automation. This system incorporates a slim-finger design that allows a sample-mounting process with no beam stop interference. It is important to have little-to-none beam stop interference when performing radiography and CT applications as well.
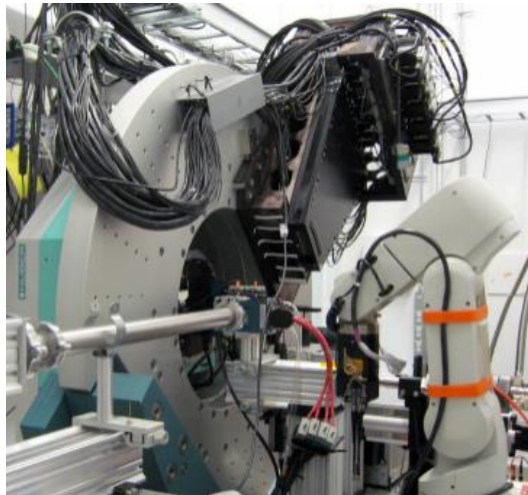
Figure 2-8. Robot-based sample-exchange automation system at APS Beamline 11-BM [Shu et al., 2002]

Similarly, Wasserman et al. [2012] at APS developed a fully automated x-ray crystallography system for drug discovery. The Cryogenic Automated Transfer System (CATS) robot performs queuing, mounting, and centering of samples (shown in Figure 2-9). The CATS can operate unattended for days at a time and has a failure rate of less than 0.1%. Parameters used in their software include: the location of the sample (4 parameters), x-ray energy, specimen-to-detector distance, initial φ angle for the crystal goniostat, number of images, spacing in φ for successive images, exposure time, etc.
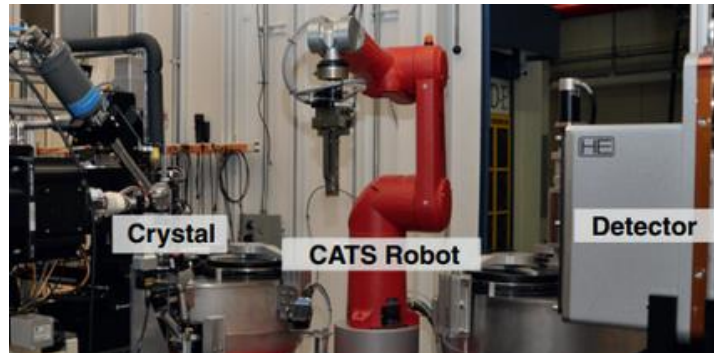
Figure 2-9. Crystallography end station at APS, showing the crystal position, CATS robot for crystal mounting, and CCD detector [Wasserman et al., 2012]

Chamberlain et al. [1996] discuss remote handling of radiographic equipment, including the guide tube and radioactive source. There requirements included positioning a 5 kg collimator with 2 mm offset accuracy and 1 degree direction accuracy. They concluded that a suspended 5 DoF Cartesian robot gave the preferred handling solution, because its large payload allowed heavy radiographic equipment to be mounted on the robot. This works shows that industrial, rotary robots are not the only solution to automating radiography applications.

Peterson et al. [2014] focused on the safety of the gripper interlock system for a gantry robot that handled 3013 canisters (same canisters as shown in Figure 1-4). Their system used relay logic to prevent a can from releasing except at designated locations. A collision sensor provides a signal to shut down the robot immediately whenever the part that is held deflects in the horizontal plane, or in the vertical axis. The grippers also feature mechanical fail-safes that maintain the grip on the canister if electrical power or pneumatic pressure is lost. These same types of safety features can be incorporated into the imaging robotic system to prevent potential damage to the payload, surrounding environment, and the robot.

2.5   TARGET HANDLING IN RADIOACTIVE ENVIRONMENTS

The particle accelerator facilities at CERN (the European Organization for Nuclear Research) have a remote target exchange system which consists of a six DoF industrial Kuka robot mounted on a linear axis (see Figure 2-10). These manipulators are used for the ISOLDE (Isotope Separator On Line Device Experiment). Their purpose is to reduce radiation exposure to personnel (the dose level at the target is 100 rad/hr) and reduce facility downtime when scheduled maintenance or breakdown repairs are needed. Even when the beams are no longer on, personnel access to certain areas of the accelerators is not possible until sufficient time has passed for the radiation levels to reduce due to decay. Remote inspection therefore allows the possibility for diagnosis to start before personnel access is possible; this offers earlier understanding of the problem and preparation of the repair and, as a result, reduced down time of high-value facilities. [Kershaw et al., 2013]

The robots are pre-programmed to carry out transfers of radioactive targets along predefined paths. They provide storage of parts, visual inspection, and increased flexibility. The issue of radiation damage to electronics has been addressed by removing and locating the electronics outside the radioactive area. Non-radiation-tolerant components, such as the wiring loom and some motor components, are replaced with radiation resistant alternatives. The robots use resolvers rather than encoders for axis position measurement, which allows for the relocation of electronics away from the robot arm possible without the need for major changes of the robot controller. The robot includes a gripper that is compatible with existing target interfaces. [Kershaw et al., 2013] For NDT imaging applications, it would be beneficial to add a linear axis in order to increase the robot's workspace.

Figure 2-10. Target area with suspended robot at CERN. [Kershaw et al., 2013]

2.6   RADIATION TRANSPORT CODES

Neutronic calculations are required to support the physics, safety, and engineering efforts in designs that involve high radiation fields. Monte Carlo codes such as Monte Carlo N-Particle (MCNP) [Pelowitz, 2011] give results based on the true physics of the problem and – as long as the geometry and physics options are correctly specified – thus the true solution with relatively high confidence. MCNP is a radiation transport code that has been under development for over half a century. For Monte Carlo codes, the particle flux is only calculated in regions specified by the user. Monte Carlo codes are typically slow to run, but accurately model and mesh complex geometries. Monte Carlo treats energy and direction as continuous during transport. High computational costs must be paid if high fidelity in energy, direction, location, and geometric detail is desired.

MCNP can be used for neutron, photon, and electron or coupled neutron/photon/electron transport, including the capabilities of calculating eigenvalues for critical systems. Point wise cross section data are used in MCNP calculations. For neutrons, all reactions given in a particular cross section evaluation (such as ENDF/B-VI) are accounted for. MCNP uses databases that describe all neutron interactions with materials, and these databases have been well tested though national and international data committees and are therefore considered very reliable. For photons, the code accounts for incoherent and coherent scattering, the possibility of fluorescent emission after photoelectric absorption, absorption in pair production with local emission of annihilation radiation, and bremsstrahlung radiation. A continuous-slowing-down model is used for electron transport that includes positrons, k x-rays, and bremsstrahlung, but does not include external or self-induced fields.

The model is submitted in the form of a text input file to MCNP. The input files contain the geometry information, source information, material information, and the type of output required in terms of standard tallies already provided in MCNP. MCNP can be used to predict and optimize the operating characteristics of the specific application, analyze beam characteristics, and to reduce radiation damage to the robotic system. With MCNP, one can analyze the effect of neutron scattering as the experiment is designed. Although there might be uncertainties in the model and, to a lesser extent in the database, one can get a representative picture of scattering in order to minimize dose collected by the hardware.

In MCNP, all tallies are normalized to one "starting" particle except in KCODE criticality problems, which are normalized to one fission neutron. Since, the MCNP results are normalized to one source particle, the result has to be properly scaled in order to get absolute comparison to the measured quantities (i.e. flux, reaction rate, fission

density, etc.). For the source definition in MCNP, the total number of source particles released from the source is defined using the NPS card.

2.7   X-Ray and Neutron Interaction and Radiographic Characterization

2.7.1   X-Ray Imaging Theory

X-rays, here defined as 0.1-10 MeV *bremsstrahlung* photons, and can interact with matter either through elastic or inelastic scattering from atomic electrons and the nucleus for higher energies. There are three dominant physical processes responsible for attenuation of an x-ray signal: photoelectric effect, Compton scattering, and pair production. At low energies, the photoelectric effect (i.e. absorption) has the largest cross section. It occurs when the total energy of an incoming x-ray photon is transferred to an inner electron, causing the electron to be ejected. Near 1 MeV, Compton scattering (i.e. inelastic scattering from bound electrons) has the largest cross section. In Compton scattering, the incoming photon interacts with an outer electron, ejecting the electron and losing only part of its own energy, after which it is deflected in a different direction. Figure 2-11 graphically illustrates the difference between photoelectric effect and Compton scattering. Above 1 MeV, pair production becomes the dominant interaction. In pair production, the photon interacts with a nucleus and is transformed into a positron-electron pair, with any excess photon energy transferred into kinetic energy in the particles produced.

The sum of these interactions gives a cross section that has a minimum at photon energies near 4 MeV. The minimum cross section provides the longest mean free path, which is 25 g/cm^2 in heavy metals. The practical importance of the distinction between mechanism is that photoelectric effect is proportional to Z^3, where Z is the atomic number of an atom in the attenuation material, whereas Compton scattering and pair

production are proportional only to Z. [Markowicz, 1993] As a result, low-energy x-rays are more sensitive to differences in composition than higher-energy ones.
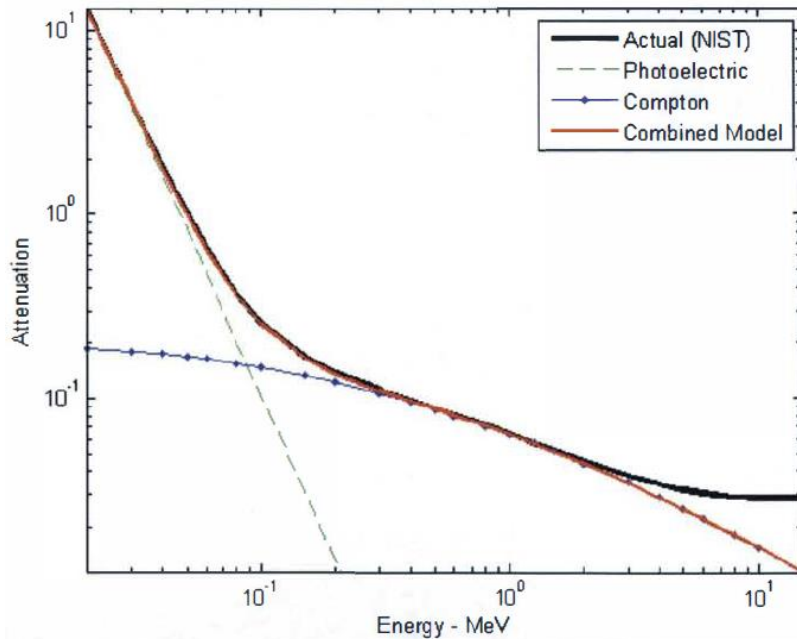
Figure 2-11. Attenuation vs. photoelectric-Compton attenuation model for Z=20.

2.7.2 Neutron Imaging Theory

Neutron imaging is complementary to x-ray imaging because of the differences in their respective attenuation coefficients, which are shown in Figure 2-12. It is apparent that there is large neutron attenuation for many light elements (H, Li, B) and a relatively small attenuation for heavier elements. X-ray and neutron attenuation depends on energy, density, and atomic number. Figure 2-12 shows the variation in attenuation as a function of Z for x-rays of 100 and 600 keV as well as thermal neutrons. Regarding x-rays, as Z and the size of the atom increases, the attenuation increases as the density of the atom's atomic electron cloud increases due to the energy-dependent x-ray attenuation coefficient. The x-ray attenuation number is linearly dependent on the density of the material (i.e. twice as many molecules of a material stop twice as many x-rays) and non-

linearly dependent on the atomic number of the material. Since x-rays interact with the electron cloud of a target atom, this type of relationship is expected. Neutrons are uncharged, so they interact with the atom's nucleus, not with the electron cloud. X-ray attenuation is non-linear with energy due to multiple effects, including the photoelectric effect.
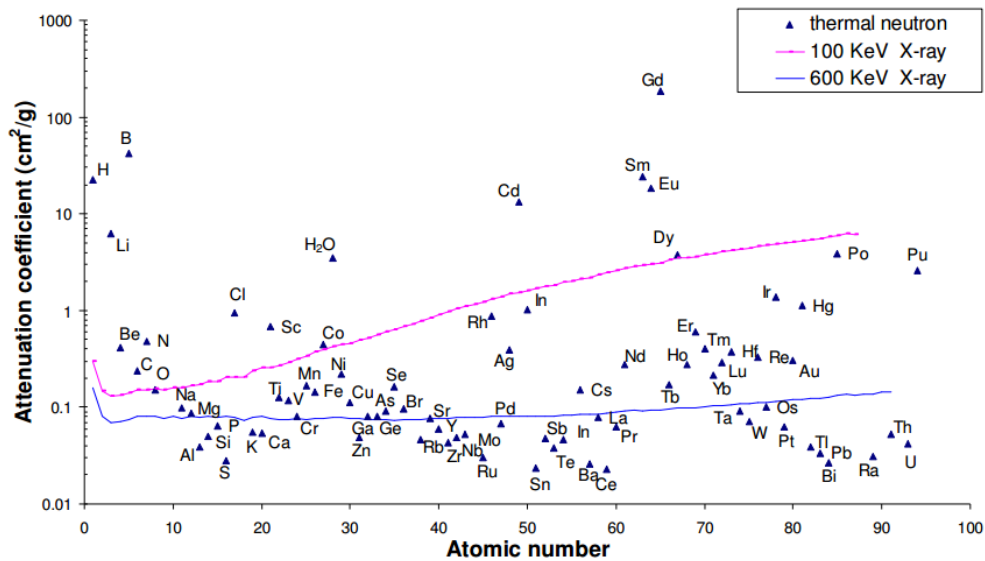
Figure 2-12. Comparison of attenuation coefficients between thermal neutrons and x-rays for various nuclides. [Cao, 2007]

Neutron imaging offers some explicit advantages over x-ray imaging. A major limitation of x-ray imaging is that x-rays are heavily attenuated in thick materials. X-ray absorption increases rapidly with increasing atomic number (Z). This limits the use of x-rays in viewing low-Z materials, such as aluminum or plastic, which are obscured by higher-Z materials, like iron or lead. In addition, x-ray scattering and detection characteristics at higher x-ray energies make difficult the measurement of important quantities like material density profiles and the detection of "buried features," such as a small void or gap deep inside an object.

Neutron cross sections, which are almost independent of the Z of the material, result in neutron imaging capable of discerning materials of similar Z and/or low Z materials even when they are present inside high Z surroundings. Also, hydrogen, which is an important element in determining the properties of many materials, can be imaged even if present in minute quantities due to its significant neutron scattering and absorption cross sections. Neutrons are also capable of differentiating between isotopes of an element. Neutron attenuation coefficients are low for most metals and high for hydrogenous materials such as water. The higher the cross-section of the material, the more likely that neutrons or gamma rays will be removed from the beam and not land on the imaging object, resulting in darker pixels. The more particles that land on the imaging object, the brighter the image.

A drawback of neutron radiography, especially when the neutron beam source is from a nuclear reactor, is that there are other types of radiation that are coincident with the fission neutrons used on the image plane that have a negative effect on the final neutron beam incident on the sample. These are in the form of radioactive fission products that decay via alpha, beta, or gamma emission. Gamma radiation is typically the primary source of radiation negatively affecting a neutron radiography system. For example, at beam port 5 at U.T. Austin's TRIGA research reactor, the gamma exposure has been previously reported using a Victoreen 450 by Cao [2007]. The exposure rate at reactor power of 950 kW is reported to be 11.266 R/hr and the gamma intensity at this point is calculated to be 6.22×10^6 $\gamma/cm^2/s$ using Equation (2-4), where I is the gamma ray intensity, E is the gamma ray energy (here assumed to be 1 MeV), $(\mu_a/\rho)^{air}$ is the mass

absorption coefficient in air [cm^2/g], and $\dot{X}$ is the gamma exposure rate. This radiation creates noise in the sensitive electronics of the CCD camera, therefore it is important to shield the camera from radiation.

$$I = \frac{\dot{X}}{1.83x10^{-8}E(\mu_a/\rho)^{air}}$$

(2-4)

2.7.3   Nucleon-Nucleus Interaction and Nuclear Resonance Imaging

The most basic nucleon-nucleus measurement is that of the total cross section. For neutrons, which interact almost entirely by this interaction when they encounter materials, the total cross section gives the mean free path, or the average distance to first collision, for neutron transport calculations. The total cross section is a measure of the effective size of a nucleus. The total neutron cross section as a function of neutron energy in the range 5 to 560 MeV is shown in Figure 2-13. The regular "waves" in the cross sections are evidence of the interference of the neutron wave transmitted through the nucleus with that passing by the nucleus. [Abfalterer et al., 2001]

Another feature based on neutron cross sections and nuclear scattering is the existence of nuclear resonances, which increase or decrease the chance for a neutron to scatter from a nucleus at particular incident neutron energies. The energies at which resonances occur are specific to each chemical element and isotope. By producing neutron beams using short proton pulses, such as done at LANSCE, neutrons of different energies can be selected based on their time of arrival at an imaging detector. If the detector can resolve neutrons that are closely spaced in time (hence in energy), then observing individual resonances is possible. By selecting images taken at certain times with respect to the proton beam pulse, an image showing the location of a particular element or isotope can be created. Energy-dispersive neutron radiography allows one to

visualize, for example, only tungsten by viewing the image at an energy where tungsten shows an absorption resonance. This is referred to as energy resolved neutron imaging. Figure 2-14 shows a neutron transmission spectrum of simulated nuclear reactor fuel pellets taken with a micro-channel plate detector. Resonance dips due to uranium and tungsten in the fuel pellets are indicated in the figure.
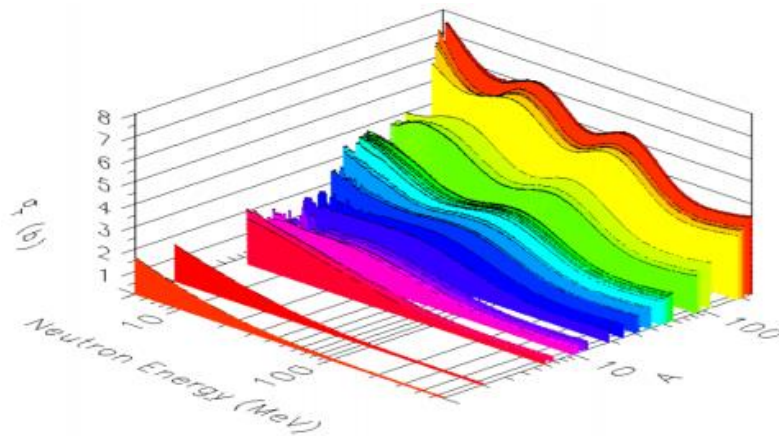
Figure 2-13. Neutron total cross sections from 5 to 560 MeV for nuclei with masses (A) from 1 to 238. [Abfalterer et al., 2001]
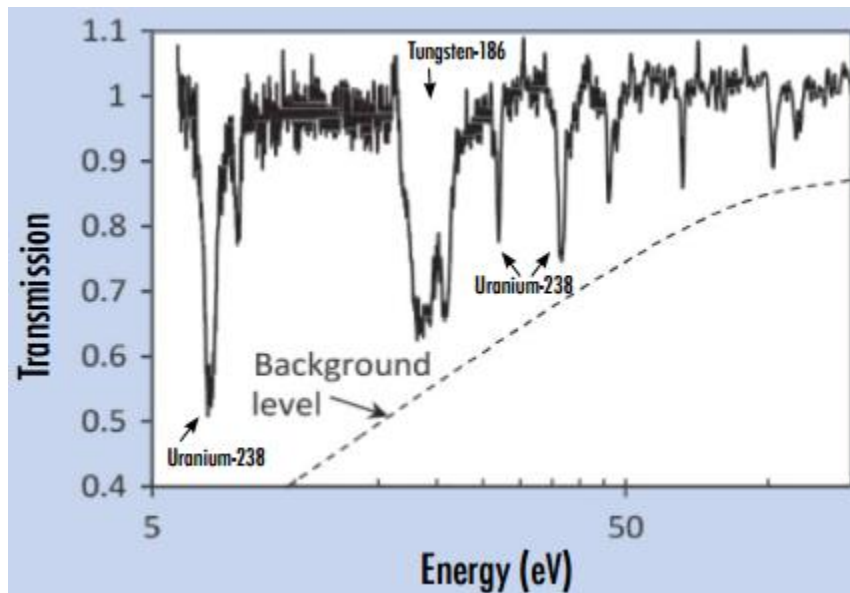
Figure 2-14.Neutron transmission spectrum showing resonance dips due to uranium and tungsten in simulated reactor fuel pellets. [Kippen et al., 2014]

2.8   RESIDUAL VIBRATIONS

Some radiography applications, especially neutron radiography, exposure times on the order of several minutes are required. Therefore, vibrations must be as small as possible while the robot is holding the part during an exposure. With robotic handling applications, due to rapid point-to-point movements, manipulators can exhibit large vibrations after reaching their destination location. Tao et al. [2006] analyzed the root cause of residual vibrations as well as developing an "acceleration smoother" in order to smooth the command trajectory and suppress vibrations. This solution can be easily implemented in practice without redesigning the robot hardware or control system. Tao achieved over 40% reduction in both vibration amplitude and settling time.

Automating NDT applications will involve a robot going through a series of motions involving accelerating to an operational speed and decelerating to a full stop. Abrupt changes in acceleration or deceleration often result in residual vibrations, which can cause part slippage and lead to long settling time and thus should be minimized The image must be taken after the residual vibrations have reduced to the point that blurriness is not an issue in the resulting image.

To reduce vibration, trajectory smoothing, which employs a multi order polynomial in time for trajectory generation, can be utilized in the control scheme. [Lambrechts et al., 2004] Trajectory smoothing provides a smooth acceleration/deceleration and accounts for the motor amplifier's electrical saturation feature. Smoothing the acceleration may cause longer commanded motion time, but shorter settling time, resulting from the vibration decaying quickly.

2.9   STANDARDS FOR QUANTIFYING ACCURACY AND REPEATABILITY

Robotic companies, as an industrial standard, publish the repeatability specifications of each robot. These specifications are determined by performing stringent

experiments in accordance with ISO 9283 [1998] or ANSI/RIA R15.05-1 [1990]. These are the norms used to define the repeatability and accuracy for the end-of-arm position of robots. If the target is always the same, and the move is repeated several times, repeatability measures the dispersion between the final points. Accuracy characterizes the distance between the cloud of points and the commanded position. The ISO 9283 and ANSIA/RIA R15.05-1 standards measure the repeatability and accuracy at pessimistic values, using maximum speed and maximum payload. A simplified summary of the protocol is as follows:

1. Warm up the robot before testing until steady state conditions are reached (i.e. thermal stability of motors and gearboxes) under a normal 71ºF environment.

2. Send identical commands to bring the robot to 3 different positions in sequence.

3. Measure the reached position using 2 cameras and an optical target carried by the robot, or other instruments.

To obtain the repeatability and accuracy from the data, the following calculations are used for N measurements, with reached position (Xr, Yr, Zr), and with commanded positions (Xc, Yc, Zc):

Average:

$$\bar{X} = \frac{1}{N}\sum_{i=1}^{N} X_r \qquad\qquad (2\text{-}5)$$

$$\bar{X} = \frac{1}{N}\sum_{i=1}^{N} X_r \quad \bar{Y} = \frac{1}{N}\sum_{i=1}^{N} Y_r \text{ , and } \bar{Z} = \frac{1}{N}\sum_{i=1}^{N} Z_r \qquad (2\text{-}6), (2\text{-}7), \text{ and } (2\text{-}8)$$

Standard deviation:

$$D_i = \sqrt{(X_r - \bar{X})^2 + (Y_r - \bar{Y})^2 + (Z_r - \bar{Z})^2} \qquad\qquad (2\text{-}9)$$

$$\bar{D} = \frac{1}{N}\sum_{i=1}^{N} D_i \qquad\qquad (2\text{-}10)$$

$$S_D = \sqrt{\frac{\sum_{i=1}^{N}(D_i - \bar{D})^2}{N-1}} \qquad (2\text{-}11)$$

Positioning repeatability according to ISO 9283:

$$RP_D = \bar{D} + 3 * S_D \qquad (2\text{-}12)$$

Positional repeatability according to ANSI/RIA R15.05-1:

$$RP_D = \bar{D} \qquad (2\text{-}13)$$

Mean position accuracy according to ANSI/RIA R15.05-1:

$$A_p = \frac{1}{N}\sum_{i=1}^{N}\sqrt{(X_r - X_c)^2 + (Y_r - Y_c)^2 + (Z_r - Z_c)^2} \qquad (2\text{-}14)$$

ISO 9283 considers the mean plus three times the standard deviation. The 3σ interval means that the position of the robot will be inside the repeatability range 99.7% of the time. Measurements of the final robot positions show that they are near the commanded point and all of the final positions constitute a cloud of points. Figure 2-15 illustrates the ISO 9283 approach of accuracy and repeatability. The random variable "distance between the point (Xr, Yr, Zr) and the barycenter ($\bar{X}$, $\bar{Y}$, $\bar{Z}$)" is D, from Equation (2-9).
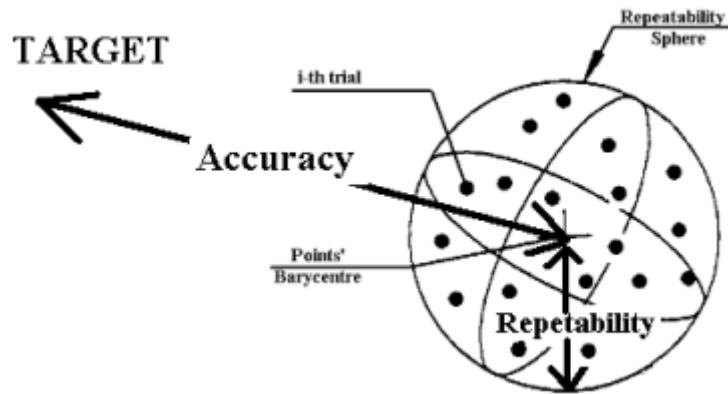
Figure 2-15. ISO 9283 approach to accuracy and repeatability. [ISO 9283, 1998]
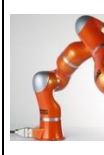
The methods and testing conditions of ISO 9283 are elaborate and complete, but they are meant for general robotic operation, whereas we want to use tests related to specific NDT tasks. Also, less than 10% of robotic companies use the complete ISO 9283 norm since it is a complex and costly method. [Nof, 1999]

2.10   SURVEY OF HIGH PRECISION ROBOTS

The asserted capabilities of various robotic systems (manipulators and hexapods) are shown in Table 2-1. Asserted values are taken at maximum payload and 100% speed. [ISO 9283, 1998] The SIA5 with the FS100 controller is approximately $56,000 total. SCARA robots typically have 4 DoF and high repeatability values. However, they could only rotate the part along the part's z-axis due to the SCARA's geometry. Therefore it would be best suited for CT applications that only requires the part to be picked up and rotated along one-axis. For large, heavy parts, hexapods could possibly be used, since they allow for the surface to be tilted with high stability.

Table 2-1. Comparison of potential robotic systems for NDT applications.

Robots	Yaskawa HP20D	Yaskawa MH5F	Yaskawa MH6	Yaskawa SIA5	Yaskawa YS SCARA	KUKA AGILUS sixx	M-850 Hexapod[2]	KUKA LWR
DoF	6	6	6	7	4	6	6	7
Payload (kg)	20	5	6	5	5	6	250	7
Repeatability (mm)	0.06	0.02	0.08	0.06	0.01	0.03	0.001	0.05
Vertical Reach (mm)	3063	1193	2486	1007	N/A	1620	N/A	1178
Horizontal Reach (mm)	1717	706	1422	559	850	901.5	N/A	790
Weight (kg)	268	27	130	30	37	52	17	16
Cost ($)	62,000			39,375				150,000

It may be necessary for the gripper to pick up the part with a stable grasp (i.e. without the part moving). Instead of using a gripper, having the robot hold a tray or rod with the part rigidly attached/fixed to it would allow the part to be radiographed without the part moving. If using a gripper, the gripper material should be as transparent to x-rays or neutrons as possible. For example, a carbon fiber hand filled with foam would be sufficiently transparent to x-rays. [Keyser, 2011] states that a 0.8 mm thick carbon fiber piece has an attenuation of about 15% at 15 keV. A lightweight carbon fiber gripper would also reduce the manipulator wear and tear and would reduce its contribution to the manipulator's overall payload without compromising strength. One such robotic hand on the market is the Kinova JACO (see Figure 2-16), which is a three-fingered carbon fiber gripper. [Kinova, 2012] There are rubber grips towards the end of the fingers for added traction. This gripper can be sold separately from the rest of the JACO manipulator and

---

[2] The travel range for the hexapod is 50 mm in the x- and y-directions and 25 mm in the z-direction

includes the required JACO Simulator box for a total of $5,750. The payload for this gripper is approximately 2 kg.

Figure 2-16. Example grasp of a Kinova JACO gripper. [Kinova, 2012]

Materials that have high neutron transparency include pure aluminum, 1050 aluminum alloy, and carbon fiber. According to Reillo [2010], at neutron energies below 200 keV, carbon fiber has a higher transmission probability than Al, due to the presence of resonances in the Al neutron cross-sections. Al has a higher neutron transmission probability than carbon fiber at neutron energies above 200 keV. A gripper could be designed using these materials for use with neutron radiography/computed tomography if the part is to be held with the gripper.

Since radiation rapidly degrades common materials used in robotic grippers, such as rubber and wire insulators, it is important to reduce exposure to these parts. Also, since the gripper is the part of the robot that will receive the highest neutron flux, choosing the appropriate material is critical to ensure reliable operation. Aluminum can be used as the primary gripper material since it has a relatively small neutron absorption cross-section, which reduces the likelihood of neutron activation. If the gripper were to become activated, aluminum has a very short half-life, and could be handled within minutes. An additional prismatic joint would minimize irradiation to electronic components in the

gripper and the manipulator. Image background subtraction can be used to decrease the impact of any background radiation. [Berger, 1977]

2.11   BUILDUP FACTOR

The buildup factor is a dimensionless multiplication factor that corrects for scattered particles. It is the ratio of the intensity of the total radiation reaching a point, to the intensity of the uncollided radiation reaching the same point. [Hopkins, 2010] It is important to include the buildup factor because it accounts for collided and scattered neutrons that still contribute to the imaging detector. The robot and gripper will cause multiple neutron and x-ray scattering. If only the unscattered particles would contribute to the detector, the buildup factor would be one. This is rarely the case however; in most cases the buildup factor will be larger than one. The buildup factor becomes more important when dealing with broad beam geometry rather than narrow beam geometry (see Figure 2-17). This is why it is important to have a collimated beam in radiography applications.
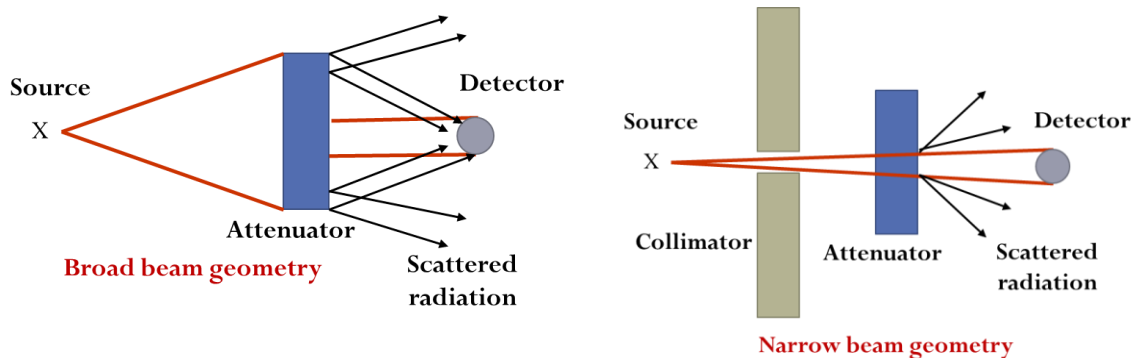
Figure 2-17. Broad beam (left) and narrow beam (right) geometry. The attenuator would be the robot in this case.

53

2.12   RADIATION DAMAGE TO ROBOTS

It was a "big bang" on July 9, 1962, that catapulted the reliability of radiation-damaged solid-state electronics to the center stage of world politics. [Hughes et al., 1989] On that day the U.S. high-altitude nuclear device Starfish was detonated. This was followed by several similar Russian tests later that year. The resulting nuclear contamination of the exoatmosphere generated sufficient electronic perturbation to the Van Allen belt to cause failure of the Telstar 1 communications satellite. This resulted in an incentive and challenge to develop survivable space electronics and acquire an understanding of the nature of radiation damage to semiconductor devices. Even to this day, interest persists in the subject of radiation damage to semiconductor devices and electronic equipment, which includes robots. Fault tolerance of industrial robots has been the subject of many studies, of which a general survey has been published. [Lumelsky and Cheung, 1993]

2.12.1 Types of Radiation Damage

One of the major challenges for robotics in high radiation environments is the expected radiation damage to its electronic devices. Radiation damage depends on the material irradiated, the type of radiation, and the energy of the incident radiation. The primary radiation environments that degrade or damage electronic materials and devices include outer space, nuclear reactors, radiation processing activities, nuclear weapon, and controlled fusion facilities. [Holmes-Siedle and Adams, 1993] Within nuclear reactors, electronic equipment is used to control robots and other machinery remotely. Radiation effects on electronics are normally divided into three different categories according to their effect on the electronic components.

Total ionizing dose (TID): Radiation energies are usually large enough to cause core-electron transitions in individual atoms. Ionizing damage occurs when energy

absorbed by electronic ionization in insulating layers, predominately SiO_2, liberates charge carriers. These charge carriers diffuse or drift to other locations where they are trapped, leading to unintended concentrations of charge and parasitic fields. Energy loss in semiconductors and inorganic insulators are ultimately converted into electron-hole pair production. Both energetic particles and photons are capable of causing ionization damage. TID effects on integrated circuits cause the threshold voltage of metal-oxide-semiconductor (MOS) transistors to change because of trapped charges in the SiO_2 insulator. Non solid state components like resistors and capacitors are far more rugged than transistors. It has been found that high resistance value resistors are more sensitive than resistors with a low resistance value. For sub-micron devices these trapped charges can potentially "escape" by tunneling effects. Commercial digital complementary metal-oxide-semiconductor (CMOS) processes can normally withstand a few Krads without a significant increase in power consumption. Modern sub-micron technologies tend to be more resistant to total dose effects than older technologies (in some cases up to several hundred Krads). High performance analog devices (e.g. amplifiers, ADC, DAC) may potentially be affected at lower doses. [Holmes-Siedle and Adams, 1993]

Ionization effects depend primarily on the absorbed energy, independent of the type of radiation. At typical incident energies, ionization is the dominant absorption mechanism, so that ionization damage can be measured in terms of energy absorption per unit volume.

Displacement damage: Starting with particles, we note that physical displacement of atoms from their original positions is the major form of damage created. The particle trajectory, and the damage produced, depends on its energy, mass, and charge, as well as the nature of the matrix. Incident neutrons may displace silicon atoms from their lattice sites of active devices and thereby affect their function by altering the electronic

characteristics of the crystal. Bipolar devices and optical devices can be very sensitive to this effect. CMOS integrated circuits are normally not considered to suffer degradation by displacement damage.

Materials exposed to an energetic-particle environments may also become radioactive. Neutrons, protons, and nuclei are all capable of transforming stable nuclei into radioactive ones by removal of nucleons, or in the case of low-energy neutrons by neutron capture. Depending on the particular atom, such induced radioactive decays with a characteristic half-life through emission of gamma rays, beta rays (electrons), and alpha particles.

Different classes of solids suffer different levels of particle-induced damage. Most vulnerable are semiconductors and insulators because significant changes in electrical properties occur. Avery [1979] noted radiation induced failures at less than 300 rads in some semiconductor devices. Metals, on the other hand, suffer some mechanical hardening and embrittlement but no appreciable change in electrical behavior. Furthermore, damage to metals from gamma and x-rays is negligible, unlike their effect in nonmetals.

Over time, displacement damage in a PN junction can partially repair itself due to dopant ions diffusing through the crystal back towards their correct positions. High temperature greatly speeds up the ion diffusions, so degraded components are sometimes heated to remove the damage faster. [Holmes-Siedle and Adams, 1993] At lower temperatures, longer times are needed to anneal the damage since the damage can stay around longer and enhance the dopant diffusion.

Soft error and single event effects (SEE): Computer circuits function by identifying small packets of charge as elemental bits of information. Any noise that modifies this charge also may change the information stored. This can happen, for

56

example, when radiation, a source of this noise, impacts and alters the electrical state of an internal node. This can cause a false logic transition, such as a bit flop. For example, this occurs when a gamma ray strikes a memory element and changes a bit value, leading to a software failure. Such errors may mean data corruption, execution of wrong commands, or even a "locking up" that requires re-initialization. In digital electronics, these errors are referred to as soft errors, soft fails, or single event upsets (SEU). SEU are an effect of SEE that occur when the deposited charge is sufficient to flip the value of a digital signal. SEU normally refer to bit flips in memory circuits, but may also in some rare cases directly affect digital signals in logic circuits. These errors do not result in permanent damage to circuits. Soft errors, do not necessarily affect the computer user, because the system may be turned off or the incorrect memory bits may be overwritten before they are used. In microelectronic circuits employed in satellites, digital avionics, high-flying aircraft, and in terrestrial electronics and computers, soft errors are a major concern. To circumvent soft-errors from occurring, analog devices can be used, or digital electronics can be remotely located outside the radiation area. In nuclear power plants, for example, computers are typically kept outside the containment building with cabling running through the containment wall to the hardware. Analog components tend to degrade gradually, whereas digital components tend to fail more suddenly. [Wyllie, 2014]

Soft errors are not a cumulative effect but an effect related to single individual interactions in the silicon. Highly ionizing particles can directly deposit enough charge locally in the silicon to disturb the function of electronic circuits. Neutrons greater than 20 MeV can generate recoils that deposit sufficient charge locally to disturb the correct function of the circuit. [Wyllie, 2014]

We are primarily concerned with the consequences of atomic displacements and ionization in materials caused by radiation. Though both processes occur for all materials,

damage to metals/inorganics is principally related to displacement effects. In the flow-chart below (Figure 2-18), radiation damage onto particle- and photon-induced categories is summarized. Of particular interest is the long-lived, as well as transient, damage produced by the particular radiation. These mechanisms are important in transistors and integrated circuits, which are prevalent in industrial robots.
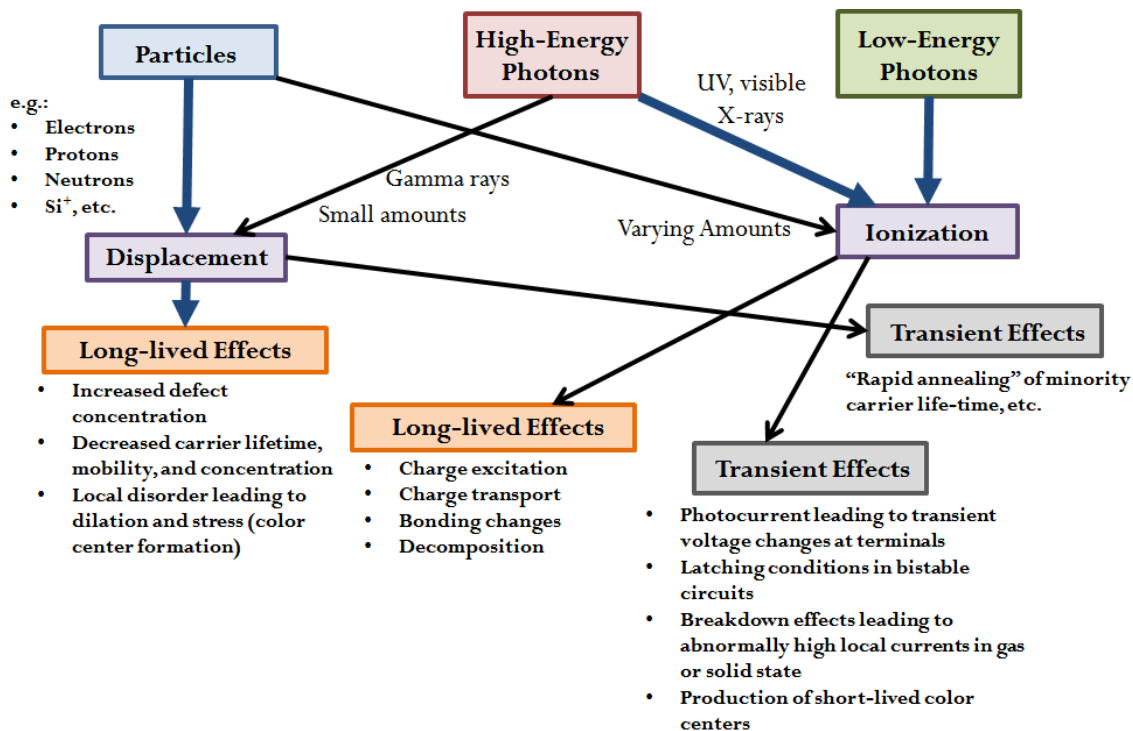
Figure 2-18. Summary of radiation-induced degradation effects in solid-state materials and devices. [Holmes-Siedle and Adams, 1993]

Previous studies have examined the effect of total irradiation dose on bipolar transistors and electronics, and found lowered current gain for increased doses. [Grillo et al., 1996] Radiation damage to bipolar transistors is characterized by a rapid decrease of the current gain in the first few hundred Krads, with a leveling off at much larger total doses. The existence of dose rate effects has been observed in radiation damage to CMOS transistors [Fleetwood et al., 1987] and silicon detectors [Ziock et al., 1994], and in both

cases they are explained by annealing which occurs during and after the irradiation. For example, for higher dose rates (on the order of Mrads) the total damage to the transistor current gain is not apparent until an annealing period of about a week at room temperature has elapsed. They showed that radiation damage increased by a large factor within the first week, but with very little change afterwards. Therefore, measurement taken directly after irradiation would yield reduced damage effects for these higher rate exposures. However, for lower dose rates, little change appears between measurements taken directly after the irradiation, and those performed a week later. Thus, for exposures lasting much longer than one week, the radiation damage in low rate exposures will have annealed out during the irradiation time and the measurements taken immediately after the final irradiation will reflect the stable radiation damage.

In order to analyze the impact of radiation-induced degradation on the reliability of the whole system, three questions must be addressed: 1) how critical is a failure in terms of the global reliability of the system; 2) how does the component degrade (sudden failure, failure over time, etc.); and 3) what degree of radiation tolerance is available for special versions of the components. The radiation induced decrease in performance or total failure of electrical motors can be caused by several mechanisms: a loss of insulation in the motor coils or in the connection wires; embrittlement of the connections; hardening of the lubricant in the bearings and gearbox; and degradation of the commutation electronics. Motors are usually vital parts of the manipulator and failure can lead to the locking of joints in a configuration where retrievability is very difficult. [Meieran, 1993]

The impact of radiation damage on an industrial robotic arm is not well understood, but there are numerous examples of systems working in similar environments [El-Guebaly, 1997]. There is an added difficulty when analyzing robot systems for

hazardous environments, over the case of more traditional robot applications. Failure rate data is typically not available for the conditions present in hazardous and/or radioactive environments. In addition, many robot systems used in these environments are "one-of-a-kind" systems. Thus there is little fault or reliability data available for these systems, even in conventional or test conditions. Clearly, the best mitigation technique is to avoid the problem, either by shielding or by reducing the electronics in the radiation environment to the minimum required to do the job.

2.12.2 Neutron Damage

Silicon electronics incur serious damage at neutron energies of 10^{14} n/cm^2. This is considered the maximum neutron flux that the robot can receive without failure. Bipolar devices on silicon tend to show changes in electrical parameters at levels of 10^{10} to 10^{11} neutrons/cm^2. CMOS devices are not affected until about 10^{15} neutrons/cm^2. [Messenger, 2014]

Miclea et al. [2005] studied the effects of neutron irradiation on the electromechanical coupling coefficient, k_p, and mechanical quality factor. The electromechanical coupling coefficient is defined as the square root of the electrical or mechanical energy produced per unit total energy consumed. They examined the behavior of these values as a function of integrated neutron fluence and doping in 13 mm diameter by 1.5 mm thick cylindrical discs prepared via powder processing and sintering. One of the two materials studied was acceptor doped with Mn and donor doped with Nb in a composition of $PbZr_{0.45}Ti_{0.49}Mn_{0.17}Nb_{0.033}O_3$ while the other, a donor doped material, had a $PbZr_{0.51}Ti_{0.463}Nb_{0.02}Li_{0.007}O_3$ composition. The authors referred to these samples as hard and soft lead zirconate titantate. Figure 2-19 shows the results of the mechanical tests upon neutron irradiation to various fluences. Evidently there is a significant change

in both properties for neutron fluences above 10^{14} cm^{-2}. This means that some damage to the material's crystal lattice can occur at these high neutron fluence rates. Most notably, there is an increase of over 100% within the mechanical quality factor in both materials at the maximum neutron fluence of 10^{18} cm^{-2}, indicating a significant increase in hardness and mechanical losses, presumably due to irradiation induced defects. In comparison, aluminum and its alloys have demonstrated high tolerance to neutron bombardment, with void formation not observed in 99.9999% pure aluminum until fluences greater than 1.5 x 10^{19} n/cm^2 at neutron energies greater than 0.1 MeV. [Packan, 1971]
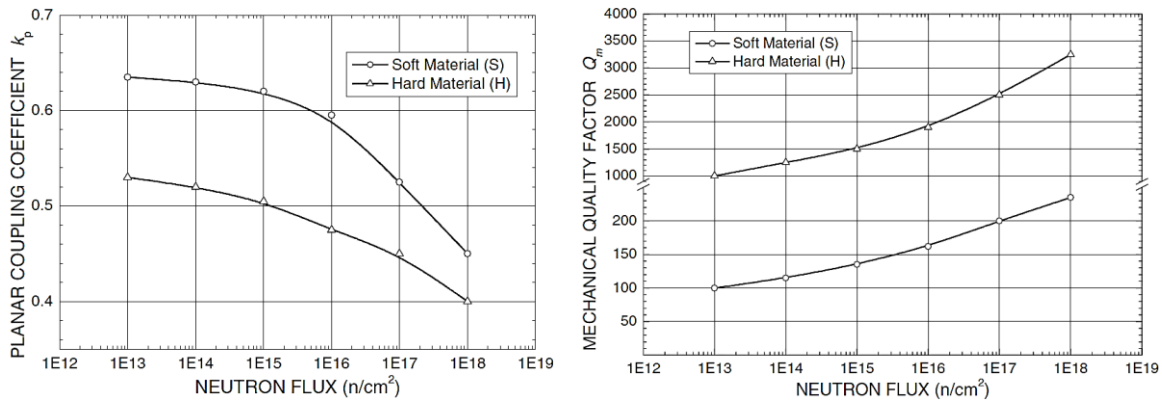
Figure 2-19. Changes in electromechanical coupling factors (left) and changes of the mechanical quality factor (right) as a function of the neutron fluence for irradiated samples of the acceptor doped (hard) and donor doped (soft) disks. [Miclea et al., 2005]

2.12.3 Radiation Tolerant Components for Robots

Passive transducers without any built-in signal processing have been used for decades in the nuclear industry. Measurements of temperature, pressure, acceleration and strain have been achieved using mineral insulated systems, avoiding any organic material in the transducer or in the cable. The radiation tolerance of such components is usually very high. However, for remote handling, the radiation tolerance is not so straightforward, although remote transducers can be constructed without embarked electronics. Most of the available commercial products for position and force sensing

focus on very small dose rates, over long periods, or very short energy pulses. Their developments were triggered by space or military market incentives. They usually tolerate gamma doses up to 1 Mrad. In nuclear reactors and reprocessing plants, remotely controlled equipment will see higher doses accumulating above 100 Mrad. [Decreton et al., 1997]

Robots using radiation tolerant design techniques can successfully be applied to robotic equipment to give reliable and safe solutions for tasks in hazardous environments. Sias and Tulenko [1993] have addressed the availability of rad-hardened microcomputers for robotic applications. For example, a modified Staubli Unimation Puma 760 robot operated in the Windscale Vitrification Plant (WVP) at Sellafield for approximately 740 days, performing over 10,000 swabs on about 700 containers (Figure 2-20). Dose rates at the surface of the containers reached 1 Mrad/hr. Parts that were modified to make the robot radiation tolerant included motors, brakes, optical shaft encoders, seals, bearing, limit switches, greases, adhesives and paint, as well as electronic components. The total dose estimated to have been received by the wrist and forearm areas of the robot is approximately 180 Mrad. [Meiran, 1993]
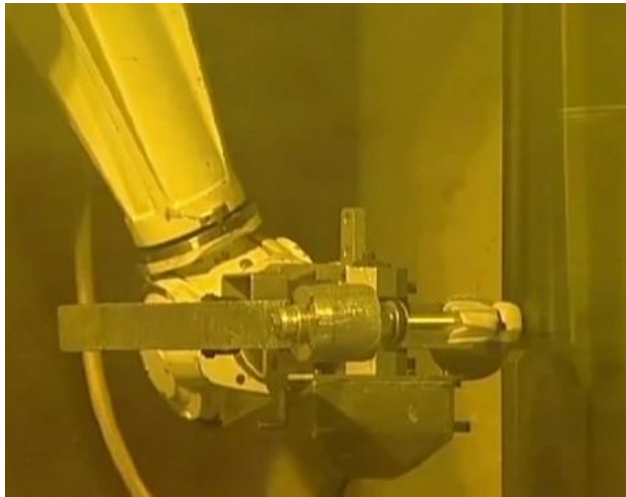
Figure 2-20. WVP robot swabbing a radioactive container. [Meiran, 1993]

Since radiation rapidly degrades common materials used in robotic grippers, rubber and wire insulators, a simple 4-bar linkage, two-fingered gripper will be designed and utilized initially (see Figure 2-21). Exposed wires will be minimalized since neutrons degrade rubber and wire insulators. Also, since the gripper is the part of the robot that will receive the highest neutron flux, choosing the appropriate material is critical to ensure reliable operation. Aluminum 6061-T4 will be used as the primary gripper material since it has a relatively small neutron absorption cross-section (making it nearly transparent to thermal neutrons), which reduces the likelihood of neutron activation. If the gripper were to become activated, aluminum has a very short half-life, and could be handled within minutes. Aluminum and its alloys are widely used in water-cooled research reactors due to their low thermal neutron absorption cross-section, their high tolerance to radiation damage, short activated total half-life, adequate strength, corrosion resistance, and low cost. Work done by King et al. [1973] on Aluminum 6061 showed that the alloy increases slightly in strength but loses ductility as a result of low fluence irradiation. King et al. [1973] discovered that age-hardened 6061 aluminum demonstrates the best resistance to void formation of any irradiated aluminum alloy studied. The design

will also include a prismatic joint utilizing a ball screw extender with a 30 cm range, capable of lengthening the distance from the last joint of the robot to the location where the object is grasped. This prismatic joint will allow the irradiation to electronic components in the gripper and manipulator to be minimized. This gripper design would better suit the SIA10 manipulator than the SIA5, which have payloads of 10 and 5 kg respectively, since the total weight of the design is 4.16 kg.
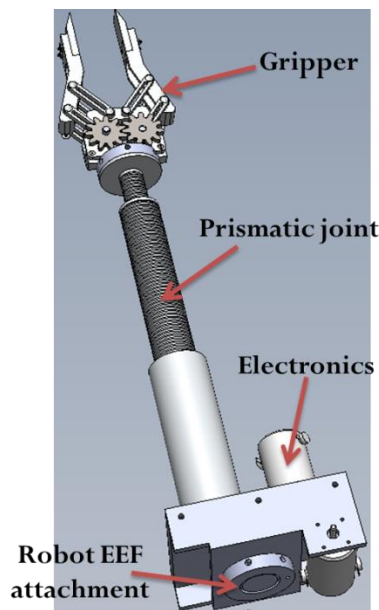
Figure 2-21. Gripper designed to be used in high neutron radiation environments.

2.13 LITERATURE REVIEW DISCUSSION

Utilizing robotics for NDT imaging applications greatly reduces radiation dosage to personnel. It also allows for automating these processes, resulting in the elimination of manual steps. Since automating imaging processes results in less time spent performing the process, it leads to reduced amounts of radiation energy produced. It also reduces or eliminates time-consuming and costly re-shoots. Automating imaging processes significantly increases productivity, since personnel no longer lose time positioning the

part, the film or radiographic plate, and the active source in the relative locations needed to produce each image. It also reduces the induced wear from on/off operations of an x-ray source. Robotic systems are now in use in NDT facilities. Some facilities have been using robotic systems for years to conduct in-motion radiographic inspection.

Before the full-impact of robotics in imaging can be felt, they will have to be able to see, feel, and measure shapes, sizes, and spatial relationships. A number of different sensing systems have been developed and are currently tested. O'Neil [2013] discusses computer vision techniques to accurately identify certain objects using an inexpensive Microsoft Kinect and a computer algorithm. Force and torque sensing, derived from external devices or from internal signals, can be used to identify the mass of the grasped part or unwanted collisions. Motion planning and obstacle avoidance can be implemented in computer algorithms utilizing software such as ROS [2013] and Kinematix [Kinematix, 2013].

Manual imaging inspections, with regards to repeatability and throughput, are constrained by the operator. This fact in combination with the increasing complexity of imaged objects means that imaging systems must become more sophisticated and capable, while remaining easy to operate.

Some NDT techniques, such as eddy-current inspection and ultrasonic testing can be readily automated since tasks are primarily hard-coded, but could also benefit from improved sensing. Automating other NDT techniques, such as radiography and CT, is not a trivial process since the imaging parameters can vary greatly from one part to another. This is where the importance of a flexible robotic manipulator system designed to work in a hazardous environment and by engineers with multidisciplinary knowledge comes into play. This chapter has demonstrated that automation for varying NDT tasks is a growing field; however, others have yet to exploit the full flexibility of robotics. This

makes the work presented here both feasible and necessary in order to realize the possible

efficiency gains that flexible automation can provide NDT applications.

Chapter 3: Evaluation of Hardware Feasibility

3.1   INTRODUCTION

The design of a flexible motion control system for non-destructive testing applications in radioactive environments is complex, requiring comprehension and utilization of knowledge from multiple domains in order for the motion system to complete its required task(s) successfully and safely. These domains include robotics, mechanical and nuclear engineering, as well as pertinent considerations from non-destructive testing, metrology, and safety. To alleviate many of the complexities encountered in this design task, a robotic imaging system is created utilizing the Robot Operating System (ROS), which is the *de facto* standard software framework used in robotics research. [ROS, 2014] MCNP, a general and powerful Monte Carlo transport code for particle transport simulations and nuclear analyses, is utilized to evaluate interactions with the radiation field. These tools are used to design and automate a neutron imaging system in radioactive environments. To ensure compatibility with the radiation levels in the environment, the automated system integrates custom-designed shielding. The validity of the design was demonstrated using a Yaskawa SIA5 manipulator with Yaskawa's most advanced controller, the FS100. Integration design required use of MCNP [Pelowitz, 2011], ROS, and simulation software for mechanical design integration of the robotic system in the radioactive environment.

Elements of design and analysis from multiple disciplines, including robotics, nuclear science, nuclear safety, materials, economics, and non-destructive testing must be taken into account in order to successfully deploy a robot in radioactive and other hazardous environments. Development work on the robot included modification to ensure compatibility with radiation levels in the area along with recovery methods to ensure that the system can be recovered in the event of failure. There is need to carefully consider

recovery techniques in the event of failure of the robotic system in radiation areas. The robot's control electronics will be sited outside the radiation area to avoid unnecessary damage. Mock up testing has been used extensively to validate the design choices and ensure compatibility of the robotic system and imaging device with each other.

3.2 VISION-BASED CALIBRATION TECHNIQUE FOR INDUSTRIAL MANIPULATORS USED IN HAZARDOUS ENVIRONMENTS

Successful performance of material handling operations in a confined radioactive environment requires a robot to perform tasks involving accurate positioning of its EEF. A vision-based calibration technique for autonomous industrial manipulators used in hazardous environments was developed. This calibration technique is capable of obtaining accurate EEF positioning for systems that complete tasks requiring accuracy. Experiments and applications, based on the calibration technique, have been carried out and demonstrated with a 7 DoF, 5 kg payload Yaskawa SIA5.

The problem of defining the robot's location with respect to its environment so that it can perform hazardous-material-handling tasks safely and accurately is described in detail by Hashem [2012]. The specific application area explored is a manipulator deployed through a gloveport of a nuclear material handling glovebox, but can be used in different applications. The average localization accuracy the manipulator achieved after calibration is in the mm range. A vision-based calibration method can be utilized to achieve simple and fast calibration for a robotic system. After calibration, the robot must be able to operate in possibly cluttered environments and with incomplete *a priori* knowledge concerning the tasks. It is important that the calibration method is semi-automatic, robust, adaptable, flexible, precise, and/or rapid.

3.3   VALIDATION OF THE FEASIBILITY OF THE ROBOTIC SYSTEM / REPEATABILITY AND ACCURACY TESTS

The robot needs to meet certain performance requirements, including high repeatability, precision, stability, and accuracy. The robotic system must be able to precisely position and align parts, and parts need to be held still (i.e. must be kept stable) while the image is taken. Any movement of the specimen during exposure causes image blurring. The SIA5 manipulator has been experimentally validated [Hashem, 2013] to have the necessary repeatability, accuracy, and precision to successfully complete radiography and CT tasks.

Repeatability and accuracy experiments for validation of automating imaging applications at PF-4 are discussed. Variance must be small enough to allow accurate measurements of 250 µm, so it must be at least an order of magnitude smaller or 25 µm. Therefore, the robot must remain still within 25 µm while holding a part for film radiography applications. Most precision requirements come from CT applications.

3.3.1   Repeatability Test Overview and Results

Repeatability is usually the most important criterion for a robot. Typically, according to ISO 9283 [1998], a robot is sent to a taught position a number of times under the same conditions and the error is measured at each return to the position after visiting several other positions. The explicitly defined testing points surround the measuring workspace. Repeatability is then quantified using Equation (2-13).

The repeatability of NRG's Yaskawa SIA5 manipulator was tested. For this test, a digital dial indicator with a resolution of 0.001 mm was used. [Mitutoyo, 2015] A Yaskawa SIA5 manipulator, bolted down to a table, moved along a predefined path to various points within its workspace until it reached the dial indicator. For the test, a path was created where the manipulator exercised each axis (i.e. performing a Cartesian move)

69

for approximately 15 path positions. The manipulator then performed a joint move towards the dial indicator so that the EEF faced the indicator. A Cartesian move was then performed, resulting in the SIA5's EEF pressed against the dial indicator and the recording of the measurement. An overview of this procedure is shown in Figure 3-1. This was repeated ten times for each set velocity and acceleration in the x-, y-, and z-directions. The maximum variance is calculated as shown in Equation (3-1). All of the moves were planned offline before executing them on the hardware.
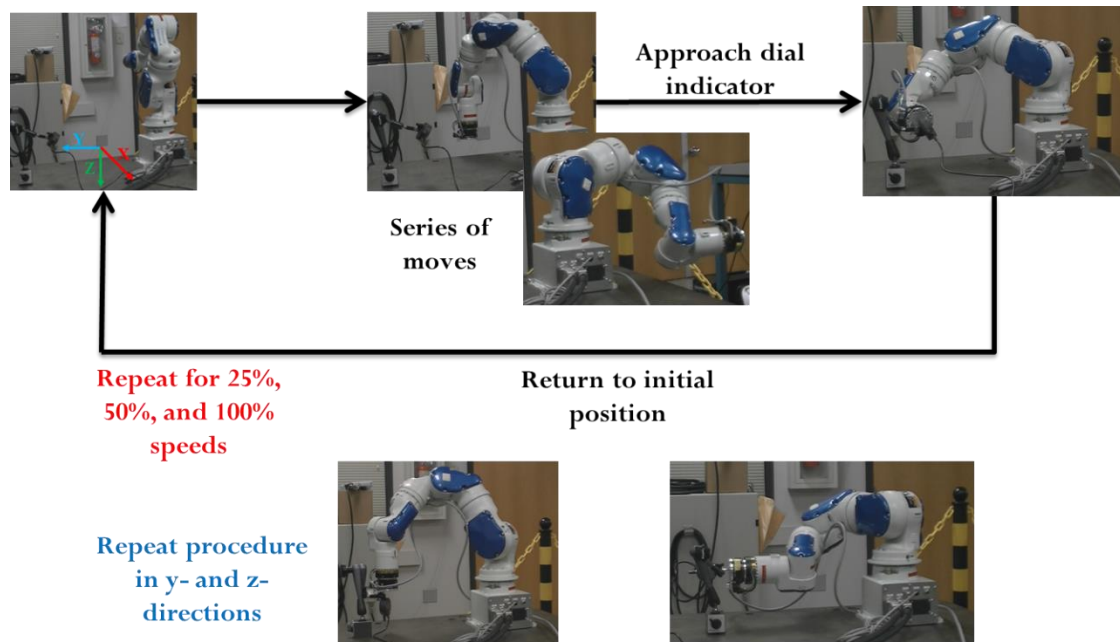
Figure 3-1. Yaskawa SIA5 manipulator performing repeatability test shown in initial configuration (top-left), Cartesian moves to different position (not all moves shown) (top-middle), and Cartesian move to testing position in x- (top-right), y- (bottom-left), and z-directions (bottom-right).

A 2.3 kg Robotiq gripper was attached to the manipulator's EEF to determine if adding a payload had any noticeable effects on the repeatability. The test shown in Figure 3-1 above included a force/torque sensor attached to the EEF that weighed approximately 0.5 kg. The test included the gripper attached to the EEF without the force/torque sensor. A similar path was taken as in Figure 3-1. It was determined that adding 1.8 kg (i.e. 2.3

kg gripper minus the 0.5 kg force/torque sensor) to the robot's EEF does not adversely affect the robot's repeatability. Adding a larger mass to the robot's EEF is discussed later in this section.

$$Max.Var. = \frac{\sqrt{(X_{max}-X_{min})^2 + (Y_{max}-Y_{min})^2 + (Z_{max}-Z_{min})^2}}{2} \qquad (3\text{-}1)$$

The repeatability of the robot is different in different parts of the working envelope and also changes with speed and payload. ISO 9283 [1998] specifies that accuracy and repeatability should be measured at maximum speed and at maximum payload. This results in pessimistic values whereas the robot could be much more accurate and repeatable at light loads and speeds. Repeatability is also subject to the accuracy of the EEF, such as a gripper.

The raw dial indicator measurements, normalized to the first reading, are shown in Figure 3-2. The resultant positioning repeatability, according to ISO 9283 [1998] standards (Equation 2-12) is 17.9 µm for 25% maximum speed, 18.6 µm for 50% maximum speed, and 16.0 µm for 100% maximum speed. From a purely visual observation, the largest vibrations during robot motion occurred with the maximum speed set to 50%, which could contribute to the larger repeatability errors. Noticeable vibrations only occurred while the robot was in motion. The following section discusses vibrations while the manipulator is stationary.

When the dial indicator was placed near the edge of the workspace for the x-direction test, the repeatability values (according to ISO 9283 [1998]) were on average several microns higher: 19.5 µm for 25% maximum speed, 10.8 µm for 50% maximum speed, and 23.8 µm for 100% maximum speed. The raw dial indicator measurements, normalized to the first reading, for this test are shown in Figure 3-2. It is apparent that repeatability deteriorates as the robot moves close to the edge of its workspace. Speed

71

also seems to have a greater impact on repeatability as the robot nears the edge of its workspace. As a result of this analysis, it is recommended that the robot positions a part to be imaged within the center of its workspace envelope. This should limit the robot to position the part within it dexterous workspace.
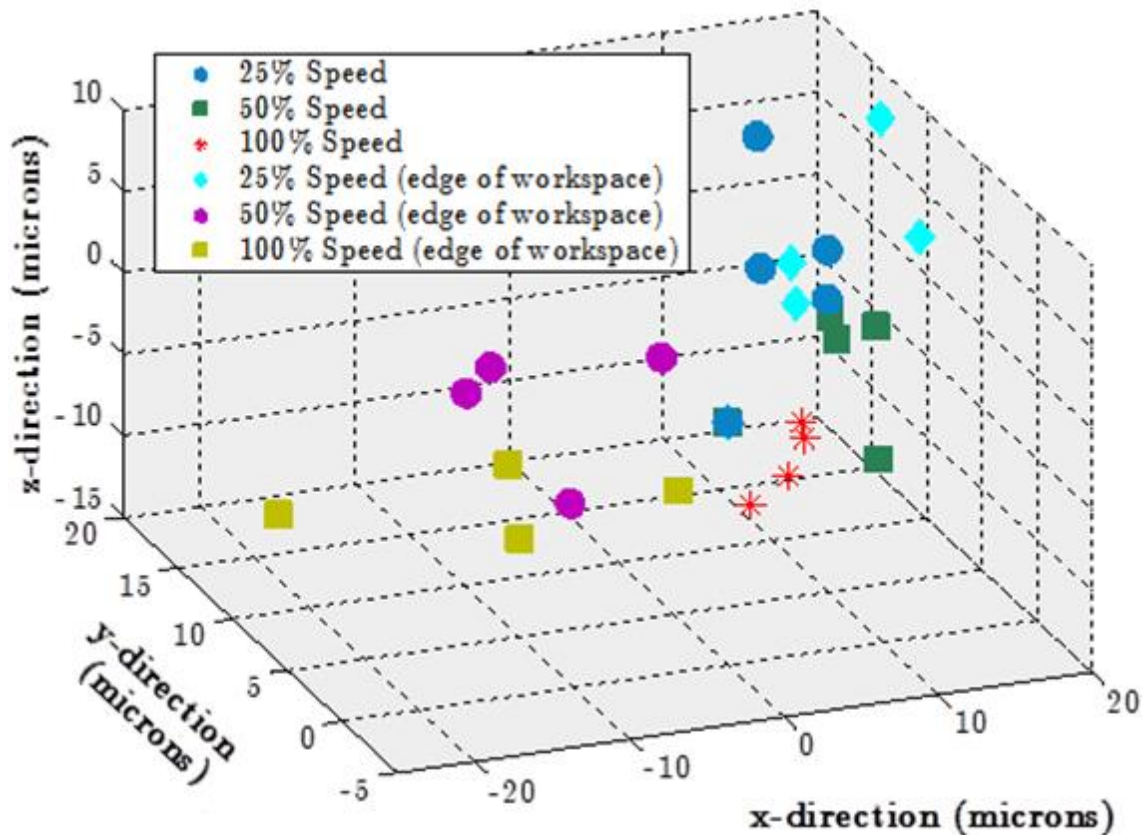
Figure 3-2. Yaskawa SIA5 manipulator experimental repeatability measurements. Data points are normalized so that the first measurement is at the origin (0,0,0).

The resulting maximum variance must not exceed the specification of 250 μm. The repeatability results are shown in Figure 3-3. A run was completed, with ten measurements taken for each run, for 10%, 20%, 40%, 60%, 80%, and 100% velocity and acceleration percent. The largest repeatability error resulted from when the velocity and acceleration percent was set to 60%. From a purely visual observation, the largest

vibrations occurred when the velocity and acceleration percent was set to 60%, which could contribute to the larger repeatability errors. Noticeable vibrations only occurred while the robot was in motion; it was shown that while the manipulator was stationary, vibrations are insignificant. The repeatability values obtained, approximately 0.01 mm, are several orders of magnitude less than the asserted repeatability for the Yaskawa SIA5, which is indicated with the black lines in Figure 3-3. Asserted literature values are taken at maximum payload and maximum speed, according to ISO 9283 [1998].
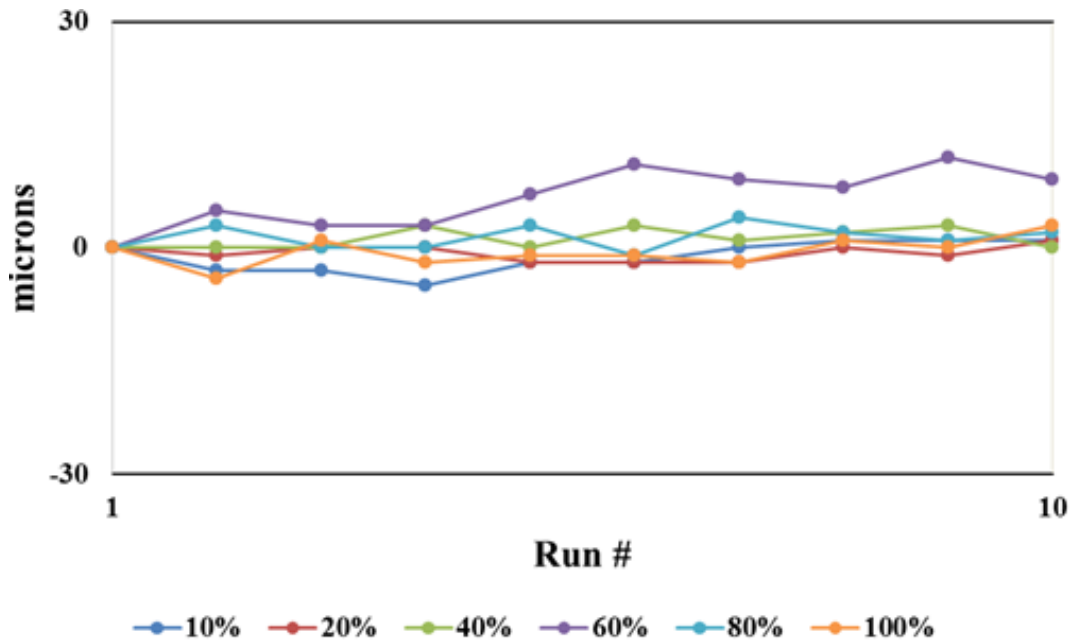
Figure 3-3. Yaskawa SIA5 manipulator repeatability results. The black line represents the asserted 0.06 mm repeatability for the Yaskawa SIA5 manipulator.

The repeatability of the robot can also be determined using actual radiograph images. This test was performed using a 225 keV micro-focus with a Varian amorphous silicon flat-panel detector (PaxScan 2520, *Varian Imaging Products,* Palo Alto, CA). The Varian panel's pixel pitch, which is the physical distance between the pixels in the imaging device, is 127 μm at 1:1 magnification. The magnification of the system is a

function of the distances from the source to the object and from the source to the detector. The system pixel pitch will differ depending on the magnification, where the system pixel pitch is equal to the imaging system pixel pitch divided by the magnification. For example, if the magnification is 10:1, the effective system pixel pitch is 12.7 µm. The micro-focus has a small focal spot size (i.e. x-ray emission point). In ordinary x-ray radiography the resolution in the captured images is 25 µm for film and 100 µm – 1 mm for digital. The micro-focus allows imaging down to the 2-3 µm level. Therefore, it is important for the robot's repeatability and resolution to be on this level as well. The distance between the source and object should be minimized to increase magnification so that micron level motions can be resolved. However, decreasing the source to object distance increases focal spot blur. Lower energies and higher exposure times can help reduce image blurring. Blurring in the captured images should be minimized so one can distinguish the micrometer level differences between images.

Ten radiographs were taken of a BB attached to a plastic screw that the robot was holding. The robot would complete a similar repeatability motion (at relatively low speed) as mentioned earlier in Chapter 3 and then each image was taken. Each of the images were compared by looking at the pixel intensity values and location relative to other images. The analysis was performed using MATLAB as shown in Figure 3-4. The light blue rectangle shows the zoomed in section that is highlighted by the pixel map on the right. The differences in pixel intensity relate to the differences in the location of the BB. It was found that there was approximately a 1.3 pixel difference in BB location along the x and y axes between the images. For this test, the source to object distance was 171.45 mm and the source to detector distance was 1701 mm, so the magnification or zoom factor was 9.92. Therefore, the effective system pixel pitch was 12.8 µm (i.e. 127

74

µm divided by 9.92). The corresponding repeatability value would then be ±17 µm (i.e. 12.8 µm times 1.3 pixel value difference). This compares well to the ±17.9 µm repeatability value obtained using the dial indicator with the robot moving at 25% maximum speed. It is important to use the `void setGoalTolerance()` function in ROS to set the tolerance to a sufficiently low value. This is the tolerance that is used for reaching the goal. For joint state goals, this will be the distance for each joint, in the configuration space (radians). For pose goals this will be the radius of a sphere (m) where the EEF mush reach.

75

Figure 3-4. Repeatability analysis method using a micro-focus x-ray source and a flat-panel detector. The effective system's pixel pitch is 12.8 μm. The zoomed in pixel map on the right shows the intensity value of each pixel and its location.

With CT scans, it is important that images be precisely located relative to each other. The first and last images are a good way to check this and should be the same (i.e. robot is positioned in the same position and orientation) so that the reconstruction algorithm can correctly reconstruct the images into a 3D model. Figure 3-5 shows the first and last images of two separate CT scans that were performed, each with the robot holding different objects in different orientations. The first set of images show the robot holding a glass container half-filled with water. The second set shows the robot holding a plastic screw with two BBs attached (the two BBs are overlapping). Each scan requires the SIA5's EEF to move from -180° to 180°, so the first and last images should be similar. As one can see from the radiographs and histograms in Figure 3-5 the first and last images of both scan sets are virtually identical. The actual system setup is described in detail in Chapter 6.

77
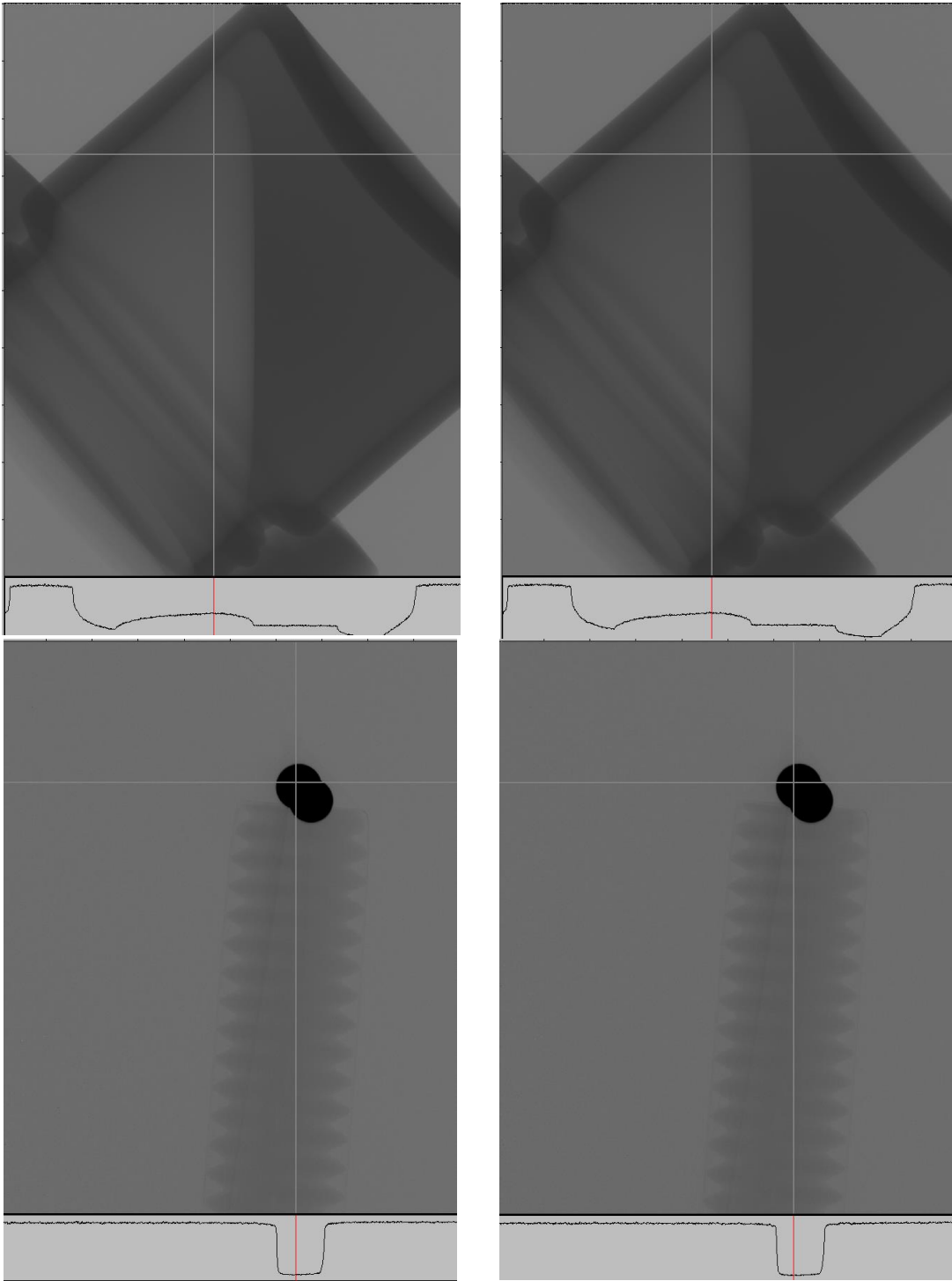
Figure 3-5. First (left) and last (right) images of two sets of CT scan data. Each image is rotated 90 degrees counter-clockwise from the actual setup.

78

3.3.2 Backlash Test Overview and Results

The accuracy/backlash of NRG's Yaskawa SIA5 manipulator was tested to see if backlash has any noticeable effects. Since harmonic gears are used in the SIA5, backlash is expected to be minimal. However, in higher precision work, backlash needs to be accounted for. The ability of a robot to go to a specified position without making a mistake is essential in radiography applications. A digital dial indicator with a resolution of 0.001 mm was used. The following procedure was used to quantify the accuracy/backlash of the robotic system. The SIA5 was moved to an initial right-side configuration (see Figure 3-6(a)). The manipulator then performed a Cartesian move towards the dial indicator so that the EEF faced the dial indicator. Another Cartesian move was then performed, resulting in the SIA5 pressing against the dial indicator and the recorded measurement. Then the SIA5 performed a joint move to a left-side configuration (closely mirroring the right-side initial configuration). Two Cartesian moves executed in succession resulted in the EEF pressing against the dial indicator and the measurement recorded. An overview of this procedure is shown in Figure 3-6. This was repeated roughly six times for each set velocity and acceleration.

(a)   (b)   (c)
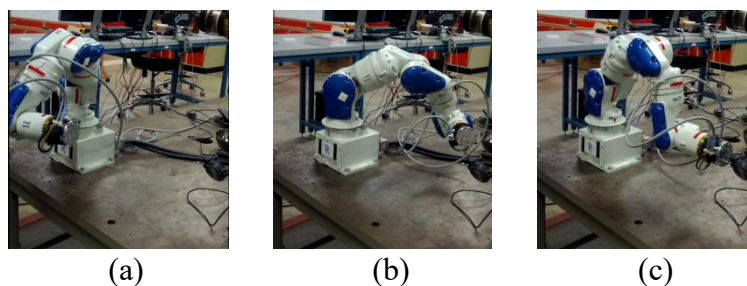
Figure 3-6. Yaskawa SIA5 manipulator performing accuracy/backlash tests shown in (a) initial right-side oriented configuration, (b) initial left-side oriented configuration, and (c) Cartesian move to final EEF position.

The raw dial indicator measurements from the backlash test, normalized to the first reading are shown in Figure 3-7. A run was completed, with approximately 6

measurements taken for each run, for 10%, 20%, and 60% velocity and acceleration percent. There are no noticeable correlations to accuracy results and the set velocity and acceleration percent. The purple and light blue data points are shown to demonstrate the repeatability performance of the SIA5 if only the right-side or left-side orientation approach, respectively, is taken. Errors due to backlash are noticeable, but they do not cause the SIA5's accuracy to fall beyond LANL's 250 μm variance allowance, which is indicated with the black lines in Figure 3-7. The accuracy values obtained are a few orders of magnitude less than the 250 μm precision requirement defined by LANL for radiography applications at PF-4.
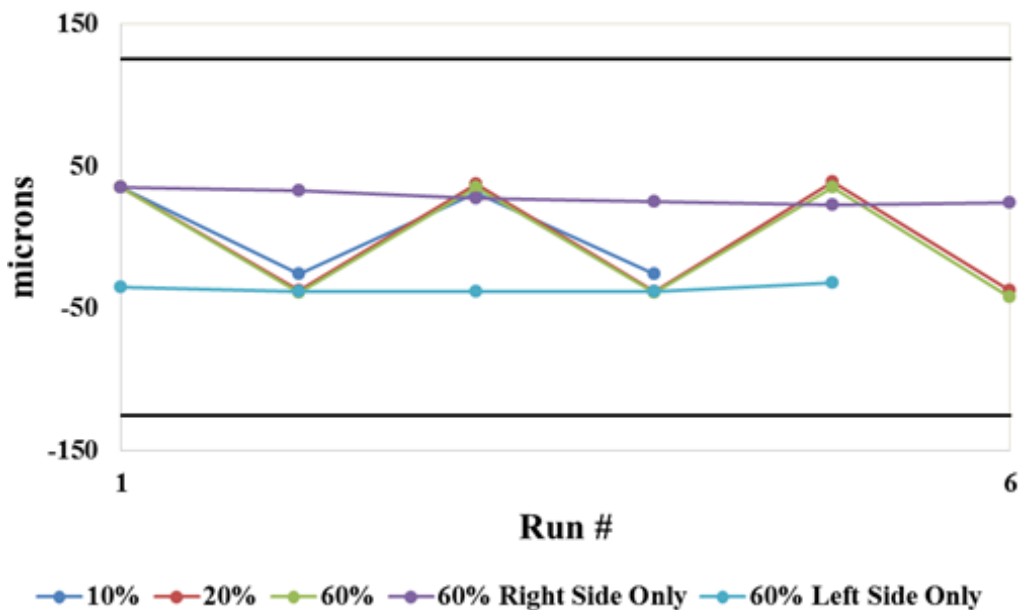
Figure 3-7. Yaskawa SIA5 manipulator experimental accuracy/backlash results. The purple and light blue data points are shown to demonstrate the repeatability performance of the manipulator if only the right or left side approach, respectively, is taken. The black line represents the 250 μm LANL requirement.

3.4   RESOLUTION AND VIBRATION TESTS

Resolution for a robotic system is the minimal commanded step for a joint. The resolution value is the smallest incremental move that the robot can physically produce.

80

To test the resolution of the robot's EEF, the robot was commanded to move the minimal step in Cartesian space by computing a mini-trajectory in ROS. The same micro-focus system was used to acquire the images as described earlier. An example test is shown in Figure 3-8. For the resolution test conducted, the distance from the source to the object was 12.7 cm and the distance from the source to the detector was 167.6 cm. Therefore the magnification was 13.2 and the effective system pixel pitch is 9.62 μm (i.e. 127 μm divided by 13.2). The difference between the images are shown in Figure 3-9. The x-direction is facing up in the images. There was approximately a 3.5 pixel difference between the two images. This value needs to be divided in half to get the actual distance traveled because the differences in both images are highlighted. Therefore, the actual distance traveled was 1.75 pixel, which relates to a 16.8 μm resolution (i.e. 9.62 μm times 1.75 pixels). The joint resolution of the robot will be lower than this value since the resolution possible for the EEF is a function of the joint resolution and the configuration of the robot.
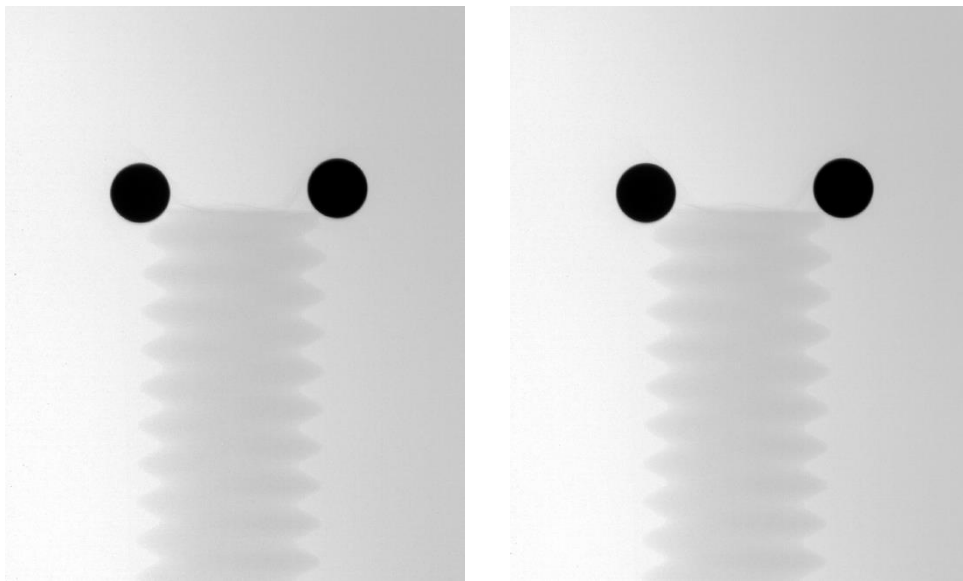
Figure 3-8. Resolution test. The robot was commanded to move a minimal amount in Cartesian space along in the positive x-directions while holding an object with two BBs attached.
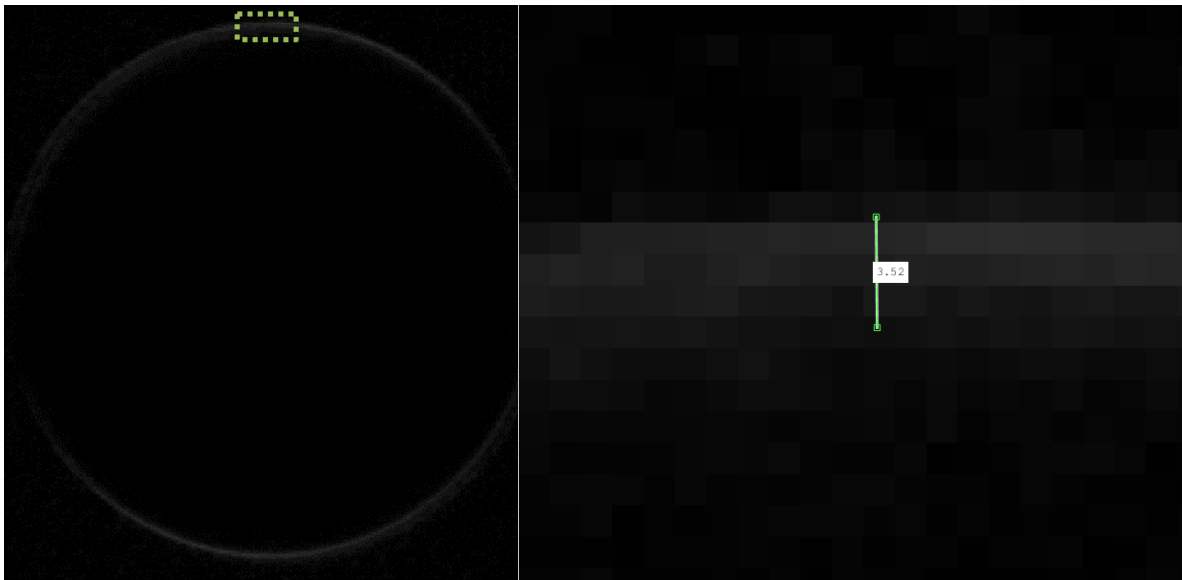
Figure 3-9. Differences between BB locations on two resolution test images. The dashed rectangle (not to scale) (left) shows the zoomed in section with the difference in pixels measured (right).

Two types of vibrations that are explored are static and tracking vibration. Static vibration is the amplitude of impact of vibration on the EEF position while the robot is not moving. Tracking vibration is the amplitude of impact of vibration on the EEF position while the robot is moving. Tracking, which is the ability to follow the exact same EEF path, is also explored.

3.4.1   Vibration

For NDT imaging tasks the robot cannot move more than 250 μm when it is stationary. A focusable 635 nm laser pointer and a Nikon D90 camera were used for this test. The laser pointer was mounted and rigidly fixed on the SIA5's EEF using a clamp, laser pointer holder, and yellow tape to prevent movement of the laser pointer with respect to the EEF (see Figure 3-10). A whiteboard was positioned in the direction that laser pointed, with the laser pointer and the whiteboard orthogonal to each other. The distance from the laser pointer to the whiteboard was 6.47 m. The distance from the

camera lens to the whiteboard was 1.34 m. The tripod with the camera mounted on it was positioned between the robot and the whiteboard, allowing for a full view of the laser's motion on the whiteboard. All photos were taken with the camera aperture set to f/22, ISO set at 100, and the lens at 18 mm. The camera's shutter was opened and closed to start and end the picture using a remote control to prevent movement of the camera.

The robot was set to move between four different locations using joint moves only; the first move moving joints 4 and 6, the second moving joints 2, 4, and 6, the third moving joint 4, and the last moving joints 2 and 4 (see Figure 3-11). The test was run with the lights off, so the laser would be the primary source of light captured by the camera.

| (a) | (b) | (c) |
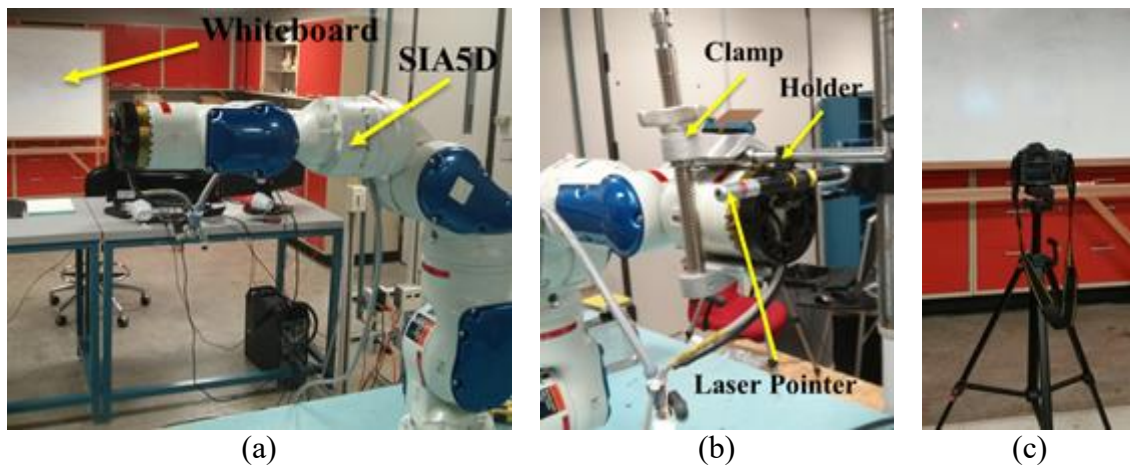
Figure 3-10. Repeatability and vibration test setup (a) SIA5 starting position with whiteboard in view without laser pointer attached (b) laser pointer setup at EEF (c) camera/tripod position.
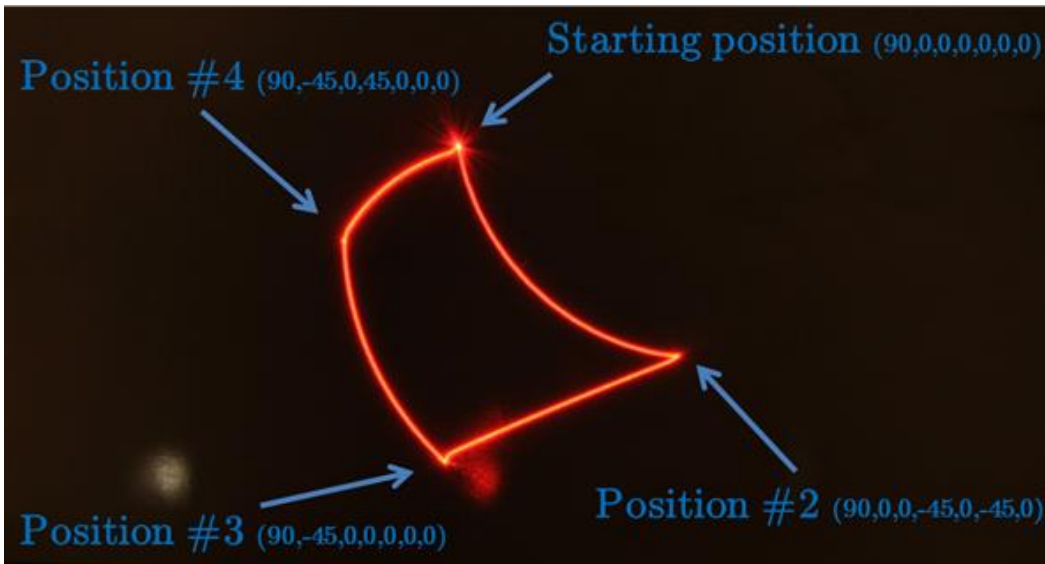
Figure 3-11. **Overview of laser pointer repeatability test with positions and relative joint angles.**

As one can see, the ability to track a path with joint moves is high. Taking long exposure pictures show that the robot motion is smooth with joint moves, therefore the tracking error is low.

To show how a small change in joint position effects the tracking ability of the robot, the path shown in Figure 3-12 (a) below was followed except that the 5th joint of the SIA5 was 0.1° instead of 0°. Figure 3-12 (a) shows both paths taken, with joint 5 at 0° resulting in the top path and joint 5 at 0.1° resulting in the bottom path. It proves that if one joint is off by a small angle, such as 0.1° for joint 5, then the laser pointer would be off by about 14 mm on the whiteboard. The SIA5 was also set to move to four different locations in the y-z plane using Cartesian moves only. Figure 3-12 (b) below shows the resulting laser path with the robot completing four cycles at 10% maximum speed. The exposure time was 234 sec. The notable difference between the joint moves and Cartesian moves is that the resulting laser path is fuzzy while the robot is performing Cartesian moves. This results in an increase in tracking vibration. To follow a Cartesian path, the robot interpolates between successive points along the path, which causes the fuzziness.

84

<center>(a)   (b)</center>
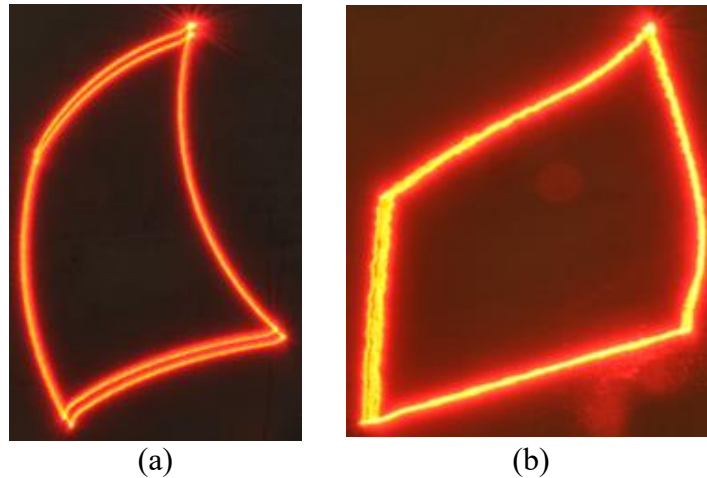
Figure 3-12. Tracking ability (a) of the SIA5. Top path taken with joint 5 at 0°. Bottom path taken with joint 5 at 0.1°. Result of a laser pointer repeatability and vibration test (Cartesian move) (b).

To test static vibrations, two pictures of the laser pointer were taken while the robot was at rest. The differences between pictures were then analyzed (Figure 3-13 and Figure 3-14). It is important to note that the difference in a majority of the pixels is due to the reflection of the laser pointer on the whiteboard
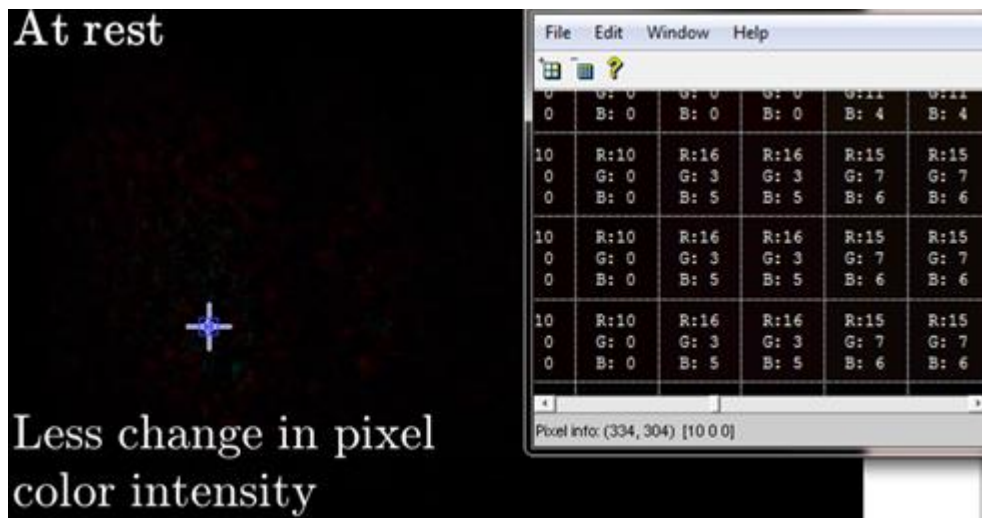
Figure 3-13. Values of pixels in comparison of two different images taken while robot is at rest.

10 pixels wide   Difference in majority of pixels is due to reflection of laser pointer and white board
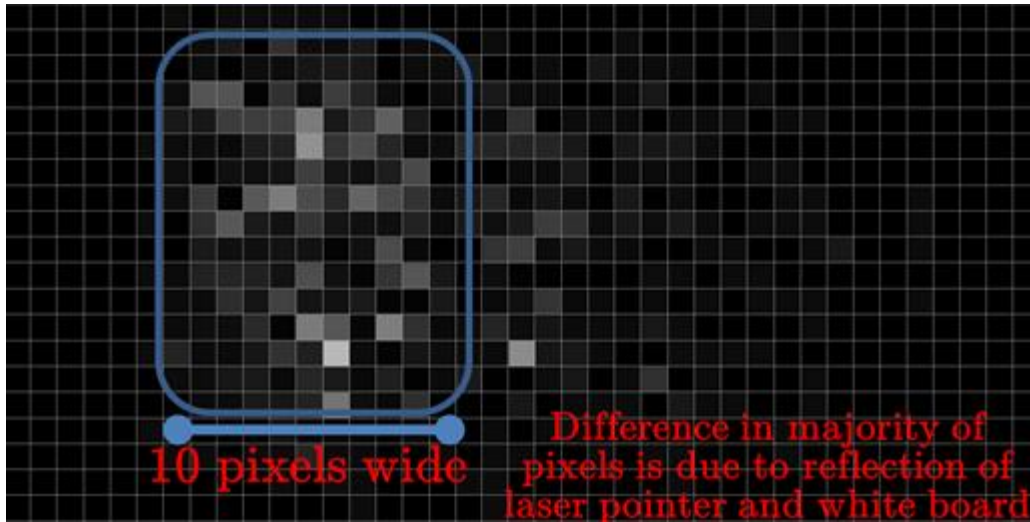
Figure 3-14. **Difference values of pixels in grayscale of two different images taken while robot is at rest. The lighter pixels have the highest change in pixel value.**

An additional repeatability test was performed with the laser pointer. Pictures were taken of the laser pointer during different cycles at the same taught location (Figure 3-15 and Figure 3-16). This also tested static vibrations since the pictures were taken while the robot was at rest. When comparing the difference in pixels while the robot is between cycles at the same taught position and while the robot is at rest, one can see that there is less difference while the robot is at rest. Therefore, the variance due to static vibration is less than the variance due to repeatability of the SIA5.
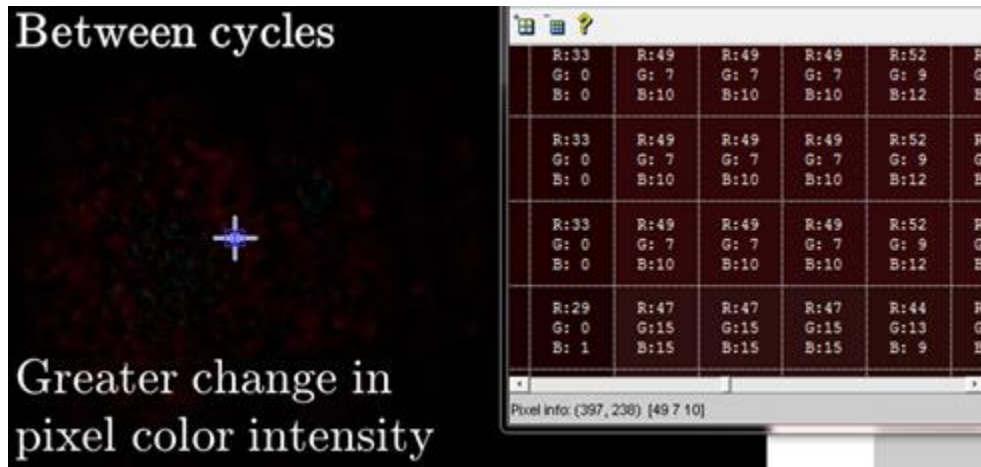
Figure 3-15. Values of pixels in comparison of two different images taken at two different cycles at the same taught position.
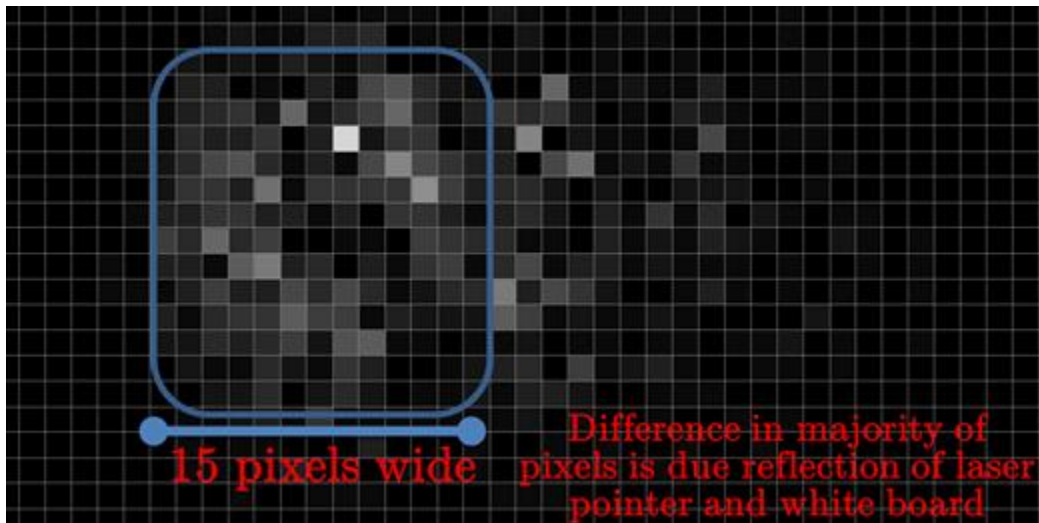
Figure 3-16. **Difference values of pixels in grayscale of two different images taken while robot is at two different cycles at the same taught location. The lighter pixels have the highest change in pixel value.**

3.5   EEF GRIPPERS/TOOLS

Currently the system has two tools available, a Robotiq 2-finger adaptive gripper and a multi-purpose vacuum gripper, used for picking up a variety of objects. The main material of the Robotiq gripper is aluminum. The vacuum gripper is made of aluminum, rubber, and plastic. Most of the electronics for the Robotiq gripper are housed in a control box that is separate from the gripper, therefore minimizing electronic components that

87

might be affected by radiation. Hence, radiation damage to the gripper is minimized and not an issue unless the radiation levels are so high combined with long exposure times that the gripper may heat up depending on the energy of the radiation. Both gripper are relatively inexpensive and are easily replaceable if they are damaged.

With the vacuum gripper it is important to note that the suction strength is equal to the pressure differential times the surface area that the gripper is attached to the object to be picked up. The vacuum gripper can be used with compressed air or a vacuum pump. The vacuum to the gripper is controlled by an Arduino board [Arduino, 2015]. The Arduino software is interfaced with ROS so that it is streamlined with the robotic software. The microcontroller publishes the data as a ROS topic. The use of ROS is discussed in greater detail in Chapter 4.

Because there may be several different parts to image, it is important to capture grasp parameters between the robot and the part. When an object is picked up, it is important to know where that part is in relation to the EEF of the robot. One way to accomplish this is to have the part fixed to the EEF, but this would require the operator to manually attach and detach the part. Another method is to have a pattern on the gripper so that when the robot picks a part up, the part will attach to the pattern in a fixed manner. [Teague, 1988] This way, the part's position and orientation are known and are the same every time that part (or a similar part) is picked up. Various tool changers could be incorporated into the robotic system, so that the system could autonomously interchange tool changers to pick up parts with differing geometries.

3.6   SHIELDING FOR ROBOTIC SYSTEM

A radiation beam poses a risk to the robotic system equipment, i.e. robot, controller, gripper, etc., and therefore must be adequately shielded. Shielding is used to

decrease the number of neutron and photons striking the robot. The goal in shielding neutrons includes multiple stages: slowing the neutrons down, absorbing the neutrons, and shielding for secondary radiation (e.g. prompt photons from activation). Elements such as boron, lithium, cadmium, and gadolinium have high neutron absorption cross-sections at thermal energies. Materials containing such elements are well suited as shielding for neutrons and prevent neutron activation. Some nuclei induce a deviation of the neutron from a straight trajectory, producing neutron scattering reactions. Occurring in most isotopes, they are especially strong in hydrogenous materials. Materials containing a high proportion of hydrogen such as polyethylene and concrete are the most effective for elastic scattering at all energies. An example shielding structure would be to first have 0.5 in. of Boral to absorb thermal neutrons, followed by 1.5 in. of stainless steel. The steel can absorb a considerable proportion of the energy of fast neutrons and gamma rays. Fast neutrons must be slowed down before they can be captured. This can be accomplished by inelastic scattering with heavy elements, such as Fe, and by elastic scattering with light nuclei. Inelastic scattering of high energy neutrons occurs mostly with iron, which degrades the neutron to a much lower energy. Then a 4 in. polyethylene layer would help moderate epithermal neutrons to thermal energies (elastic scattering). Another 0.5 in. layer of Boral is repeated to filter out thermal neutrons. The resulting slow neutrons are then readily captured in (n,γ) reactions. As neutrons are moderated in the polyethylene layer, photons are emitted as excess energy is released. Photon radiation is produced as a result of these capture reactions and shielding must be provided to absorb this radiation. Pb or another material with high photon absorption cross section can be used as a shield against the emitted photons. Therefore a 10 in. layer of lead serves to absorb these photons.

Shielding prevents degradation and damage to the robot. An example MCNP calculation showed that thermal neutrons can be attenuated almost completely by only 0.5 cm thick boral. However, commercially available boral, is expensive for even thin plates, and multiple plates of boral would need to be used to sufficiently shield the robot. Shielding for an x-ray source primarily consists of Pb, or other high Z materials such as concrete.

3.7 EFFECT OF ROBOT ON IMAGE QUALITY

Neutron activation is of concern when performing neutron radiography or CT. Activation occurs when a neutron is absorbed by the nuclei of a target object, a compound nucleus is formed, and then energy is released as the nuclei de-excites. Fortunately, if the neutron beam flux is fairly low ($\sim10^5$ n/cm^2/s or less), significant activation is not induced. Higher neutron fluxes will result in higher activities. Neutron fluxes on the order of $10^{12} - 10^{14}$ n/cm^2/s are the most efficient neutron sources for high sensitivity activation analysis induced by epithermal and thermal neutrons. [Molnar, 2014] Elements such as aluminum, which is a primary component of many robots, has a small thermal neutron absorption cross-section (~0.2-0.6 x 10^{-24} cm^2), which reduces the likelihood of neutron activation. If the robot were to become activated, these elements have very short half-lives, and could be handled within minutes. However, short half-lives mean larger impacts on real-time imaging background. Elements such as cobalt pose a challenge, since it could become activated and would require years (5 year half-life for ^{60}Co) to decay to the level that it could be handled. Stainless steel, a common alloy in robotics, is made up of several elements, including cobalt. Therefore, activation is more of a problem when dealing with stainless steel than it is for aluminum.

The SIA5 robot is mainly composed of cast aluminum. Neutrons interact with the aluminum atoms through neutron capture reactions. Resulting radioactive nuclei beta decay to excited energy states, which then emit gamma-rays as the nuclei de-excite to their respected ground states. These energetic gamma-rays scatter and interact with the surrounding medium, including the imaging device. Background events are also registered by the detector due to scattered neutrons. X-rays cause image noise by depositing extra energy in the converter screen, adding fogginess to the image. Increasing the distance between the radiographed object and the imaging device reduces the possibility of scattered neutrons falling on the image. However, the image spatial resolution is reduced as this distance increases due to source spot size.

The robot will create activation products once placed in the beam port while the beam is on, therefore an activation product analysis of the robot must be performed. Radiation background will cause background radiation to influence radiograph image quality in future measurements, which can be reduced with beam collimation. Image background subtraction decreases the impact of any background radiation, as described by Berger [1977].

An example activation calculation on the SIA5's primary material, cast aluminum, is shown in Table 3-1. This calculation was performed using the neutron activation calculator from the WISE Uranium Project [2012]. All of the daughter elements decay either by beta decay (*beta*) or electron capture (*e$^-$ capture*) into stable isotopes. Decay by electron capture results in the emission of an atomic x-ray, which can degrade image quality. The maximum thermal neutron flux at BP5, which is approximately 1.2×10^6 n/cm^2/s was used. The duration of irradiation was 5 min. As one can see, the highest activity activation product results from the ^{27}Al$(n,\gamma)^{28}$Al reaction, but ^{28}Al is relatively short-lived with a half-life of 2.24 min. Radionuclides with shorter half-lives typically

91

result in higher activity. However, due to the high activity resulting from this reaction, the decay of ^{28}Al by 4.6 MeV betas will cause image degradation, including noise in dark images (i.e. readout of the detector without an exposure) and image afterglow or ghosting. Noise in the dark images is commonly the result of lag: the carry-over of image charge generated by previous exposures into subsequent image frames. Ghosting is the change of sensitivity or gain of the detector as a result of previous radiation exposures. An activation product that would cause more of a concern with regards to robot activation would result from the ^{55}Mn$(n,\gamma)^{56}$Mn reaction, which has a 2.578 hour half-life. This results in needing to wait a longer period of time before handling the robot. This activation analysis can be repeated for every component of the SIA5 manipulator. It is important to note that the activation analysis performed here overestimates the actual activation amount. The calculation performed does not take into account neutron transport, the interaction of neutrons with materials, which would reduce the neutron intensity as the beam travels through the robot's materials. Therefore in reality, the activation values would be lower than those in Table 3-1.

Activation with subsequent decay is calculated using:

$$A_1(t) = \varphi N_0 \sigma_0 \left(1 - e^{-\lambda_1 t_i}\right) e^{-\lambda_1 t_i} \tag{3-2}$$

where φ is the neutron flux (n/cm^2/s), N_0 is the number of atoms irradiated (atoms), σ_0 is the microscopic cross-section of what is irradiated (cm^2), λ_1 is the decay constant for what is produced, and t_i is the irradiation time. [Soete, 1972] One can decrease activation with shorter exposure times, using digital detectors over film, and implementing shielding and collimation.

Table 3-1. Neutron activation analysis of 10 kg of cast aluminum (i.e. the primary constituent of the SIA5 manipulator) in a thermal neutron flux of 1.2 x 10^6 n/cm²/s for 5 min.

Original Nuclide	Reaction	Activation & Decay Products	Half-Life	Daughter Decay
1 kg Si	33.08 g ^{30}Si (n,γ)	1.859 kBq ^{31}Si	157.3 min	1.5 MeV *beta*
55 g Fe	3.081 g ^{54}Fe (n,γ)	226.5 mBq ^{55}Fe	2.7 years	0.2 MeV e^- *capture*
	171.1 mg ^{58}Fe (n,γ)	149.9 mBq ^{59}Fe	44.53 days	1.6 MeV *beta*
10 g Cu	6.85 g ^{63}Cu (n,γ)	1.612 kBq ^{64}Cu	12.7 hours	1.7 MeV e^- *capture* (61%) 0.6 MeV *beta* (39%)
	3.15 g ^{65}Cu (n,γ)	37.49 kBq ^{66}Cu	5.1 min	2.6 MeV *beta*
45 g Mn	45 g ^{55}Mn (n,γ)	175 kBq ^{56}Mn	2.578 hours	3.7 MeV *beta*
10 g Zn	4.751 g ^{64}Zn (n,γ)	582.5 mBq ^{65}Zn	243.9 days	1.4 MeV e^- *capture*
	1.952 g ^{68}Zn (n,γ)	88.18 Bq ^{69}Zn	57 min	0.9 MeV *beta*
5 g Ni	3.369 g ^{58}Ni (n,γ)	16.6 μBq ^{59}Ni	75000 years	1.1 MeV e^- *capture*
	189.4 mg ^{62}Ni (n,γ)	2.198 mBq ^{63}Ni	96 years	0.07 MeV *beta*
	49.56 mg ^{64}Ni (n,γ)	20.68 Bq ^{65}Ni	2.52 hours	2.1 MeV *beta*
8.825 kg Al	8.825 kg ^{27}Al (n,γ)	42.96 MBq ^{28}Al	2.24 min	4.6 MeV *beta*

Table 3-2. The same table as above, but with the original nuclides normalized from 1 to 10 g.

Original Nuclide	Reaction (n,γ)	Activation & Decay Products	Half-Life	Daughter Decay
2.02 g Si	66.67 mg ^{30}Si	3.746 Bq ^{31}Si	157.3 min	1.5 MeV *beta*
1.05 g Fe	58.87 mg ^{54}Fe	4.328 mBq ^{55}Fe	2.7 years	0.2 MeV e^- *capture*
	3.27 mg ^{58}Fe	2.864 mBq ^{59}Fe	44.53 days	1.6 MeV *beta*
1.01 g Cu	688.4 mg ^{63}Cu	162 Bq ^{64}Cu	12.7 hours	1.7 MeV e^- *capture* (61%) 0.6 MeV *beta* (39%)
	316.5 mg ^{65}Cu	3.768 kBq ^{66}Cu	5.1 min	2.6 MeV *beta*
1.04 g Mn	1.04 g ^{55}Mn	4.049 kBq ^{56}Mn	2.578 hours	3.7 MeV *beta*
1.01 g Zn	477.4 mg ^{64}Zn	58.54 mBq ^{65}Zn	243.9 days	1.4 MeV e^- *capture*
	196.2 mg ^{68}Zn	8.862 Bq ^{69}Zn	57 min	0.9 MeV *beta*
1 g Ni	673.9 mg ^{58}Ni	3.321 μBq ^{59}Ni	75000 years	1.1 MeV e^- *capture*
	189.4 mg ^{62}Ni	439.6 μBq ^{63}Ni	96 years	0.07 MeV *beta*
	9.912 mg ^{64}Ni	4.136 Bq ^{65}Ni	2.52 hours	2.1 MeV *beta*
10 g Al	10 g ^{27}Al	48.69 kBq ^{28}Al	2.24 min	4.6 MeV *beta*

3.8   GEOMETRIC MODEL OF THE ROBOTIC SYSTEM IN MCNP

A simplified geometrical computational model of the SIA5 manipulator system was developed in MCNP based on engineering drawings. In MCNP, the geometry of the

system under investigation is defined by objects called cells, which are each filled with a designated material and bounded by a surface. Cylinders were used to explicitly model the casing of the SIA5 system components (i.e. links of the robot) which contain most of the mass. The interior however, is more complicated as it contains cables, wires, actuators, harmonic gears, and other small and geometrically complicated components. Therefore, the interior components were modeled as a homogeneous mixture of materials, such as Al, Fe, and Cu. Voids in components were taken into account by adjusting their densities. More details on the modeling are presented in Chapter 5.

3.9   MODELING NETL'S TRIGA NEUTRON RADIOGRAPHY BEAM PORTS

3.9.1   TRIGA MARK II Research Reactor, Beam Ports 3 and 5 Overview

The Nuclear Engineering Teaching Laboratory (NETL) at U.T. Austin houses beam ports that can be utilized for radiography applications. Two of these beam ports, BP3 and BP5, were used in this work. BP5 is the primary beam port for neutron radiography since it has a larger beam size and is almost completely enclosed by concrete shielding to reduce noise to the imaging device. The source of neutrons is a TRIGA Mark II research nuclear reactor capable of 1.1 MW steady state power, creating a neutron flux of $5x10^6$ neutrons/cm^2/s at the neutron imaging plane in BP5 [Cao, 2007]. The detailed core model (see Figure 3-17) has three dimensional details of the core, reflector, and beam port penetrations. This model was used only to provide neutron source information for the simplified MCNP model of BP3 and BP5.
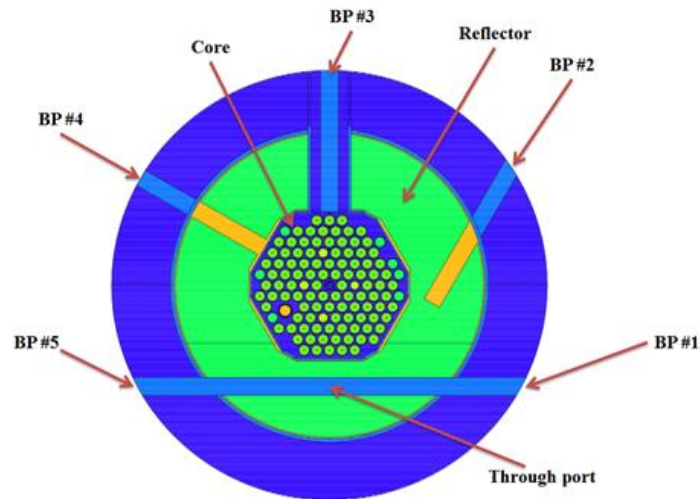
Figure 3-17. MCNP model of TRIGA reactor.

A neutron scintillation screen, mirror, lens, and CCD camera were used to acquire radiographs as shown in Figure 3-18. The cooled, light sensitive CCD chip of the camera captures the light emitted from the neutron-sensitive scintillation screen. A scintillation screen and CCD camera are utilized to obtain digital radiographs, in which differences in pixel intensity are related to differences in neutron attenuation. The converter material used to convert neutron to light was an Applied Scintillation Technologies ^{6}LiF ZnS plastic scintillator, doped with copper, aluminum and gold, which is ideal for CCD coupling, and has dimensions of 17.78 cm x 17.78 cm x 0.42/0.43 mm. The scintillator has a high thermal neutron absorption. Lithium scintillators are generally neutron specific, which reduce signal from secondary gamma rays. This reduces the need to filter gamma rays. Lead blankets were used to cover the camera-scintillator system and keep out light. Borated polyethylene blocks and lead bricks provided neutron and gamma ray shielding respectively. They also functioned to decrease the x-ray background and decrease x-ray hits to the camera, thus decreasing camera noise. The imaging device used is an Andor iXon+ 885 EMCCD camera with a 1004 x 1002 active pixel area on the chip, effective pixel pitch of 35 μm (5 cm diagonal size), and a dynamic range of 14 bits. A

95

Tamron 90 mm Macro lens was used with the CCD camera at an aperture value of f/2.8. The smaller the number, the larger the aperture; meaning the lens is more open and more light comes in. [ANDOR, 2008] MATLAB was used to acquire images from the CCD camera and communicate with ROS. The reactor power was set to 950 kW during exposure.
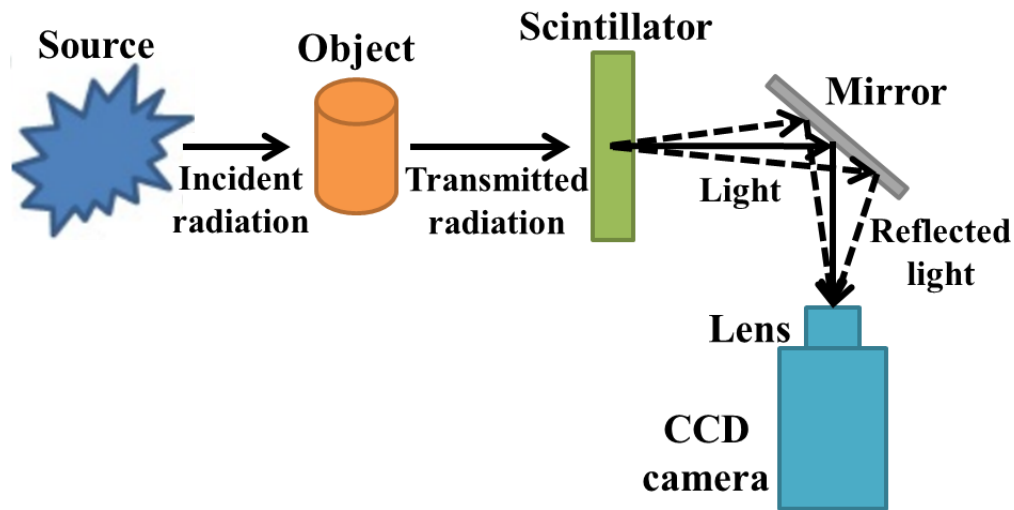
Figure 3-18. Schematic of scintillator-mirror-camera radiography system.

The L/D ratio (i.e. ratio of the length from the inlet aperture to the object divided by the diameter of the inlet aperture of the neutron collimator), determined from collimator geometry, is 160, where L=320 cm and D=2 cm. A stepper motor allows for on-line focusing ability. A schematic of BP5 is shown in Figure 3-19.
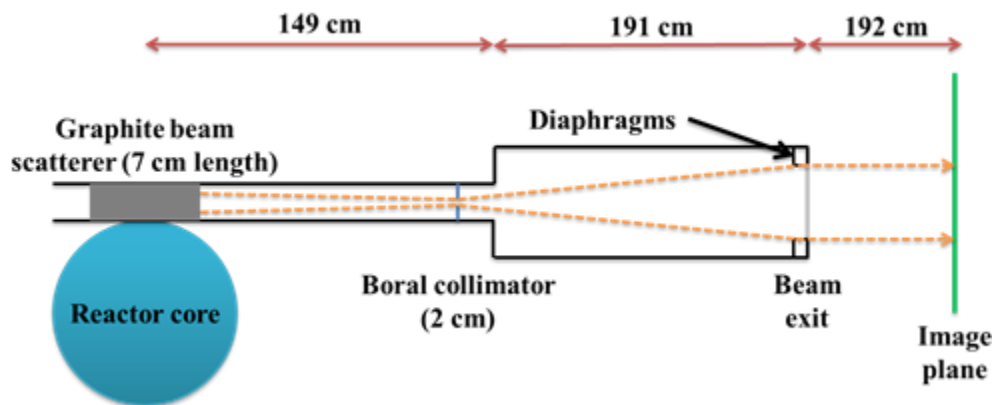
Figure 3-19. Schematic of beam port 5 neutron collimator system (not to scale).

The neutrons in BP5 are predominantly composed of thermal neutrons (i.e. 0.01 to 0.03 eV). Neutron imaging is performed mainly in the thermal region due to the large cross sections for attenuation and detection in this energy range. Neutrons in the fuel region of the reactor are born from the fission of ^{235}U at an average energy of 2 MeV. BP5 is tangential to the reactor and provides a high intensity, fast, collimated beam of neutrons. It includes a graphite beam scatterer, thermalization column, gamma filter, and three stages of neutron collimators. Graphite, which has a high neutron scattering cross section, scatters the neutrons and removes, on average, 14% of their incident energy per collision. This graphite scatterer creates a small disk source, of size according to the primary collimator diameter, emitting neutrons down the collimator. The neutron beam is then shaped by three stages of collimators and confined by a primary diaphragm (boral) of 2 cm in diameter. The outgoing neutron beam is about 20 cm in diameter at the exiting position of the wall and has a divergence angle of 2.4°. [Cao, 2007] The diaphragms collimate neutrons to form the neutron beam by allowing thermal neutrons to pass them only through holes at the center. The neutron beam decreases by 1/r from the beam line of the beam port, so it is more intense in the center.

After neutrons travel through the collimator, they enter the beam port cave, as shown in Figure 3-20. The beam port has a dual shutter system layered with lead and then borated polyethylene to shield gamma radiation and neutrons, respectively. To make an image, the shutters are opened while the reactor is shut down. The reactor is then started and brought to a power of 950 kW, which is the maximum allowable power for experiments in order to stay below regulatory limits. Currently, the sample to be imaged is placed on an aluminum sample holder in front of the scintillation screen. Neutrons are attenuated in the imaging target, and then the scintillator converts the neutrons into visible light. A front surface mirror is placed at a 45° angle from the scintillator screen to turn the direction of the incoming light 90°, which protects the camera from direct exposure to the high radiation field of the neutron beam. The optical lens coupling projects the image onto the camera, which is focused remotely. The mirror used is a 95% aluminum coated reflective 254 x 254 x 3 mm glass first surface mirror from Rolyn Optics. The system requires vibration stability to avoid blurring the acquired images. Lead, boron, and polyethylene shielding is used around the camera to reduce the backscatter and to protect the lens and electronics. The electrical signal from the CCD camera is sent to a PC where image processing and reconstruction occurs. The CCD camera is placed in a light-tight aluminum box with extensive lead shielding positioned around it to act as a gamma filter that reduces background noise. The MCNP model of BP5 (Figure 3-21), is used to establish design parameters, such as the location and orientation of the robot and shielding. It is important to note that the color of the structures does not indicate anything, it is just the coloring system used by MCNP.
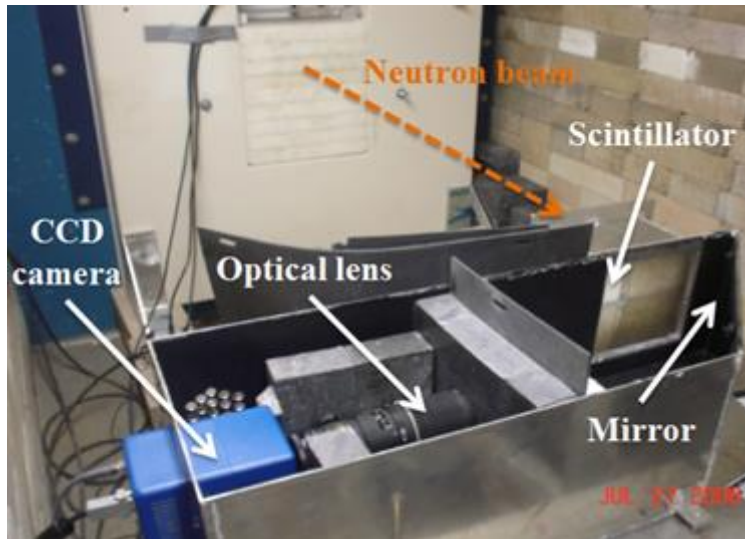
Figure 3-20. Experimental beam port 5 neutron radiography setup.
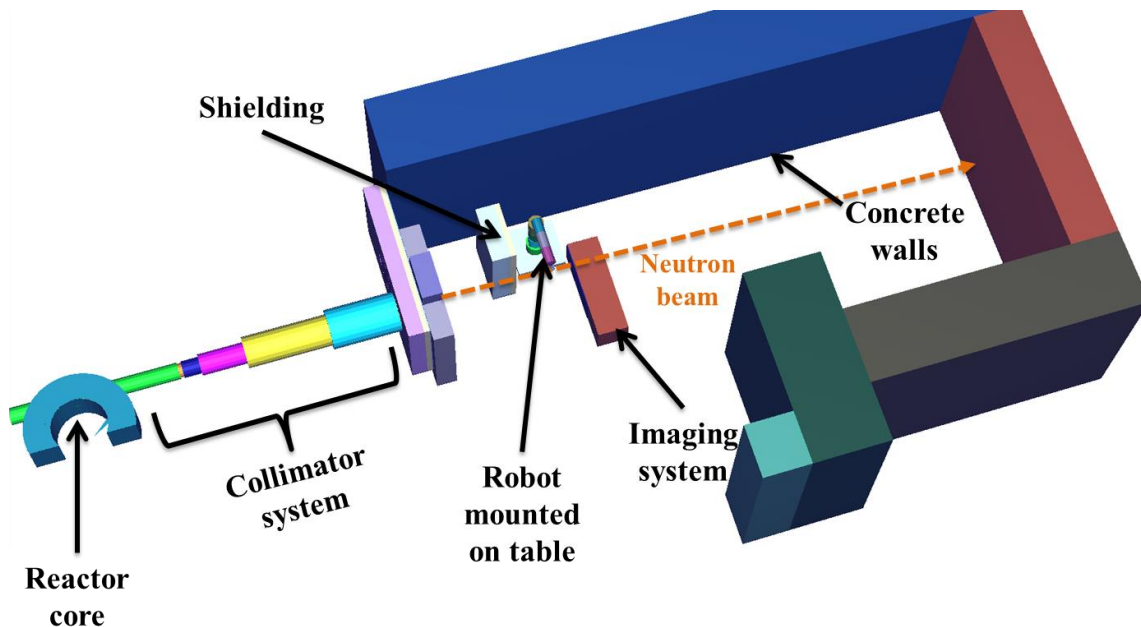
Figure 3-21. BP5 radiography system with robotic imaging system installed.

Neutron radiography was also performed using BP3 at NETL. In BP3, a cold neutron beam is supplied by the Texas Cold Neutron Source (TCNS), which is housed in one of the five beam port facilities associated with the U.T. Austin's 1.1 MW TRIGA Mark II nuclear research reactor. The TCNS irradiation facility allows one to subject the

sample to an effective thermal neutron flux of about 5.32×10^6 neutrons/cm^2/s (i.e. the effective thermal neutron flux with the reactor operating at 950 kW)). [Révaya et al., 2007] A photo of the TCNS is presented in Figure 3-22.
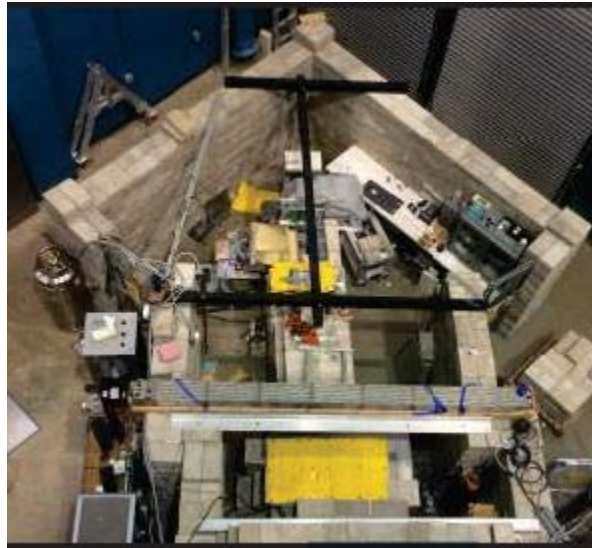
Figure 3-22. **Arial photo of BP3 at NETL.**

Generally a higher quality image is obtained when there is a higher neutron flux, which results in a lower exposure time, rather than vice versa. There is a linearly proportional relationship between reactor power and neutron flux at the image plate. Several images are acquired before the sample is put in place so the presence of a significant flux gradient within the neutron beam can be negated.

3.9.2 MCNP Model of Beam Port 3 and 5 with Robotic System

MCNP models of BP3 and BP5 were utilized to validate the robotic radiography system. Criteria included neutron and gamma dose rates, shielding materials, effect of the robotic system to the neutron flux at the imaging plane, location and placement of the robotic system, grasp planning, and motion planning of the robotic system. A simplified geometrical computational model of a robotic part positioning system in the beam ports

for neutron radiography applications were used. MCNP models of BP3 and BP5, created in previous research at U.T. Austin, were modified to create this deck. [Cao 2007] Initially the neutron and photon *importances* had to be changed for several cells in order for this model to run successfully. After the model was verified, the robotic system was placed in the simplified MCNP model for each beam port. The impact of the neutron source itself on the robot is evaluated in Chapter 5. As dose to the SIA5 may potentially be significant in cases where the manipulator is relatively close to the neutron beam, several robot and shield configurations are analyzed to reduce dose to the manipulator's electronics. Radiation fields are spatially dependent hazards that can damage manipulators or cause premature failure of mechanical components and sensitive devices. The manipulator's effect on the neutron intensity to the imaging system as well as the flux and dose received by the manipulator was studied.

3.9.3   Neutron Source in Beam Port 3 and 5

When dealing with direct contributions to a point detector from a planar surface source, the ARA (area of source) parameter with the SDEF card is required. Both BP5 and BP3 sources are defined as disk surface sources in MCNP. The source is located at the beam port exit to expedite MCNP runtime.

Figure 3-23 shows the thermal neutron beam that is modeled after U.T. Austin's TRIGA BP5, and Figure 3-24 shows the sub-thermal neutron beam modeled after BP3. Figure 3-25 shows the comparison of the two neutron sources, normalized. These are the actual TRIGA neutron beam energy distributions applied using source probability (SP) and source information (SI) cards in MNCP. The SI card gives the set or range of values for the variable and the SP card gives the probabilities associated with the values of the SI card.

101
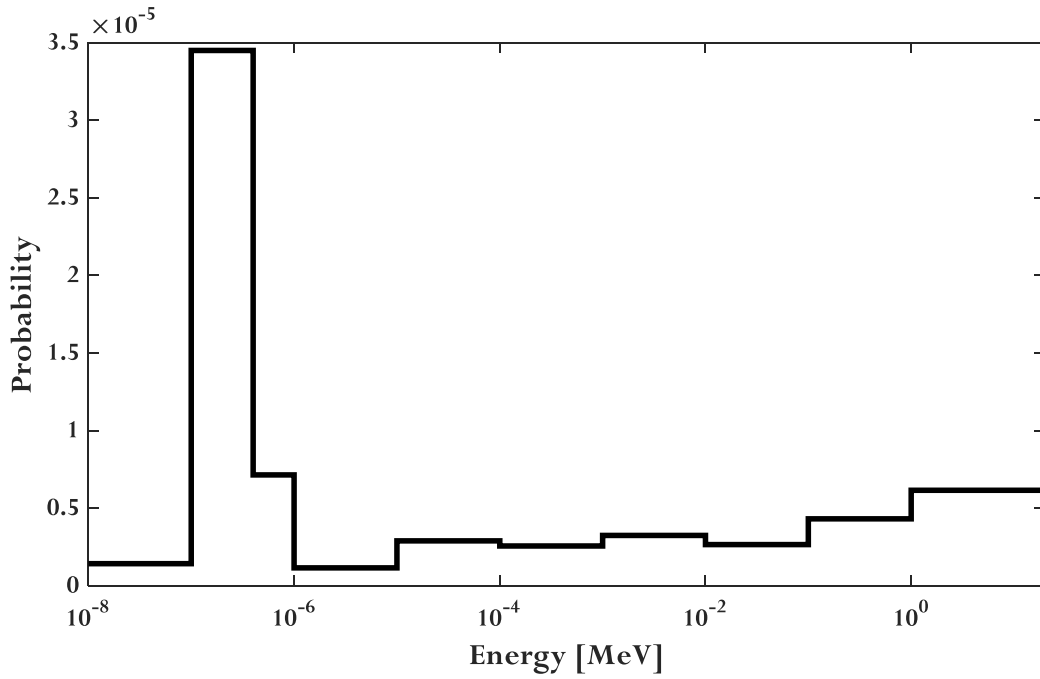
Figure 3-23. BP5 thermal neutron source probability histogram.
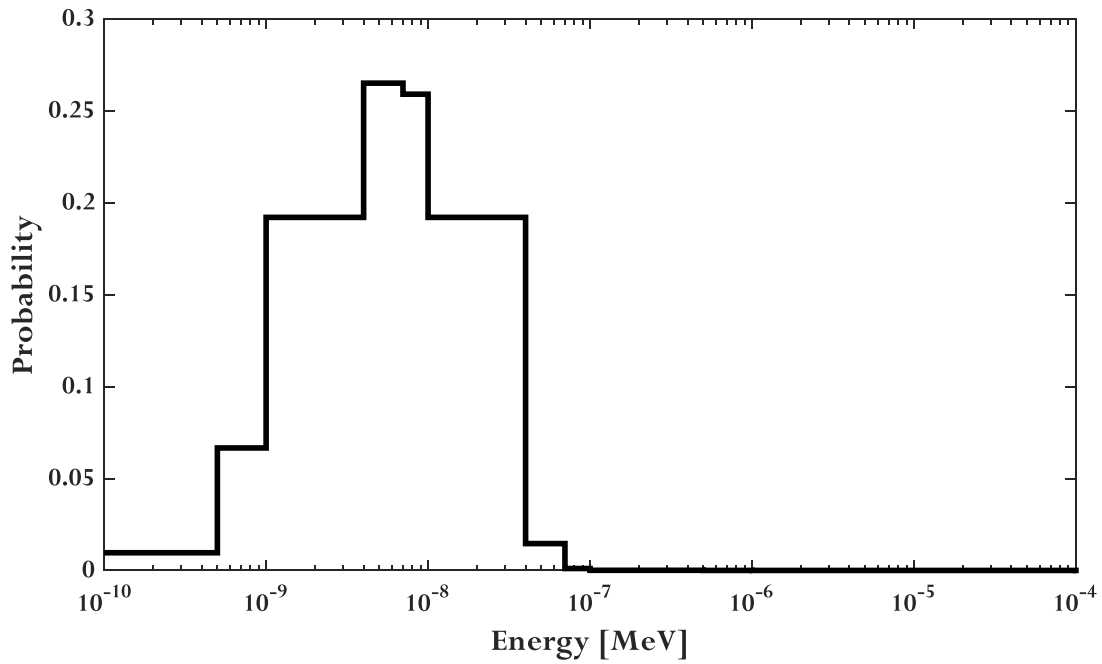
Figure 3-24. BP3 sub-thermal neutron source probability histogram.
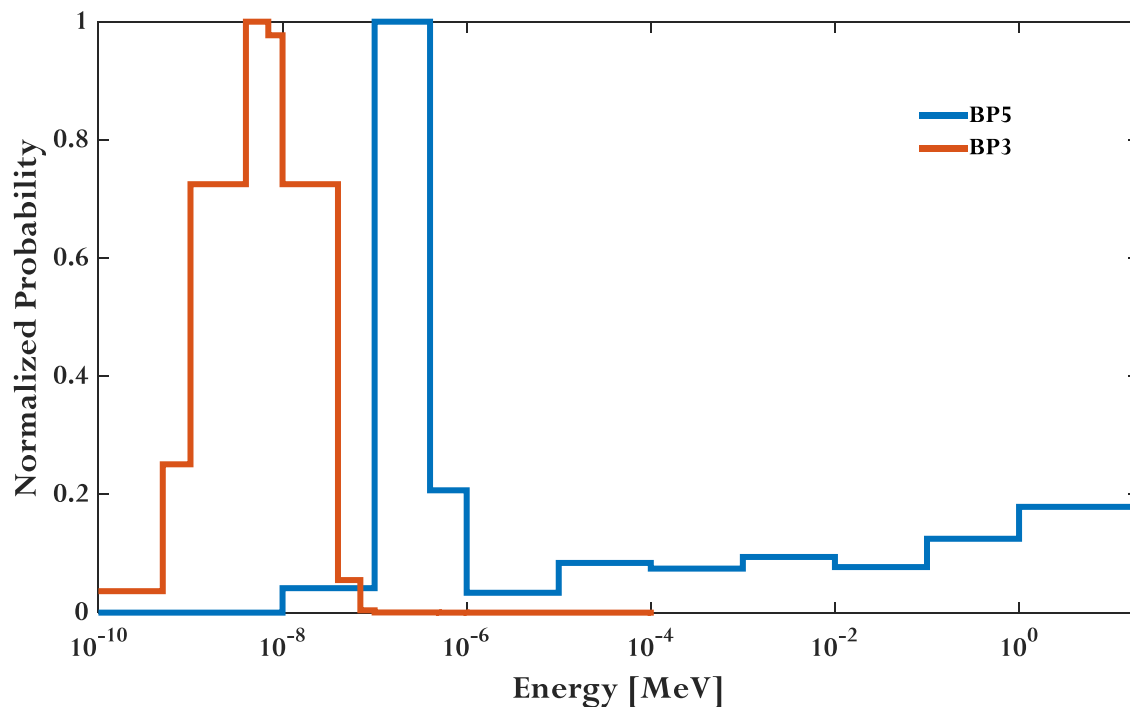
Figure 3-25. Comparison of BP5 and BP3 normalized neutron source probabilities.

MCNP calculations were also performed for the beam size and uniformity. The MCNP detector flux pinhole camera tally was used to estimate the flux image at the image plane. The pinhole size can be adjusted to the region of interest to improve statistics. The FIR tally in MCNP was used to acquire the beam source profiles of BP5 and BP3 (see Figure 3-26 and Figure 3-27 respectively), which show the direct neutron flux near the imaging detector. This tally uses an array of point detectors to measure the flux at various points on a grid. From the Figure 3-26 and Figure 3-27 it can be observed that the neutron flux is more intense in the center. It can be seen that the flux near the image plane is approximately 40 cm wide on each side. To make the beam uniform as a function of distance from the centerline, one needs to specify "sp2 -21 1" for the SDEF card in MCNP. Currently it is decreasing by approximately 1/r from the center line of the

beam port. The MCNP simulated beam intensity profile will be checked with the actual intensity profile in Chapter 6.
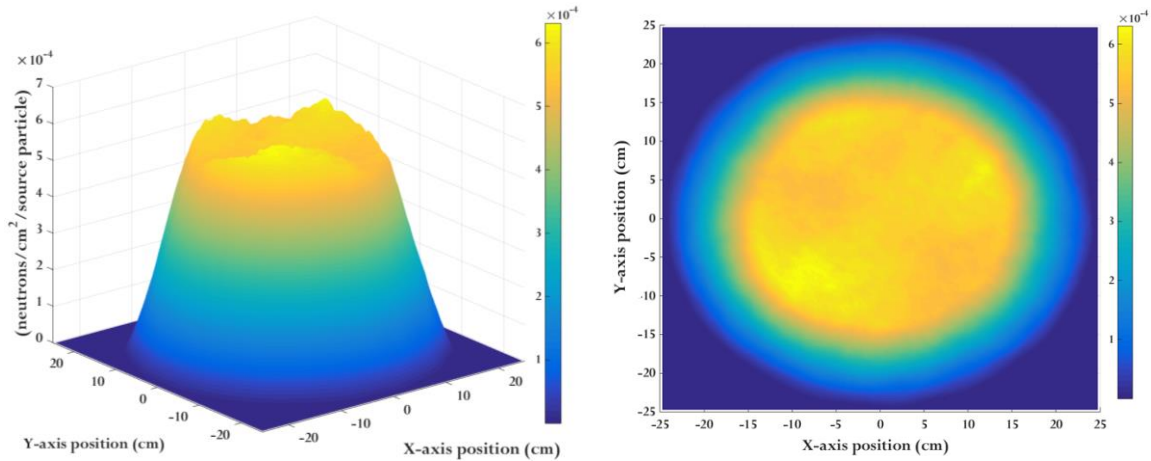
Figure 3-26. BP5 source profile. The simulated direct neutron flux image at 2.8 m from the aperture plane. This is roughly the flux seen at the imaging plate without the robot or simulated sample in place.
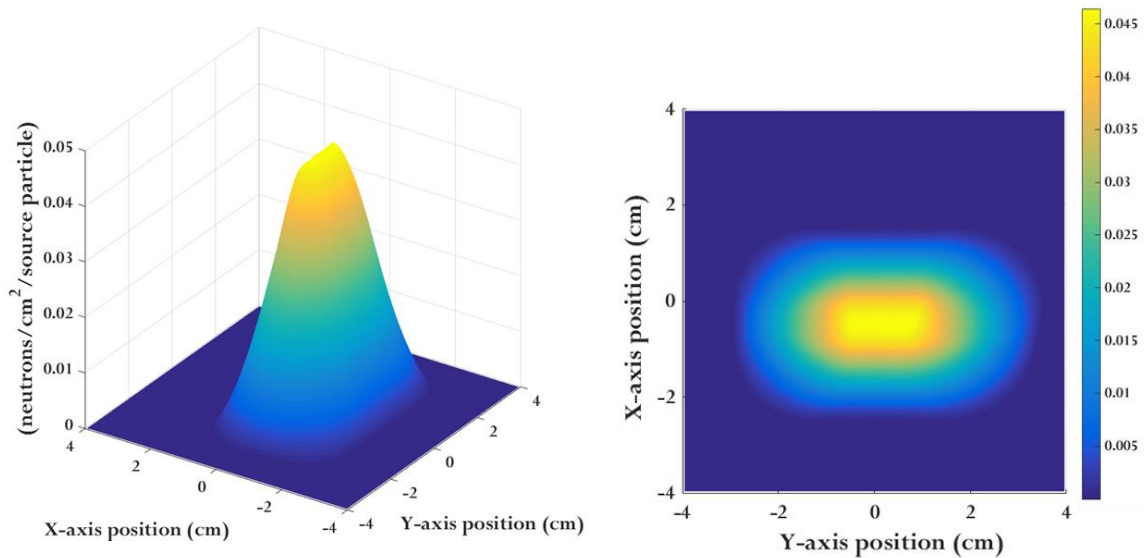
Figure 3-27. BP3 source profile. Contour plot of the simulated direct neutron flux image near the imaging plate without the robot or simulated sample in place.

104

3.10   HARDWARE FEASIBILITY SUMMARY

This chapter has shown that NDT automation is feasible with the available hardware. The repeatability and accuracy of the SIA5 manipulator used in this work has been shown to be feasible for the required NDT imaging tasks. The resolution of the SIA5 in Cartesian space was found to be 16.8 μm, whereas the joint resolution of the robot will be lower. Any vibration that occurs while the robot is stationary has been shown to be less than the resolution of the imaging acquisition devices used in this work, so vibration will not adversely affect the resulting image. Vibration that occurs during robot movement is inconsequential since images are only taken while the robot is stationary. Neutron activation analyses showed that the addition of the robot to the NDT system will not adversely affect radiographic image quality. Ideally, more tests could be conducted into the accuracy and repeatability of the robot grasping objects. For multiple, similar parts, the robot will need to grasp each part in a repeatable manner so that resulting radiographs are the same.

Chapter 4: Evaluation of Operational Software Feasibility

4.1 INTRODUCTION

Software development for a robotic system spans several layers from low-level device drivers to high-level decision making. Robotic systems also consist of different types of hardware, such as grippers, depth imagers, force/torque sensors, manipulators, etc., assembled to address a specific problem or application area. Thus researchers must write an exhausting amount of code and time porting old code to new systems just to get a system to function properly before they can add their own original contributions. Collaboration also becomes difficult because different labs and companies have their own software architecture. This chapter will discuss the operational software and its feasibility for NDT imaging applications in order to determine if existing software can provide the necessary control capability for NDT applications.

4.2 ROBOTIC SYSTEM SOFTWARE

Flexibility is a key consideration for potential users of automated imaging systems. Using traditional teach pendants to manually program robots for imaging of components is time consuming. Complex shape surfaces, as opposed to symmetrical geometries, pose a number of challenges from the point of view of path programming. When discrete points on the inspection path are recorded manually, i.e. "teaching", the process can be arduous, and requires that the location can be accessed by the operator. Therefore, the software needs to be able to provide accurate robot trajectories, eliminating the need to use the "teach" method.

There is also a need for robotic systems that can recognize complex and unorganized objects with little or no prior knowledge about the pose of geometry of the

parts. Therefore, the software, with the assistance of a depth sensor such as the Microsoft Kinect, must include image acquisition and processing abilities.

4.2.1 Robot Operating System

Traditionally, industrial robots have been programmed in complex proprietary languages that are difficult for anyone but experienced robot programmers to understand. Motion controllers are wide and varied, and are usually programmed using a PC library or another proprietary language. In today's automation environment, motion controllers, and robots must be tightly integrated. In order to meet challenges associated with complex systems of several hardware pieces and software of varying abstraction, the Robot Operating System (ROS), which is a flexible framework for writing robot software and has become the standard for scientific and academic research, is employed. [ROS, 2013] ROS is distributed under a BSD license as free and open-source software. At its core, ROS provides a framework for facilitating interprocess communication among many independent processes that run as separate nodes in a graph. [Quigley et al., 2009] On top of this framework, a large software ecosystem provides tools and capabilities for a wide range of robotics applications. ROS includes device drivers, visualization tools, simulators, message passing and parsing, package management and more. A suite of ROS capabilities called MoveIt is utilized. [Chitta et al., 2012] MoveIt provides modeling, visualization, and the advanced motion planning necessary for online trajectory computation. It uses a probabilistic motion planner that robustly computes trajectories that avoid collisions, kinematic singularities and joint limits. A library was created to provide a convenient interface for interacting with the robot and environment using ROS and MoveIt using high-level commands, such as "stow robot", "pick", and "place". ROS was installed on an Ubuntu Linux 12.04 (Precise Pangolin) operating system.

In order to accomplish motion planning, robot trajectory execution, and integration with other hardware, it is necessary to have a suitable framework. Development of the manipulation framework for the arm has been accomplished with ROS. The resulting trajectories are sent to the robot via Yaskawa's FS100 controller, which allows for monitoring of the system for excessive forces and/or collisions. ROS was used for motion planning of the robot as well as a tool for facilitating interprocess communication between the imaging acquisition device and the robotic manipulator. Research groups, hobbyists, and enthusiasts have contributed to the project with such interest that there is now an enormous code base that provides a convenient springboard for robotic and human-machine system development with a standardized interface allowing for seamless addition or subtraction of devices in a modular, adaptive framework. ROS is a peer-to-peer system in which system components run as nodes on a distributed network. These nodes interact with each other through a standardized messaging system. This provides a strong separation between the interface and implementation that simplifies code reuse and collaborative system development. ROS also provides visualizations of the system components as well as the communication and interdependencies. The node graph for our system is shown in Figure 4-1. The joint trajectory action node is used for path planning as it determines optimal motion plans for the robot while obeying collision and geometric constraints. The pickup and place node identifies and locates known objects in the environment. The planning scene node includes the workspace model, which defines how the robot is configured within the environment. ROS has made it easier than ever before to integrate the latest developments in the research community into practical robotic systems.
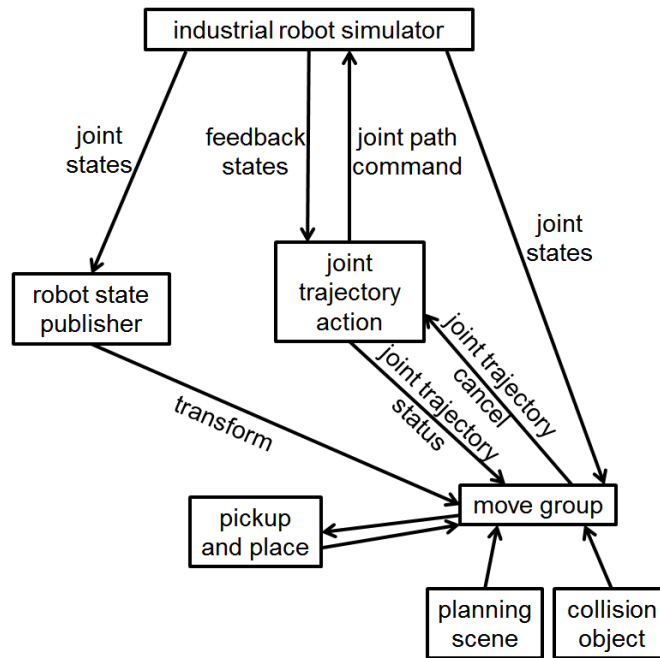
Figure 4-1. ROS nodes and system components.

It is necessary for the software used for commanding the robot to integrate capabilities such as motion planning, part modeling, capturing of environment, collision detection, obstacle avoidance, grasping, etc. while still meeting the imaging performance requirements. The software framework needs to be precise and have online motion planning built in. The precision of the motion plans will be demonstrated via the radiography images obtained in Chapter 6. The software should also be written so that the NDT engineer can easily and safely command the robot via clear and intuitive interface modes.

MoveIt is used for motion planning (Figure 4-2). The robot must be able to orient samples in 3D space to achieve abilities such as computed tomography and helical scans. To support transitional autonomy and to maintain system flexibility, the system uses an advanced probabilistic motion planner for efficient online motion planning. If a repeated move is desired, it can be hard-coded.

ROS includes several visualization capabilities. RViz [ROS, 2014] (Figure 4-3) was used to visualize the robot joint states, the testing environment, and evaluate proposed trajectories for collision detection and kinematic feasibility. Simulations were performed using both the SIA5 manipulator as well as the Yaskawa SIA10 manipulator, which is also a 7 DoF robot, but with a 10 kg payload.
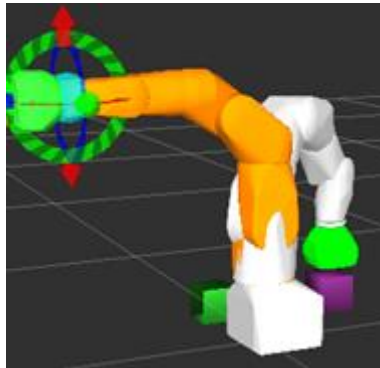
Figure 4-2. **ROS MoveIt pick and place simulation with the SIA5 manipulator picking up one of the objects (colored purple) and moving it to the place position. The white robot represents the current location of the manipulator, and the orange robot shows the initial position of the manipulator.**
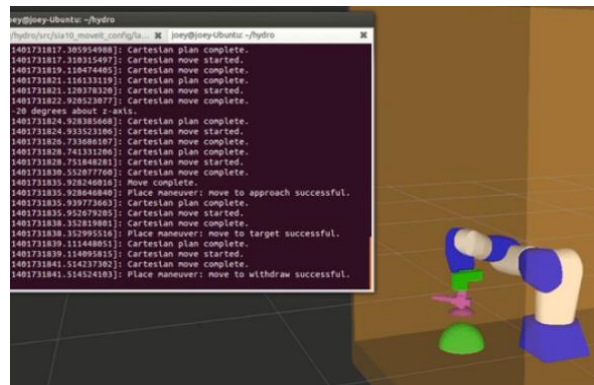
Figure 4-3. RViz visualization of example radiography application.

4.2.2 Capabilities

The NDT robotic system must be capable of performing pick and place motion planning, Cartesian moves, joint interpolated moves, joint motion, obstacle avoidance, and collision detection. The architecture ensures that the paths proposed by the operator

are collision free and kinematically feasible. Thus safety and robustness are assured without adding a significant burden on the operator who may not be a robotics expert.

Known objects are added to the motion planning and collision environment once the code is run, which allows the code to be more versatile and flexible. These objects can be inserted directly as shape primitives (i.e. box, cylinder, etc.) or triangle meshes created from STeroroLithography (STL) files that are commonly exported from CAD software packages. These shapes can either be known to exist at particular positions or identified using a 3D depth sensor. Known objects can also be shapes recognized by a semantic perception pipeline. Since objects are not hard-coded into the environment, users are able to add their own environments in a few lines of code without having to manually import files to build their environment each time the code is run. If the vision system detects an object that is not currently in the simulated environment, the object could be added to the collision map as a primitive that would then be used in collision avoidance. Any motion planning would then attempt to find a path that avoids this collision object. Point clouds that have been identified as objects can be added to the scene as a single object or multiple objects.

Many robots have some capability to pick up objects found in the environment. Once the robot has picked up an object it may wish to move in the environment without hitting the object against other objects, as doing so may represent a safety hazard, disrupt the current task, damage the object, or cause the robot to drop the object. The object needs to be accounted for when checking states for collisions. Attaching an object to the body of the robot means that the object will move when the robot moves (see Figure 4-2); this functionality allows the motion planner and the trajectory monitor to deal with situations where the robot has grasped something and requires avoiding collisions between the grasped object and the environment. Obstacle avoidance is constantly

111

running in the background, so the robot will avoid any collisions with objects while it moves around the scene.

4.2.3 Motion Planning Library

ROS comes packaged with the Open Motion Planning Library (OMPL), which contains a number of popular sampling-based motion planning algorithms [Moll et al., 2012.]. OMPL allows the user to use these planners in their application code by inputting minimal high-level commands. OMPL's planners all perform collision avoidance and model-based collision detection, which will take user-specified 3D models to generate a valid workspace. This work utilizes a version of the Rapidly-expanding Random Trees (RRT) sampling-based planning algorithm included in OMPL to achieve collision-free motion plans.

4.2.4 Collision Detection and Obstacle Avoidance

Samples imaged with the robotic system can be radioactive prior to the experiment or activate during measurements when irradiated with neutrons. Collision of the sample containment with surrounding objects can cause damage to the sample, sample container, or hardware and lead to possible contamination of the environment with radioactive material. Industrial robot controllers' collision detection often rely on detection of a servo fault or current limit spike. Collision detection at this level avoids major damage to robotic components but should be avoided to preserve the lifespan and integrity of the source, detector, robot, and the imaged part. Visual feedback from a camera system could provide data when an undesirable object enters the workspace.

4.2.5 Collision-Free Path Planning

When performing point-to-point and reactive motion planning, collision detection is a necessity. It is required for the robot system to check for collisions during motion

planning to avoid obstacles. The architecture ensures that the paths proposed by the operator are collision free and kinematically feasible. Collision-free path planning is important because of the risk of damage to delicate imaging equipment and samples.

Collision-aware path planning. ROS provides model-based collision avoidance and detection. For this work, it is necessary to have *a prioi* knowledge of the robot's workspace. For imaging applications, the workspace is usually fully defined and all geometric obstacles known prior to starting the automation system. Therefore, all obstacles can be accounted for in software. This greatly improves accuracy provided there is accurate collision detection within the simulation. Industrial robot arm control and movement between computer simulation and actual hardware is virtually identical. This effectively negates the need for human interaction inside the radiation environment port for neutron and x-ray imaging tasks. The software automatically finds the path to the target position and avoids obstacles, joint limits, etc. Motion planning inputs by the user can be interactive (i.e. RViz plugin[3]), ROS actions[4], and C++/Python API. Then ROS performs motion planning using kinematics, path planning, and collision checking. Finally, the trajectory execution is sent to the robot. With traditional robot programming, motion types are typically limited, but well-defined. A joint or linear motion is completed via interpolation between the starting and ending locations. There is usually a single motion task. Figure 4-4 shows the basics of ROS motion programming. Motion types are flexible and goal-driven, with constraints. There is minimal control over the actual path, but collisions are avoided.

---

[3] The user can move the robot through a GUI using the motion planning plugin to RViz.

[4] ROS actions communicate via a "ROS Action Protocol", which is built on top of ROS messages. The client and server then provide a simple API for users to request goals (on the client side) or to exectute goals (on the server side) via function calls and callbacks. An action specification then defines the goals, feedback, and result messages with which clients and servers communicate. Examples of ROS actions include moving the robot to a target location, performing a weld and returning the point cloud, detecting the handle of a door, etc.
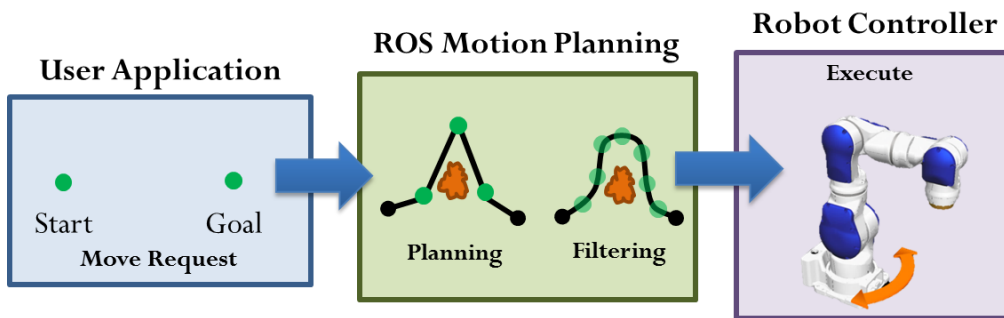
Figure 4-4. ROS motion programming.

The reachable workspace of the SIA5 was calculated and is shown in Figure 4-5. This shows the workspace boundaries of the manipulator with a Robotiq 2-finger gripper inside of a box. From Figure 4-5 it is obvious that the range of motion from the axis of rotation around z to the last point of the EEF, in the y-axis direction is roughly 0.73 m. It should be noted that this range is only theoretical. The workspace is often broken down into a reachable workspace and dexterous workspace. The reachable workspace is the entire set of points reachable by the manipulator, whereas the dexterous workspace consists of those points that the manipulator can reach with an arbitrary orientation of the EEF. The dexterous workspace is a subset of the reachable workspace. To acquire the SIA5's workspace, MATLAB was used to record the EEF path at 10 Hz as the robot moved to random locations. Joint interpolated motions were used to complete each move.

A collision object (Figure 4-6) was added to the robot's workspace to demonstrate the collision avoidance capability of the software. The reachability workspace of the SIA5 with the collision object added is shown in Figure 4-7. It is apparent that the robot automatically avoids the collision object, as shown by the lack of motion inside the dashed red circle.
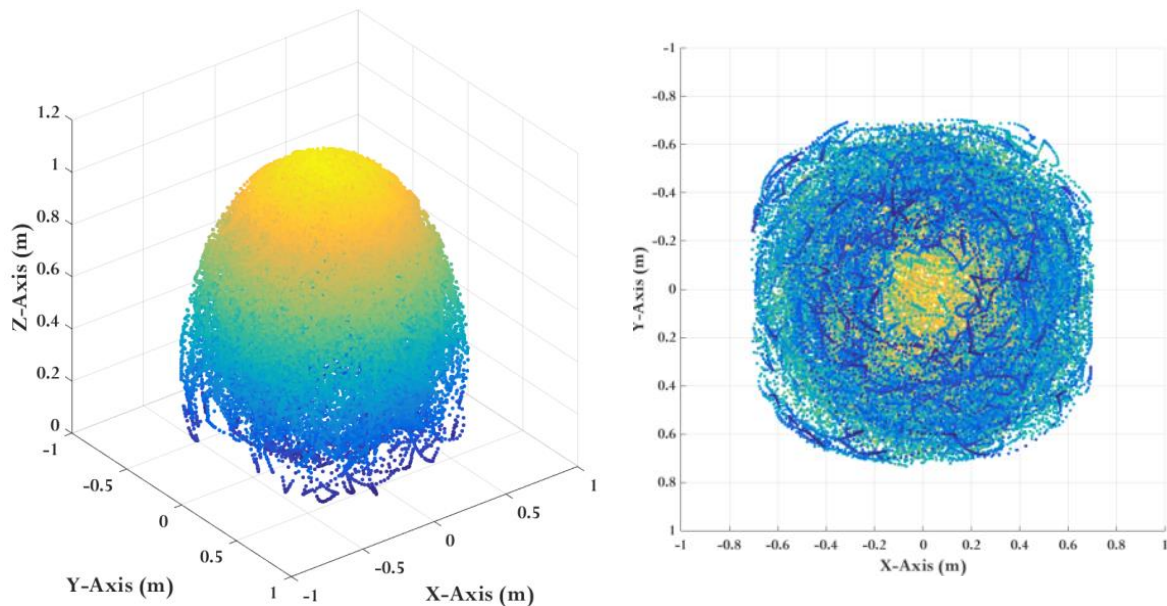
Figure 4-5. Workspace of SIA5 inside box. The base of the robot is located at (0,0,0). The maximum and minimum for all three axes are: 0.7038 and -0.7065 (x-axis); 0.7332 and -0.7018 (y-axis); and 1.1075 and 0.0475 (z-axis). Each point in the workspace is calculated from the robot's base to the EEF (i.e. joint 7). Isometric view (left) and bottom view (right) are shown.
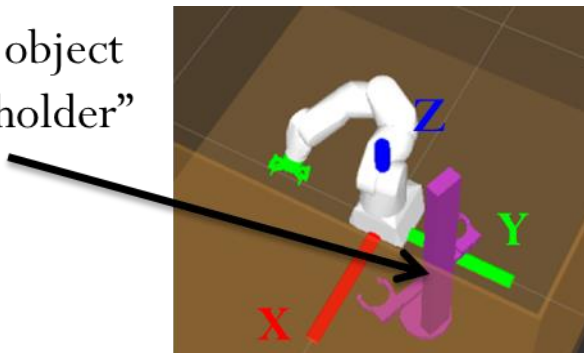
Figure 4-6. SIA5 with collision object in workspace.
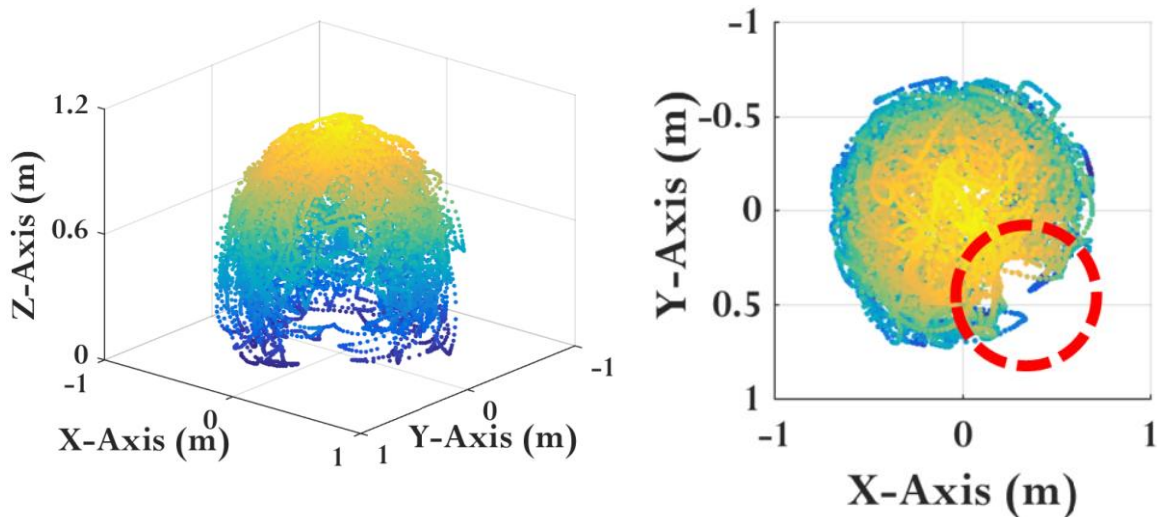
Figure 4-7. Workspace of SIA5 inside box with collision object. The maximum and minimum for all three axes are: 0.6911 and -0.6980 (x-axis); 0.7202 and -0.7021 (y-axis); 1.1084 and 0.0530 (z-axis). Each point in the workspace is calculated from the robot's base to the EEF (i.e. joint 7). Isometric view (left) and top view (right) are shown. The dashed red circle indicates the location of the collision object. Note that the lines in 2D are projected from above.

For NDT applications, the workspace problem is a bit more complex since the constraints on the system will likely be somewhere between the reachable space and the dexterous space. In addition the kinematic constraints may be different for each test. However, proper alignment of regions of the robot's dexterous space with the source beam should provide more than adequate capability to complete normal motions required for NDT imaging.

4.2.6 ROS-Industrial

ROS-Industrial (ROS-I) leverages the capabilities of ROS for industrial applications. ROS-I (Figure 4-8) is an open-source project to broaden the advanced capabilities of ROS to new industrial applications. [Edwards and Lewis, 2012] For our system, ROS-I provides hardware drivers for the FS100 controller. These drivers provide the ability to execute precomputed trajectories through the native Yaskawa controller protocols. As part of the work presented here, these drivers have been significantly

modified to permit on the-fly point streaming to the controller without first precomputing the trajectory. This is essential for sensor-in-the-loop or human-in-the-loop operation. In the course of the current work, we have developed a high-level software library to simplify interaction with MoveIt and ROS industrial for the application programmer.
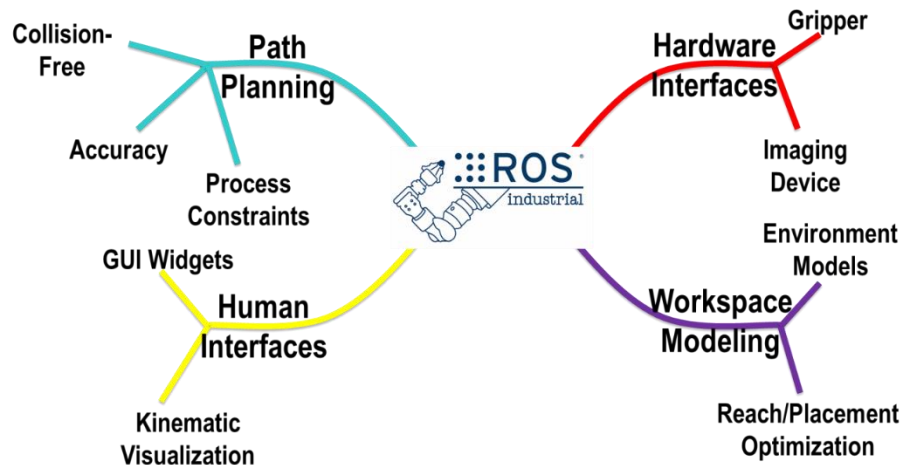
Figure 4-8. ROS-I capability map.

4.2.7   Micro-Commands

CT and helical scans can require more than 4,000 images to be taken at sequential angular steps. This requires the robot to achieve joint angle movements less than 0.1 degrees. In order to do this, the software computes a mini trajectory at each step so that the robot can achieve the small joint angle movement. There are four points along each trajectory; point one and four are the starting and ending point respectively. Without performing this mini trajectory, the minimum increment a robot can move via a simple joint motion command (i.e. `arm->move()`) is 0.287 degrees.[5] Therefore you have to perform a joint trajectory motion to achieve smaller joint moves. The same mini trajectory can be used to give micron level commands to the robot for Cartesian motions.

---

[5] This minimum joint value increment was determined experimentally using an SIA5 manipulator, FS100 controller, ROS Hydro, and Ubuntu 12.04. More work needs to be done to determine if this is a ROS, FS100, SIA5, or MoveIt limitation and why.

4.2.8 Risk Analysis

A risk analysis was carried out, identifying breakdown recovery as a particular area of concern because of the potential handling of radioactive material and the restrictions on personnel access as radiation levels increase. The robotic system therefore includes features to either avoid foreseeable problems or to enable recovery in the event of failure when the robots are handling highly radioactive parts. One example of problem avoidance is the implementation of collision avoidance. Another example is robot joint current monitoring during operations; if a joint current exceeds its threshold value, the robot will stop. This monitoring allows detection of problems before the robot generates large forces on fixed surfaces or other equipment in the area. This ensures recovery is not hampered by the robot having to cut out after exceeding the maximum joint current limit.

The system permits the operator to easily cancel autonomous execution at any time and revert to teleoperation, or issue new high-level motion commands, such as "stow robot behind shielding" or "place part down", without the need to restart any hardware or software. The user is kept in-the-loop, so they are able to intervene in the case of an emergency.

4.3 ROBOTIC SYSTEM PLANNING ALGORITHMS AND SETUP

A robust motion planning algorithm is essential for task completion in hazardous environments. The planning algorithm was implemented in C++ utilizing the ROS software framework. A typical procedure begins with the robot arm grasping the part. After a successful grasp (which can be confirmed via vision, F/T sensor, or joint torque calculations via joint currents [Schroeder, 2013], the arm would then position the part for imaging. The system is designed to provide autonomous completion of tasks. However, the software system permits operation across an autonomy spectrum, providing human-

in-the-loop supervision. This gives the operator options for handling unforeseen circumstances. Below is a list of standard operating procedures utilizing the robot.

1. Move to *Home* position. Moves the robot to a pre-defined position via joint moves.

2. Move to an *Approach* position via a joint interpolated motion.

3. Move down to *Pick* a part from the part storage tray. The robot executes a Cartesian move to the object in a pre-grasp pose, grasps the object by automatically closing the Robotiq gripper or actuating the vacuum gripper, and returns to the pre-grasp pose.

4. Move back up to a *Retreat* position above the table. Similarly as before, this is achieved via a Cartesian motion.

5. *Position* the object in front of the beam path. The robot moves the object to the approximate beam location via joint motions, and executes a Cartesian move to position the object in the desired beam location. The object is automatically positioned and aligned by the code depending on the imaging application required. For example:

   a. Rotate object about x-y-z axes

   b. Translate

   c. CT scan

   d. Helical scan

6. *Acquire* the image. This process is continued until the entire application is completed.

7. *Place* the object back down in the storage tray. A joint motion is used to move to the approach pose and then a Cartesian move is implemented to the final position. The robot then moves to the retreat position via a Cartesian move.

8. *Pick* up the next object, repeating the steps above.

4.3.1 System Setup

ROS also allows for hardware besides robots to be integrated into the application code. For this task, it is necessary for the imaging device to be automated and correlated with the robot's motions, the pneumatic vacuum gripper valve to be toggled to open and close, and the Robotiq 2-finger gripper to open and close. This is achieved via publisher/subscriber nodes within the ROS framework. When an image is ready to be taken (e.g. the robot has just completed a rotation and come to a stop during a CT scan) ROS publishes a message to the imaging device to acquire and image. The imaging device is constantly looking for this published message. The imaging device can then publish a message back to the robot after it has completely acquired the image, telling the robot to continue. ROS libraries also allow for the integration of the Arduino microcontroller IDE using the ROS communication protocol. By publishing commands within the application code, the user can use an Arduino microcontroller to send high and low voltage signals to different pins to actuate the vacuum gripper valve.

While the hardware system is composed of off-the-shelf components, the software system is custom-built to provide the flexibility required to automate difficult tasks. Figure 4-9 shows a general overview of the major software and hardware system components and interactions with each other. ROS includes the robot software and application code (e.g. pick, place, etc.). To ease integration, the software is organized as a set of nodes that communicate via a standard messaging protocol that allows various hardware drivers and algorithms to efficiently share data. This system has been developed to simplify application-level programming.
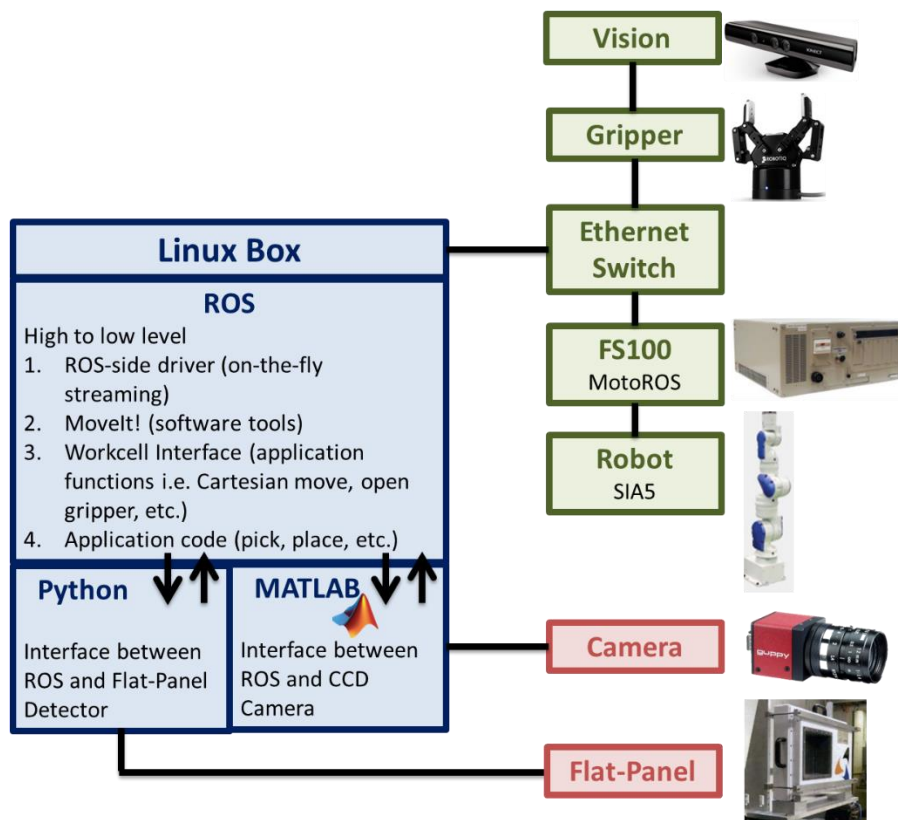
Figure 4-9. System setup.

4.3.2 Integrated System Architecture

A system architecture has been developed for integration of radiography imaging with a robotic manipulator. The goal of this section is to describe the architecture and its handling of data for use in robotic imaging applications. The architecture utilizes ROS, Python, and MATLAB. The platform aims to autonomously perform complete imaging applications, such as radiography, CT, and helical scans, where images are automatically acquired at each step in the scan, through communication between the motion control and image acquisition. The architecture is modular in nature so that different imaging devices can easily be substituted into the platform.

The utilization of ROS allows for communication between the robot and the imaging devices using scripting languages (C++, Python, and MATLAB) all on the same

121

PC. The code to run the robot is written in C++, the flat panel acquisition software is written in Python, and the CCD camera [Allied Vision, 2015] software runs using MATLAB. ROS has tools to communicate between all three systems. The algorithms for communication between the systems are relatively simple and easy to modify as shown in the presented pseudocode in Appendices D-F. ROS creates a publisher "talker" node that broadcasts a message to either the flat panel detector or CCD camera when the system is ready to acquire a radiograph. A node in ROS is the term used for an executable that is connected to the ROS network.

Line 12 in Appendix D tells the master node that a message is going to be published on the topic `acquire_image`. This lets the master tell the flat panel detector or camera node that are subscribing to the `acquire_image` topic when to acquire an image. Line 58 in Appendix D tells the master node to subscribe to the `acquire_image` topic. This topic tells the master node whether to continue with the robot application if the image acquisition has finished, or to wait if the image acquisition device has not yet completed the exposure time or completed the saving process of the radiograph. The master node subscribes to this topic in a loop, so that it will constantly check to see if the robot can continue operation.

4.3.3   ROS and Flat Panel Detector for X-Ray Imaging

Acquiring radiographs via a flat-panel detector (PaxScan 2520) [Varian Imaging, 2011] is implemented in Python. The Varian panel, which uses a Gigabit Ethernet interface, is custom-made so that it is radiation tolerant to high-energy x-rays. The implementation is generalized as shown below. The python script (Appendix E) publishes a message to the ROS master node, telling it when the radiograph has been acquired, and

listens to the master node to know when the robot has completed its motion and the system is ready to acquire a radiograph.

4.3.4 ROS and CCD Camera for Neutron Imaging

A MATLAB script is integrated with the robot-scintillator-mirror-CCD camera system for neutron imaging. MATLAB includes libraries for many different types of Gigabit Ethernet CCD cameras. To exchange messages with nodes on the ROS network through MATLAB, the Robotics System Toolbox is needed, which provides the interface between MATLAB and ROS. [MathWorks, 2015] Example code is shown in Appendix F. This code functions similarly to the python script in that it subscribes (i.e. listens) to the ROS master node when an image is to be acquired and publishes (i.e. talks) to the master node when the image has finished saving.

4.4 DETECTING OBJECTS TO BE GRASPED

Robots operating in unstructured environments must be able to perceive and reason about the world around them in order to execute motions that accomplish tasks. The robotic system has to be able to autonomously detect and track objects to be imaged. This includes the ability to recognize objects of interest in the environment and their location to support obstacle avoidance, task planning, and grasping. A method is described to allow the recognition and localization of objects. This method allows a robotic system to recognize and interact with these objects when the object location is not fixed or known *a priori*. By integrating an autonomous real-time system for identifying object and their relative poses (i.e. location and orientation), the robotic system can locate specific objects in order to pick them up. The goal of this is to increase autonomous operations with a fully integrated real-time machine vision support. The detected objects can be modeled as a collision layer in ROS after their pose has been determined;

therefore the ROS software would not allow the robot to run into these objects, objects to collide with the environment, or allow collisions between objects. Even if this software obstacle avoidance layer fails, an active alarm system is also incorporated to warn the operator of potential object closeness before objects collide, therefore greatly increasing system and object safety. This system provides an additional layer and support for robotic imaging systems, particularly work involving objects that need to be grasped. This system is also flexible enough to meet individual imaging application procedural needs by integrating different types of identification and alarm methods. Introducing technology and a human interface provides a user-friendly feedback system to alert the operator of near-proximity instances before collisions occur via visual monitors and audio alarms.

The system's object identification method relies on recognition of a marker. However, the primary and preferred action is to have objects to be imaged in a storage tray (see Chapter 6 for more information) with the objects modeled into the simulated environment offline. Even so, it is desirable for the system to be robust for one-of-a-kind objects that are not in a storage tray. In this manner, the system will have multiple methods for identifying objects' locations.

4.4.1 Significance and Background of Imaging System

Safety is a top priority for all work done at DOE national laboratories such as LANL. The use of neutron or x-ray sources for imaging purposes involves detailed procedures, unique environments with specialized tools and working conditions, and most importantly many layers of safety considerations and regulatory requirements that must be met before, during, and after work is performed. Within all of these constraints,

errors occur that lead to pause or stop work conditions and time spent filling out documentation to report the incidents.

Work by O'Neil [2013] has been performed to turn depth sensor measurements into a representation of the objects present in a glovebox. This process happens in two steps. First, the points from the depth image are separated into clusters representing individual objects by a Euclidean clustering scheme. Each cluster is then passed to a recognition algorithm that determines what it is, and where it is. This information allows the determination of the object's position and orientation relative to a specified coordinate system. This object recognition software can be used to identify objects that cannot be easily labeled. The software also has the advantage of recognizing objects in real-time and the ability to differentiate between objects of similar shapes but different sizes. A dataset of objects to be imaged will need to be established and can be expanded upon if needed.

The imaging system created for this work will use similar software to identify objects present in the environment through a sensing system while removing the responsibility solely from the worker to tell the robot where the objects are and if a collision is about to occur. The implementation of this system will reduce the safety infractions by warning the operator(s) of approaching collisions within the robotic imaging system combined with obstacle avoidance on the software level.

4.4.2   Imaging System Approach

The ROS developer community has provided ROS compatible device drivers for many common cameras and imaging systems including the Microsoft Kinect for Xbox 360 (see Figure 4-10) used in this work to provide visual marker, object recognition, and tracking. The basic ROS installation includes the Point Cloud Library (PCL) or point

cloud image processing. [Rusu, 2011] This makes integration of perception convenient because image acquisition and processing are done directly in ROS. ROS provides file-system and runtime tools that greatly simplify creation of a modular pipeline that integrates easily with other control system components. However, neither ROS nor PCL provide a complete recognition pipeline.
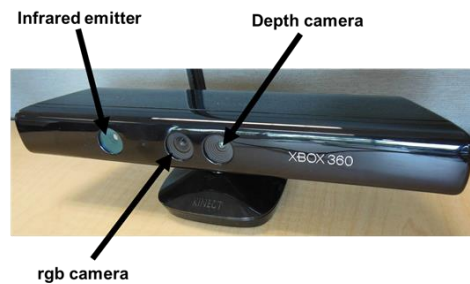
Figure 4-10. Microsoft Kinect for Xbox 360 has both rgb digital video camera and a structured infrared depth camera. It produces an image that consists of a depth value for each pixel. This capability is used to measure the location of objects in 3D world coordinates.

For this work, a ROS software package called `ar_kinect`, which utilizes PCL, was modified and used for visual marker recognition and localization using 3D data from a Kinect. These markers are used to tag objects for identification and tracking (see Figure 4-11). Niekum et al. [2015] also used these visual fiducials to determine the location of and to track relevant pre-determined task objects using combined visual and depth data from a head-mounted RGB-D camera on a PR2 robot. The `ar_kinect` package has a single node that takes rgb point clouds from the Kinect and outputs a transform between the camera and a recognized marker. The node works by creating an rgb image from the point cloud, finding the corners of the marker, and then computing a transformation to an ideal marker geometry using methods from PCL. The published topic, containing the current marker pose relative to the camera is sent to the ROS simulation and the audio and visual alarm system, which calculates distances between objects.[6]

---

[6] The original code can be found here `https://github.com/mikeferguson/ar_kinect`.
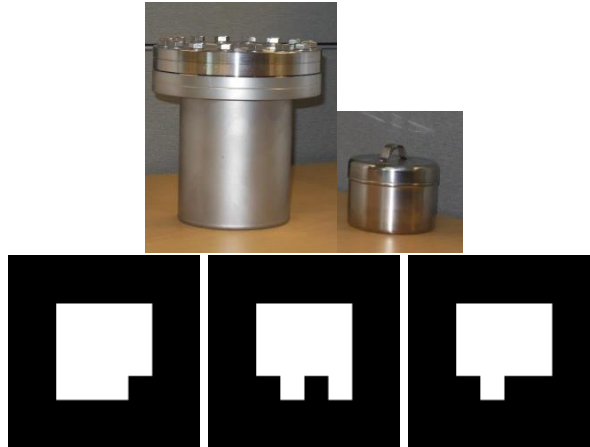
Figure 4-11. Examples of objects to be imaged (top) that can be visually marked with a marker (bottom) that allows identification, location, and tracking.

Once the visual markers are identified, each specific object is cross-referenced with a known list of objects to be imaged. The object can then be modeled in the ROS simulation with accurate location. It is assumed that the possible objects have already been modeled with a 3D CAD program. When two or more objects come within close proximity, a warning audio alarm is played, notifying the operator that a collision might occur and that they need to increase the distance between the objects. The alarm is repeated until the objects are moved to safe locations. If the objects are not moved to a safe location, the robot will stop its movement to prevent a collision.

4.4.3   Imaging System Proof-of-Principle

The concept of marker recognition and proximity warning alarms has been validated in a proof-of-principle experiment (see Figure 4-12).
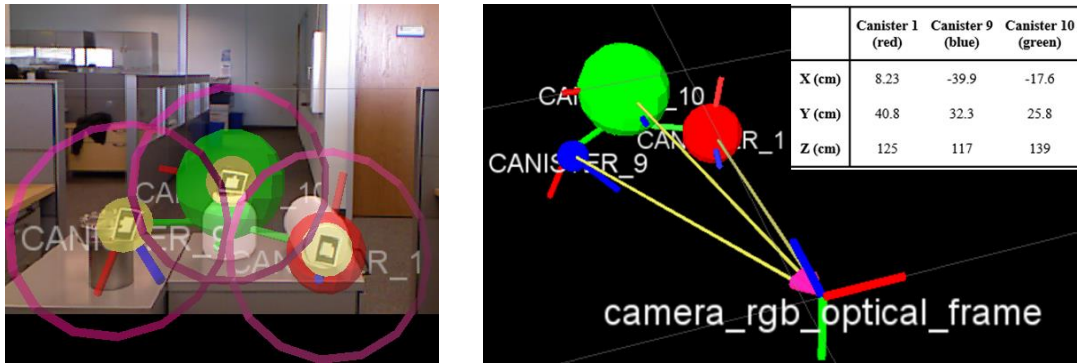
Figure 4-12. Proof-of-principle experiment. Three objects are recognized by their visual marker (left). The objects are shown in 3D space with different colored spheres showing when a warning audio alarm will sound (right). Identified locations of the objects are shown and updated in real-time. The camera's x-axis is shown in red, y-axis in green, and z-axis in blue.

The method of creating a safety layer and warning system to eliminate unwanted collisions between objects, robot, and environment and to alert operators of these possible collisions by measuring the location of objects in 3D space in a non-obtrusive manner has been described in detail with this proof-of-principle work. The system has been designed to be real-time and unobtrusive to any non-destructive imaging work.

The system's workflow is outlined as follows:

1. Most objects in the workspace can be labeled with a unique visual marker read by the vision system. The marker does not degrade the resulting x-ray or neutron image quality and is used for recognition and localization of the object.

2. Once the visual marker is identified, the specific object is cross-referenced with a list of known objects (i.e. *a priori* information block) to model the object in its actual location in the ROS simulation environment. The location of the object is also determined. With the Xbox 360 Kinect, the locating accuracy is approximately +/- 3 cm, but this value can be improved by using newer rgb-depth sensors like the Asus Xtion Pro, which has a 640x480 resolution and improved accuracy by a factor of 10.

3. Some objects are difficult or impossible to physically mark. A 3D object recognition system (that looks up objects in a database and tries to match said objects,

similar to the system by O'Neil [2013]), can be used to identify and localize those objects. An approach for this object recognition process would be to first segment and cluster the scene to find objects. Located objects are then cross-referenced with those already identified with the visual markers. Any marked object is dropped from further processing. The object recognition code will attempt to locate and recognize the object.

4. The robot performs the task, while the vision system continues tracking the objects and their positions in the ROS simulation environment.

5. The code computes the distances between the objects and an alarm is sounded if they reach certain proximity. Another alarm sounds if objects collide.

The goal of the imaging system is to successfully identify and locate objects to be imaged in order for the robot to grasp the objects and to provide an additional layer of safety with regards to collisions. This is additional to other safety layers such as the objects' locations going to the ROS simulation for obstacle avoidance and audio and visual alarms outputted to the operator. The setup of the system is shown in Figure 4-13.
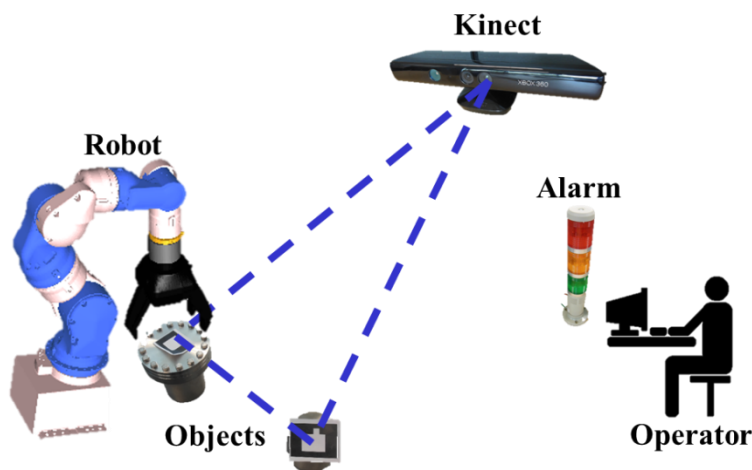
Figure 4-13. System setup. The Kinect sensor, robot, visually marked canisters, alarm system, and the operator are shown. A monitor displays the perceived environment, identified objects, visual markers, and distances between the robot, objects, and environment to the operator.

4.4.4   Imaging System Challenges

Several challenges must be negotiated to implement real-time sensor systems in a radiation imaging environment. The Xbox Kinect is an optical sensor and recognition of hidden objects, occluded objects, or occluded labels is a concern. Hidden objects can be mitigated by introducing additional Kinect sensors in the environment and taking advantage of multiple observation vantage points. The integration of multiple sensors is accomplished via the ROS software. Many radiation imaging environments are tailored for a specific use and operation. Some use x-rays and others use neutrons for radiography and/or computed tomography applications. The location of the robot and the number of imaged objects can vary greatly from one application to the next. Thus each environment may be considered as unique and precludes a uniform implementation of the real-time sensor system to all nuclear imaging environments. The system will be individually installed and implemented. Each workspace will require evaluation for individual needs and concerns as well as equipment installation limitations to meet safety and regulatory requirements. But in every case, the fundamental software packages can be re-used with minimal modification and reduced design time and costs. This can easily be accomplished in order to address the precise needs of a single workspace because the sensor system is flexible. Sensors such as the Kinect are susceptible to radiation damage. However, experimental experience to date infers their usable life is reasonably long if they are kept outside of the direct beam and their low cost makes them easily replaceable.

4.4.5   Summary of Imaging System

The robotic imaging-alarm system provides five key contributions to this work:

1. Identifies objects' poses in real-time so that the robot can autonomously grasp objects.

2. Allows accurate positioning of objects in the simulated environment so that obstacle avoidance is incorporated between the robot and object, objects and the environment, and between objects.

3. An active alarm system warns operators with visual indicators if two or more objects are approaching safe limits.

4. Improves overall autonomous performance of the robotic system and quantitatively reduces (or eliminates) collisions incurred in the workspace.

5. The modular nature of the vision system, which is due to the ROS framework, allows for easy addition and/or deletion of components/nodes in order to build upon the system or to complete a new task without needing to change the entire software structure.

4.5   OBJECT ALIGNMENT WITH BEAM USING VISION

Once an object has been grasped by the robotic part positioning system, the robot needs to align the object with the x-ray or neutron beam, preferably autonomously. A vision recognition system can identify the center of the object or another location of interest on the object and align that location within the incident x-ray or neutron beam. Despite variations in object sizes and orientations, this process can be completed robustly and in under a minute using a single camera. If the robot fails to place the object in the beam path, an operator can manually intervene and move the robot to the required location.

Wasserman et al. [2012] demonstrated the ability to automate sample alignment as shown in Figure 4-14. Once a crystal has been placed on the sample stage, a vision recognition system identifies the center of the nylon loop containing the crystal and places the center of this minute sample stage within the incident x-ray beam. The vision software system identifies several reference points for where the sample is mounted (red

and green crosses). The centroid of the sample mount (orange cross) is brought to the position of the x-ray beam (yellow box).
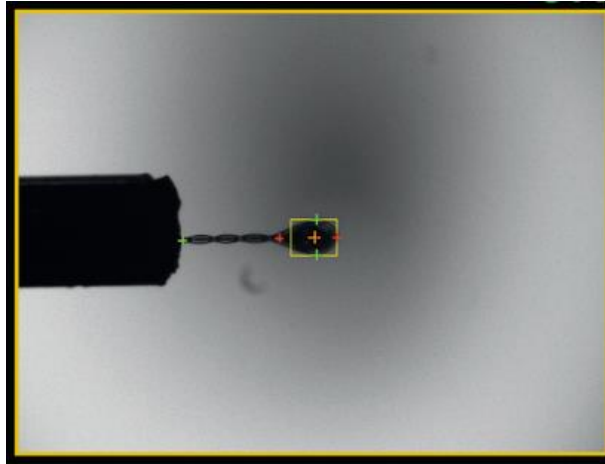
Figure 4-14. Automated sample alignment in an x-ray beam. [Wasserman et al., 2012]

4.6   SOFTWARE FEASIBILITY SUMMARY

This chapter has shown that the available software discussed here meets the requirements for NDT. The software components needed to build a safe, reliable, and feasible automated NDT system were presented. The integrated ROS software system that combines robotic software and communication with peripheral hardware such as image acquisition devices makes simple and high throughput automated radiograph acquisition possible. The software presented in this chapter paves the way for fusion of robotics and NDT imaging techniques in the future. The modular nature of the software due to the ROS nodes makes the implementation flexible, allowing for fast integration of future research efforts. Different portions of the software and hardware integration are implemented as individual ROS nodes.

Chapter 5: Radiation Damage

5.1 INTRODUCTION

The nuclear industry has used remotely controlled manipulators from its very beginning. In recent years, an evolution towards advanced teleoperation has been observed, where robotic features are added to the basic manual control. In nuclear applications, a significant cause of malfunction is radiation-induced damage. Although the first mechanical master-slave manipulators were intrinsically tolerant to the damaging effects of ionizing radiation, the advanced features of modern robots, with sensors, drives and electronic circuits, have increased their sensitivity to radiation.

The selection of cost-effective equipment and its level of environmental qualification for these tasks is a complicated process. The handling of contaminated items, for example, does not require a high level of radiation tolerance but does require attention to surface finish and possible contamination traps. At the other extreme, the handling of highly irradiated fuel or certain types of waste can entirely prohibit the use of standard electronics and many organic materials. It should be noted that reliability of the robot will depend on dose rate and Total Integrated Dose (TID), as well as other factors.

The sensitive components installed on advanced manipulators can be divided into three categories: 1) the drives (usually electrical actuators with bearings, gear boxes and position feedback devices); 2) the sensors (distance and force sensors, cameras, etc.); and 3) the cables and other communication devices (including line drivers, multiplexing circuits, analog to digital converters, radio links and even the preamplifiers needed for some sensors). For each category, the radiation hardening level required will depend on their location with respect to the radiation sources (near the end effector or near gantry tracks or walls) and on their frequency of use (e.g., a tool used a small number of times, compared with protection systems in use permanently). [Houssay, 2000] The robot's

controller can and should be kept out of the radiation environment due to its large amount of electronics.

Potentially, the most radiation sensitive parts of a robotic system are the electronic components. The electronic parts that are the most susceptible to radiation effects are the semiconductors, the semi-insulators, and insulators. The most important of these are the silicon family of parts. Non-semiconductor based electronic and electromechanical components such as servo-motors generally exhibit much greater radiation resistance. For robotic applications in radiation environments, the primary radiation effects of concern are TID and the neutron-induced displacement damage. Single event upsets produced by high energy neutrons and space radiation are only of minor importance for the vast majority of robotic applications except for those in space.

Structural materials in radioactive environments, such as found in a nuclear reactor, are damaged by radiation from fission reactions. Incident radiation carries a certain amount of energy, which is transmitted to the material through various processes (e.g. elastic and inelastic scattering of neutrons). If enough energy is transmitted to an atom of the material, that atom can be displaced from its position in the molecular structure, leaving a vacant site behind (vacancy), and the displaced atom eventually comes to rest in a location among lattice sites, becoming an interstitial atom. The interstitial vacancy pair is of main importance for radiation effects in solids and is known as a Frenkel Pair (FP). The presence of the FP and other consequences of irradiation damage determine the physical effects, and with the application of stress, the mechanical effects of irradiation. The radiation damage event is finished when the displaced atom (also known as the primary knock-on atom, PKA) comes to rest in the lattice as an interstitial. [Was, 2007] As the vacancies, interstitials, and voids caused by repeated displacements build up, the crystalline molecular structure of the material is weakened.

134

Figure 5-1 illustrates the displacement mechanism. For materials such as metals and semiconductors, where key properties like material strength and conductivity are highly dependent on the crystalline structure, repeated radiation-induced displacement can severely impact the material's ability to perform it intended function, reducing the service life of any component made of that material.
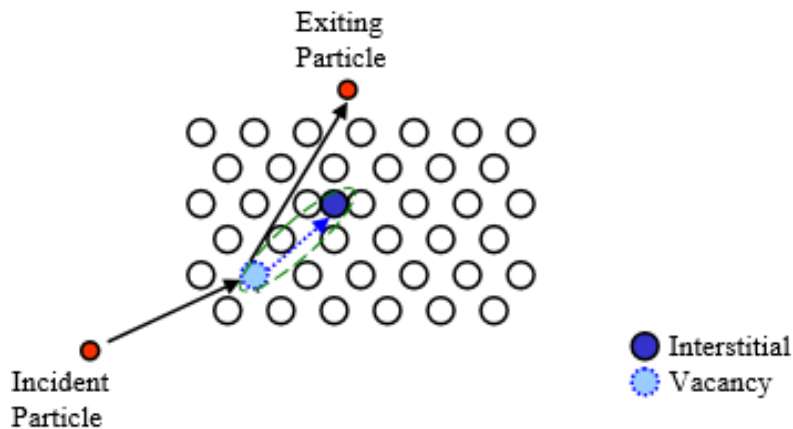
Figure 5-1. Schematic of neutron damage. The collision between an incoming particle and a lattice atom subsequently displaces the atom from its original lattice position.

A single incident particle can cause a cascade of collisions to occur to a portion of the affected material (e.g. Si) lattice atoms. These collisions are produced by both incident "heavy" particles (*p, n, ions*) and secondary particles. Defects (vacancies, interstitials, FPs, dislocations) are produced along the tracks of the secondary particles and in clusters at the end of these tracks as shown in Figure 5-2.
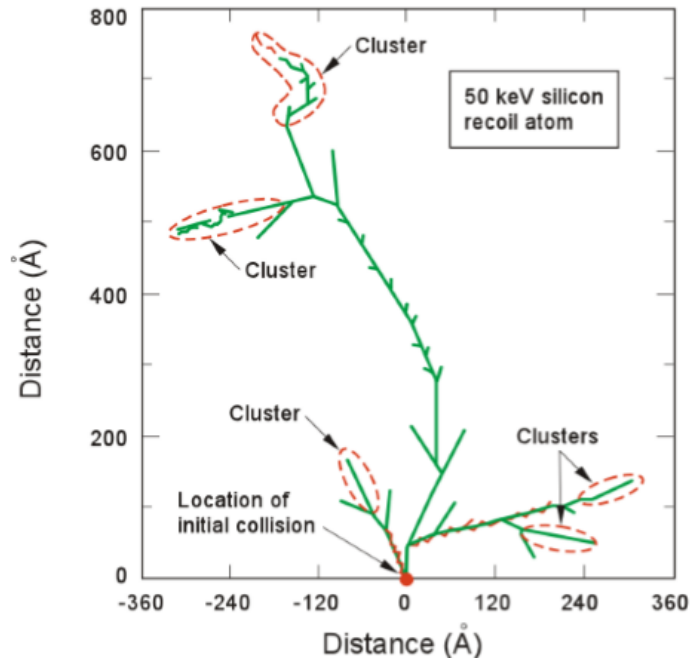
Figure 5-2. Displacement cascade damage from movement of silicon atom after primary collision. [Was, 2007]

Damage in a material creates defects; defects can diffuse and create larger defects, leading to embrittlement and weakening of structural materials and reduced semiconductor efficiency. In this chapter, we identify the areas where the neutron radiation flux in the manipulator is maximum and perform calculations of the Displacement-Per-Atom (DPA), the dose rate, the neutron flux, and neutron spectra in those areas using MCNP [Pelowitz, 2011], a Monte Carlo code that can calculate neutron flux or fluence.

5.1.1 Displacements Per Atom (DPA)

A standard parameter in the determination of radiation damage in materials is the displacement per atom (DPA), an integral magnitude that includes information about the material response (displaced atoms) and the neutron fluence (magnitude and spectrum) to which the material was exposed. DPA is not a measure of initially created lattice defects in the material but a measure of the harming energy deposited by neutrons in terms of the

136

number of atoms permanently displaced from their position to a stable interstitial position. DPA is the magnitude usually used to correlate damage on materials irradiated under different neutron conditions and is the value of interest.

The DPA rate is a derived quantity, which can be obtained dividing R, the number of displacements per unit volume and time, by the atomic density N of the material,

$$R_{DPA} = \frac{R}{N} = \frac{\sigma_D \varphi}{2E_D} = \eta_{MC} \frac{R_{D,MC}}{2E_D} \qquad (5\text{-}1)$$

where E_D is a certain threshold energy that must be overcome before an atom can be displaced. This threshold energy is fairly small and represents the amount of energy required to overcome the atom's mass and the bonds holding it in place. The displacement cross-section, σ_D, is the product of the number of atomic displacements produced by a radiation particle at a given energy times the differential probability that the radiation particle at that energy level will transfer enough energy to an atom to knock that atom out of its matrix site, integrated over all energies above the displacement threshold. That is, the damage cross-section accounts for both the probability of interaction and the total number of expected interactions across a radiation particle's life. This is unlike most cross-sections, which solely represent the probability of a given interaction occurring. The particle flux is given as φ. MCNP can calculate the cross-section times flux value and provide the damage rate, $R_{D,MC}$. Since this is a computational tool to evaluate the damage rate, an efficiency factor, η_{MC}, accounts for deviations between calculation and reality. The standard efficiency factor for these calculations is 80%, based on experiment-to-calculation comparisons.

5.1.2 Overview

We are going to use MCNP to evaluate the rate of material damage incurred by exposure to a neutron flux. The example we use is that of a remote-operated robot intended for use in high-radiation environments, which is tested using one of the TRIGA beam port facilities. To do this we use macrobodies to create the robot geometry, define composite materials, and use tally multipliers to obtain a specific reaction rate. We discuss each of these features as we develop the model and then look at the specific post-processing needed to get neutron damage results.

We are seeking to determine the damage that a robot will experience due to exposure to neutron flux. Once the neutron damage is calculated using MCNP, several possible shielding materials will be analyzed to determine the most efficient way of minimizing neutron damage.

5.1.3 Neutron Damage to Robots

Remote-operated robots like the one studied here allow access and manipulability to areas that would otherwise be inaccessible due to radiation levels, enabling repairs, maintenance work, inspection, or other tasks. An example of this is the Fukushima plant in Japan, which is using robotic inspection to determine the extent of damage inside the contaminated reactor buildings.

These robotic servants are not invulnerable, and radiation exposure will result in damage to the components. A Monte Carlo tool like MCNP enables one to perform high-fidelity calculations necessary to determine the neutron damage rate.

It is important to be aware of how far from the radiation source and beam the robot and gripper need to be to reduce the intensity of the radiation received by a certain factor or percentage. This can be accomplished by looking at the beam profile at the robot's location. Figure 5-3 shows the cross section plot of the BP5 source intensity.

Figure 5-4 and Figure 5-5 show the x- and y-axis cross section plots of the BP3 source intensity. The x-axes of the plots represent the distance from the center of the source. These figures show how far away from the beam that the robot must move when not acquiring images to significantly reduce radiation dose. If an extendable gripper is used, this method can help determine how long the gripper's extension must be to keep the robot out of the higher radiation areas. The gripper receives the highest amount of radiation compared to any other part of the robot since it is holding the part to be imaged.
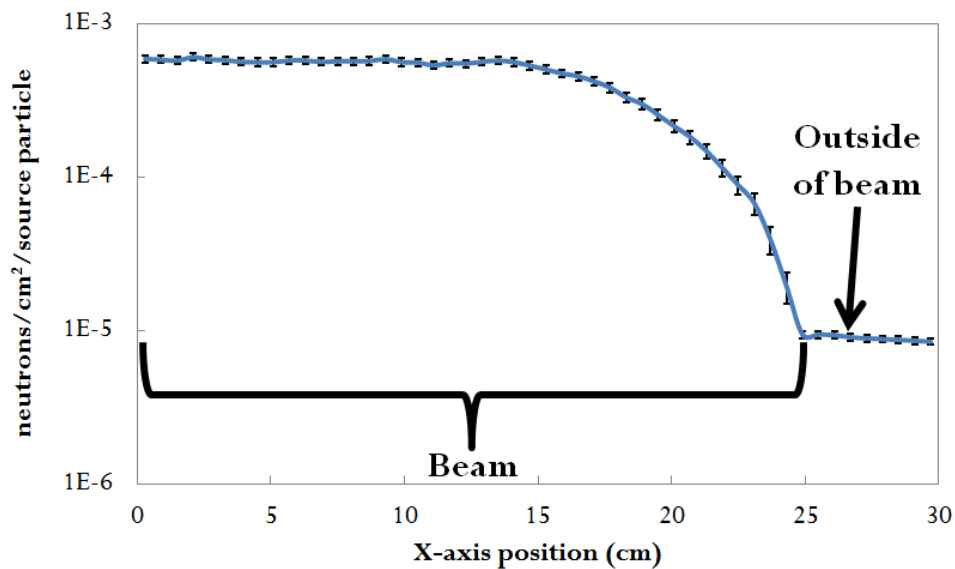
Figure 5-3. BP5 beam profile cross section. This type of plot is used to determine the distance the robot needs to be away from the beam in order to minimize radiation dose and damage.
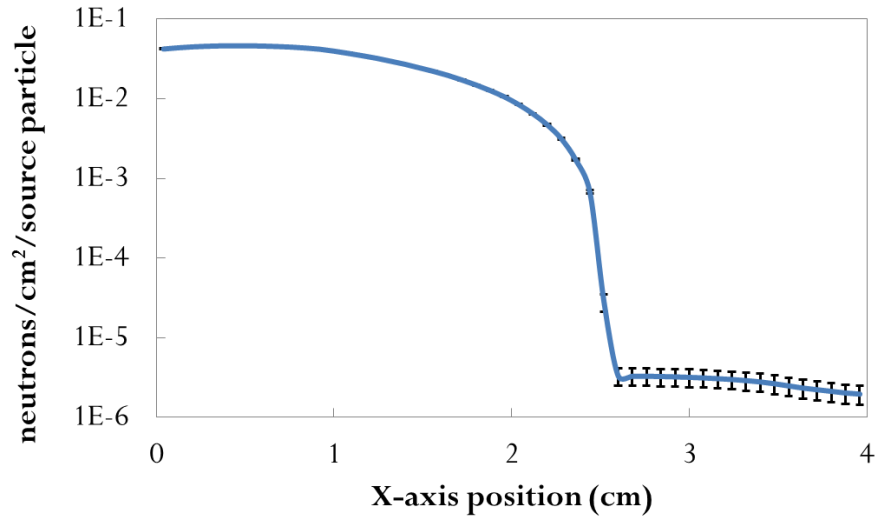
Figure 5-4. BP3 beam profile showing the x-axis cross section. This type of plot is used to determine the distance the robot needs to be away from the beam in order to minimize radiation dose and damage.
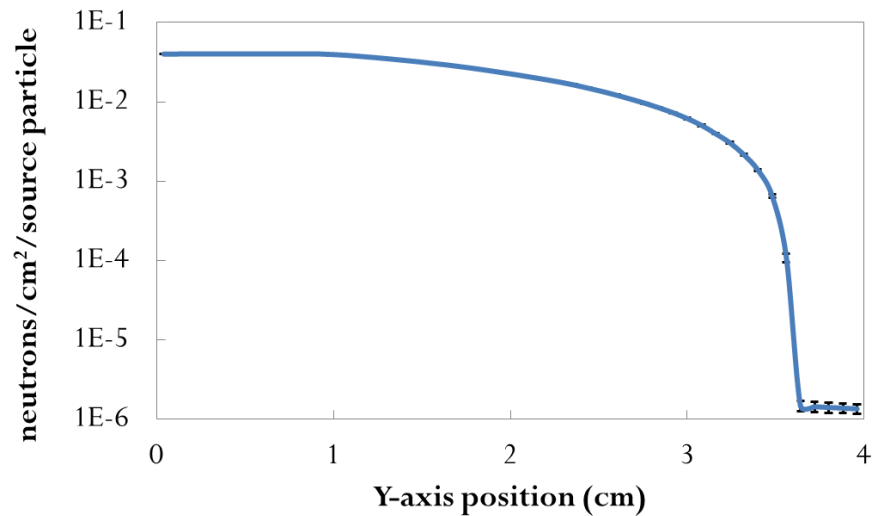
Figure 5-5. BP3 beam profile showing the y-axis cross section. This type of plot is used to determine the distance the robot needs to be away from the beam in order to minimize radiation dose and damage.

5.2 MCNP MODEL

The MCNP model discussed below is for BP5, but one was also made for BP3 and can be found in Appendix A. The models for the two beam ports are similar in nature, which is why only one is discussed in detail.

140

5.2.1 Geometry

The MCNP model represents a concrete enclosure built around the terminus of BP5 in the TRIGA reactor. Figure 5-6 shows a top-down schematic of the model. The neutron beam is emitted from a disk source representing the neutron flux distribution at the terminus of the beam port into a 6 m x 2.5 m x 1.4 m concrete enclosure with 0.4 m thick walls. Source Information (SI) and Source Probability (SP) cards are used to capture the beam port neutron distribution as accurately as possible. Two right parallelepiped (RPP) macrobodies are used to define the concrete walls and the space between them. The robot is placed at the center of the enclosure and is represented in the model as a series of three nested cylinders: an 8 cm diameter cylinder representing the internal structure, a 16 cm diameter cylinder representing the shell, and a cylinder of varying thickness representing the shielding. The robot is 70 cm tall. Three right circular cylinders (RCC) macrobodies define the robot and shield. In MCNP, the geometry of the system under investigation is defined by objects called cells, which are each filled with a designated material and bounded by a surface. Cylinders were used to explicitly model the casing of the SIA5 system components (i.e. links of the robot) which contain most of the mass. The interior however, is more complicated as it contains cables, wires, actuators, harmonic gears, and other small and geometrically complicated components. Therefore, the interior components were modeled as a homogeneous mixture of materials, such as Al, Fe, and Cu. Voids in components were taken into account by adjusting their densities.
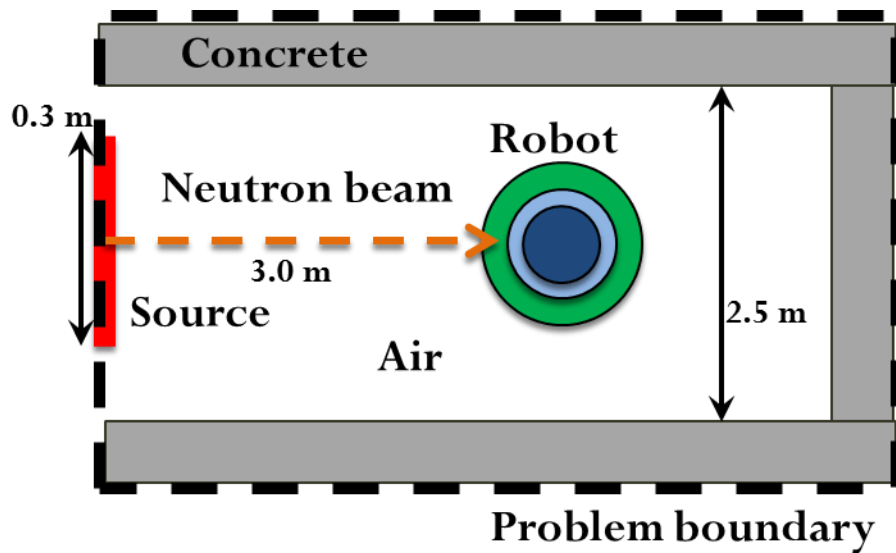
Figure 5-6. Top-down view of the simplified BP5 robot neutron damage model. The dark blue circle represents the robot's interior, the light blue circle the robot's exterior shell/casing, and the green circle the shielding around the robot. Not shown to scale.

5.2.2 Composite Materials

The shell of the robot is composed of AC4C-T6, an aluminum alloy with traces of Si, Fe, Cr, and other metals (92.19% Al, 6.95% Si, 0.4% Mg, 0.2% Cr, 0.18% Fe, 0.04% Mn, 0.04% Cu). The interior of the robot is a custom composition representing a homogeneous smear of the various components (10% Si, 5% Cu, 10% Ni, 10% Fe, 5% nitrile rubber ($C_4H_6*C_3H_3N$), 10% PVC, 15% Delrin (CH_20), 35% air). It is important to note that due to lack of accurate information on the exact material details, the material compositions and the densities listed above are estimated based on visual inspection of accessible components and communications with personnel from Yaskawa. [Nieves, 2013] The composition of the shielding is the parameter varied, where several options were studied, including polyethylene, rubber, aluminum, and iron. For the shielding materials, the maximum thickness of each material was used for a 2.5 kg weight limit. Results for all these shielding options are presented.

MCNP requires materials be broken down into constituents for which cross-sections are available (e.g. elements or isotopes). Most analyses can get away with element-level decomposition. For example, there are no cross-sections for stainless steel, but it can be defined as 70.17% elemental iron, 19% elemental chromium, 9.25% elemental nickel, 1% elemental manganese, and trace elements. However, some cross-section data (like the damage cross sections of interest in this problem) are only available at the isotope level. For example elemental iron would need to be further broken down into 91.75% ^{56}Fe, 5.85% ^{54}Fe, 2.12% ^{57}Fe, and 0.28% ^{58}Fe.

For the robot model, there are two composite materials: the robot shell and the robot interior. The robot shell is an aluminum alloy and the interior is a homogeneous smear of multiple materials. Both of these are broken down to the isotopic level to illustrate how complex composite materials can get (Table 5-1).

Table 5-1. MCNP composite material definitions for robot shell and robot internal structure

AC4C-T6 Al Alloy for robot exterior		Robot internals composition	
Atomic number followed by atomic mass	Weight fraction	Atomic number followed by atomic mass	Weight fraction
29063	-0.027668	1001	-0.019149
29065	-0.012332	6000	-0.137684
14028	-0.064100	7014	-0.270883
14029	-0.003246	8016	-0.161070
14030	-0.002155	14028	-0.092330
12000	-0.400000	14029	-0.004670
26054	-0.010521	14030	-0.003100
26056	-0.165157	17000	-0.056726
26057	-0.003814	18000	-0.004489
26058	-0.000508	26054	-0.005845
25055	-0.040000	26056	-0.091754
24050	-0.008690	26057	-0.002119
24052	-0.167578	26058	-0.000282
24053	-0.019002	28058	-0.068077
24054	-0.004730	28060	-0.026233
13027	-0.921900	28061	-0.001140
		28062	-0.003634
		28064	-0.000926
		29063	-0.034585
		29065	-0.015415

5.2.3   Neutron Damage Tally

After the geometry and materials have been specified, MCNP can calculate neutron damage rates. The ACE cross-section library available for MCNP has neutron damage cross-sections, stored under interaction identifier MT=444. MCNP can calculate damage rates using an F4 flux tally and the damage cross-sections to specify the desired interaction. A flux multiplier card (FM card) instructs MCNP to do this using the continuous cross-sections in the ACE library. The FM card in this problem is of the form:

$$FMn \quad c \quad m \quad (rxn\ list)$$

where c is a user-supplied multiplicative constant ($c = 1$ in this application[7]), m is the material number for which reaction rate is calculated, and *rxn list* is the ENDF reaction type, given by MT numbers. The reaction number for this application is 444. The FM card essentially provides a multiplicative factor to be applied to the raw tally results. For this application, the flux passing through a region with a specific cross-section needs to be multiplied to get a reaction rate in that region. MCNP allows one to use any material in the model as the source of the cross-section data. Thus one can define pure elemental materials for each element of interest and supply these materials as the source of the cross-section. This allows the combination of the flux, which is based on the material actually in the region of interest (i.e. the composite material), with a "pure" cross-section, therefore, obtaining reaction rates just for the region and material of interest. These pure materials that are specified for use in tallies only are shown in Table 5-2.

---

[7] It is possible to rework the FM card to calculate the DPA rate entirely in MCNP. This is implemented by defining the constant, c, as $\eta/2E_D$, times any time-conversion factor, such as the number of seconds per year.

Table 5-2. MCNP pure materials specified for use in neutron damage tallies.

Pure Al		Pure Si		Pure Fe	
Atomic number followed by atomic mass	**Weight fraction**	**Atomic number followed by atomic mass**	**Weight fraction**	**Atomic number followed by atomic mass**	**Weight fraction**
13027	-1.000000	14028	-0.922300	26054	-0.058450
		14029	-0.046700	26056	-0.917540
		14030	-0.031000	26057	-0.021190
				26058	-0.002820

Pure Cu		Pure Ni	
Atomic number followed by atomic mass	**Weight fraction**	**Atomic number followed by atomic mass**	**Weight fraction**
29063	-0.691700	28058	-0.680770
29065	-0.308300	28060	-0.262330
		28061	-0.011400
		28062	-0.036340
		28064	-0.009260

There are two regions of interest in the robot, the exterior and interior components. In the outer shell, reaction rates for Al, Si, and Fe are needed, while in the interior of the robot, reaction rates for Si, Fe, Cu, and Ni are needed. The other elements in these regions are either present in low concentrations or are not likely to experience damage (e.g. air). To cover these combinations, seven tallies are required, one tally for each material/region combination. For example, to find the neutron damage rate in Al in the outer shell of the robot, the set of tallies needed are:

$$F4: N \quad material \; \# \; for \; composite \; AC4C - T6$$

$$FM4 \quad (1 \quad material \; \# \; for \; pure \; Al \quad 444)$$

5.3   RESULTS

The resulting tally is the neutron damage rate, or damage cross-section times flux. This result needs to be converted to DPA however. As discussed earlier in this chapter, DPA is the reaction rate over the threshold energy. Threshold energies for Si, Cu, Al, Ni, and Fe are shown in Table 5-3.

Table 5-3. Threshold energies for the materials of interest in this application. [Olander, 1975]

Element	Threshold Energy (eV)
Si	25
Cu	22
Al	16
Ni	24
Fe	24

BP3 and BP5 of U.T. Austin's TRIGA reactor were rebuilt for this work with a simplified disk source located at the front surface of beam scatter. It is assumed that beam line neutrons mainly come from beam scatter. This model can be used to analyze the shielding effect and dose assessment of the beam ports. To expedite MCNP runtime, the disk source is moved to the beam exit. As one can see, BP5 has a thermalized neutron spectrum (Figure 5-7), and BP3 has a sub-thermal neutron spectrum (Figure 5-8). Figure 5-9 shows a comparison of the two beam ports' neutron energy spectra. In order to acquire the neutron energy spectra in MCNP, the F4 tally was used. The uncertainty in the flux measurements are shown in the error bars.
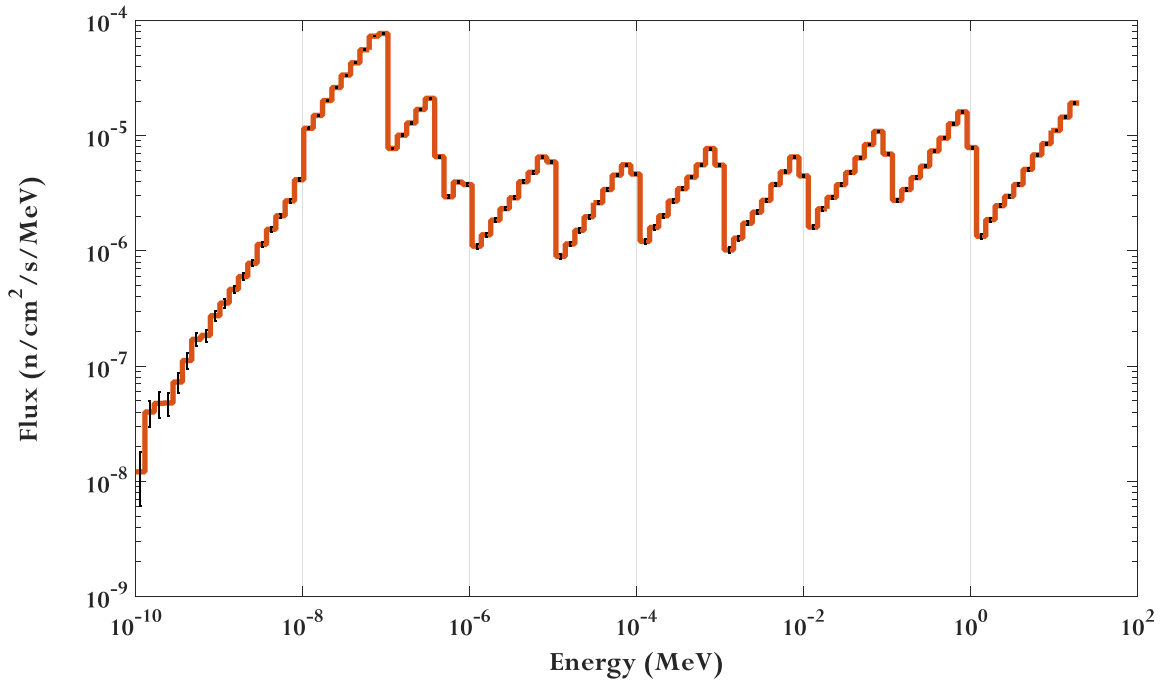
Figure 5-7. BP5 thermal neutron energy spectrum at robot location.
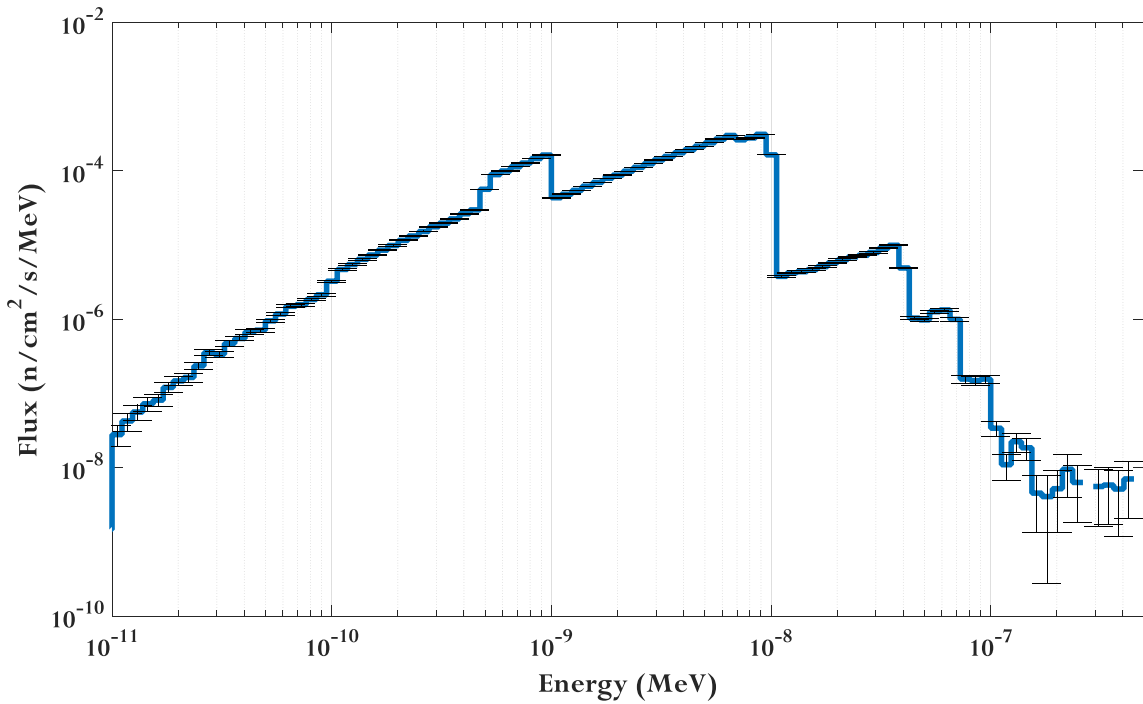
Figure 5-8. BP3 sub-thermal neutron energy spectrum at robot location.

147
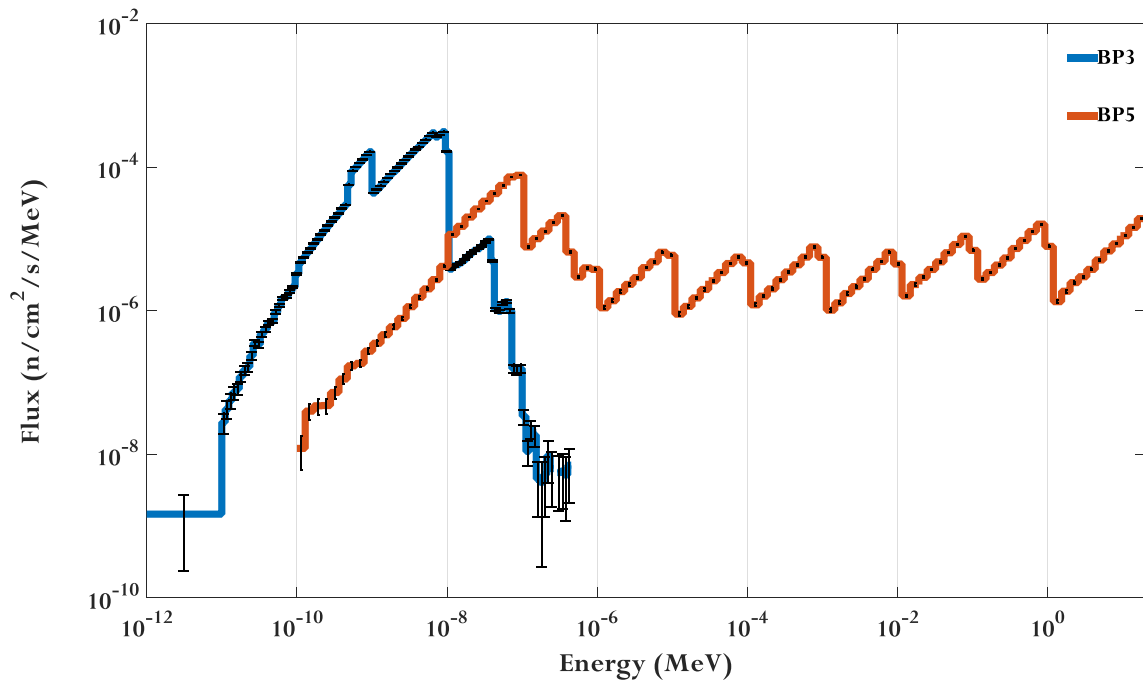
Figure 5-9. BP3 and BP5 neutron energy spectrum comparison.

To calculate the DPA rate, Equation (5-1) is used. It is important to note that the damage rate, R, has units of interactions/sec., the efficiency factor, η, is 0.8, and the threshold energy, E_D, can be found from Table 5-3. MCNP calculates the reaction rates in reactions per second, while damage rates are commonly expressed in DPA per year. Thus, the MCNP values are multiplied by the number of seconds in a year to obtain the results for various shielding types, which are shown in Figure 5-10 through Figure 5-13 for the exterior and interior of the robot in BP5 and BP3. For BP3, only the borated polyethylene shielding was considered due to its effectiveness in reducing the DPA rate compared to the other shielding materials. At these DPA rates, the materials will experience some radiation hardening and embrittlement, which occurs at greater than 0.1 DPA, but changes such as phase instabilities, irradiation creep, and volumetric swelling from void formation will not occur until a DPA value of greater than 10 is achieved. [Zinkle, 2012]

148

Polyethylene, as a low-Z material, is the most effective shield. These results include error bars that are based on taking the relative uncertainty from the MCNP tally results and multiplying the DPA per year by this relative error. This approach assumes that there is no uncertainty in the displacement threshold energy, which is a reasonable approximation. The uncertainty in the results indicates clear distinction between the different types of materials, but it is difficult to resolve between the two polyethylene cases, or between the two metals (i.e. Al and Fe). 500,000 neutron histories are tracked, to achieve a relative uncertainty of roughly 1% or less while maintaining reasonable speed (i.e. the deck runs in about two minutes on a basic laptop).
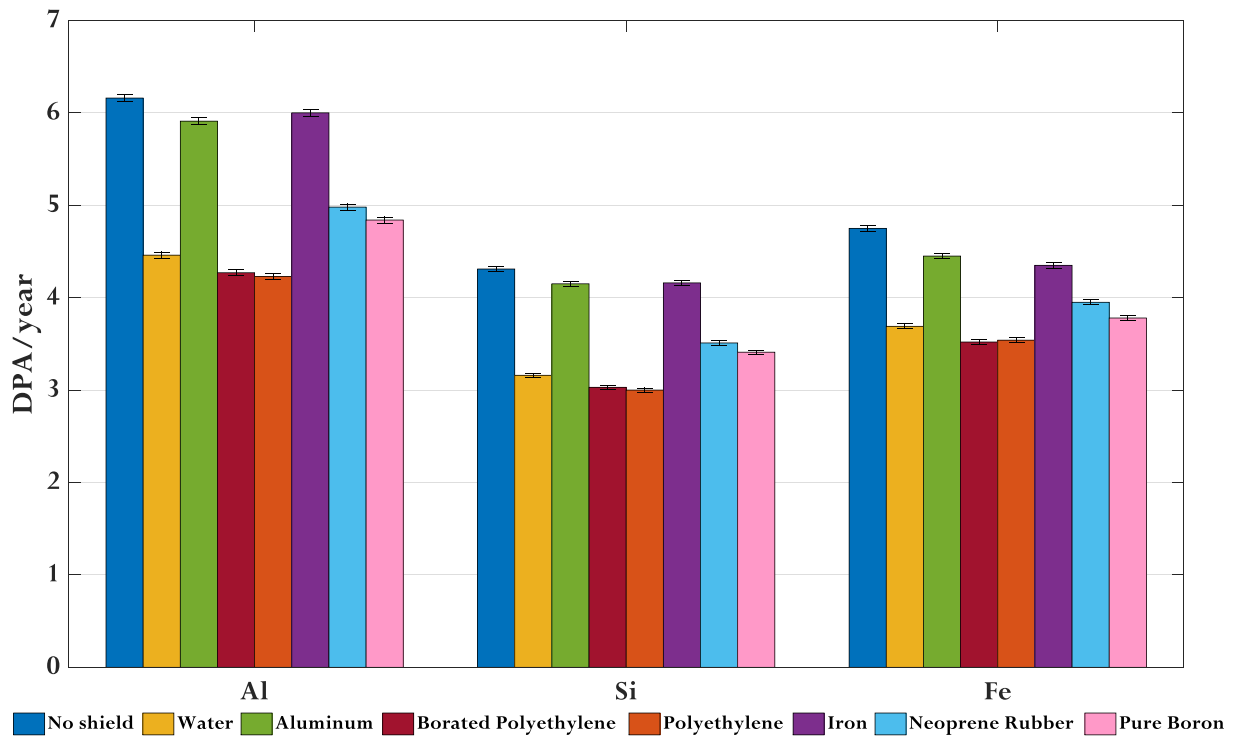
Figure 5-10. BP5 outer shell DPA rates with various shielding materials.

149
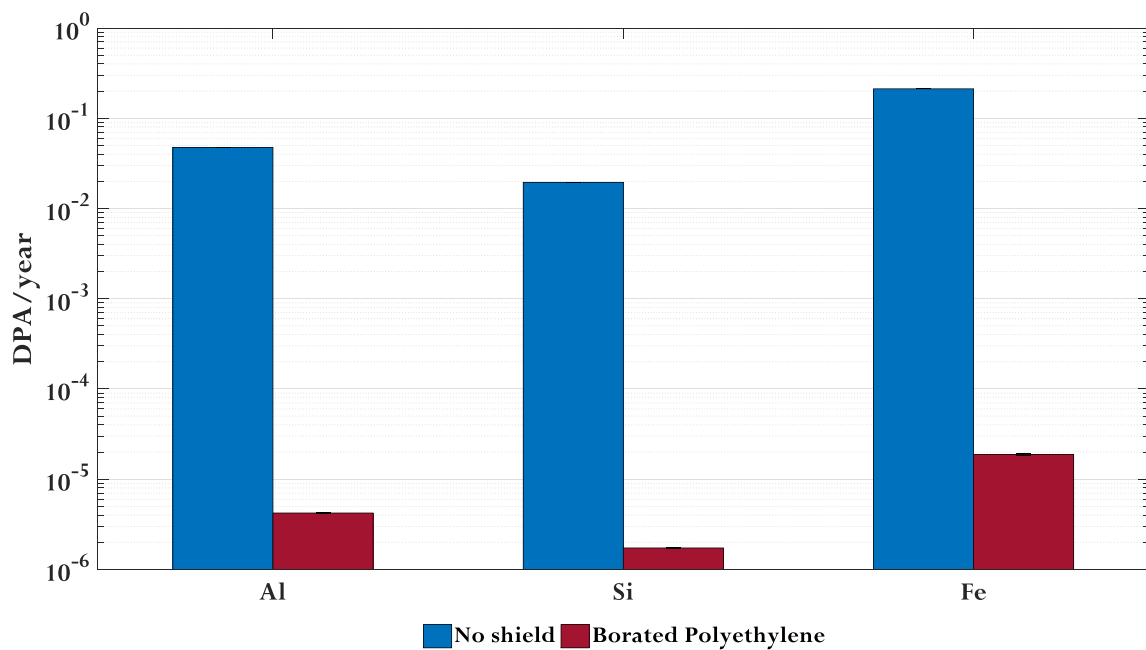
Figure 5-11. BP3 outer shell DPA rates with no shielding and borated polyethylene shielding.
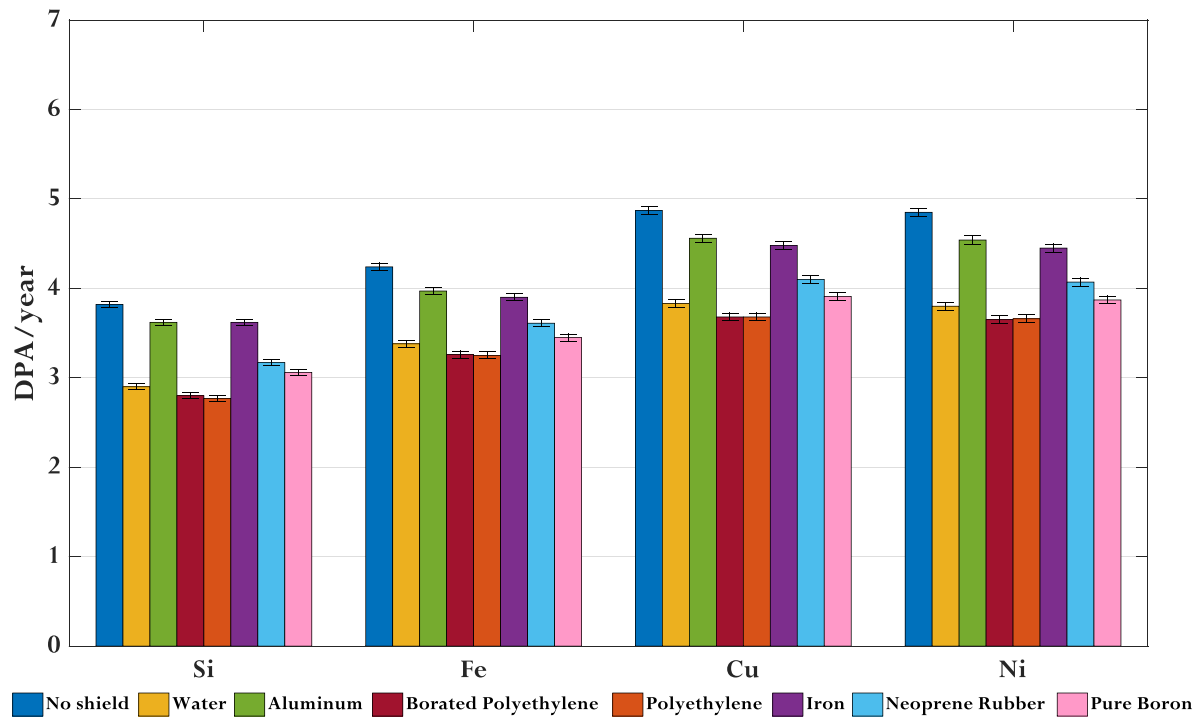
Figure 5-12. BP5 interior DPA rates with various shielding materials.
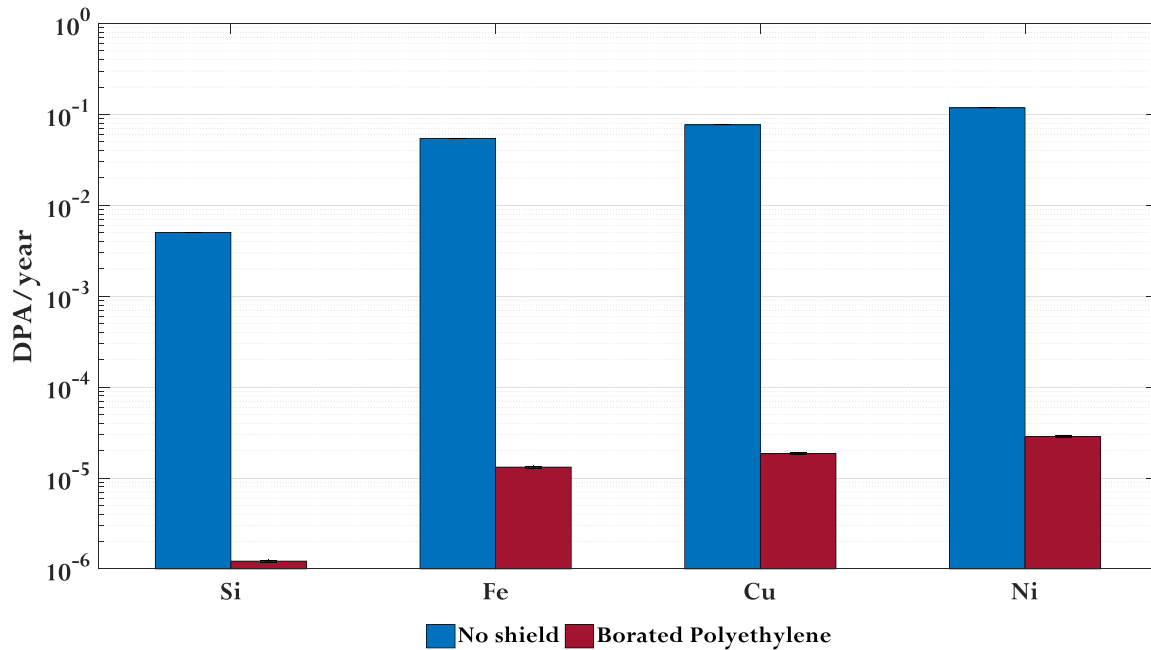
Figure 5-13. BP3 interior DPA rates with no shielding and borated polyethylene shielding.

In Figure 5-14 through Figure 5-17 the DPA rate in each energy group is plotted as a function of neutron energy for each case in BP3 and BP5. Figure 5-18 shows the comparison of DPA rates in the shell and cladding of the robot for the two beam ports. Horizontal step interpolation is used. From Figure 5-16 one can see that as radiation penetrates the robot, the neutron spectrum hardens, reduces the rate of DPA and accordingly decreases the contribution of thermal neutron damage. The DPA rate starts increasing again above energies greater than 200 eV as can be seen in Figure 5-17. This is due to elastic scattering neutron reactions where intermediate and fast neutrons collide and transfer a significant part of its kinetic energy to the scattering nucleus. The total kinetic energy is conserved in elastic scattering of neutrons, and the energy lost by the neutron is transferred to the recoiling nucleus. These statements can be translated into numbers observed in Table 5-4 and Table 5-5, which present the spectrum of neutron flux

and the rate of DPA for six commonly used energy groups for four cases of BP5 and BP3 mentioned earlier.

From Table 5-4 it may be observed that the greatest contribution to DPA rate on the Al shell of the robot corresponds to the fast flux (with 66% of the total) and the slow to intermediate group (with 33%). These contributions together correspond to less than half of the fraction of the total flux (38%) where the contribution due to the thermal to epithermal flux is 49% of the total flux.

From Table 5-5, it may be observed that the greatest contribution to DPA rate (with 65% of the total) on the Si in the inner surface of the robot (without a shield) is due to the cold neutron group corresponding to 99% of the total flux. The 35% of the remaining damage is due to the thermal to epithermal flux (that is 1% of the total flux). By adding the shield to the robot, the greatest contribution to DPA rate (with 59% of the total) is due to the thermal to epithermal neutron group. The 41% of the remaining damage is due to the cold neutron group. This is due to the shielding stopping most of the neutrons below 1E-9 MeV as one can see in Figure 5-15.
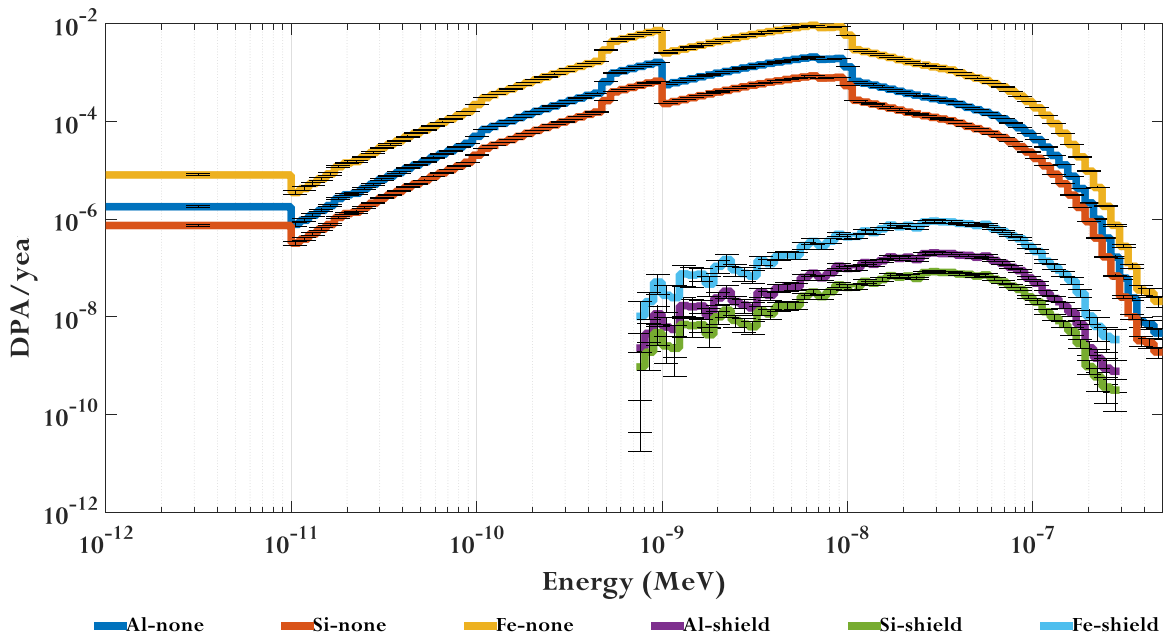
Figure 5-14. BP3 DPA rate versus neutron energy on the shell/cladding of the robot.
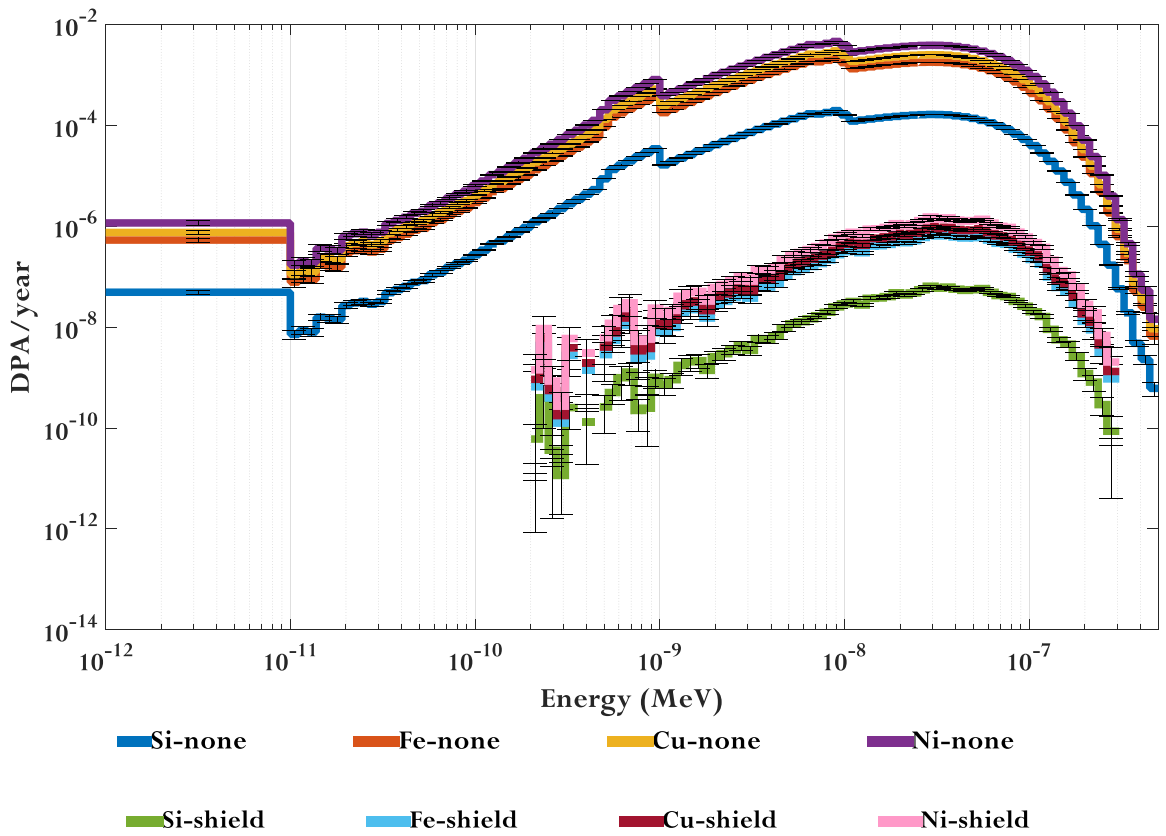
Figure 5-15. BP3 DPA rate versus neutron energy on the interior of the robot.

153
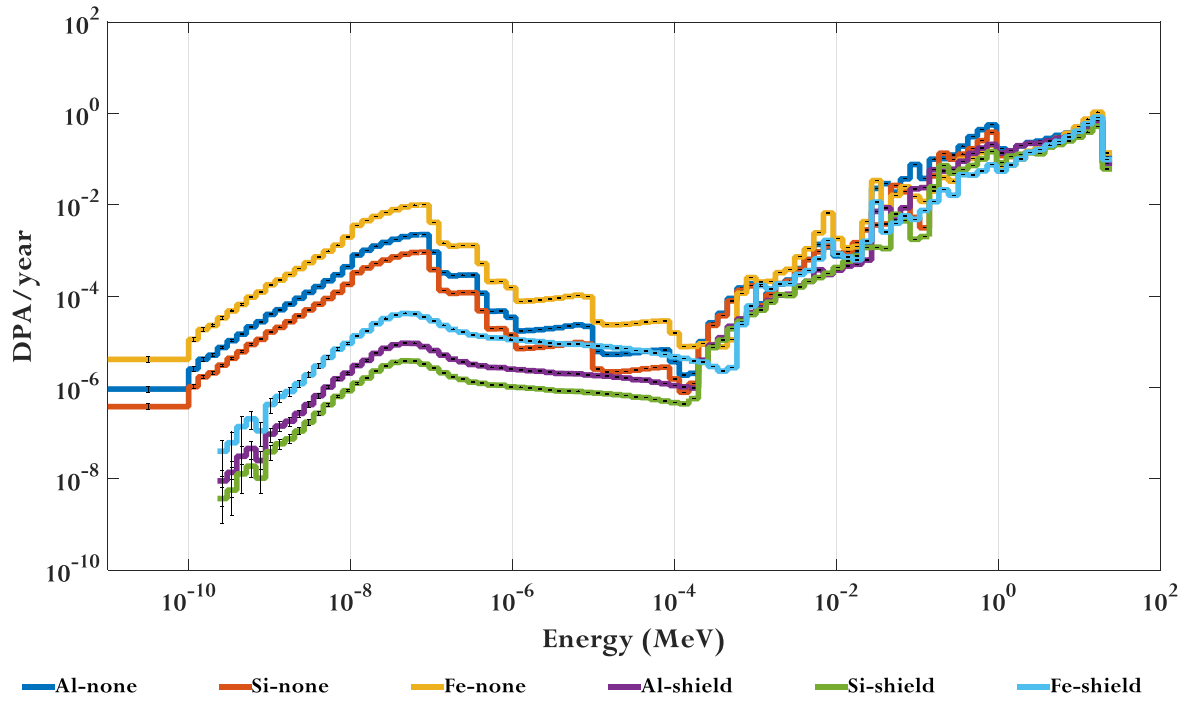
Figure 5-16. BP5 DPA rate versus neutron energy on the shell/cladding of the robot.
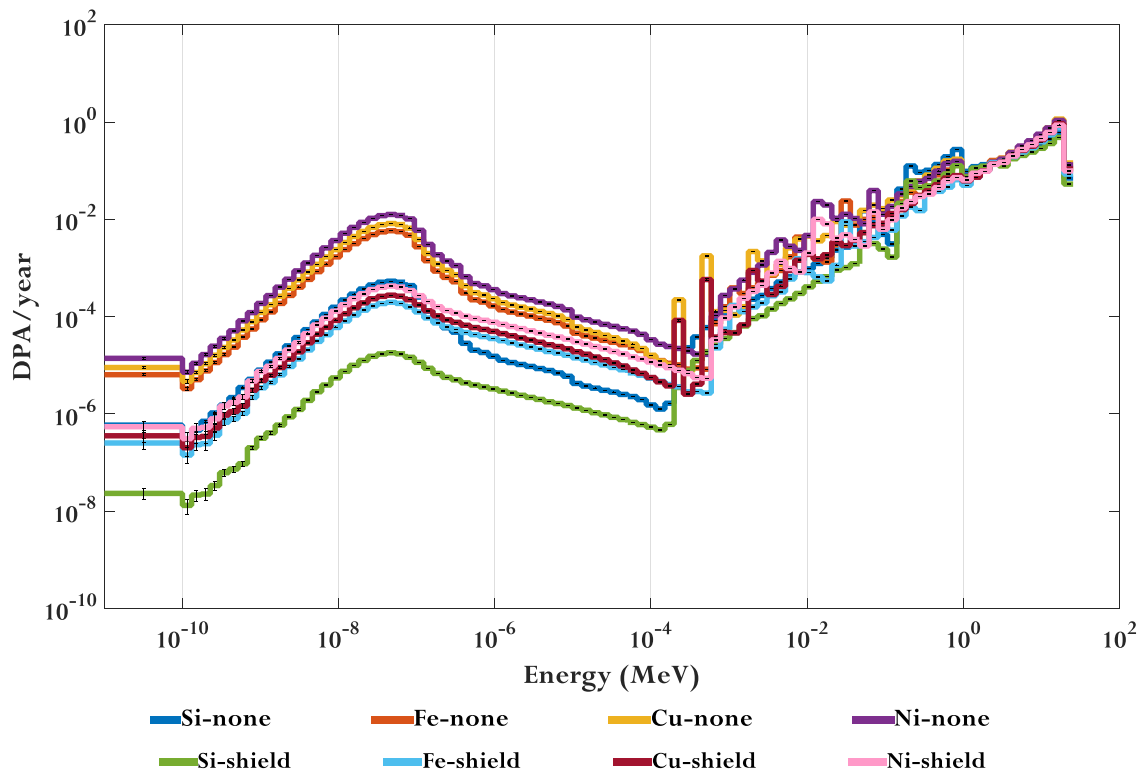
Figure 5-17. BP5 DPA rate versus neutron energy on the interior of the robot.
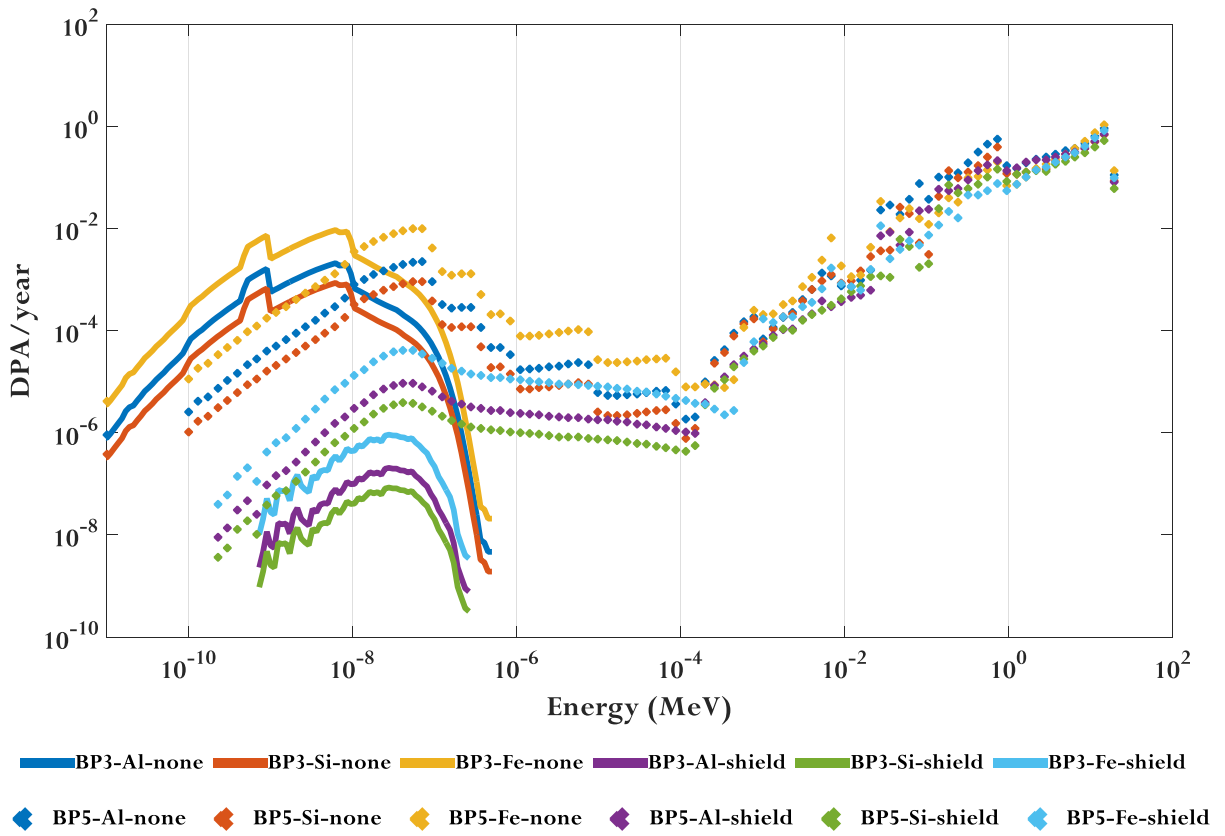
Figure 5-18. BP3 and BP5 DPA rates versus neutron energy on the shell/cladding of the robot.

156

Table 5-4. BP5 flux and DPA rate spectrum for different energy groups. The percent contribution is given by %f.

Energy group			Flux spectrum		DPA rate spectrum			
					Al shell no shield		Al shell shield	
	MeV		n/cm^2/s/MeV	%f	year^{-1}	%f	year^{-1}	%f
0	to	2.5e-8	6.15E-05	8	4.63E-03	0.07	1.90E-05	0.0004
2.5e-8	to	4e-7	3.77E-04	49	1.18E-02	0.2	6.47E-05	0.002
4e-7	to	1e-6	1.35E-05	2	2.10E-04	0.003	8.44E-06	0.0002
1e-6	to	1e-5	2.87E-05	4	1.95E-04	0.003	1.96E-05	0.0005
1e-5	to	1	2.05E-04	27	2.07	33	8.62E-01	20
1	to	20	8.56E-05	11	4.11	66	3.45	80
	Total		7.71E-04	100	6.19	100	4.31	100

Energy group			Flux spectrum		DPA rate spectrum			
					Si inner no shield		Si inner shield	
	MeV		n/cm^2/s/MeV	%f	year^{-1}	%f	year^{-1}	%f
0	to	2.5e-8	6.15E-05	8	1.39E-03	0.04	4.83E-05	0.002
2.5e-8	to	4e-7	3.77E-04	49	3.01E-03	0.08	1.20E-04	0.004
4e-7	to	1e-6	1.35E-05	2	6.70E-05	0.002	1.19E-05	0.0004
1e-6	to	1e-5	2.87E-05	4	8.86E-05	0.002	2.04E-05	0.0007
1e-5	to	1	2.05E-04	27	1.01	26	4.69E-01	16
1	to	20	8.56E-05	11	2.88	74	2.38	84
	Total		7.71E-04	100	3.89	100	2.85	100

Table 5-5. BP3 flux and DPA rate spectrum for different energy groups. The percent contribution is given by %f.

Energy group			Flux spectrum		DPA rate spectrum			
					Al shell no shield		Al shell shield	
	MeV		n/cm^2/s/MeV	%f	year^{-1}	%f	year^{-1}	%f
0	to	2.5e-8	4.55E-03	99	4.50E-02	95	2.02E-06	48
2.5e-8	to	4e-7	4.55E-05	1	2.49E-03	5	2.18E-06	52
4e-7	to	1e-6	1.22E-08	0.0003	1.97E-08	0.00004	0.00E+00	0
	Total		4.60E-03	100	4.75E-02	100	4.20E-06	100

Energy group			Flux spectrum		DPA rate spectrum			
					Si inner no shield		Si inner shield	
	MeV		n/cm^2/s/MeV	%f	year^{-1}	%f	year^{-1}	%f
0	to	2.5e-8	4.55E-03	99	3.29E-03	65	5.02E-07	41
2.5e-8	to	4e-7	4.55E-05	1	1.74E-03	35	7.14E-07	59
4e-7	to	1e-6	1.22E-08	0.0003	7.67E-09	0.0002	0.00E+00	0
	Total		4.60E-03	100	5.03E-03	100	1.22E-06	100

In Figure 5-19 through Figure 5-24, level curves of the DPA rate on the inner surface of the robot are plotted at the level corresponding to the maximum detected with MCNP for both beam port cases. The mid plane of the robot is at the corresponding (0,0,0) coordinates. The x-y axis views represent a top-down view of the robot, the x-z axis views represent a side view of the robot orthogonal to the neutron beam, and the y-z views represent a side view of the robot in the same direction as the beam direction. One can see from these level curves that the highest DPA rates in the robot occur at locations closest to the neutron beam. Peaks in the DPA rates occur in the exterior of the robot. As neutrons penetrate the robot, the DPA rate gradually decreases as the exterior and interior components of the robot attenuate the neutrons. The added borated polyethylene shielding is shown to reduce DPA rates by approximately a factor of two. DPA rates in BP3 are significantly lower than that in BP5 due to BP3's smaller beam size and lower neutron intensity.
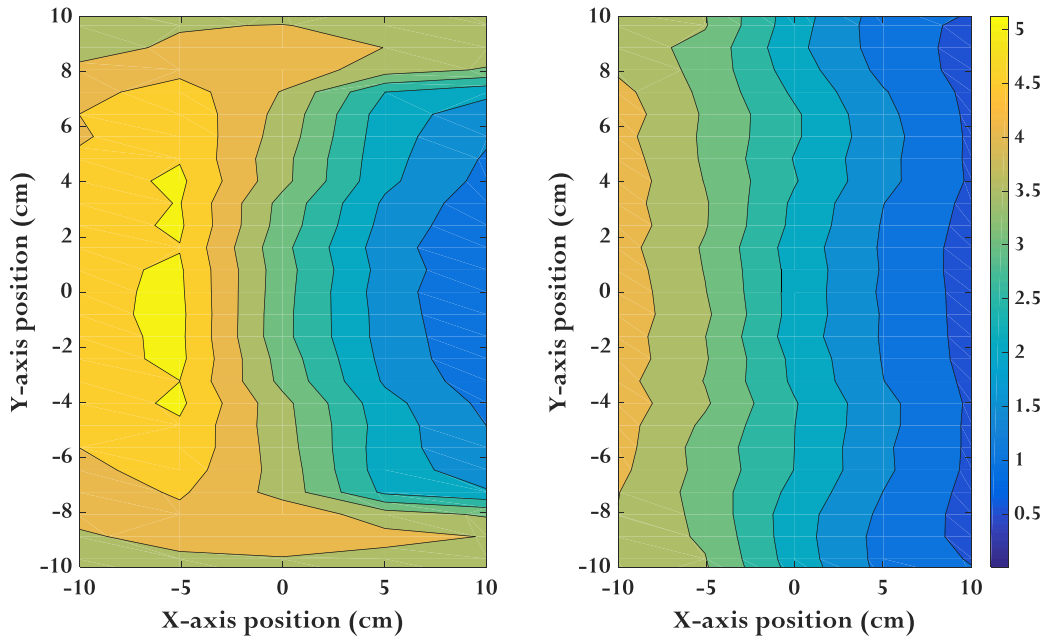
Figure 5-19. BP5 x-y axis view. Rate of DPA/year on the inner surface of the robot without shielding (left) and with shielding (right). The average relative error is 4.6% and 5.4% for the no shield and with shield configurations respectively. This is a top-down view of the robot with the neutron beam coming from the left to the right of the figures. The radius of the interior of the robot is 4 cm and the radius of the entire robot (interior and exterior) is 8 cm.
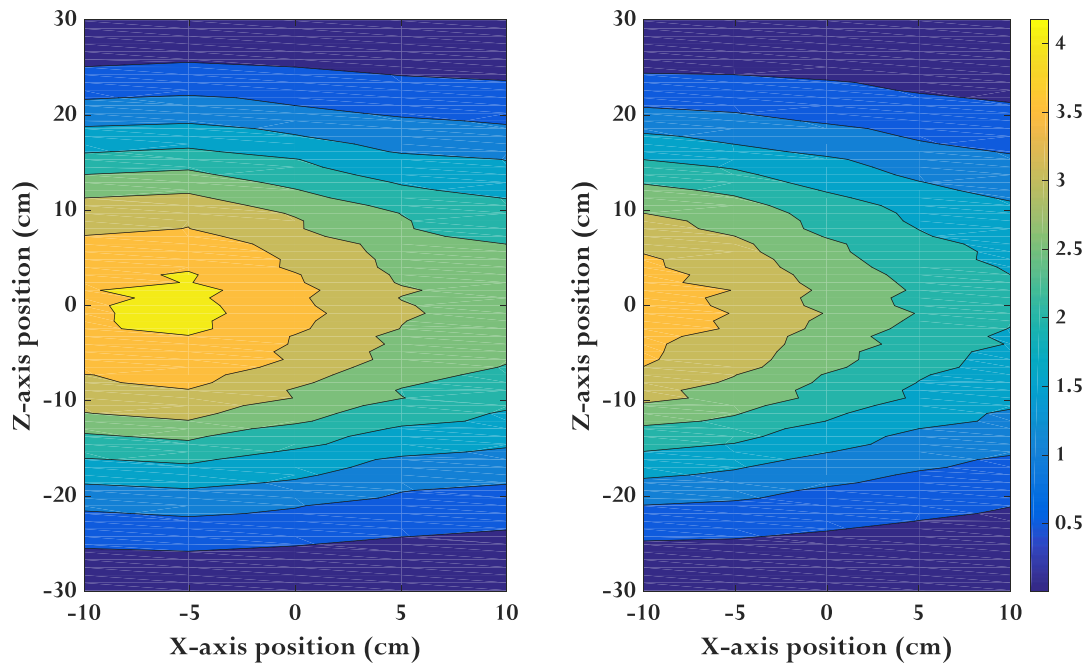
Figure 5-20. BP5 x-z axis view. Rate of DPA/year on the inner surface of the robot without shielding (left) and with shielding (right). The average relative error is 4.5% and 5.2% for the no shield and with shield configurations respectively. This is a side view of the robot with the neutron beam coming from the left to the right of the figures. The length of the robot is 70 cm, the radius of the interior of the robot is 4 cm, and the radius of the entire robot (interior and exterior) is 8 cm.
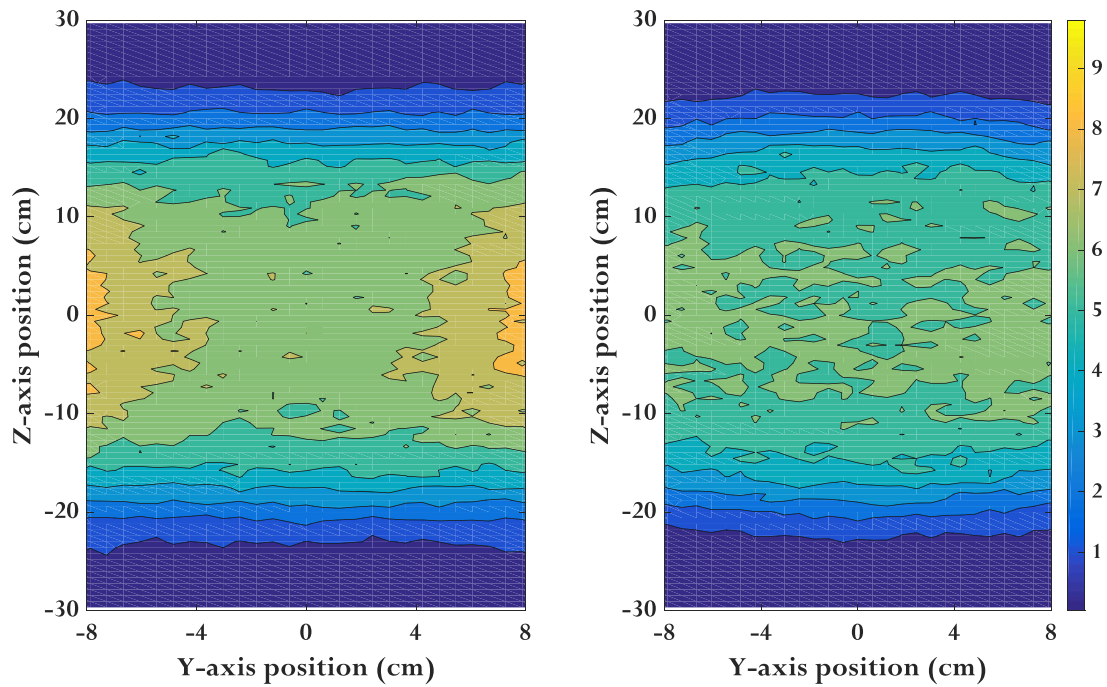
Figure 5-21. BP5 y-z axis view. Rate of DPA/year on the inner surface of the robot without shielding (left) and with shielding (right). The average relative error is 7.8% and 8.6% for the no shield and with shield configurations respectively. This is a side view of the robot where the neutron beam would direct into the page. The length of the robot is 70 cm, the radius of the interior of the robot is 4 cm, and the radius of the entire robot (interior and exterior) is 8 cm.
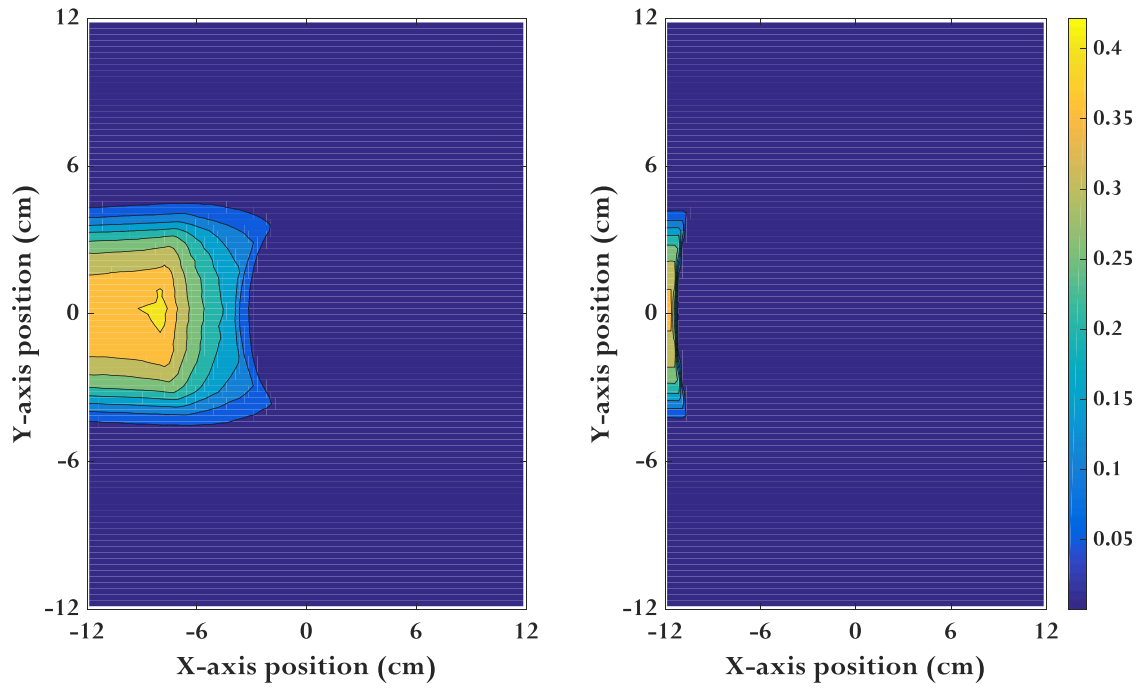
Figure 5-22. BP3 x-y axis view. Rate of DPA/year on the inner surface of the robot without shielding (left) and with shielding (right). The average relative error is 6.9% and 14% for the no shield and with shield configurations respectively. This is a top-down view of the robot with the neutron beam coming from the left to the right of the figures. The radius of the interior of the robot is 4 cm and the radius of the entire robot (interior and exterior) is 8 cm.
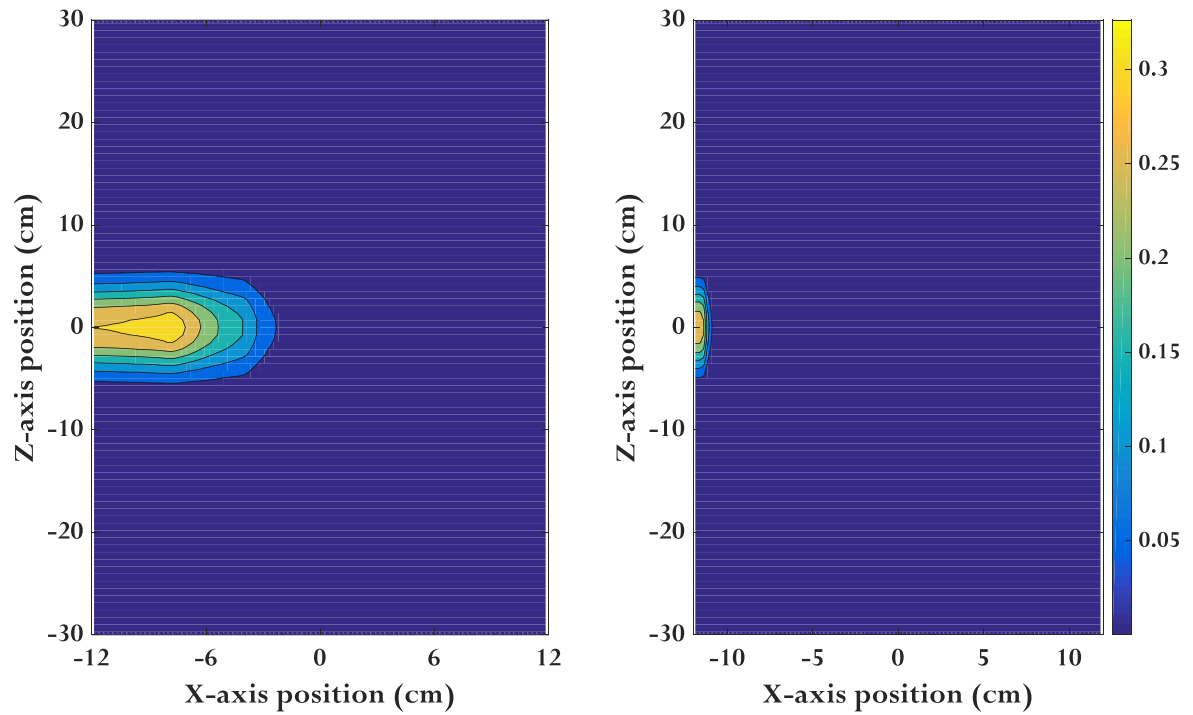
Figure 5-23. BP3 x-z axis view. Rate of DPA/year on the inner surface of the robot without shielding (left) and with shielding (right). The average relative error is 6.2% and 4.6% for the no shield and with shield configurations respectively. This is a side view of the robot with the neutron beam coming from the left to the right of the figures. The length of the robot is 70 cm, the radius of the interior of the robot is 4 cm, and the radius of the entire robot (interior and exterior) is 8 cm.
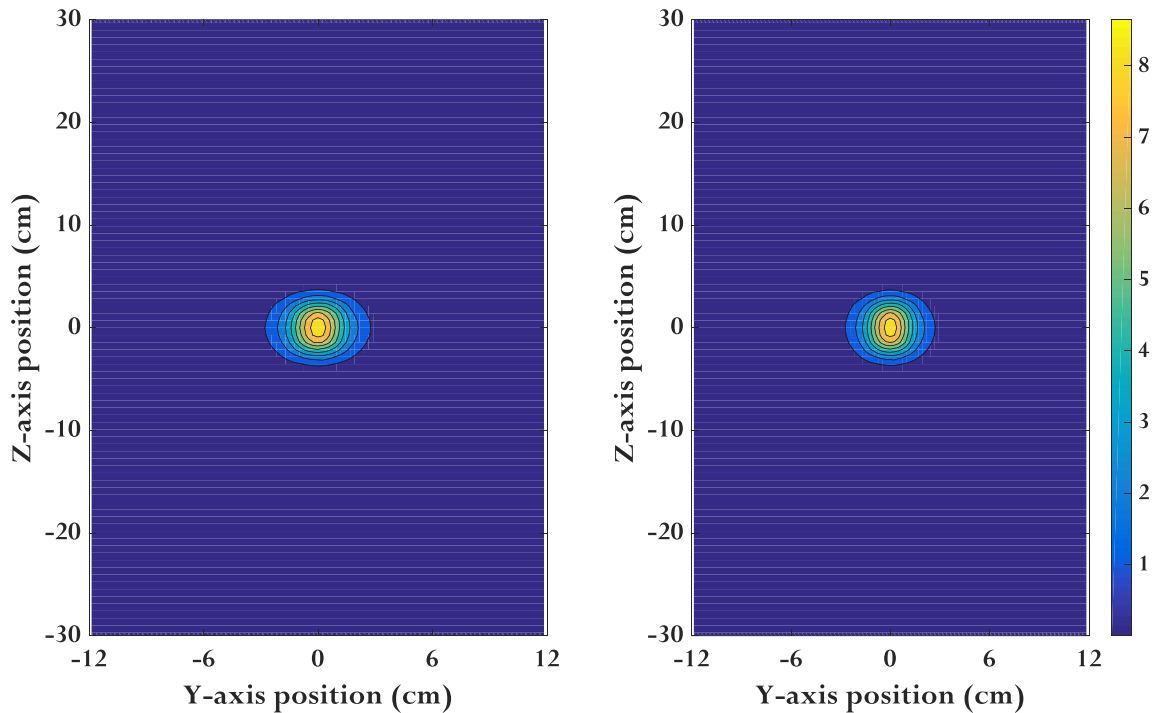
Figure 5-24. BP3 y-z axis view. Rate of DPA/year on the inner surface of the robot without shielding (left) and with shielding (right). The average relative error is 4.8% and 2.5% for the no shield and with shield configurations respectively. This is a side view of the robot where the neutron beam would direct into the page. The length of the robot is 70 cm, the radius of the interior of the robot is 4 cm, and the radius of the entire robot (interior and exterior) is 8 cm.

5.3.1 TRIGA BP5 Flux & Dose Calculation with Robotic System

To help predict more closely what radiation doses may be imparted to critical areas of the robot, a simulation analysis procedure was developed. The procedural steps included modeling of the environment and radiation source, simulating the imaging operation, and tracking the doses imparted to the robot. The reactor is a source of neutrons and gamma rays, so both types of radiation must be taken into account in the MCNP model. Neutrons of varying energies are produced by fission in the reactor core and scatter their way down the various beam ports. BP5 was used for this analysis since it has been shown in the previous sections to have higher radiation fluxes and a larger beam size than BP3. The tangential nature of BP5 reduces the presence of fast neutrons and photons in the neutron beam, since neutrons must scatter to get into the beam tube. The

164

most desirable traits of a neutron beam for neutron radiography include: a high thermal neutron intensity, a low fast neutron intensity, a low gamma radiation intensity, a large area coverage for the neutron beam so that larger objects can be radiographed, and a low beam divergence. Collimators are used to limit the outward spread of the neutron beam. In addition, the neutron flux at the center of the collimated beam should ideally equal the neutron flux at the edges of the beam. Neutron divergence within the beam can cause an uneven exposure across the image.

Since the modeling dimensions were large, a very large number of particle histories were required to obtain the results with reasonable errors (less than 10%). The average energy absorbed in the robot [MeV/g/source neutron] was tallied. Tally values were then multiplied by total source strength (neutrons/sec) and converted to dose equivalent:

$$H = S * D * Q * C \tag{5-2}$$

where H is the dose equivalent [mrem/hr], S is the neutron source intensity [n/cm^2/s], A is the surface area of the disk surface source, which is 1170.0 cm^2, D is the absorbed dose [rads/source neutron], which is the tallied value [MeV/g/source neutron] times 1.6×10^{-8}, Q is the average quality factor, and C is 3,600,000, which is the conversion factor from [rem/sec] to [mrem/hr]. In order to calculate dose in MCNP, the DE and DF cards must be used, which provide a table of energy bins and the conversion factors for these energy bins respectively.

A rough estimate of neutron source intensity at the beginning of the intermediate collimator is 1×10^7 n/cm^2/s. An overall quality factor of 10 was used to convert absorbed dose to dose equivalent. Figure 5-25 shows the neutron dose absorbed at the base and

EEF of the robot for various robotic configurations inside BP5. Gamma dose at the two different robot components were calculated in MCNP and are shown in Figure 5-26 below. The units of R, rad, and rem can sometimes be acceptably interchanged. For instance, for gamma radiation, an *exposure* of 1 R causes an *absorbed dose* in a person of about 1 rad, which results in a *dose equivalent* of 1 rem. This is due to the basis for the definitions of the units and the relative biological effectiveness of gamma radiation. An absorbed dose of 1 rad from fast neutrons, however would result in a dose equivalent of about 10 rem. For thermal neutrons however, this quality factor is 2 (i.e. 1 rad would result in 2 rem for thermal neutrons). [U.S.NRC, 2014]

These results are compared to experimental dose rates obtained in Section 5.4.1. It is apparent from Figure 5-25 and Figure 5-26 that the EEF of the robot receives the highest neutron and photon doses.
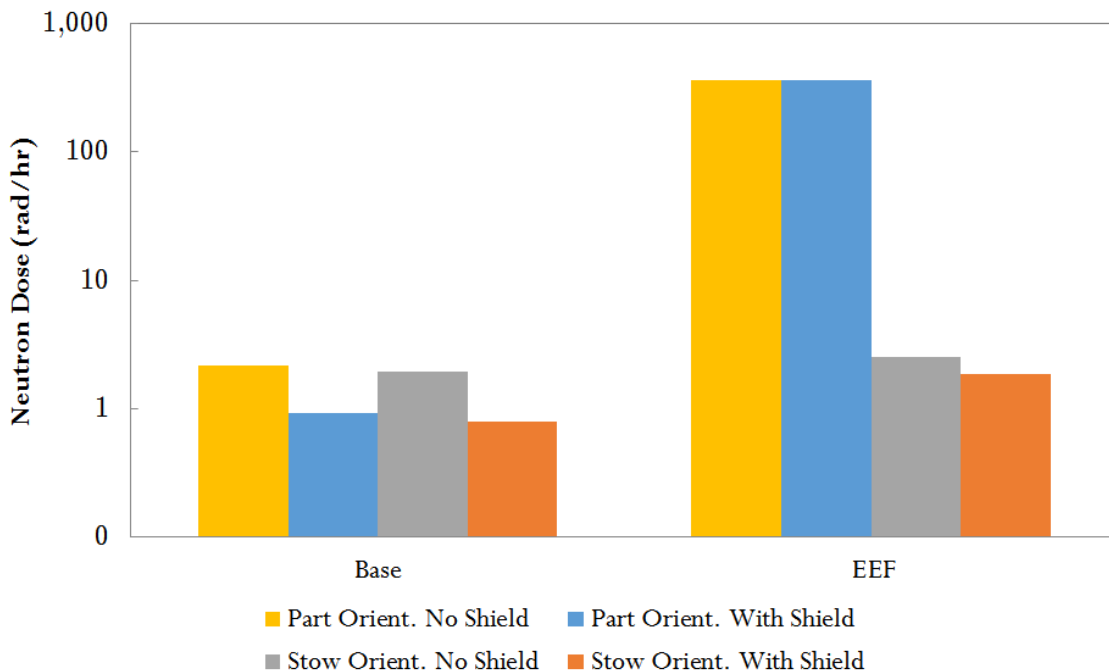
Figure 5-25. **MCNP neutron dose for various robotic configurations inside BP5.**

166
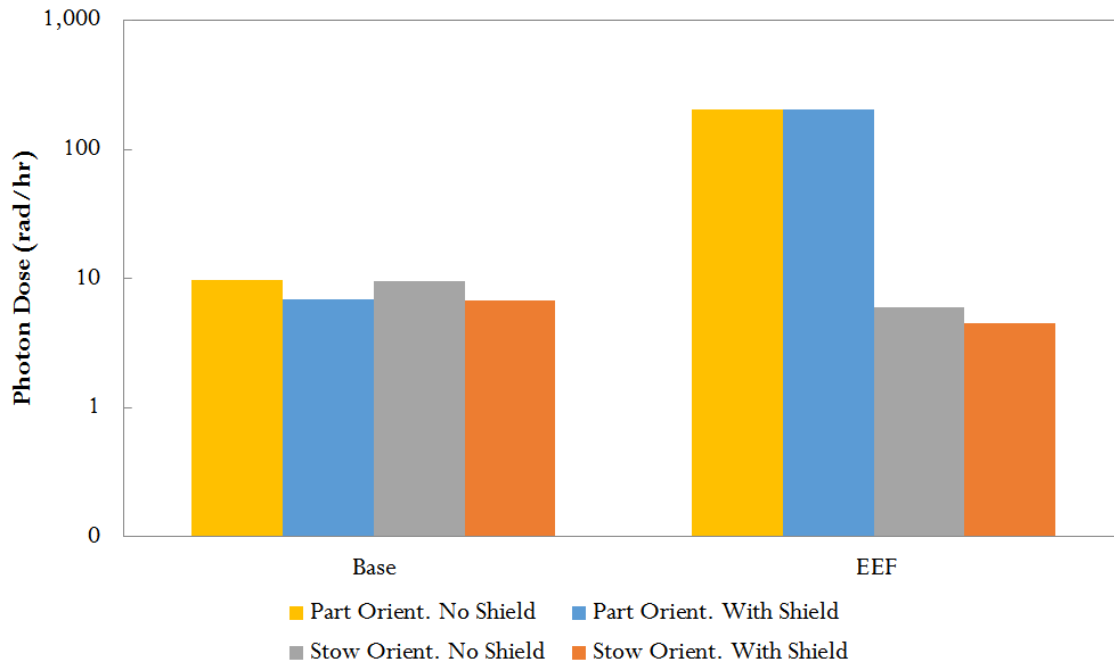
Figure 5-26. **MCNP photon dose for various robotic configurations inside BP5.**

MCNP is also used to gain insight into the effectiveness of the experimental area's configuration. When particles interact with the robotic shielding interface, reflections occur as particles scatter off the shielding, imaging equipment, robot, and part to be imaged. Quantifying the magnitude of this effect and developing an accurate model of this behavior is important. One method of accomplishing this is to analytically investigate the importance of shielding thickness and material on reflections. MCNP mesh tallies were used to show the neutron dose (Figure 5-27 below), neutron flux (Figure 5-28 below), and neutron and photon sources in beam port 5 (Figure 5-29 below and Figure 5-30 below). For each scenario, a grid was superimposed on the environment of interest, and the respective tally was calculated using Monte Carlo methods at each grid point. The beam divergence is noticeable in Figure 5-27 and Figure 5-28. One can see in Figure 5-30 below that a high intensity of gammas are produced at the unshielded areas of the robot, at the ^{27}Al light-tight box, and at the rear wall where neutrons are

absorbed by the concrete and gamma radiation is emitted. A high intensity of gammas is significant, because photons scattering is a major cause of error in imaging. Elements such as iron and hydrogen in the moderating piece produce gamma rays when they capture thermal neutrons. When using neutrons for imaging, higher energy neutrons will backscatter in the room. Concrete floor and shielding blocks are a main contributor of backscattered neutrons. To minimize this, one can design the facility to have concrete materials further away from the imaging device. Also, a pit under the imager could be made to reduce backscatter.
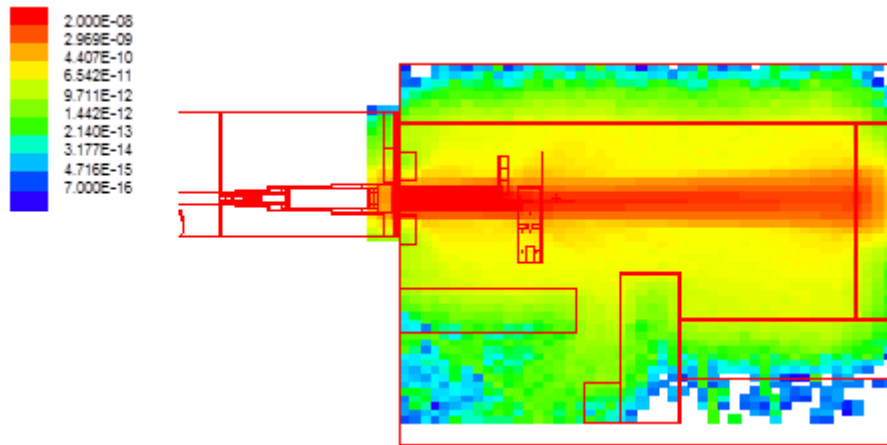
Figure 5-27. Neutron dose intensity in beam port 5. Red indicates high dose and blue indicates low dose.
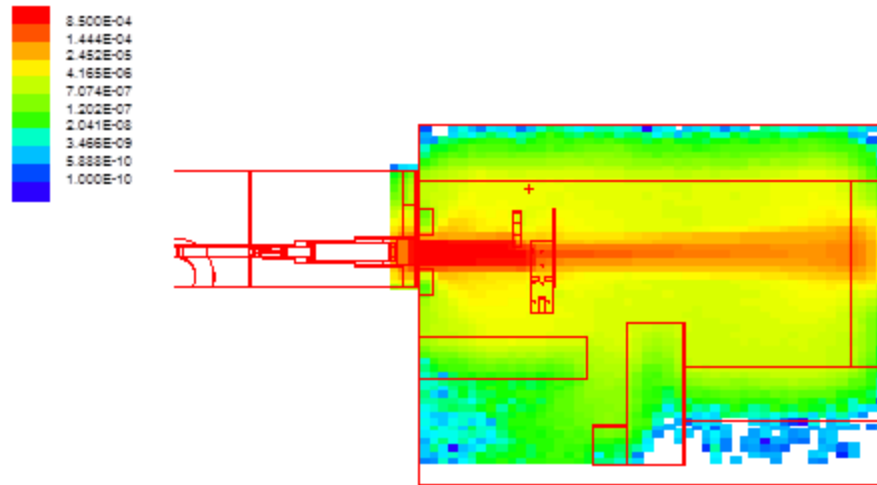
Figure 5-28. Neutron flux intensity in beam port 5. Red indicates high flux and blue indicates low flux.
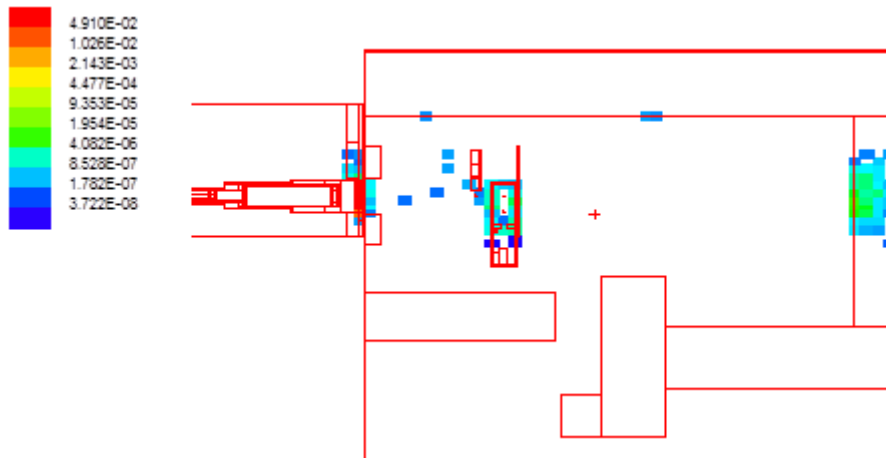
Figure 5-29. Plot of source tally showing measurement of where neutrons are created in beam port 5.
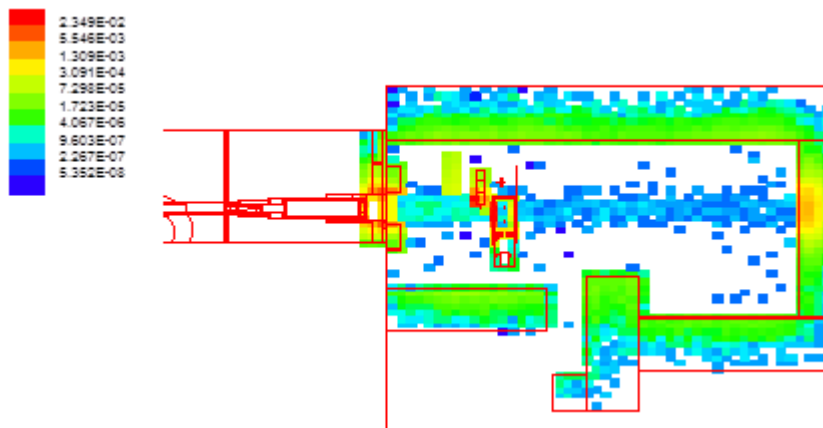
Figure 5-30. Plot of source tally showing measurement of where photons are created in beam port 5.

169

5.3.2 Neutron and Photon Calculations of BP5's and BP3's Robotic System in MCNP: Conclusions

MCNP simulations were used to characterize the radiation environment and for radiation protection shielding design. Figure 5-31 shows a more advanced model of the robot with fixed shielding that can be used in the MCNP model. This model uses distinct cylinders for the individual links of the SIA5 robot, but MCNP runtime is longer due to the added complexity and the results obtained are similar to the ones presented in this chapter using the simplified model of the robot. The robotic manipulator's location, geometry, and material specifications were included in this simulation.

It is essential to use an advanced neutron transport code, such as MCNP to computationally support the experiment by calculation of neutron flux and doses. Further work will be completed on how to reduce the dose to the robotic positioning system and the effect of the robotic system on neutron and photon transport.

This MCNP work shows that a robotic system for neutron radiography applications at the TRIGA reactor and other similar environments is feasible. Additional steps to minimize radiation damage may be taken through optimization of task planning and execution. Installing shielding could substantially reduce imparted doses. With the appropriate shielding and robotic motion planning, the neutron and gamma dose rates should not harm the robot's electronic components. The testing of the actual system is described in Chapter 6.
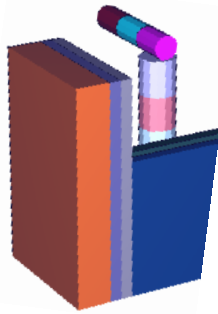
Figure 5-31. More complex model of robot geometry with shielding

5.4   REAL-WORLD QUALITATIVE TESTING

It is difficult to make conclusions from the literature regarding exactly how much radiation will "kill" a robot. Results can vary widely depending on the type of device and even between manufacturers of the same component. Dose rate and component temperature have an impact, so it is difficult to directly apply results of someone else's experiment to another application. The robot in this work was constantly run in environments at room temperature, so elevated temperatures did not have a significant impact on radiation damage. However, as the robot and gripper are run, they do heat up, possibly causing a slight increase of radiation degradation. Therefore in real-world applications, it is always beneficial to conduct qualitative testing of the actual system.

5.4.1   Experimental Validation of the MCNP Dose Calculations

Before the full-scale use of a robotic system for handling parts to be radiographed is possible, the determination of the radiation dose profile, in operational mode, is necessary to provide adequate radiation shielding to the robot and to make sure the addition of a robotic system does not degrade image quality. Actual photon (5 keV to >40 MeV), thermal neutron (0.25 eV to 40 keV), and fast neutron (40 keV to 40 MeV) dose rates were measured within BP5 using Landauer Luxel®+ dosimeters with the optional

Neutrak® 144 detector. [Landauer, 2005] These results are compared to the MCNP results and can also be used to normalize the MCNP model in order to make it more accurate.

The layout and results are shown in Figure 5-32. The dose rates are determined at a reactor power of 950 kW. Ten dosimeters were placed 36 in. from the ground, the height of the beam center, and were evenly spaced out except for dosimeter #10. A PC hard drive was placed directly behind dosimeter #10 in order to simulate an object to be radiographed. The hard drive increases photon and neutron scattering. The imaging system was also inside BP5 place during the dosimetry experiment, but the robot was not. As expected, the locations with the highest dose rates are situated in the neutron beam path. As you move further away from where the neutron beam enters the beam port, the photon and neutron dose rates decrease.

These neutron and photon dose rates, which range from about 50 mrem/hr to 100 rem/hr, are hazardous to humans. However, a robot could operate safely in this environment as it has been shown that a total dose greater than 5,000 rads delivered to silicon-based devices and 1,000 rads in general electronics on the order of minutes is needed to cause long-term degradation. [Messenger, 2014]
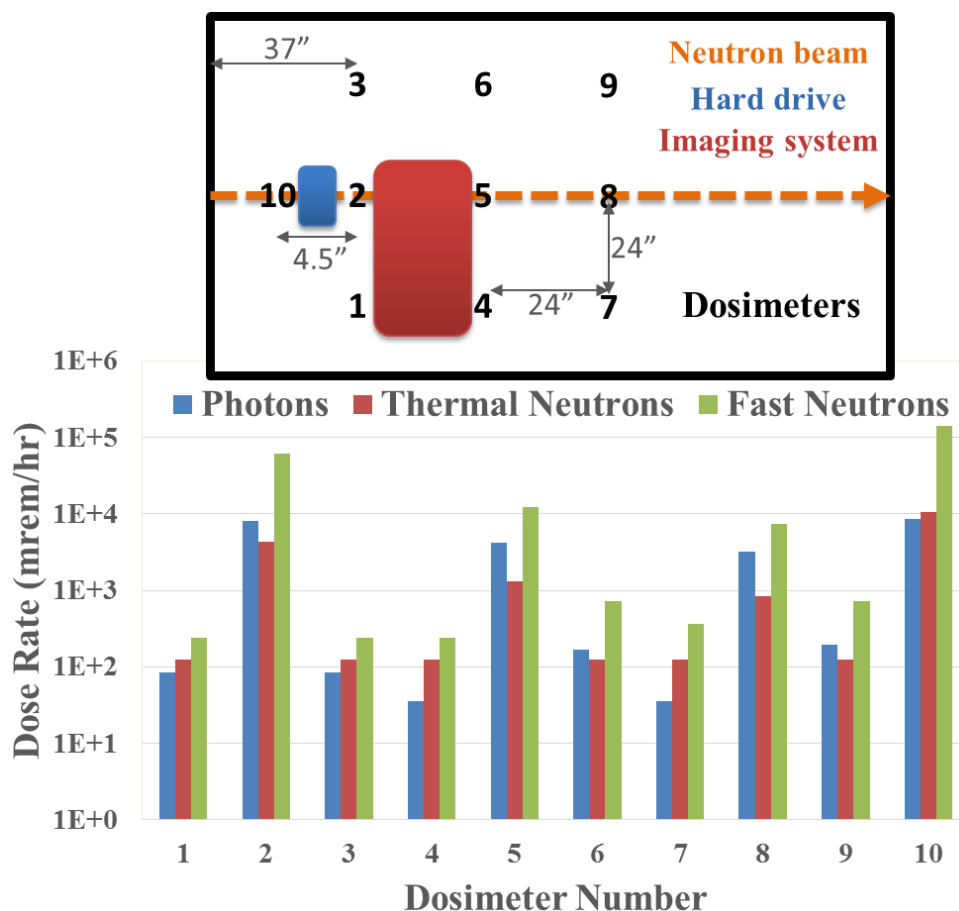
Figure 5-32. Experimental dosimetry of BP5 layout and resulting photon and neutron dose rates at a reactor power of 950 kW.

The reactor power cannot be brought to full power or shut down instantaneously. Even with a reactor scram, the power does not instantly drop to zero. At shutdown, the power drops to about 5% of what it was before the scram in about 0.6 sec., and then continues decreasing for an 80 sec. period. Therefore, the ramp up time it takes to get to full power and ramp down time contribute to the overall incurred dose. The square wave feature is used to decrease the ramp up time to a minimum; however the maximum reactor power for this feature is 500 kW.

5.4.2   Comparison of Measured Dose Rate Data to Modeled Dose Rate Data

To help determine the accuracy of the MCNP BP5 model, the measured dose rates were compared to predicted data from the MCNP simulation. To validate the MCNP modeled results, the data must be compared to real-time benchmark measurements. Measured data at dosimeter number five was compared to the data estimated by MCNP, since this location most closely corresponds to the robot location in the model. First, it is to be determined whether the MCNP data is useful. The relative error and the variance of the variance (VOV) computed by MCNP answers this question. With each MCNP output file, ten statistical checks are included to assist the user in determining the reliability of the predicted data. A relative error of less than 0.1 is the desired relative error to be obtained at the end of the computation. VOV is the estimated relative variance of the estimated relative error. VOV ranges from 0-1 with a VOV of 1 being least confident. The VOV in this case was 0.089. Then, it can be determined how the model compares to the measurements. At dosimeter location number 5, the photon, thermal neutron, and fast neutron dose rate are 4152, 1316, and 12085 rem/hr respectively (Figure 5-32). From, Figure 5-25 and Figure 5-26, the MCNP calculated dose rates are 205, 1454, and 7270 rem/hr for the photon, thermal neutron, and fast neutron dose rates respectively. Remember that an absorbed dose of 1 rad from fast neutrons results in a dose equivalent of about 10 rem, 1 rad from thermal neutrons is equivalent to about 2 rem, and 1 rad from photons is equivalent to 1 rem. The experimental and theoretical thermal and fast neutron dose rates match relatively well, with less than 10% difference for the thermal neutron dose rate. The large difference in photon dose rates is due to the hard drive that was added for the experimental test. This hard drive was not included in the MCNP simulation. This hard drive, placed directly in front of the beam path, creates a large amount of photons and photon scattering, which might explain the increased photon dose.

5.4.3 Commonly Found Robot Materials & Their Radiation Thresholds

The purpose of this section is to provide the low-level threshold dose for radiation damage to materials commonly found in robots. An important finding is that a total dose of less than 10^5 rads produces no significant degradation of mechanical or electrical properties, except for semiconductor devices. [Bruce and Davis, 1981] Semiconductor devices function through designed imperfections in crystal structure and are quite sensitive to further disruption of those structures by displacement processes. Also, at this level, no significant synergistic effects of radiation combined with other environmental stresses, such as elevated temperature, were identified. With a few exceptions (e.g. semiconductor devices), inorganics and metallics are more radiation resistant than organic materials. Much of the total dose absorbed by inorganics/metallics does not produce displacements and is dissipated with no net effect, whereas much less of the total dose absorbed by organic materials is dissipated. Most is used to initiate or accelerate chemical reactions through ionization and excitation of absorber atoms. Metals are the most radiation resistant of the materials used in robotic systems. Neutron fluences much higher than the neutron fluences seen in these applications are required to affect the mechanical properties of metals. Metals are immunized against damage from gamma rays. Exposition of metals to very high dose gamma dose rates (10^{12} rads) generates some heat that may be indirectly damaging to the system, and after long-term exposure (several decades) to those high dose rates, some defects may be detected like an increase in tensile and yield strength and a decrease in ductility. These defects can be annealed, and the metal would recover its mechanical properties.

It is extremely difficult to define a level of failure, since the performance of a material is defined with many physical properties: mechanical, electrical, thermal, optical, etc. A slight change in any of these properties may have tremendous effects on a

system or may cause no effect. Therefore the following values of radiation damage threshold in Table 5-6 are only an estimation of radiation effects on materials.

Table 5-6. Radiation damage thresholds. [Bruce and Davis, 1981]

Material	Lowest Reported Threshold (rads)	Property Changed
Butyl rubber	7×10^5	Tensile strength
Silicon	1×10^6	Oxidation resistance
Polyvinyl chloride (PVC)	5×10^5	Thermal resistance
Polyurethane	10^6	Compression
Polyester	10^5 to 10^6	Elongation
Polyethylene	3.8×10^5	Elongation

The effects of gamma rays on polymers and plastics, ceramics, and lubricants, important materials used in robots are described.

Polymers and plastics: Radiation damage to plastics results in cracking, embrittlement, blistering, and an increased sensitivity to mechanical stress. Polymers such as PVC do not suffer important degradation under irradiation but the hydrogen chloride slowly shows its effects and completely destroys the integrity of the plastic.

Glass and ceramics: Fragility increases for some glasses and ceramic at exposures greater than 10^6 rads. Ceramics are used as a dielectric in capacitors and also in some coatings. Ceramics are not as tolerant as metals to radiation but are more resistant than organic materials. Radiation effects on ceramics include dimensional swelling that causes a decrease in density. Changes in the optical properties of some glasses are noted at 10^4 rads. [Bruce and Davis, 1981]

Oil lubricants: Damage is possible if the dose is greater than 10^6 rads (oxidation and thermal stability). Chemical degradation of the organic molecules result in an increase in viscosity that may ultimately lead to a polymerization to a solid state and a destruction of the additives that result in modified physical properties. [Bruce and Davis, 1981]

176

5.5   CONCLUSIONS

DPA rates in a robot were calculated using MCNP. Calculating the DPA for irradiated materials in a particular facility requires a knowledge of the neutron spectrum as well as specific information about displacement damage in that material. The methods demonstrated in this chapter can be applied to determine the radiation damage to robots and other objects in other radioactive environments and applications. DPA calculations are important across nuclear engineering, as they determine how the service life of tools and components, such as the robot analyzed in this chapter, are affected by exposure to radiation. The results developed here can be compared to other data to determine if the DPA rate is acceptable, or will limit the robot's use. Based on the results, the maximum DPA rates occurred in BP5. Table 5-7 contains the DPA damage rates per effective full power year [DPA/efpy], which would be the worst case, with the reactor on for the entire time. Real-world damage rates will be significantly lower since the reactor will not be on the entire year and the robot will not be directly in the beam path the entire time. For comparison, the damage rates for fuels and cladding in LWRs are extremely high (approximately 1 DPA/day) in reactors. High burn-up fuels experience in excess of 150 DPA/day in cladding. [Heinisch et al., 2004] Figure 5-33 illustrates the required in-service operating environments and DPA for core structural materials in various types of reactors. The DPA rates determined in this work (Table 5-7) are similar to those found in thermal reactor materials (Figure 5-33), which is expected since the TRIGA reactor is a thermal reactor. However, more study is needed to define the robot failure, and then find the DPA for the corresponding neutron fluence and energy spectrum that caused the robot to fail.

Table 5-7. Displacement damage rates in DPA per effective full power year (DPA/efpy) for Al, Si, Fe, Cu, and Ni in a 7-DoF robot with and without shielding.

	DPA/efpy	
Material	No shielding	Borated Polyethylene shielding
Al	6.1	4.2
Si	4.2	3
Fe	4.8	3.5
Cu	4.9	3.6
Ni	4.8	3.6
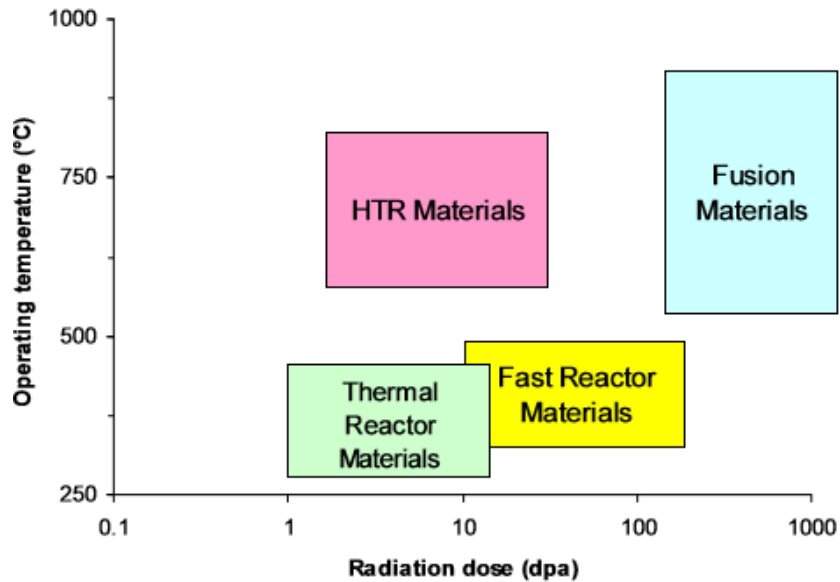
Figure 5-33. Operating conditions for core structural materials in different power reactors. [Heinisch, 2004]

Also, based on the results, a low-Z material such as polyethylene or water will provide the most effective neutron shielding. One recommendation would be to use shielding for all robot stow locations. For example, after completing a radiograph, and while the radiation source is still on, have a shielded area that the robot can "hide" behind (see Figure 6-1). Another recommendation would be to use radiation hardened components for the EEF, which would receive the highest dose since it is the part of the robot that would be the closest to the beam center location. One could also remotely

178

replace the most sensitive electronic components of the robot since radiation damage imposes limitations in terms of operating lifetime.

Chapter 6: Automated NDT System Implementation, Experimentation, and Demonstration

6.1 ROBOTIC RADIOGRAPHY PART POSITIONING SYSTEM

Previous chapters have provided substantial detail on the methods used to determine the reliability, safety, optimization, and execution of a robotic system for non-destructive imaging purposes. This chapter shows how the methods discussed previously can be used in deployed systems. Two main application areas are discussed; the first demonstration shows the robot performing neutron radiography at U.T. Austin's TRIGA reactor, and the second demonstration shows the robot performing x-ray imaging at a high energy x-ray source at LANL. These two application areas demonstrate how the work presented in this document supports the feasibility and necessity of a robotic system for non-destructive imaging by exploiting the flexibility of robotics to gain efficiency and adhere to ALARA principles. All of the grasp, motion planning, and image acquisition communication in the following applications are performed in ROS, demonstrating how ROS and ROS-Industrial simplify integration of complex robotic systems under a common operating framework and how ROS allows incorporation of recent research advances into deployed systems.

For this evaluation, the part positioning robot is a Yaskawa 7 DoF SIA5 manipulator. [Yaskawa, 2012] The robot needs to be precise and stable in holding the parts still, which has been verified in Chapter 3. Such a system would need to support motion planning and grasping in the presence of radiation fields. Because the workspace may be small and contain several obstacles, it will require strong support for collision detection, obstacle avoidance, and robust motion planning. The robot will have its own shielding material behind which it could retreat when not positioning parts. A part holding area would also be provided in the shielding area. An optimized shield design,

which has been discussed previously, provides the robot with as much shielding as possible without interfering with part exchange and replacement. The required amount of shielding was calculated using MCNP. Even with the neutron beam or x-ray source at power, the robot can operate in the unshielded areas without adverse effect so long as the electronic components are out of the beam line. The shielded area exists to prevent premature failure from large dose accumulated over time. Automation capabilities can be advanced further by wheeling the robot into the environment, identifying where things are in relation to the robot using calibration methods discussed by Hashem [2012], changing parts, and acquiring radiographs.

6.1.1   Automating Neutron Radiography at NETL

A Yaskawa 7 DoF SIA5 manipulator is to be installed in BP5 at NETL. BP5 is used for neutron radiography applications. The robotic system will move parts to be radiographed and will eliminate the need for a human to enter the beam port area. The proposed robotic neutron radiography system at NETL is shown in Figure 6-1.

The Nuclear Engineering Teaching Laboratory at U.T. Austin has a TRIGA Mark II research reactor (950 kW) capable of performing thermal neutron radiography and CT (Figure 6-2).
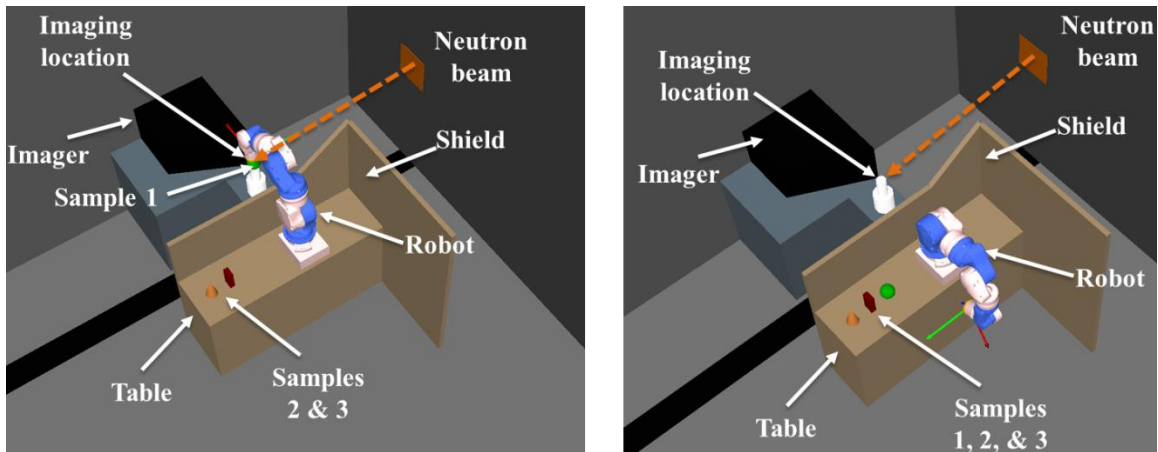
Figure 6-1. Proposed robotic neutron radiography system in shielded manipulator configuration (left) and deployed manipulator configuration (right).
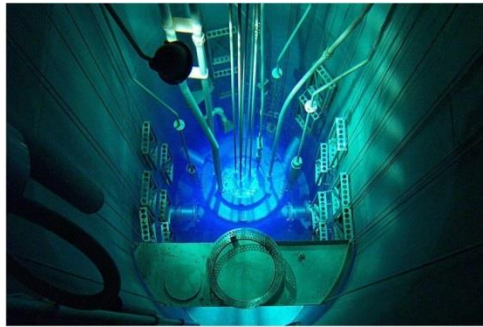
Figure 6-2. U.T. Austin TRIGA reactor.

6.1.2 Automating Radiography and Tomography Applications at LANL

The SIA5 robotic system can also be used for imaging applications at LANL. LANL offers radiography and tomography sources in the form of neutrons, protons, and x-rays. Flight path 5 at LANSCE is used for low energy neutron (thermal and epithermal) radiography and tomography. Using the low-energy beams, LANSCE can achieve greater than 200 μm spatial resolution of the elemental and isotopic components of objects. At LANSCE, protons are accelerated up to 800 MeV, and then bombarded at a tungsten spallation target to produce a "white" spectrum of neutrons (continuous in energy) at 1-600 MeV. Flight path 5 utilizes thermalized neutrons from the Lujan target. A liquid mercury shutter controls the neutron beam transmission from the target. Figure 6-3 shows

182

a layout of LANSCE and its flight paths, including flight path 5. Figure 6-4 gives a view of flight path 5 from above. A Varian 2520 amorphous silicon flat panel detector is utilized with a Perkin Elmer 16x16 "light detector". The light emitted from the neutron scintillation screen is captured by a narrow array of small photodiodes in direct contact with the screen on the amorphous silicon flat panel detector. The diodes accumulate charges, which can be read out at high frequency, permitting "real-time" neutron imaging. It takes approximately 2-3 hours for a single exposure. Epithermal neutrons are primarily selected from a broad energy neutron spectrum for neutron radiography. A tomography station is located 60 m from the neutron source.

High energy neutron CT is performed at LANSCE on Flight Path 15R. Higher energy neutrons are required to penetrate thicker objects. High energy neutrons offer an advantage over high energy x-rays for doing CT because x-ray scattering and detection characteristics at high energies make measurement of density profiles and buried feature detection difficult. At higher neutron energies, one can image features inside thick and dense materials.
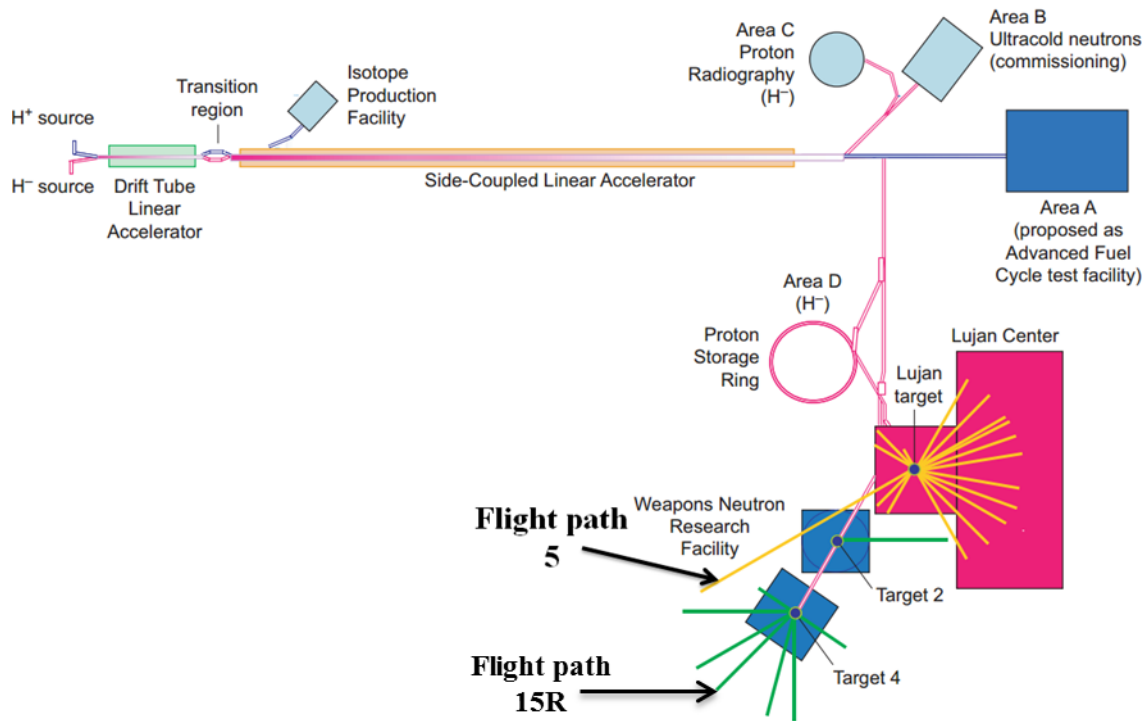
Figure 6-3. Layout of the LANSCE facility. [Schoenberg and Lisowski, 2006]
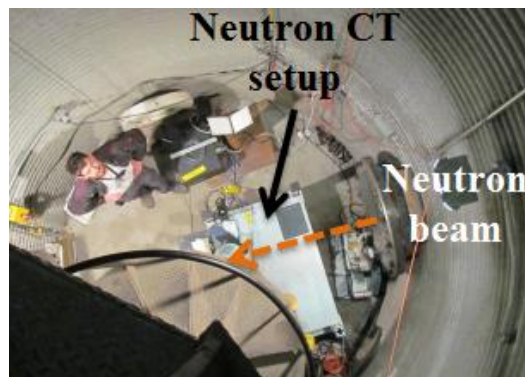
Figure 6-4. Flight path 5 as viewed from above. This station is located 9 m underground, with access provided by a spiral staircase. The large neutron beam spot available in this station enables better imaging of large objects. [Lacerda and Schoengberg, 2012]

Proton radiography is possible at the Proton Radiography (pRad) Facility at LANSCE. The pRad facility provides a unique capability for the study of dynamic process using 800 MeV protons and a magnetic-lens imaging system (see Figure 6-5). Because protons interact with materials through both the strong nuclear force and the

electromagnetic force, transmission measurements allow simultaneous imaging and determination of material properties.

Figure 6-5. The pRad facility at LANSCE provides 50 ns wide H⁻ beam pulses with approximately 10^9 protons per pulse that are spaced in time intervals predetermined by experimental requirements. Transmitted and scattered protons are imaged by an electromagnetic lens system and recorded by a scintillator-mirror-camera system. A magnet magnifier lens provides a factor of 7 magnification for small systems with spatial resolution to roughly 15 µm. [Lacerda and Schoengberg, 2012]

At LANL, virtually all plutonium operations occur within PF-4 at Technical Area 55 (TA-55, Figure 6-6), which uses a 6 MeV peak *bremsstrahlung* x-ray source for radiography applications. Robot motion paths would need to be preplanned in the PF-4 tunnel due to the high safety requirements of the facility.

Figure 6-6. Plutonium Facility (PF-4) at LANL. [LANL, 2013]

The Non-Destructive Testing and Evaluation (AET-6) group at Los Alamos National Laboratory (LANL) is responsible for research, and application of state-of-the-art methods for inspection and NDT. Capabilities include: x-ray and neutron radiography; dye penetrant inspection; ultrasonic testing; eddy current inspection; digital radiography; computed tomography, and x-ray fluorescence. They have a 225 keV source, a 450 keV source, and a 6-20 MeV microtron source. LANL radiography applications include NDT on parts and components to find material defects, Department of Energy (DOE) stockpile maintenance, science-based stockpile stewardship programs, and industrial applications.

TA-8 at LANL, has a M22 microtron accelerator from Scanditronix that is used as an x-ray source for high-energy x-ray radiography applications (Figure 6-7). A microtron is a type of particle accelerator concept originating from the cyclotron in which the accelerating field is applied through a linear accelerator structure. The kinetic energy of the particle is increased by a constant amount per field charge (one half or a whole revolution). The microtron at TA-8 is a bremsstrahlung x-ray source that accelerates a pulsed beam of electrons to one of the following four energies: 6, 10, 15, or 20 MeV. Magnets have to be tuned to each of these four energies, and the magnets would have to be re-tuned to get different energies, which is a delicate process. The microtron is not an x-ray source in itself: the x-ray beam is generated by impinging an electron beam on a tungsten converter. The dose of 650 to 2400 rads/min at 1 m is relatively high compared to that of most flash radiographic sources.

Figure 6-7. The location of the microtron at TA-8 for high-energy x-ray radiography applications (left) and the interior of the microtron facility at LANL. [LANL, 2013]

6.2 COMPARISON OF FLEXIBLE ROBOTIC SYSTEM TO HIGH-PRECISION MOTION-STAGE SYSTEMS

Achieving mechanical stability is of primary importance for NDT applications, specifically radiography and CT applications, when implementing either flexible robotic systems or mechanical motion-stage systems. System dynamic performance of multi-dimensional stage groups (i.e. motion stages) is dependent upon both individual component behavior and the system configuration. While an image is taken, the radiation source, the sample it impinges upon, and the image detector must remain stable, with known relative positions and orientations to one another.

Automated positioning systems and robots reduce the need for manual manipulation of objects and increase beam utilization efficiency. This approach enables researchers to generate more data. However, the introduction of flexible manipulators can increase the difficulty of data acquisition due to the increased complexity of the system. With automated systems, users do not have to spend time accessing the sample, so that time is available for more data collection. Also, a robot never gets tired, so you do not get fatigue-induced errors that incur with prolonged periods of manual operations. While motion-stages also reduce the need for manual manipulation of objects, robotic

187

automation does so to a greater degree. Motion stages are typically confined to smaller workspaces and rotation about a single axis. Table 6-1 shows a comparison summary of the advantages of flexible automation vs. motion-stages in various important areas.

Table 6-1. Comparison of flexible automation and motion-stages. A check mark indicates which type of system typically has an advantage in each listed area.

Area	Flexible Automation	High Precision Motion-Stages
Workspace	✓	
Motion flexibility	✓	
Programmability	✓	
Beam utilization	✓	
Ease of use		✓
Cost		✓
Handle different objects	✓	
Handle different tasks	✓	
Payload		✓

6.3   NETL TRIGA Reactor: Neutron Radiography Beam Port

6.3.1   Measured Flux Values

A thermal neutron flux can be determined via gold foil activation. This allows the cadmium ratio (i.e. ratio of thermal-to-fast neutrons) to be calculated. Gold works well for cadmium ratio calculations since it has a large thermal neutron absorption cross-section (98 barns). Characterization of the beam was performed using foil activation analysis to find the neutron flux in BP5. The flux monitors used in this case were two Al-Au activation foils. The relevant reaction in this case is $^{197}Au(n,\gamma)^{198}Au$. The Al is present only to dilute the Au, which reduces the activity of the sample and minimizes Au self-shielding. One foil was irradiated bare while the other was encapsulated in a 0.2 mm thick Cd shell. The Cd is an effective thermal neutron absorber so the induced activity in the Cd shielded foil represents only the epithermal flux while the bare foil represents both

188

thermal and epithermal contributions. The foils were irradiated simultaneously side by side at the imaging detector position, 74 in. away from the beam shutter, for 2 hours at 950 kW power. After irradiation they were left to decay to allow some of the Cd and Al activity to decay, and then the samples were counted on an HPGe gamma spectrometer system. The initial activity of the ^{198}Au was extrapolated from the 411 keV photopeak. The detector efficiency for the 411 keV photopeak was determined to be (5.27 ± 0.118) x 10^{-3} at current detection geometry. The yield of 411 keV gamma rays is 0.9558 γ's per ^{198}Au decay. By comparing the activities for each foil it is possible to estimate the epithermal (< 0.4 eV) and thermal (> 0.4 eV) neutron fluxes. The 0.4 eV Cd cutoff, corresponds to the approximate energy above which Cd becomes transparent to neutrons. Full details of the method can be found in ASTM E262 [2008] The corresponding cadmium ratio, which is the total reaction rate over the epithermal reaction rate, is 2.56, and the corresponding thermal flux is 2.4 x 10^6 n/cm^2/s at 950 kW reactor power.

6.3.2 Comparison of Measured Neutron Flux to Modeled Neutron Flux

MCNP is used to get the overall shape of the flux spectra. However, experimentally found flux gives a better estimate of magnitude. To circumvent this issue, the MCNP derived flux is normalized and readjusted with values of the flux determined through conventional flux monitors (i.e. two Al-Au activation foils) as described in the previous section. The MCNP flux results are based on units of histories rather than seconds. Therefore the actual flux in MCNP is determined by:

$$flux\left[\frac{n}{cm^2s}\right] = F4\ tally\left[\frac{n}{cm^2*source\ particle}\right] * \eta[1.65\ for\ thermal\ reactor] *$$

$$\frac{Power[MW]}{Q\left[200\frac{MeV}{fission}\right]} * 10^6\left[\frac{J}{s*MW}\right] * \left[\frac{MeV}{1.602x10^{-13}J}\right] \quad\quad (6\text{-}1)$$

6.3.3 Initial Autonomous Radiography Testing at NETL

For preliminary testing, the SIA5 robot was moved and installed in the reactor bay at NETL, outside of the BP5 cave to perform x-ray radiography feasibility tests. A collimated ^{137}Cs 662 keV x-ray source was utilized with x-ray film. The setup is shown in Figure 6-8. The automated radiography process consists of the SIA5 manipulator identifying the object and its location, picking up the object to be radiographed, translating the object into the center of the collimated x-ray beam, rotating the object about its x-, y-, and z-axes while keeping the object in the beam line, and finally placing the object back down safely. This process can be repeated for multiple objects. Figure 6-9 shows this process and the motion capabilities of the robotic system through a series of images. Digital radiography allows multiple images to be taken at different orientations, whereas the film must be replaced after every exposure. A 16 hour exposure time was required due to the low intensity of the ^{137}Cs source.

X-ray film can be used in the neutron radiography beam ports by placing a gadolinium plate between the neutron beam and the x-ray film. The gadolinium plate converts neutrons to gammas through an (*n,γ*) reaction.

190
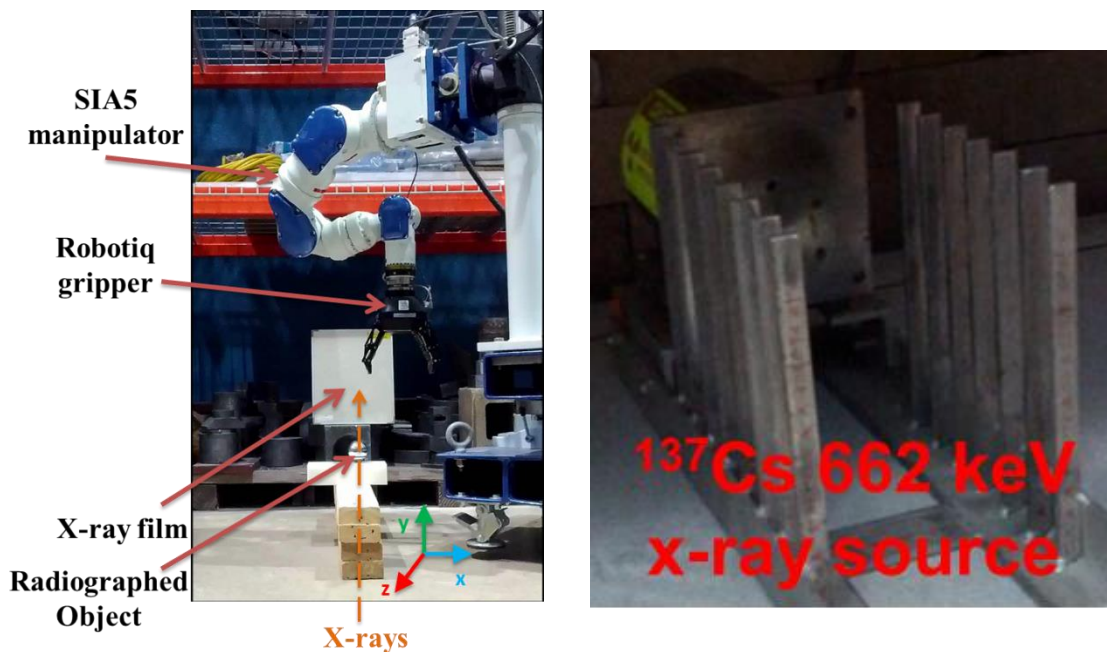
Figure 6-8. SIA5 manipulator holding and orienting a part to be radiographed using x-ray films in the reactor bay at NETL (left). A ^{137}Cs 662 keV collimated x-ray source provides the x-rays necessary to produce an image of the object (right).
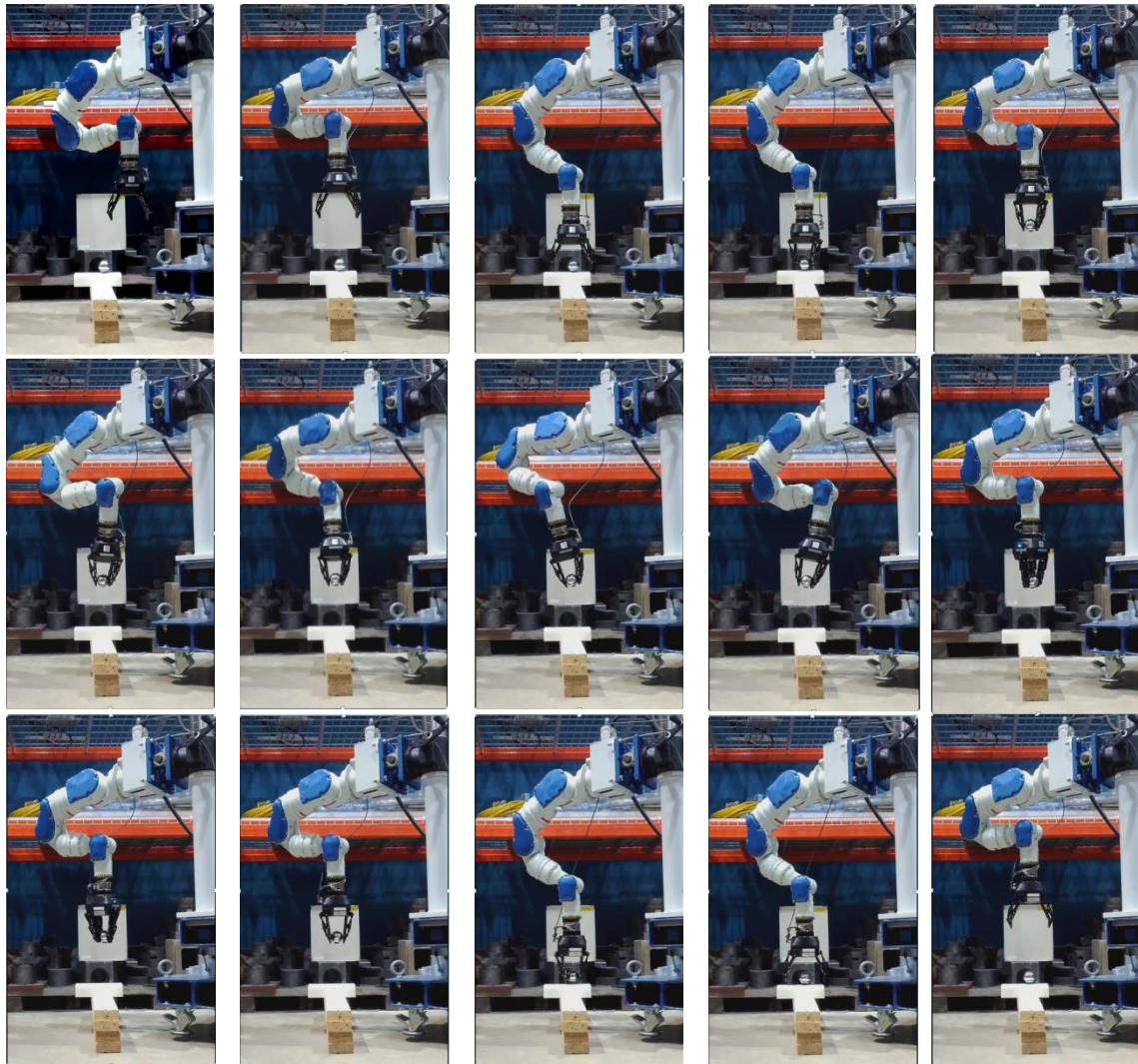
Figure 6-9. Preliminary automated x-ray radiography system with SIA5 at NETL shown through a sequence of images.

6.3.4 Autonomous Radiography at NETL's BP3

To illustrate the advantages of using a robotic manipulator with neutron imaging, mock-up depleted uranium fuel rods, each consisting of five pellets prepared from urania (UO_2) powder, were characterized by thermal neutron radiography. To simulate cracks and voids resulting from irradiation and burn-up in a fuel pin, tungsten and gadolinium inclusions were embedded in the mock-up pellets. These rodlets contained defects similar to that seen in irradiated fuel rodlets in order to assess the capabilities of NDT techniques.

192

They can be used to establish sensitivity for density, visualization of voids/cracks, and inclusions of different materials. A Yaskawa SIA5 7 DoF industrial manipulator from Yaskawa [2012] handled the fuel rods and provided advanced and flexible motion capabilities and imaging techniques that would be difficult to achieve with only linear and rotary motion stages. The goal of this effort is the characterization of irradiated fuel pins or even spent fuel, as well as to offer better guidance for expensive destructive examination of irradiated fuel pins. By imaging fuel rods, one can see the effect of the development of irradiation and burn-up damage in nuclear fuel over time (Figure 6-10). Since the technique is non-destructive, the time evolution of fuel rod damage can easily be measured this way. With the ability to predict how the composition and structural integrity of fuel pellets evolve during their duration in a reactor, one can improve the performance of nuclear modeling codes such as MARMOT. [Idaho National Laboratory, 2015] This will accelerate the understanding of processes occurring during irradiation and ultimately improve nuclear fuel. Activated fuel rods coming from a nuclear reactor can achieve dose rates of approximately 20 Krad/hr. Therefore, having remote handling systems in place is essential. Currently the actual irradiated fuel rods are transported in lead and stainless steel casks. To image the fuel rod, a robot could slide the lid off of the container, lift the fuel rod out, rotate the part above the container, so that if the robot fails, the fuel rod will drop back into the container, and place the part back into the shielded container. However, if there is a power failure, most robots have brakes enabled so that they cease movement and pneumatic grippers will not back drive by default.
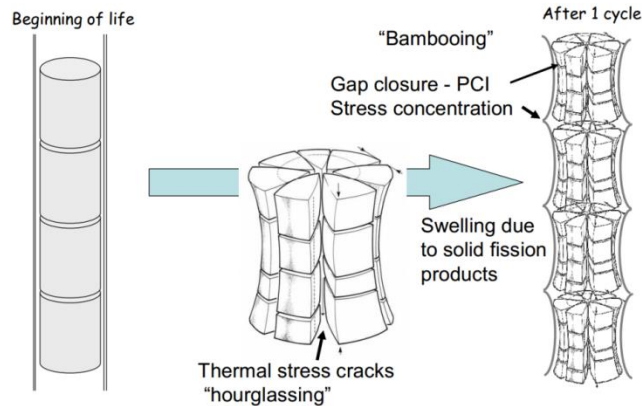
Figure 6-10. Time-dependence of the development of damage (i.e. irradiation and burn-up) in nuclear reactor fuel pellets. [YouTube, 2014]

The UO_2 in our samples is made from depleted uranium (d-UO_2 powder). The uranium content is 99.648% ^{238}U, 0.002% ^{234}U, 0.35% ^{235}U, and < 0.001% ^{236}U. The tungsten is metallic tungsten in natural isotopic composition. The fuel pellets are enclosed in a 304 stainless steel tube as shown in Figure 6-11. [Tremsin, 2013] Figure 6-12 illustrates the difference in neutron attenuation coefficients for the main components in the fuel pellets. The maximum neutron flux in the beam port occurs at a neutron energy of 8.2×10^{-2} eV, due to cooling of the neutrons by the beam wave guide. At this energy, gadolinium's neutron attenuation coefficient is roughly three orders of magnitude greater than that of tungsten, and tungsten's neutron attenuation coefficient is roughly one-half order of magnitude greater than that of depleted uranium. Materials with higher attenuation coefficients will attenuate neutrons more than materials with lower attenuation coefficients.
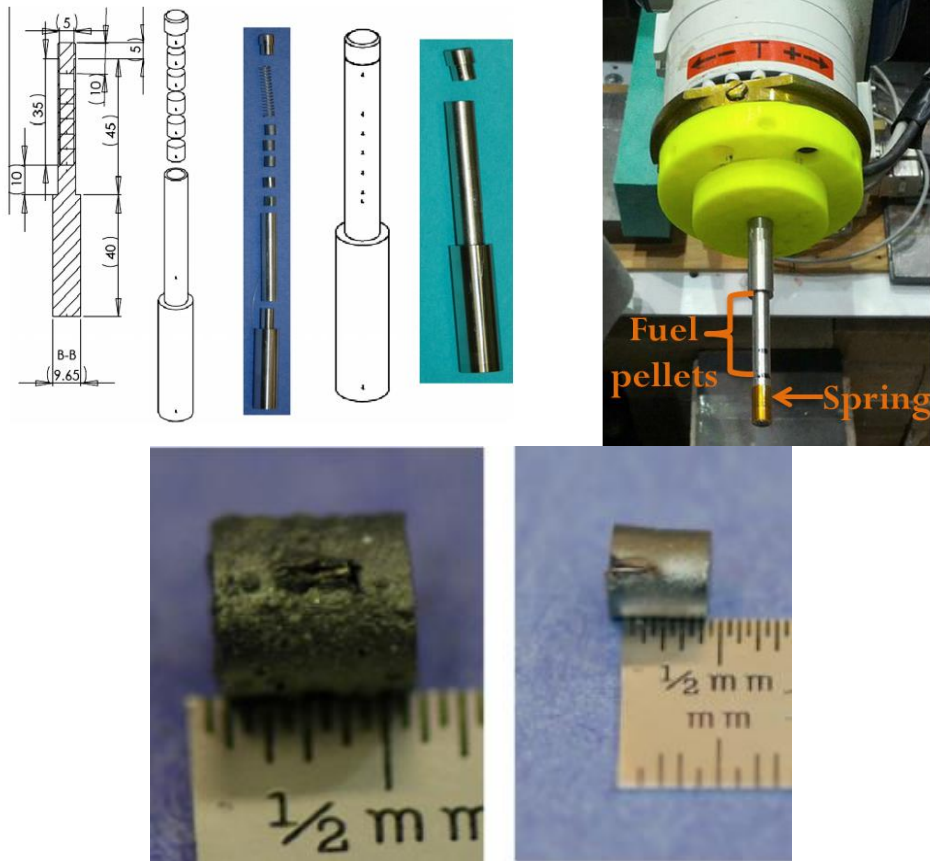
Figure 6-11. Urania mockup fuel rodlets (top-left), robot holding fuel rod (top-right), and example fuel pellets with intentionally introduced defects (bottom).
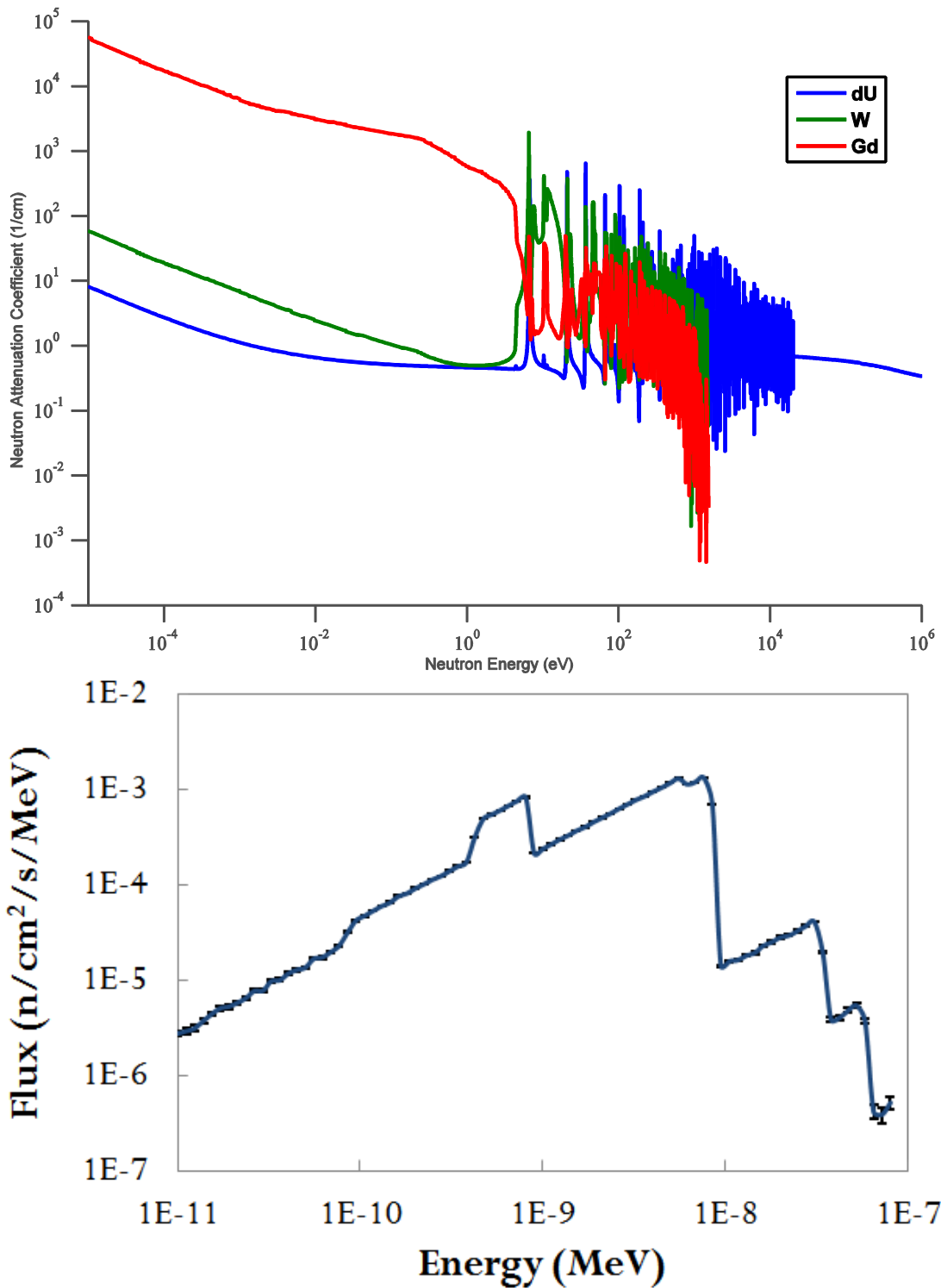
Figure 6-12. (Top) Neutron attenuation coefficients of the main components of the fuel pellets (i.e. depleted uranium, tungsten, and gadolinium) as a function of neutron energy. (Bottom) Corresponding neutron beam spectrum.

196

The depleted UO_2 fuel rod fission reaction rate was calculated to be 420 neutrons/sec, using the following equation:

$$Fission\ Reaction\ Rate\ of\ ^{235}U = \varphi N \sigma_f\ V_U \qquad (6\text{-}2)$$

where φ is the thermal neutron flux (5.3×10^6 n/cm^2/s), N is the atom density (atoms/cm^3), V_U is the volume of the ^{235}U in fuel pellets and σ_f is the thermal fission cross-section of ^{235}U (5.82×10^{-22} cm^2). A neutron activation analysis was performed looking at the fuel pellets, fuel rod cladding, beam sensitivity indicator, robotic arm, and gripper. The elemental breakdown of each of these components, along with their masses, was determined. It was found that there was no neutron activation risk of concern for this work.

To date, the integrated system has successfully demonstrated imaging of the mock-up uranium fuel rods with the necessary precision and repeatability. These demonstrations serve as a proof-of-concept that flexible automation and robotic technologies developed in research laboratories can be valuable for advanced non-destructive imaging abilities and applications. The neutron imaging was performed in BP3 at U.T. Austin's TRIGA Mark II research reactor. In this beam port, there is a thermal neutron flux of 5.3×10^6 n/cm^2/s and thermal-to-epithermal ratio of $8.1 \times 10^4 \pm 10\%$ n/cm^2/s at a reactor power of 950 kW. The neutrons in this beam port are cooled, due to the function of a beam wave guide, to an effective beam temperature of 39 ± 6 K. The wave guide acts as a neutron filter; only neutrons of a certain energy are efficiently transported down the wave guide. From Figure 6-13, one can see that there is structure in the beam, which is due to the neutron guides. When calibrating images this structure is accounted for by normalizing the blank beam measurement. The beam is a very clean neutron source and is also a divergent beam.
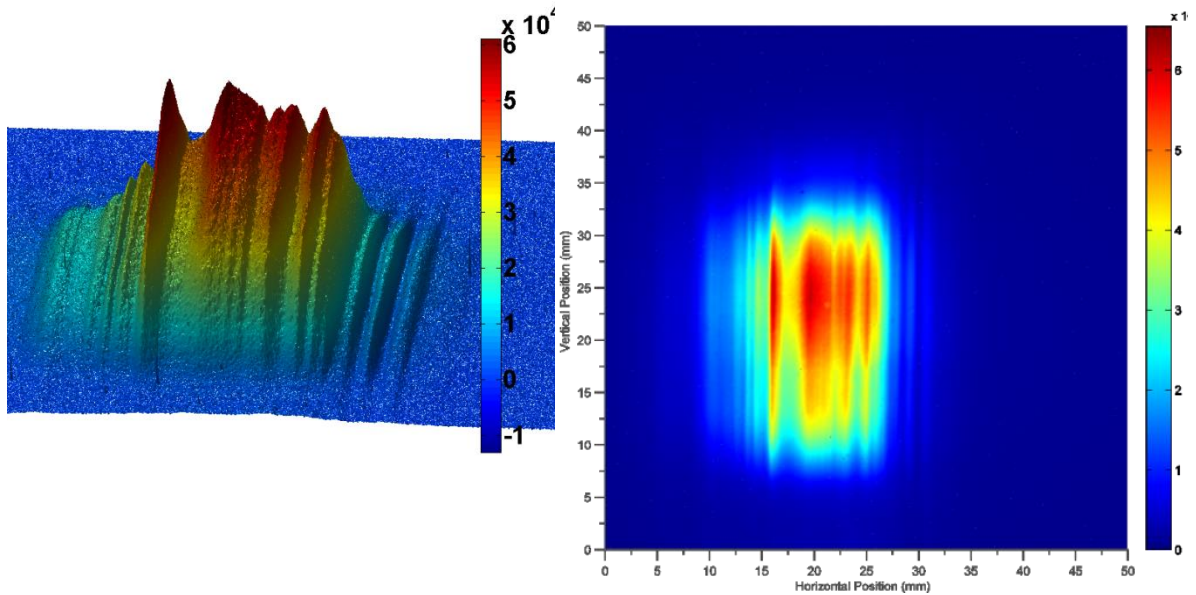
Figure 6-13. 3-D blank beam image showing beam structure due to neutron guides.

A scintillator-mirror-camera system (Figure 6-14) was utilized to acquire digital radiographs. This allows the operator to know what the radiograph looks like in real-time and allows for adjustments in part positioning to be made online. The scintillator used was a copper, aluminum, and gold doped ^{6}LiF ZnS neutron detection screen. [Applied Scintillation Technologies, 2014] The reaction that occurs is $^6Li + n \rightarrow He + triton + 4.8$ *MeV,* where the ejected triton interacts with phosphor in the scintillator to create a scintillation event. A stainless steel enclosure, along with lead bricks and lead blankets, surrounded the enclosure to shield against x-ray hits and background noise. The experimental setup is shown in Figure 6-15.
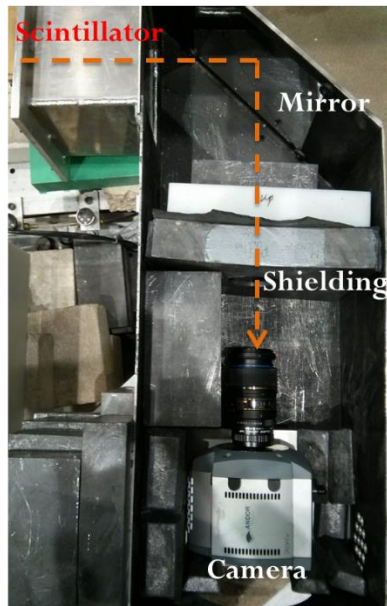
Figure 6-14. Image acquisition setup.
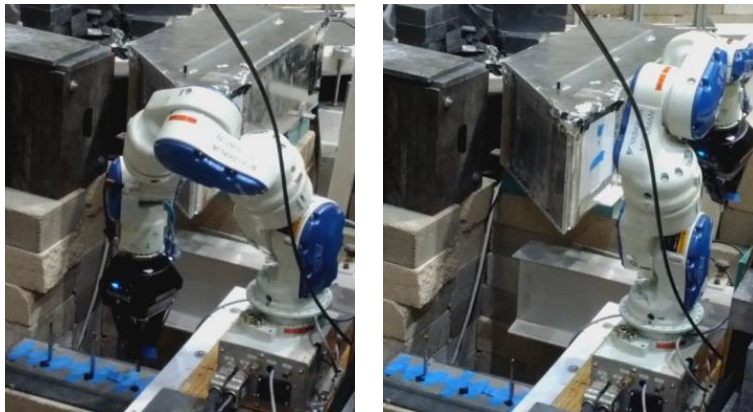
Figure 6-15. Photograph of experimental setup with robot picking up the first of three fuel rods to image (left) and robot bringing the second of three fuel rods into the neutron beam for imaging (right).

Neutron imaging consisted of a radiograph of five fuel rods with the primary focus on the fuel pellet region. Exposure times ranged between 5 and 10 min. To get the calibrated radiograph images, the raw radiograph is calibrated using a "light" and "dark" image. The "light" image is an image taken with the same parameters (exposure time, camera settings, power, etc.) but with the object removed from the beam path, so the presence of a significant flux gradient within the beam can be negated. The "dark" image

199

is also taken with the same parameters, but with the power or radiation source turned off. Multiple experiments were conducted including:

- rotating each fuel rod to various orientations,
- a vibration analysis (i.e. comparison of the resulting radiograph with the robot holding and not holding a fuel rod),
- a repeatability test,
- a computed tomography scan,
- a helical scan, and
- radiographs of the fuel rods at various orientations.

A beam sensitivity indicator was imaged first in order to determine the relative quality of radiographic images produced by direct, thermal neutron radiographic examination (see Figure 6-16). [ASTM E545, 2005] The sensitivity indicator is constructed of cast acrylic resin (methyl methacrylate), lead, and aluminum. It provides a measure of spatial resolution by means of gaps formed by the varying thicknesses of aluminum spacers between plastic supports. Images of the holes in plastic shims give a measure of radiographic contrast and resolution by means of images of small holes as differing percentages of material thickness penetrated.
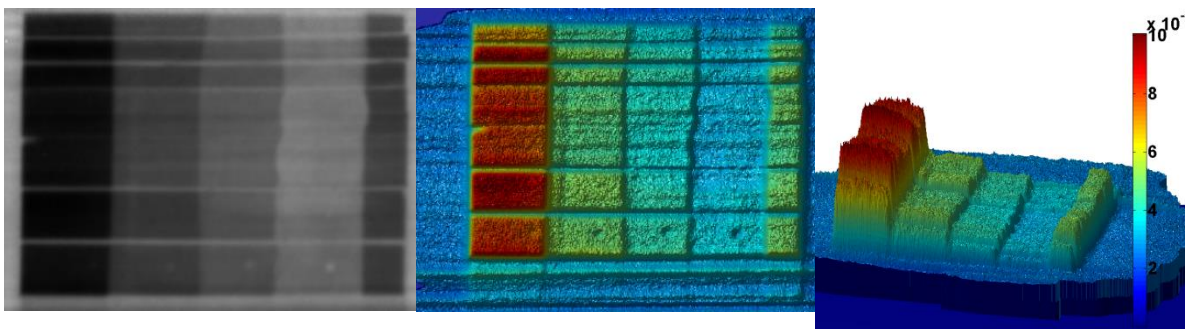
Figure 6-16. Neutron transmission image of the sensitivity indicator. The darker regions indicate areas with higher neutron attenuation coefficients.

Example results of the neutron radiographs of the five fuel rods are shown in Figure 6-17 and Figure 6-18. The process for acquiring these images consisted of the robot picking up a fuel rod, bringing the fuel rod into the beam path, acquiring an image, placing the fuel rod back down, picking up the next fuel rod, and repeating these steps until all fuel rods were imaged. Darker regions represent materials/areas with higher neutron attenuation coefficients than lighter regions. Gadolinium and tungsten inclusions appear darker than the d-UO_2. The gray regions appear to be fairly uniform d-UO_2. Thermal neutron tomography indicates the presence of flaws in the composite pellets, areal density fits to the ^{238}U demonstrate density uniformity. The gaps between rodlets are visible in the radiographic images. Voids or chips on the outside of the pellets are visible (appear black) and will be quantified as well as correlated with the actual samples in subsequent analysis. These radiographs clearly show the capability of the robot to perform neutron radiography tasks.
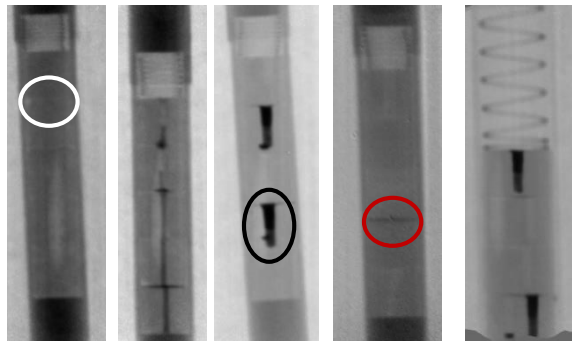
Figure 6-17. Neutron transmission images five mock-up urania fuel rodlets with engineered flaws and gadolinium and tungsten inclusions of the five pellet assemblies. The white oval indicates a void, the black oval indicates a gadolinium inclusion, and the red oval indicates a tungsten inclusion. The spring is seen in the top of each assembly.
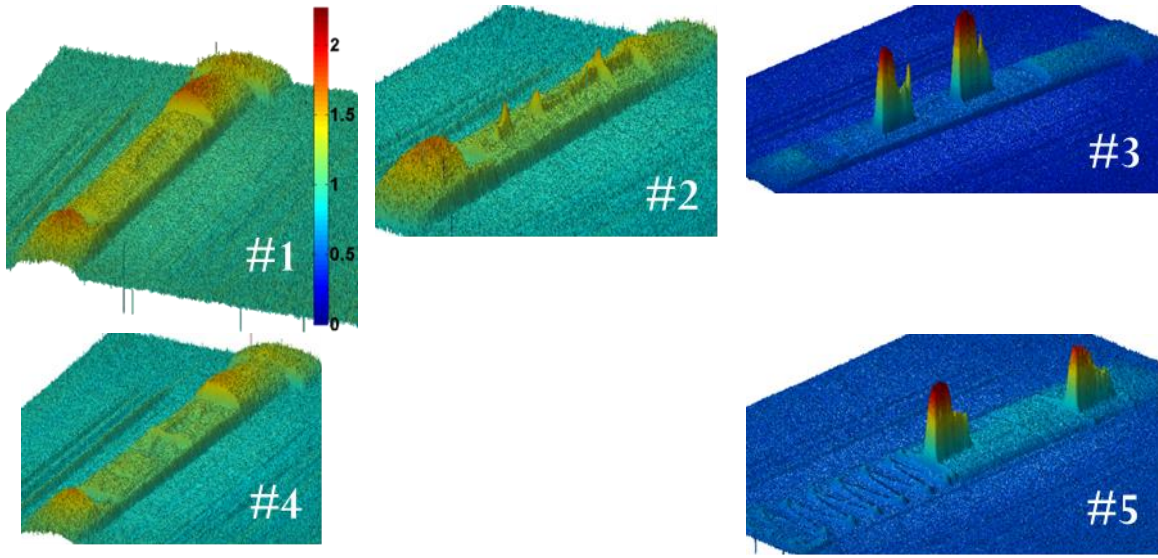
Figure 6-18. 3D radiographs of all five rods.

The source to detector distance was approximately 200 cm with the sample positioned as close as possible to the detector (Figure 6-19). Typically the distance from sample to detector is approximately 2 cm, mostly dictated by geometrical constraints imposed by the robot, gripper, and sample. As one can see the robot's workspace is confined, therefore collision detection and obstacle avoidance is implemented and necessary.

Figure 6-19. Robot demonstrating pick-and-place capability for a fuel rod placed inside of a canister.

202

Figure 6-20 shows a prelimary analysis of the areal density, expressed in atoms/barn, of ^{238}U atoms in the fuel sample as scanned along the cylinder axis of the rodlet. One can see that the areal density of ^{238}U atoms is relatively uniform in the fuel pellets except when inclusions are present. On-going analyses will correlate the variation in areal density with voids or chips observed in the tomographic reconstruction.
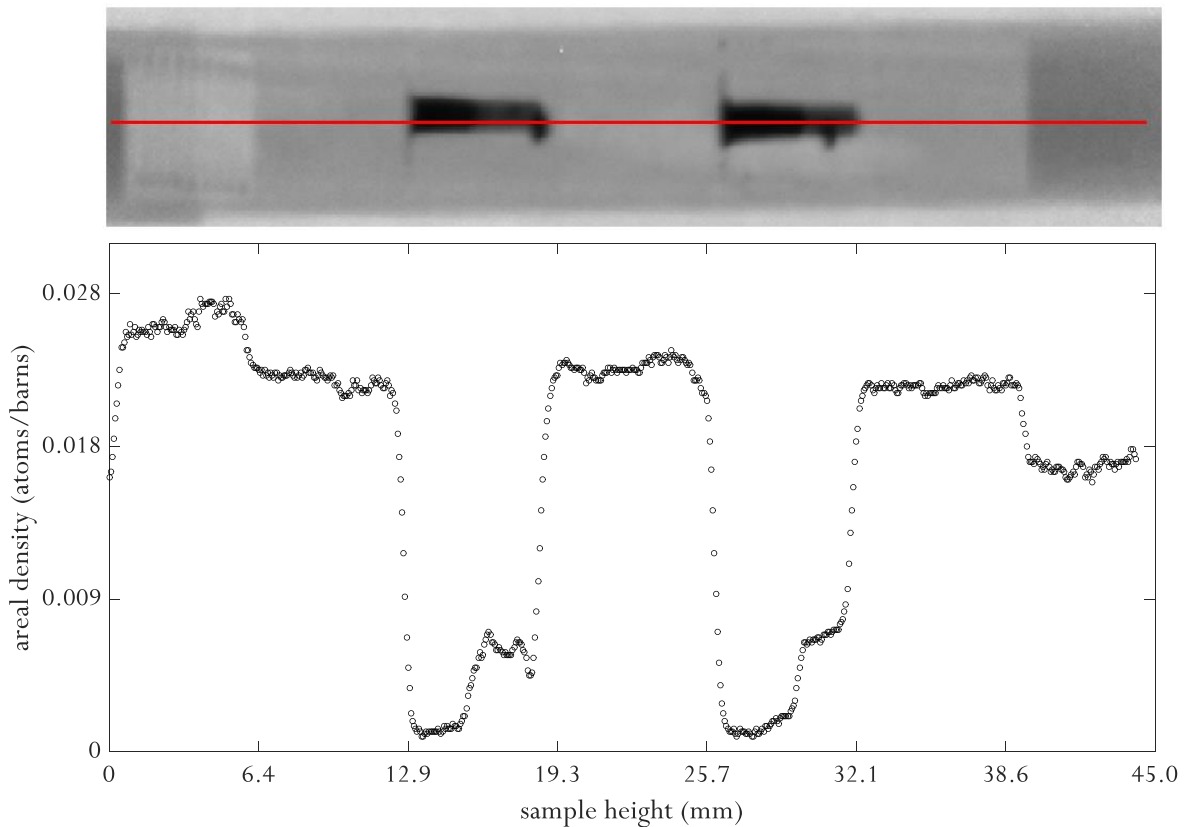
Figure 6-20. Fuel rodlet profile. Fit of the areal density of ^{238}U atoms in the fuel rodlet sample as a function of sample height. Each data point corresponds to one pixel or 50 μm. For comparison, the radiograph of the fuel rodlet is shown above with the red line representing the cross-section in which the areal density was calculated from.

The vibration test consisted of a radiograph taken while the robot was holding the fuel rod with the robot's servos on and another radiograph taken with the fuel rod placed on a flat surface, with an exposure time of 5 min. Comparing the two cases in Figure 6-21

203

(focusing on the circled regions), one can see that blurriness is not introduced when the robot is holding the part, meaning that no significant vibration is introduced when the robot is powered on.
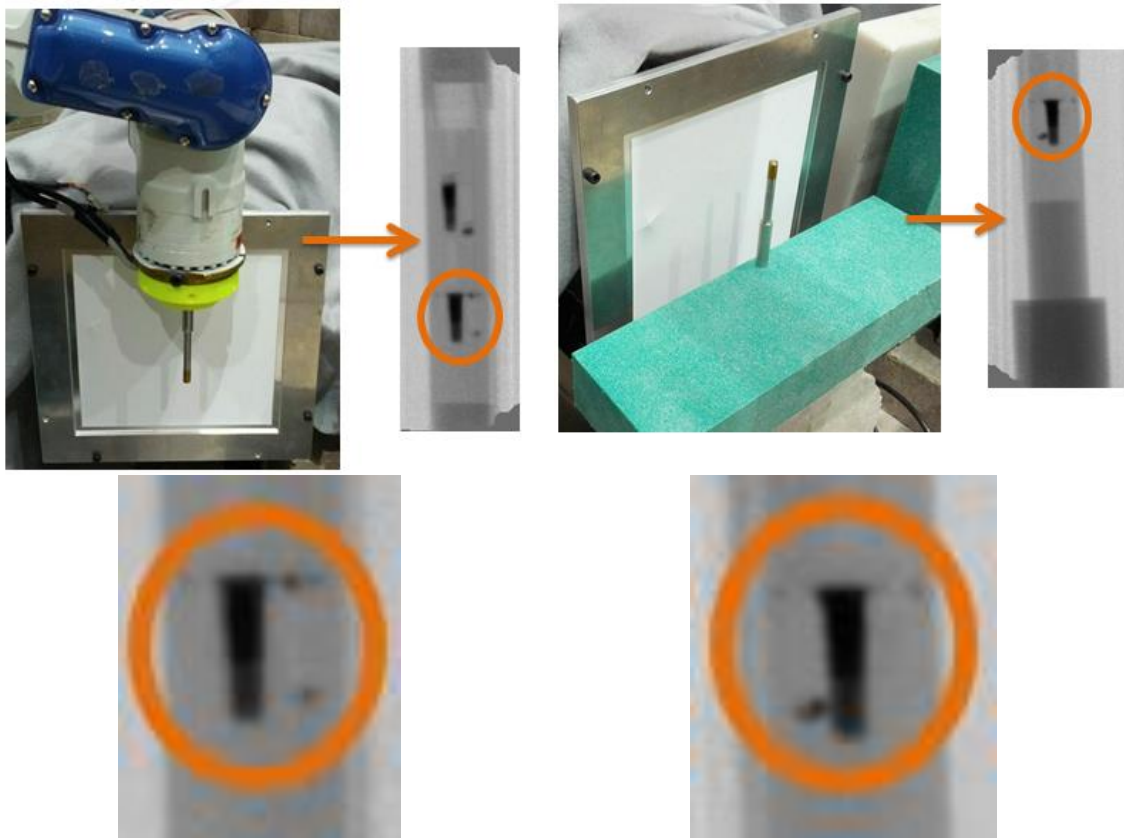
Figure 6-21. Radiograph taken with the robot holding the fuel rod with servos on (top-left) and zoomed in view (bottom-left) and radiograph with the fuel rod placed on a fixed surface (top-right) and zoomed in view (bottom-right).

A repeatability test was also performed, which consisted of taking an image with the robot holding the fuel rod in a specified location in the beam, moving the robot away from the beam, bringing the robot back to the same specified location, taking another image, and then comparing the two images using MATLAB's Image Processing Toolbox (Figure 6-22). [MATLAB, 2015] From these comparisons, it was shown that the

repeatability in the fuel rod's final location was ~0.025 mm. Similar tests performed in greater detail were described in Chapter 3.
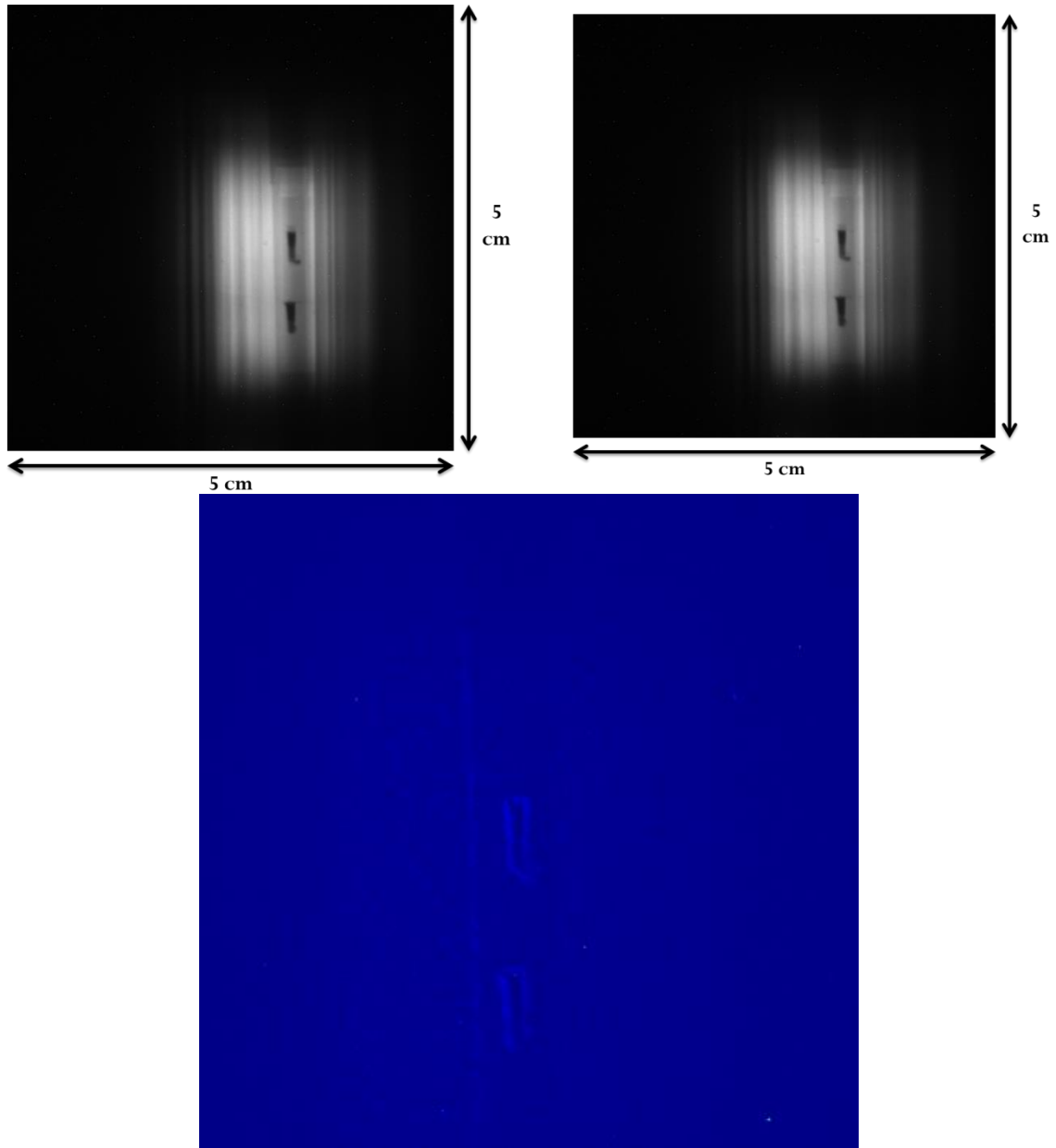
Figure 6-22. Repeatability test. First image acquired (top-left). Second image acquired (top-right). Comparison between the two images (bottom).

Radiographs were also taken, with the fuel rods at various orientations (Figure 6-23). The robot would rotate the fuel rod around the ±x, ±y, and ±z axes. This ability demonstrates the flexible nature of a robotic imaging system to easily take images at various orientations that would otherwise be difficult to achieve. The robot was able to maintain rotations around fixed but arbitrary axes in the task space.
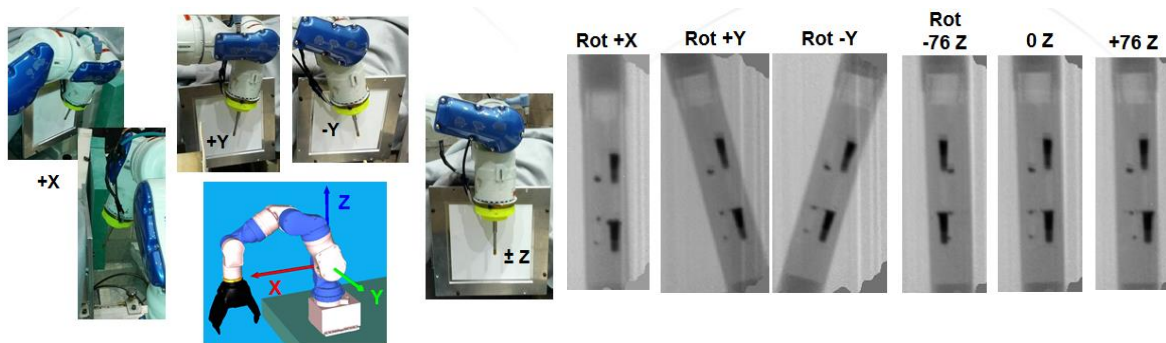
Figure 6-23. Radiographs taken at various orientations.

A computed tomography and helical scan of one of the fuel rods was performed. Neutron computed tomography is a process by which the three-dimensional neutron attenuation values throughout the object are obtained. This process requires taking two-dimensional neutron radiographs of the object while it is rotated around 360°, with images taken at certain points within the scan. Recon [Jimenez, 2013], a CPU-based reconstruction algorithm that uses a standard Feldkamp filtered back projection method, was used to reconstruct the three-dimensional map. The first and last views of the CT scan, which should be identical, are shown in Figure 6-24.

First view: -180°   Last view: +180°
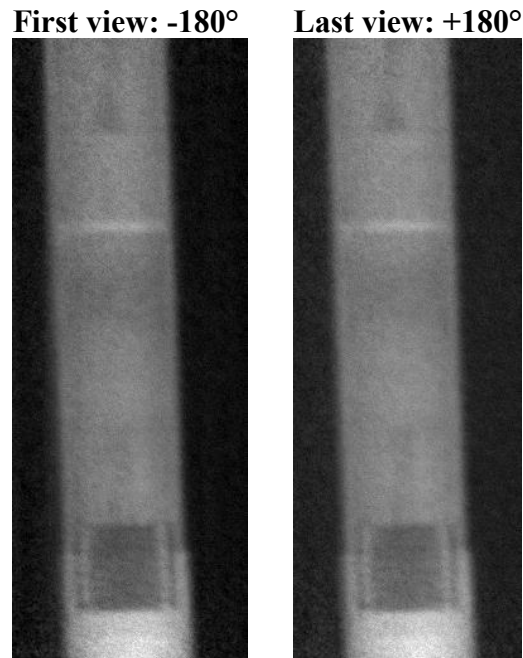
Figure 6-24. First and last views of CT scan of a fuel rod.

A helical scan was also performed (Figure 6-25), which consisted of ten images taken over 180° with an angle of inclination of 90° (Figure 6-26). In order to perform the helical scan, the robot simultaneously translated the fuel rod vertically and rotated the fuel rod at each step in the scan. To determine the translation distance needed at each step, the length of the part is divided by the number of views. Helical scans are implemented to decrease scan time when the imaged object is longer than the camera's or detector's field-of-view. It is also useful when using a point source, where the source strength is not as strong near the top and bottom of the image.
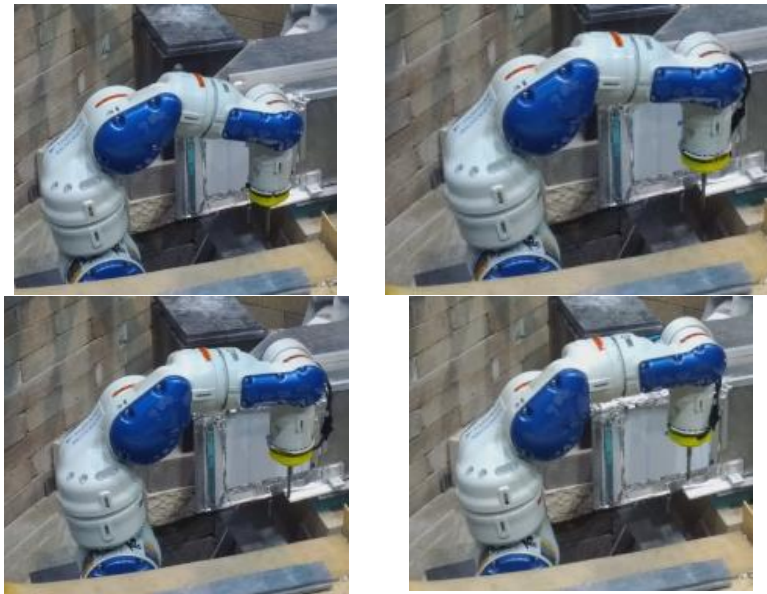
Figure 6-25. Helical scan (top-left) (top-right) (bottom-left) (bottom-right).
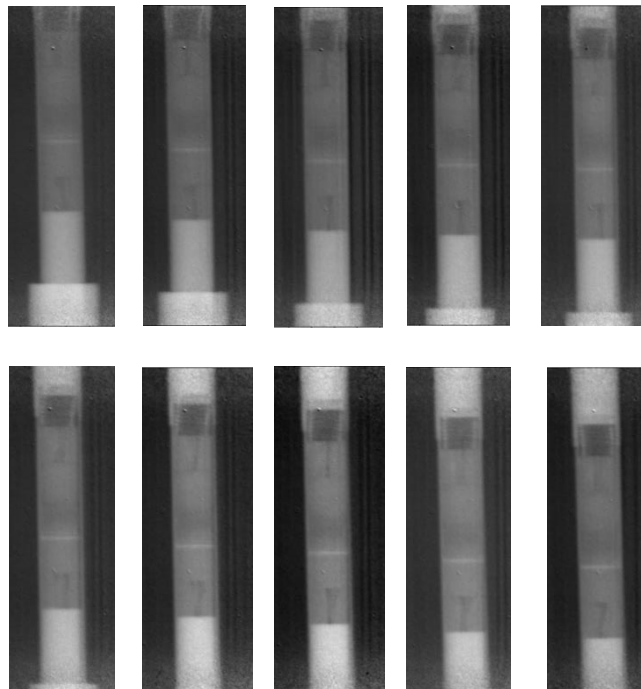
Figure 6-26. Helical scan. Fuel rod is rotated and translated at each step in the scan.

The demonstration described shows that robust and reliable imaging techniques can be achieved on a deployable system suitable for NDT automation. The neutron imaging data will provide, for the first time, highly detailed and spatially resolved

208

information on microstructure (cracks, voids, texture, defects, etc.). This will accelerate the understanding of processes occurring during irradiation and ultimately service of nuclear fuel.

6.3.5 Autonomous Imaging at LANL 450 keV Bay

The measured gamma dose rate in the 450 keV bay beam line is 51.88 Roentgen/min or 2730 rads/hr at 1 m from the x-ray source when the source is powered up to its maximum energy of 450 keV at 10 mA. A Radcal 9015 Integrating Ionization Chamber [Radcal, 2012] was used to determine this dose rate. However, the 225 keV micro-focus was used for all the tests performed, with energies less than 200 keV, which drops the maximum dose rate to approximately 1200 rads/hr. Heat sources or "liner weld" parts were imaged at 135 keV and 66 mA. A custom Varian 2520 (25x20 cm) amorphous silicon flat panel was used as the detector. The exposure time was set to 0.5 s for each image (i.e. 2 fps) with 50 frames averaged for each image. The focal spot size was set to 7 μm and a 6:1 magnification was used (source to object distance was 280 mm and source to detector distance was 1701 mm). Radiographs were taken of the parts at 0, 45, 90, and 135 degrees.

The robot autonomously picks up objects to be imaged, positions them in the beam, and places them back down. This process is repeated for multiple samples. The collected data is a result of x-ray attenuation as a function of density and atomic number. A denser region will result in a higher attenuation number (linear with density) and a higher atomic number object will have a much higher (non-linear with atomic number) attenuation number. An example radiograph of the liner weld taken with the robot is shown in Figure 6-27.
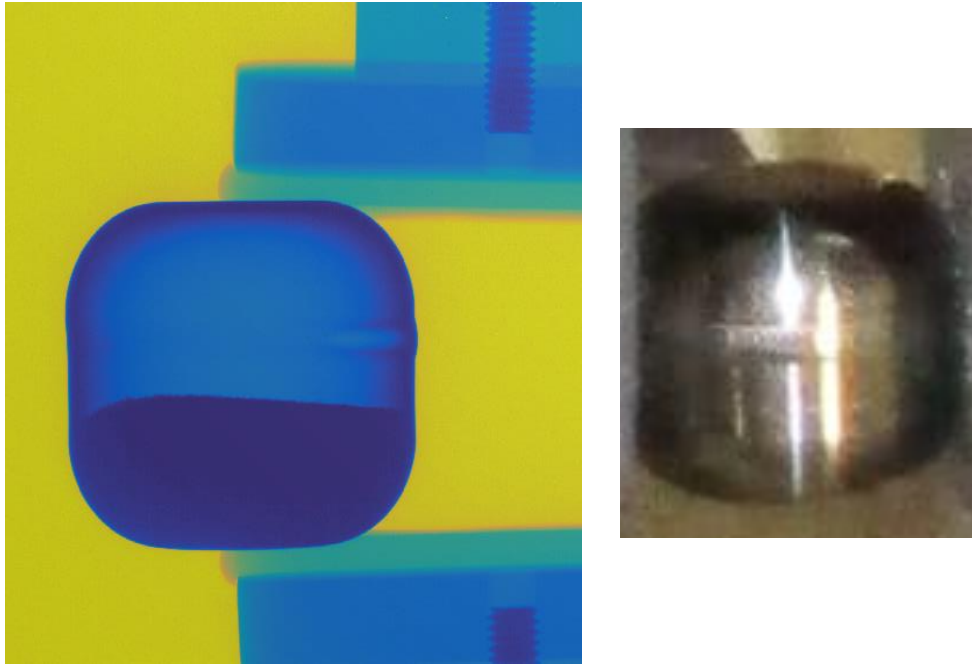
Figure 6-27. Radiograph of liner weld acquired while being held by robot (left). The gripper is visible in the radiograph, but does not affect the quality of the liner weld radiograph. A picture of the liner weld is shown on the right.

The helical scan capability, which allows one to image parts that are larger than the detector in one scan as opposed to several scans that have to be stitched together offline, was demonstrated using a mini Maglite. The capabilities and application process for helical scans are well documented by Silverman et al. [1995]. The ten images below in Figure 6-28 (left to right) show the progression of a helical scan of the Maglite. These images are just a subset of the entire helical scan from the beginning to end of the scan (rotated from 0 to 360° and translated 7 cm in total). Each progressive image in the radiographs below show the part rotated 32.73° and translated approximately 0.78 cm. The 2-fingered Robotiq gripper is visible in the first five images, however it does not obtrude the important aspects of the Maglite. The helical scan was performed at the 450

keV x-ray bay using the same settings used to radiograph the "liner welds" discussed previously.
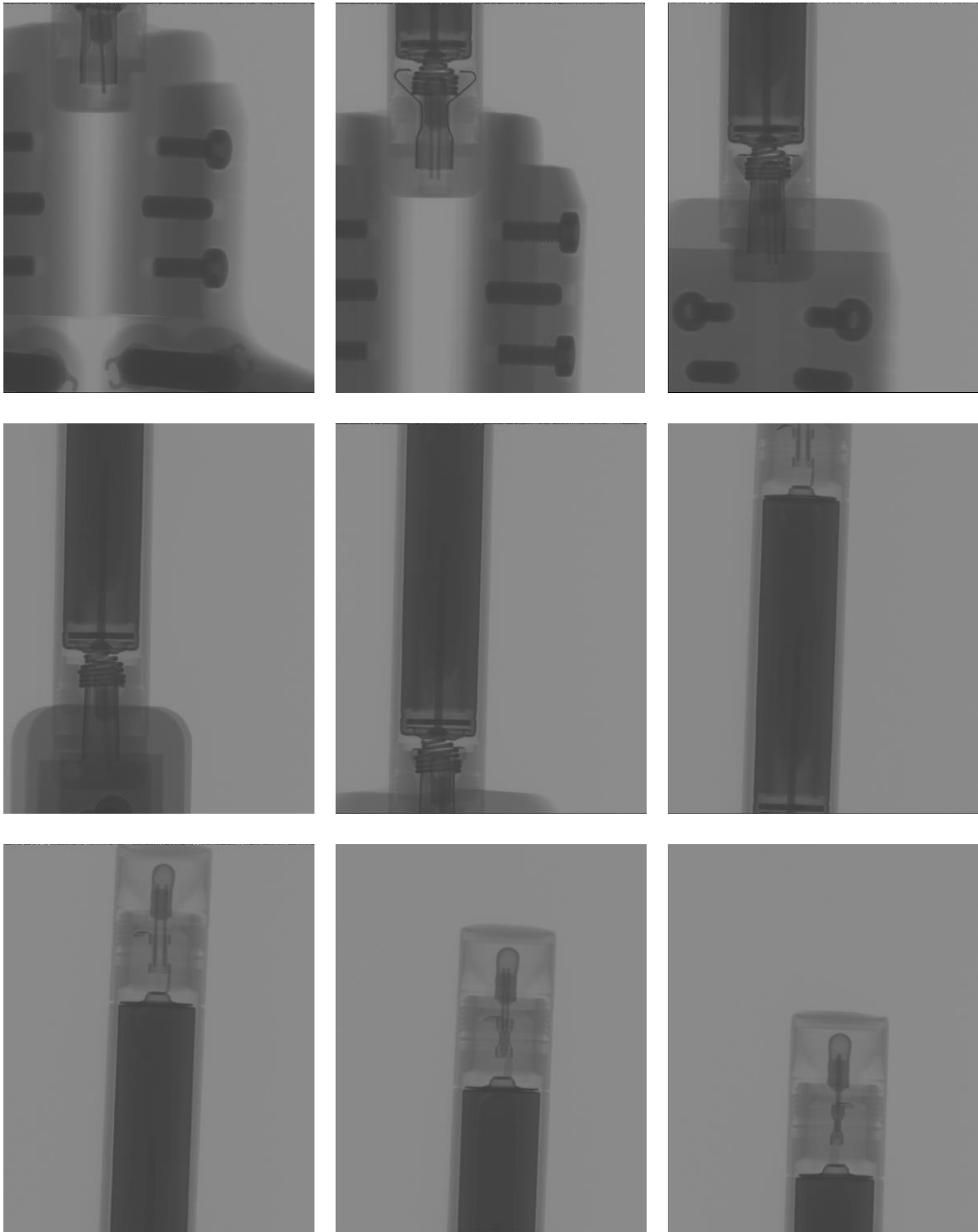
Figure 6-28. Subset of helical scan of Maglite completed using the robotic system coupled with the image acquisition system.

A glass jar with a plastic lid filled with water was radiographed at various poses to demonstrate the flexibility of the robotic system. The part was also translated so that a sequence of radiographs can be acquired that show the entire object, which is important if the part is too large for the detector. These radiographs (Figure 6-29) were acquired using the 225 keV x-ray micro-focus with an energy of 190 keV at 100 mA. Figure 6-30 shows the object's rotation progression as the robot completes a Cartesian rotation about the z-axis. The robot rotates its EEF about the object currently held in order to keep the object in the field-of-view of the detector.

Translation along –y axis   **Translation along –z axis**

Translation along –x axis   **Rotation about +z axis (20°)**

Rotation about –z axis (30°)   **Rotation about +x axis (20°)**

214
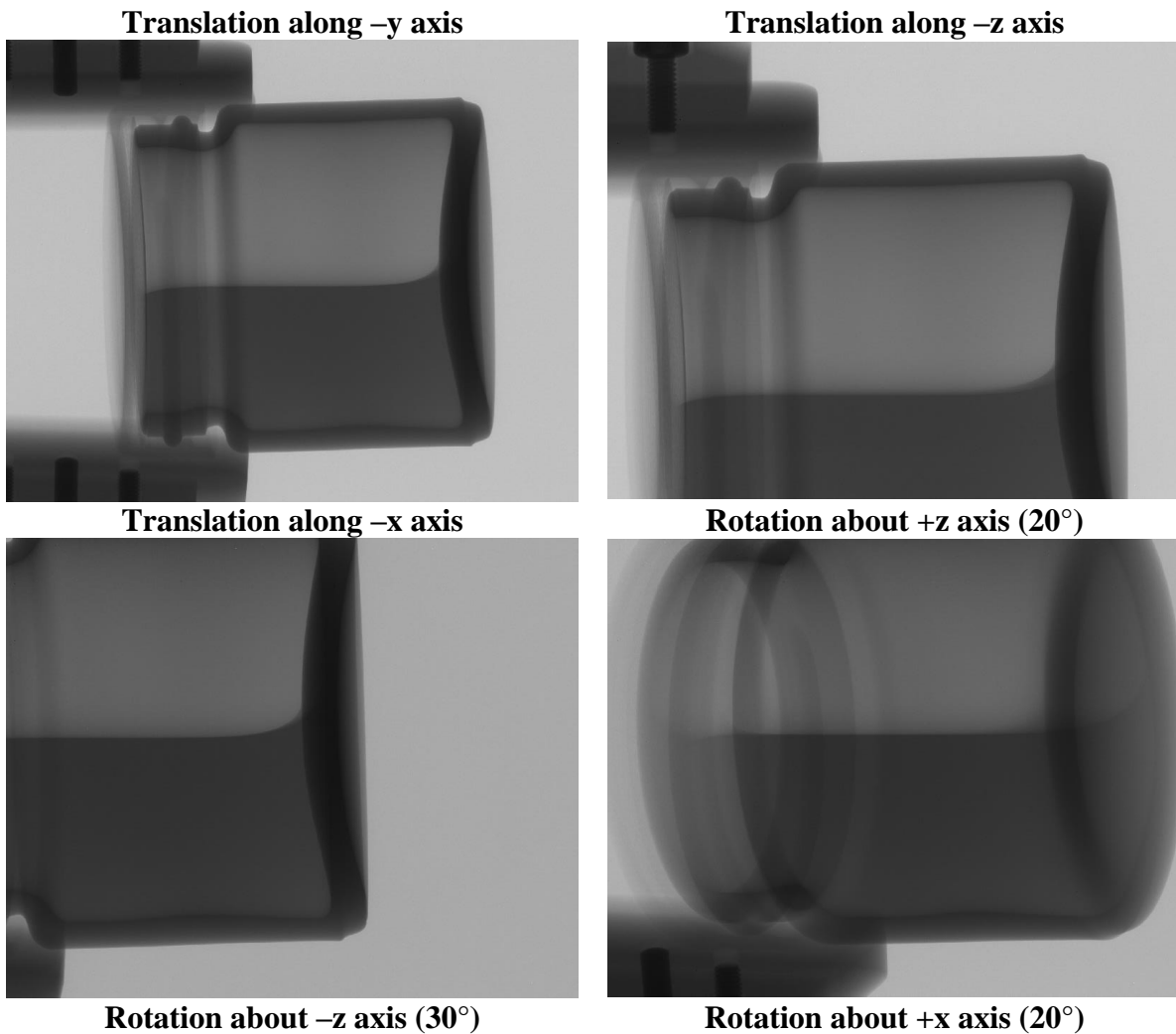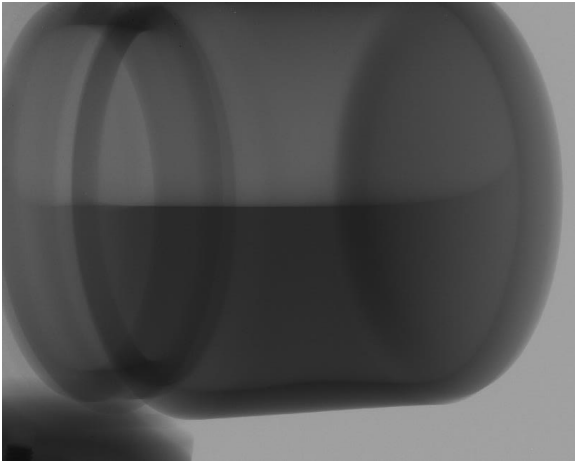
Rotation about –x axis (45°)
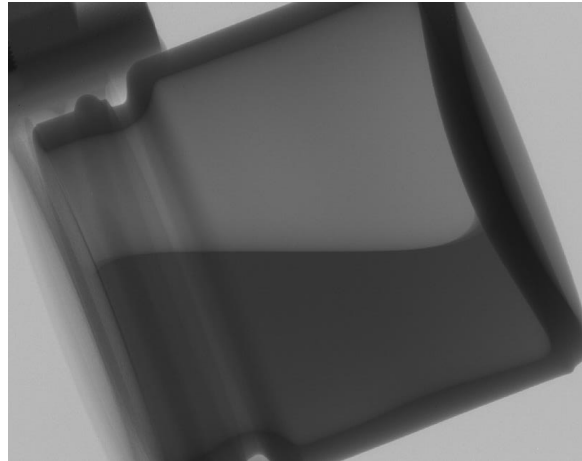
Rotation about –y axis (180°)
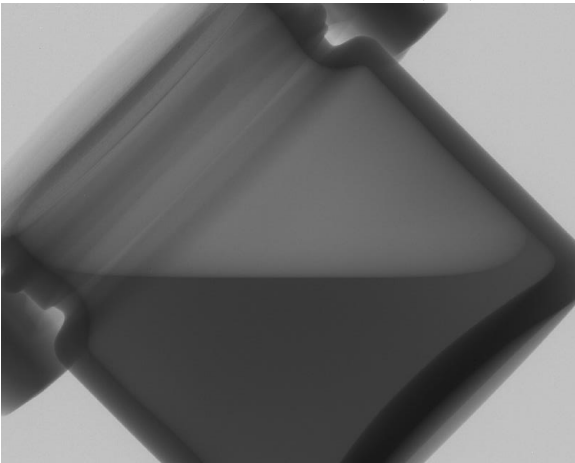
Rotation about +y axis (90°)
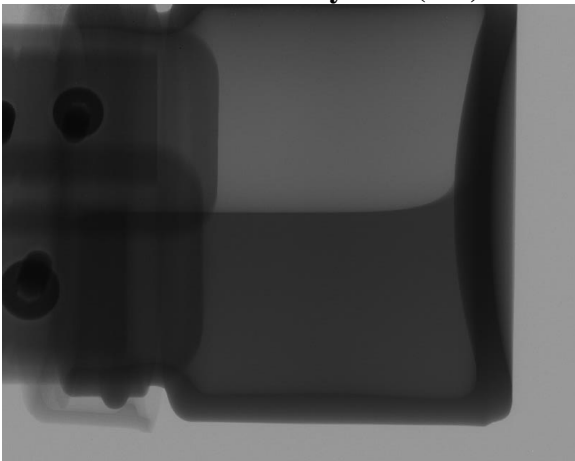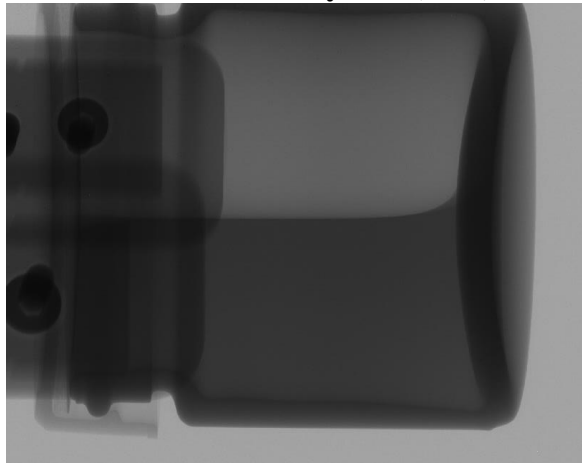
Figure 6-29. Translation and rotation radiographs of water container along x, y, and z axes showing the flexibility of the robotic system to acquire various angles and views of the part.
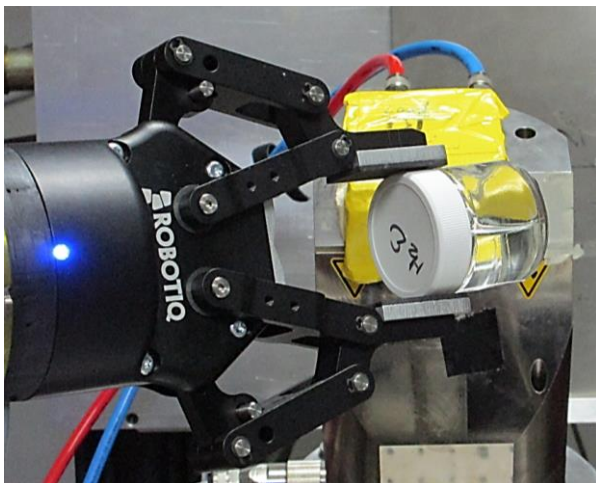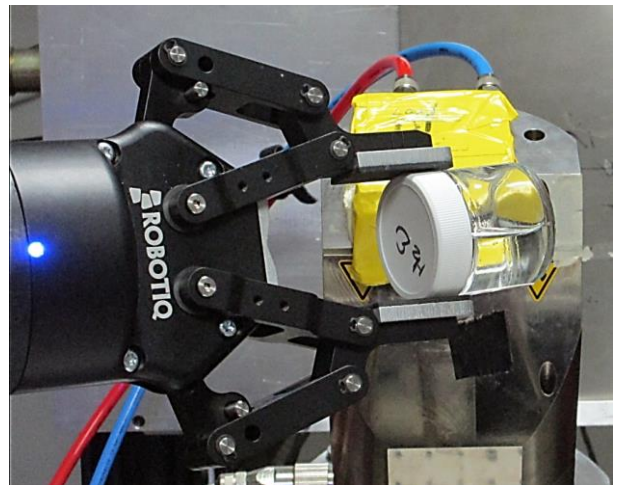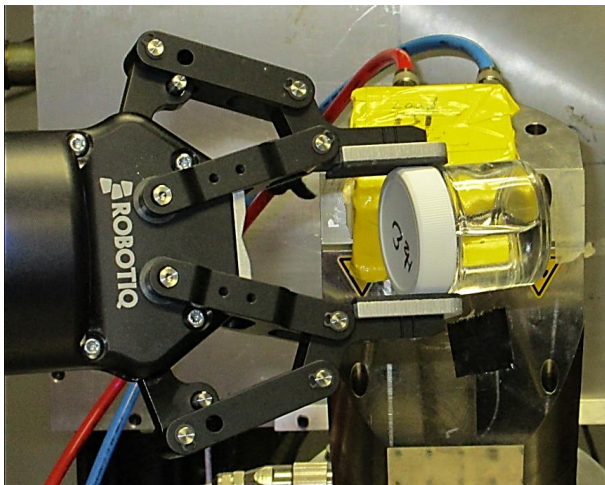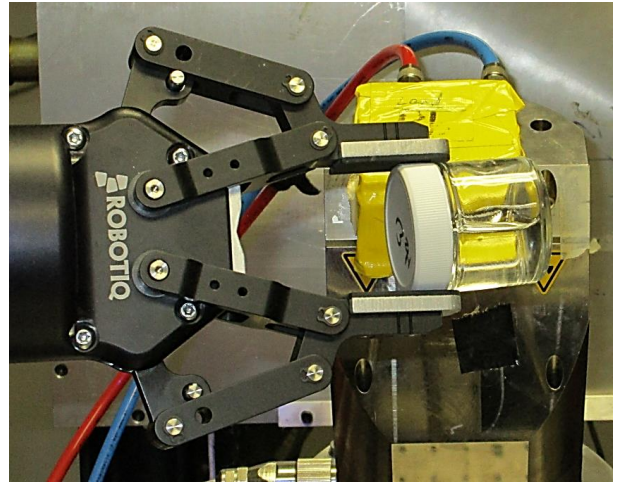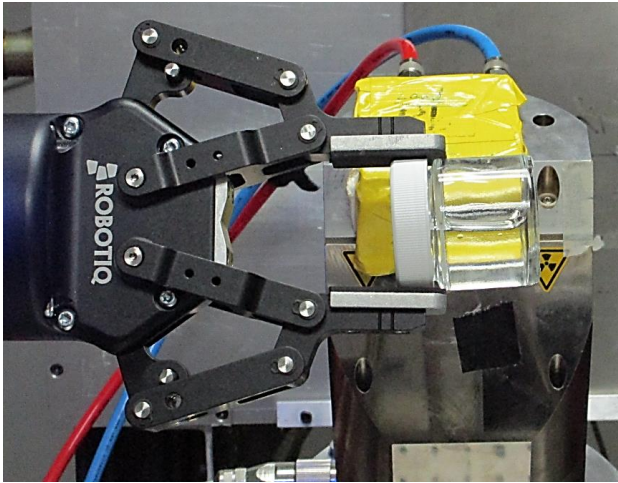
Figure 6-30. Progression of rotating the object about the z-axis while keeping the object in the x-ray beam. This is achieved by defining the object as the robot's point of rotation.

216

6.3.6 Summary of Robotic Sample Changer and Positioning System for High-Throughput Neutron and X-Ray Radiography Measurements

The demonstration task is to image different objects, one-at-a-time. The demonstration begins with the objects either randomly distributed or in a predetermined position in the area. If the objects are randomly distributed, an imaging system is used to determine their location using sensor information from a depth camera. A schematic of the generalized cycle of sample handling is shown in Figure 6-31. Figure 6-32 shows the demonstration in progress. The task is always performed in simulation prior to hardware execution to make sure the robot completes the task as expected and safely (Figure 6-33).
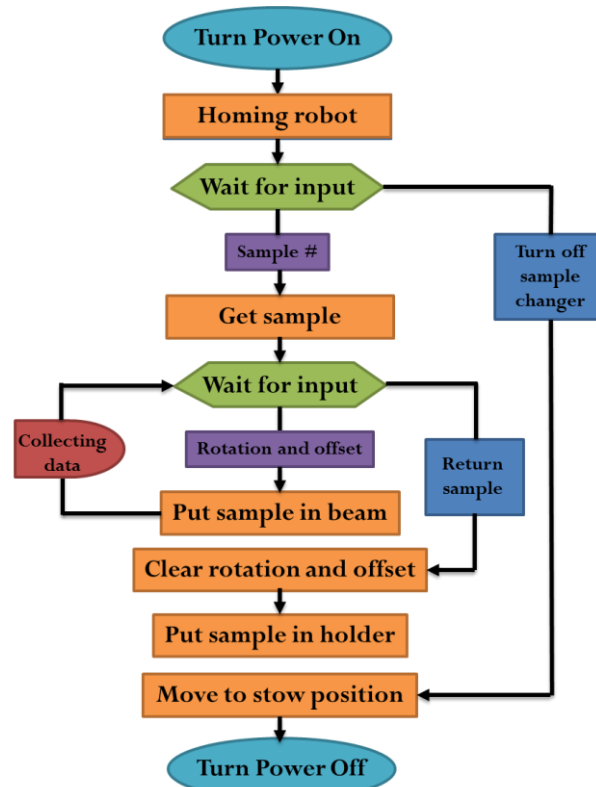
Figure 6-31. Flowchart of the sample handling process.
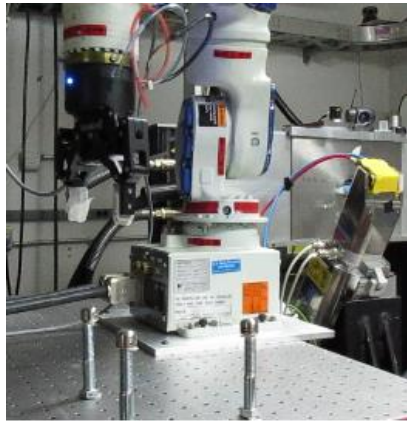
(a)

(b)
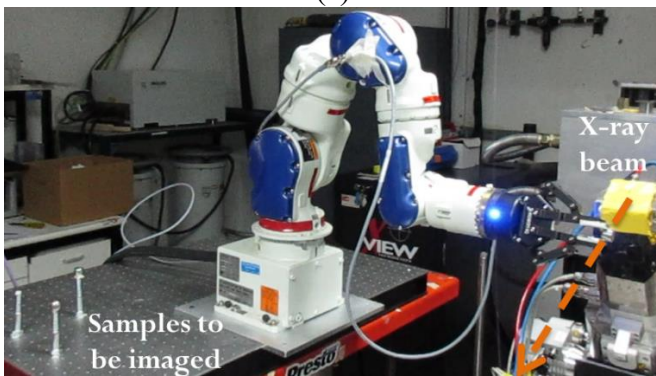
(c)

(d)

Figure 6-32. Application demonstration. The part positioning system installed in the open-air x-ray bay at TA-8. The setup consists of a computer controlled robot and a flat panel digital detector that communicate with one another autonomously (e.g. when an image is ready to be acquired). Object location identification (a). Object grasped (b). Beam placement (c). Object drop off (d). A robot can perform imaging of multiple samples without needing to have an operator turn off the beam and exchange samples. This decreases the overall time and cost to image each sample.
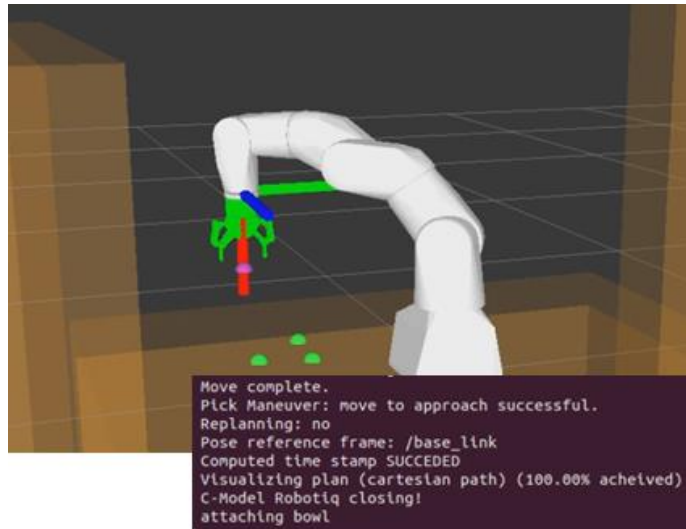
Figure 6-33. Simulation of robot performing part positioning task at LANL. Collision walls are added so that the software will not allow the robot to collide with the optical table, x-ray source, imaged parts, or detector.

The objects can also be placed in a sample-carrying tray, which allows the objects' locations to be known. In a neutron beamline, the sample-carrying tray can be made of aluminum, providing sufficient stability with a small absorption cross section of 0.231 barn (where 1 barn $= 10^{-24}$ cm^2) and a comparatively small scattering cross section of 1.495 barn [Heitmann and Montfrooij, 2012], to minimize the interaction of the sample containment with the scattered beam. In an x-ray beamline, the tray can be made of glass fiber or similar material with a low x-ray attenuation value. The gripper and robot controller are located outside the radiation area to prevent radiation damage to the electronics. The FS100 robot controller communicates via Ethernet with the data acquisition computer and controls all components of the robotic sample changer system.

To further prevent possible damage to samples and hardware by collisions, the acceleration and deceleration of the robotic arm is reduced, resulting in an average time of ~15 s to position the sample in the beam center after a "get sample" command was requested by the data acquisition computer. All sample holders are referenced to the

center of the sample tray, allowing recalibration of all sample positions with only one reference position if the sample tray is at an offset, e.g. after the robotic arm was repositioned or removed from the radiation area for maintenance. During experiments, the sample can be scanned along the z direction (vertical) and along the x and y directions (horizontal) across the entirety of the detector's field of view, allowing imaging of the whole sample volume for samples larger than the beam diameter for spatially resolved measurements. The rotational limits are ±180 degrees in the z direction, ±45 degrees in the x direction, and +60 degrees and -30 degrees in the y direction with respect to the beam center.

The robotic sample changer and part positioning system reduced the time period between the ending time stamp of the last run for a given sample and the starting time stamp for the first run of the next sample from ~5 (i.e. where an operator had to enter the radiation area and change the sample out) to less than 1 min, allowing a more efficient use of the available flux and a higher sample throughput. Considering the four minute faster sample changer, for every ~360 samples the robotic sample changer saves a full day of beam time compared to the old manual method.

Comparison of the resulting radiograph with the one using the previous manual method (Figure 6-34) shows only negligible differences within the images, proving that the new robotic sample changer performs as expected and can be used for such types of experiments. Aside from substantial improvements in the sample handling, accuracy, and repeatability, seven DoF allow for the correction of positioning offsets during operation of the sample changer. This enables a new set of experiments on imaging instruments, such as scanning large samples throughout the whole sample volume.
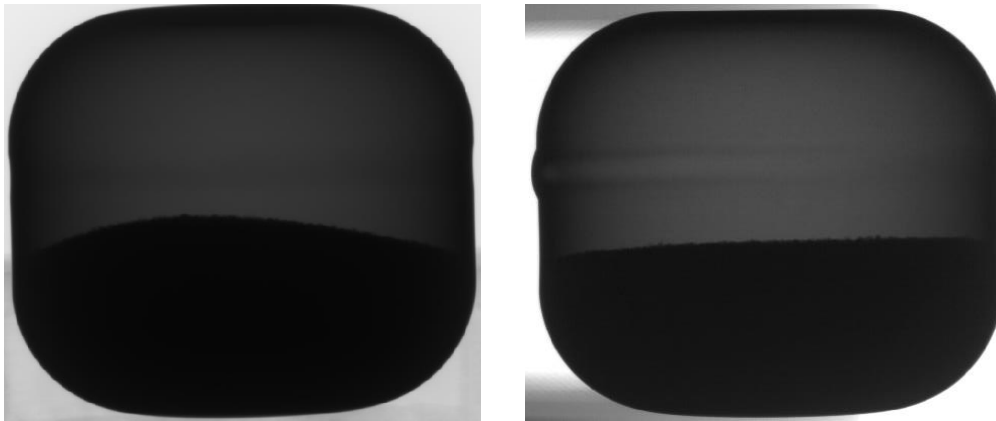
Figure 6-34. Radiograph of liner weld taken using manual method (left) and robotic method (right).

For neutron imaging, the sample or object to be imaged can be attached (typically glued) to the flat end of an aluminum rod. This rod can be wrapped in a cadmium sheet when dealing with neutrons. Cadmium absorbs thermal neutrons due to its high absorption cross section of 2520 b, hence preventing diffraction (i.e. elastic neutron scattering) from the sample holder. The end of the sample holders that are picked up by the gripper are custom machined Al pieces (Figure 6-35). A notch aligns the vertical rotation with the sample changer tray and therefore relates the sample orientation with the instrument for imaging measurements. The angle between the notch and the exiting beam direction needs to be included into the robotic software to obtain accurate images. The sample holder head has a thread in the rotation center to hold set screws for mounting the above-mentioned aluminum rod. This concept would allow special sample holders to be readily fabricated. For example, by simply gluing a nut on the sample holder head in order to hold a threaded sample. Larger or heavier samples can be clamped or screwed into special fixtures attached to the thread of the sample holder.
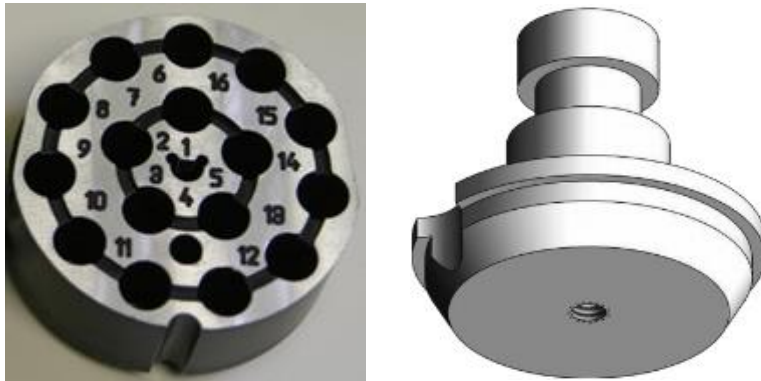
Figure 6-35. An example sample storage tray for holding up to 16 samples for use with the automated robotic system (left). Aluminum sample holder head with notch on left ensuring repeatability of sample position (right). The bottom of the sample holder head shows a screw hole where samples can be attached in different manners.

6.3.7 Specific NDT Applications

Three NDT applications that can benefit from automation are discussed in this section. These three applications involve a static source/detector with an object positioned by the robot. In Figure 6-36, two x-ray intensity transmissions are produced as x-rays penetrate two hemispheres welded together. The peaks result from the x-rays (going into the page) being attenuated everywhere except for where the hemispheres are welded together. To properly align the hemisphere so that the imaging system only sees a single peak of x-ray intensity transmission, the robotic system must align the sphere as shown on the bottom of Figure 6-36. To accomplish this task, a feedback loop is made between the robotic system and the imaging system that continuously takes digital radiographs in real-time. The robotic system, adjusts the part until a single x-ray intensity transmission is observed. Figure 6-37 shows the x-ray radiographs and intensity transmissions of actual parts. When the weld is not aligned, two peaks are visible, whereas only one peak is visible when the weld is aligned. These transmission histograms can be used to autonomously align the part with the robot. These radiographs were taken using a 225 keV micro-focus x-ray source at LANL.

222
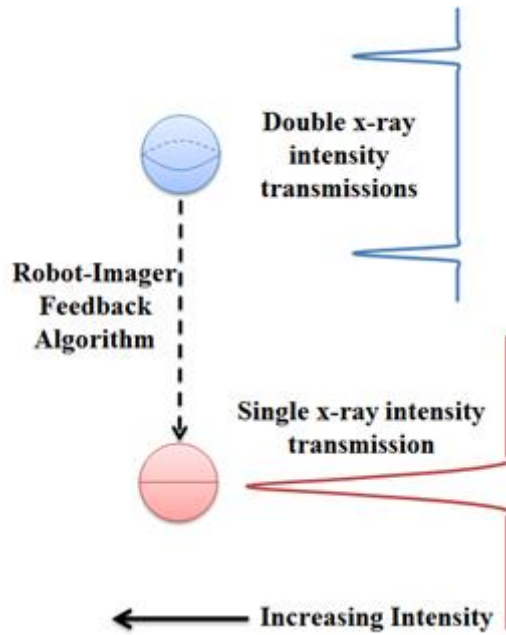
Figure 6-36. Using a feedback interface between a robot and imaging system to align a sphere for NDT.
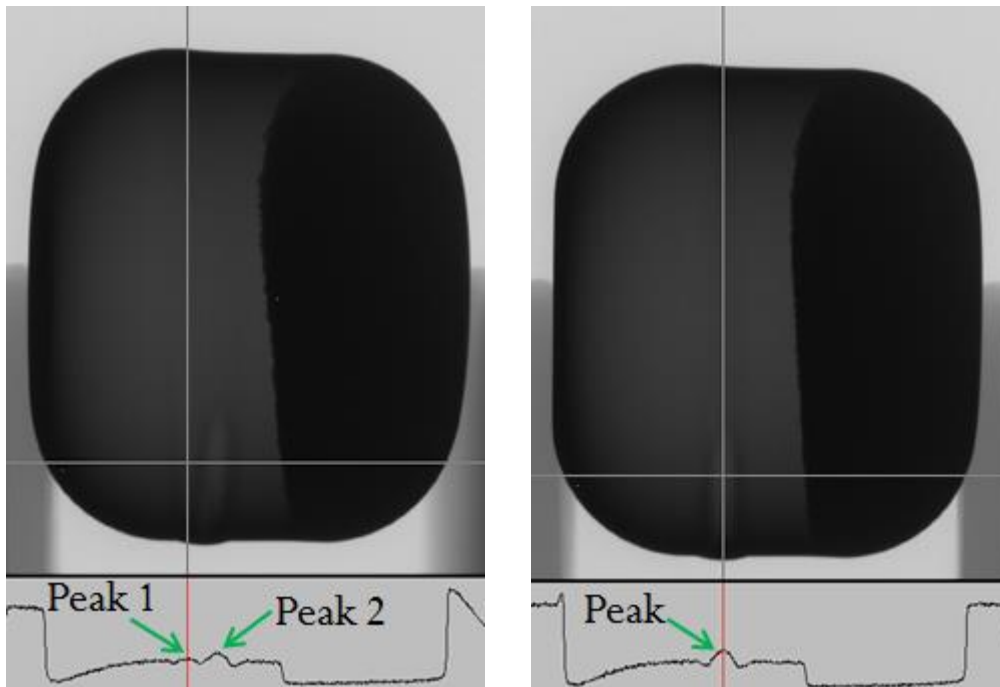
Figure 6-37. Precision alignment capability of the robot when a part's weld needs to be aligned with the detector. The radiograph on the left shows the weld not aligned and the radiograph on the right shows the weld aligned with the detector. The intensity transmission plots are shown below each respective radiograph.

223

In CT, there are cases in which a radioactive part to be examined is inside of a canister for shielding purposes. The part cannot be seen with the naked eye. This can lead to difficulties in setting up for an optimal CT of the part. An example case is shown in Figure 6-38. If the green part is the object of interest, the canister cannot simply be placed on a flat table or stand. Therefore a unique fixture must be developed to vertically align the part, and then the axis of rotation must be realigned with the part. The axis of rotation must also be shifted in 2D. Performed manually, this is a time-consuming process of alignment via trial-and-error. With a robotic system, the canister can be tilted at any angle in 3D space until the object is vertical and the axis of rotation can then be aligned accordingly, all from outside the bay.
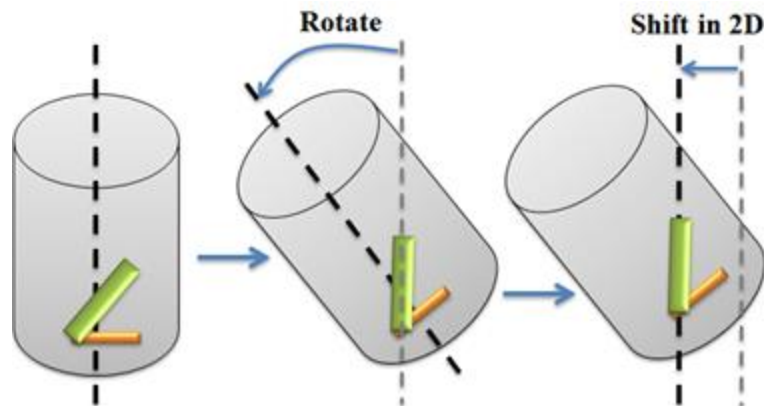
Figure 6-38. CT to be performed on a part (green object) inside of a cylindrical canister. The object of interest and the axis of rotation must be aligned. From left-to-right: green object is at an angle; can is tilted so that object is vertical; axis of rotation (dashed line) realigned with object.

There are many instances in radiography where specific views of a part are needed. One common view is a pole-shot of an object, where the beam goes through the part from the top to bottom. For example, a pole-shot radiograph of the liner weld (Figure 6-37) is seen in Figure 6-40. This radiograph was acquired using the robotic system as shown in Figure 6-39. With this system, one can acquire various views and angles of a

part, and even place the part back down and pick it up in a different orientation if a specific view such as a pole-shot is required. Without the robotic system, the operator would have to shut down the radiation source and manually reposition the part. For some specific shots, such as pole-shots, a fixture may even need to be machined to hold a part in place so that it does not move while imaged.
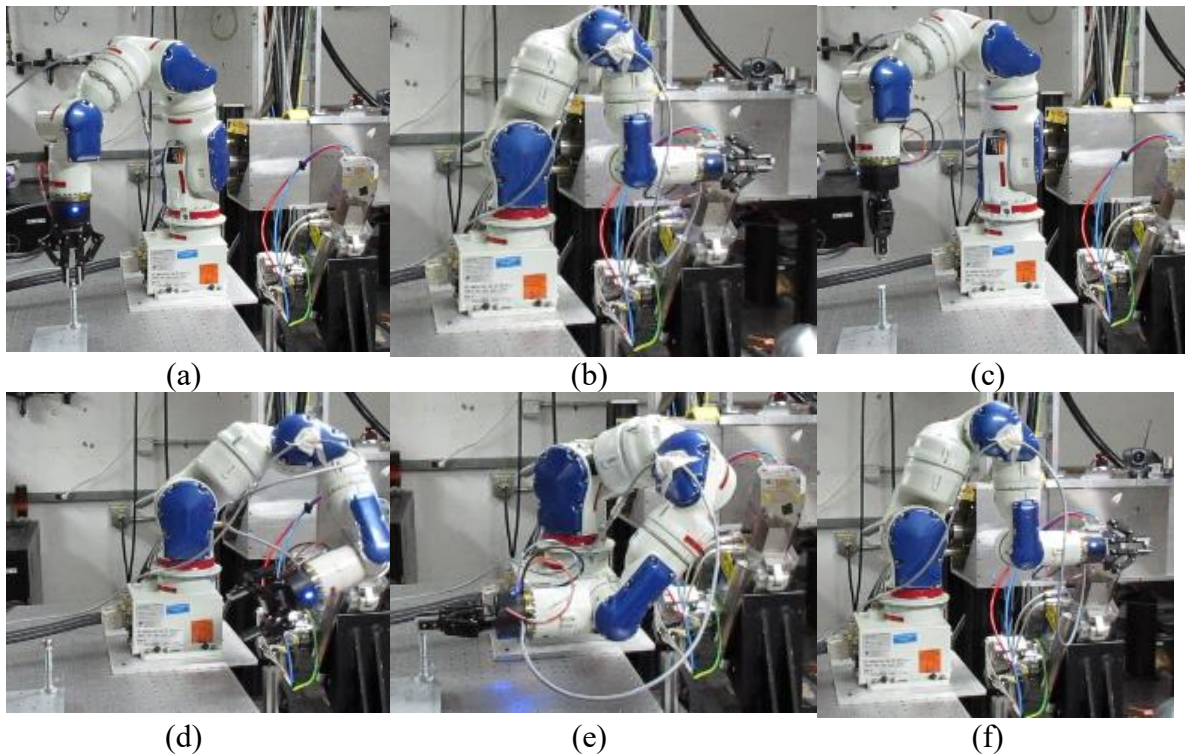
Figure 6-39. Pole-shot demonstration. Robot picking up the liner weld part from the top (a) and placing it in the x-ray beam in a regular orientation (b). Robot then places the part back down (c) and picks it up from the side (e). The liner weld can then be positioned in the beam to get a pole-shot radiograph.
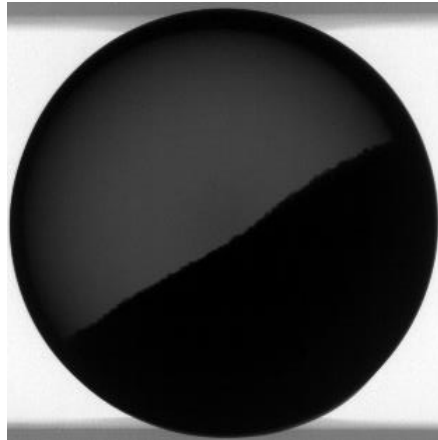
Figure 6-40. Pole-shot radiograph of liner weld object.

Demonstrated Capability

High energy neutron and x-ray sources allow sample throughput at rates of much less than one hour per sample for typical CT and helical scans. Automated sample changes with a high degree of reliability and flexibility are essential to assure safe operation and efficient use of available flux. The requirement of defect measurements, where samples need to be rotated and in some cases also tilted, requires precise changes of the orientation of the sample with respect to the beam. Thus a high-accuracy sample changer/rotator is needed. Using an automated robotic arm for sample changes therefore has the added benefit of more efficient use of the neutron beam or x-ray source without increasing the workload of the beamline personnel. Existing automatic sample changes at neutron beamlines elsewhere, such as [Hoshikawa et al., 2010], do not allow for a reorientation of the sample in the beam position around all three axes (i.e. x, y, z).

The demonstrations described in this chapter show how the work presented in this document validates the advantages gained by using a robotic system in NDT imaging applications. For a system operating under dynamic autonomy, these demonstration show the ability of the system to accept high level instructions from the operator ("Pick up object A", "Place object A", "Perform CT scan with 500 views", etc.), and transform

226

those commands into a series of low-level tasks that can be completed without further input from the operator. The added ability of having communication between the robot and image acquisition device allows for further system autonomy. With the completion of these demonstrations, we now have a six axis sample positioning capability that can be deployed on both x-ray and neutron beam lines for a large range of parts.

Chapter 7: Conclusions & Further Work

The last decade has seen rapid expansion of autonomous robotic technologies, however, very few of these technologies are successfully implemented in NDT applications. The reasons for this are that autonomous robotic systems must be able to complete NDT tasks reliably, safely, at a lower cost, and in less time than could be achieved with humans or traditional linear and rotary motion stages. This chapter summarizes the material presented in previous chapters, reviews how flexible automation is used for NDT tasks feasibly and reliably, suggests several avenues for further research that would extend the impact of the work presented here, and explores new NDT capabilities that were not possible before.

Methods and applications of using an industrial 7 DoF robotic manipulator to perform x-ray and neutron radiography and CT scans have been presented. Using a PC to interface and control data acquisition, and an industrial robotic arm and controller, the feasibility of automating radiography and CT applications has been demonstrated. Robotic systems have been deployed both at LANL and at U.T. Austin by the Nuclear Robotics Group (NRG). The obtained results demonstrate the reliability and effectiveness of using a robotic system in NDT imaging techniques. This work advances the capability of autonomous manipulation systems for NDT applications, specifically CT and radiography.

Research performed aims to expand the role of automation at nuclear facilities by reducing the burden on human operators. It has been shown through this work that robots allow for faster, more precise, and more flexible image acquisition. Robots can achieve superior accuracy in part positioning than a person and similar in accuracy to mechanical stages. The robot's control system manages collision detection, grasping, and motion

planning and eliminates the amount of time that an operator spends micro-managing such a system via teleoperation. The software and control algorithms developed for the robotic system provides flexibility, robustness, independence, safety, and other operational metrics we perceive as intelligent. The flexible robotic system also allows one to sense, move, and manipulate parts with variable programmed motions for a variety of tasks. An interest in using a robotic system is to increase the accuracy and throughput of neutron/x-ray radiography and CT systems. An automated neutron/x-ray radiography system could improve the image acquisition rate. The current image acquisition process involves repeatedly shutting down and restarting the beam. Also, even with the safeguards currently in place, the risk of an accidental exposure must be considered if personnel must routinely move in and out of the area to change parts.

The robotic positioning system would permit automatic corrections in 6 DoF, unlike standard radiography and CT systems that only permit motion in 3 DoF. If a part was radiographed in a certain position one day and in the following day, the part needs to be radiographed in exactly the same position, the robot can easily and accurately reposition and align the part accordingly.

7.1 SUMMARY

Chapter 1 introduced the idea of using flexible automation for NDT imaging applications in radiation environments to reduce personnel dose and improve flexibility and throughput. Inspection of numerous components manually is time consuming and there is the risk of radiation dose to the operator. Robotics and remote systems are an integral part of the ALARA approach to radiation safety. Robots increase the distance between workers and hazards and reduce time that workers must be exposed. The use of robotics and automation reduces personnel dose, improves precision alignment, and

improves throughput. In this effort, a robotic manipulator was implemented as the motion control system for imaging tasks. The ultimate goal of this research and development work is to bring state-of-the-art robotics to bear on automation in non-destructive imaging applications.

Chapter 2 examined and reviewed previous work in the areas of x-ray and neutron radiography, NDT automation, and radiation damage. This chapter also discussed the Robot Operating System, an exciting development in robotics research that improves the probability of system deployment by making state-of-the-art algorithms available for any system that provides drivers for ROS.

Chapter 3 presented the methods that form the backbone of the current work. Such systems have to be very precise. The feasibility of using automation for radiography at LANL's PF-4 site has been experimentally validated. Repeatability tests performed at NRG at U.T. Austin show that the Yaskawa SIA5 manipulator can achieve a repeatability of approximately 0.018 mm compared to 0.06 mm that Yaskawa states for the SIA5. Asserted capabilities from robotic companies tend to be extremely safe, since Yaskawa's declared repeatability value is taken at maximum payload, and maximum speed. [ISO 9283, 1998] Accuracy tests showed that backlash, produced noticeable effects on the accuracy, but did not cause the accuracy to fall outside of the 250 μm maximum allowed variance requirement for PF-4 radiography applications at LANL. Benefits of automating radiography and other nondestructive evaluation applications include economic incentives, hazard minimization, and downtime reduction. With digital radiography inspection, image transfer is almost immediate to the viewing device allowing inspection to take place in real time. By adding a robot to the process, additional efficiencies are gained. Robots can achieve superior accuracy in part positioning than a person and even a person with a mechanical stage.

230

Chapter 4 presented the software methods that help form the backbone of the current work. Through ROS and MoveIt, we have successfully demonstrated that the system robustly computes valid online motion plans that avoid collisions, singularities and joint limits. At no time does an operator need to teach the robot motions using the traditional teach pendant which can be time consuming and difficult to do remotely or dynamically. The system permits an untrained operator to cancel autonomous execution at any time and seamlessly revert to teleoperation, or issue new high-level motion commands without the need to restart any hardware of software. This approach offers three levels of autonomy:

- Autonomous assembly,
- high level motion commands (i.e. "Stow tool", or "Stow Robot"), and
- teleoperation.

Although this algorithm was demonstrated using a particular robot, the software base is hardware-agnostic. This allows the algorithm to be implemented on a variety of platforms that support ROS. The software developed in this work also allows for the integration of image acquisition devices to make the motion and image acquisition autonomous.

Chapter 5 illustrated how radiation damage, specifically neutrons and photons, effects robots. A complete radiation model of the radiography work cell with the robot installed is described. MCNP simulations were performed in order to find the displacements per atom in the interior and exterior robot.

Chapter 6 delved into the details of the system implementation and used the methods presented in previous chapters to perform several experiments that test and validate the advantages of using flexible automation for non-destructive imaging purposes. This chapter described how the methods presented in Chapters 3 and 4 became a part of a functional NDT imaging system implemented in ROS. Chapter 6 also

discussed several hardware application demonstrations showing how the work presented here supports autonomous part positioning for NDT imaging applications and can enhance and optimize x-ray and neutron radiography and CT systems. The integrated, robot-imaging system has successfully demonstrated imaging of mock-up fuel rods with the necessary precision, stability, and repeatability. Work completed demonstrated the application of neutron imaging techniques on UO_2 pellet fuel geometries with engineered flaws, inclusions, and compositional variations in mockup cladding approximating real rodlet geometries. A flexible sample positioning for x-ray radiography, computed tomography, and helical scanning applications at LANL has also recently been developed and demonstrated. These demonstrations have been performed using an industrial 7 DoF manipulator for imaging applications with a 225 keV micro-focus x-ray source. The system can run autonomously as well as in teleoperated mode, and it gives technicians the ability to position samples arbitrarily without entry into potentially high radiation areas. These capabilities will be further developed and eventually integrated into a final deployable system.

7.2   RECOMMENDATIONS FOR FUTURE WORK

This document demonstrates the contribution of flexible automation and MCNP modeling techniques to the area of NDT automation and imaging, which may be used to deploy systems for critical NDT tasks in the near future. However, there remains significant work to be done in the areas of robot vision, grasping, and radiation damage testing. The work presented here may serve as a springboard for further exploration. Below is a list of avenues for revision, extension, and application of the techniques presented in this thesis.

Added safety – In order to further reduce the likelihood of the robot damaging the imaged object, the robot could measure the force exerted on the object using a force/torque sensor. These measurements could then inform the robot if a collision has occurred, thus telling the robot to come to a stop or move back from the collision state. This capability has been demonstrated for other applications at the NRG [Schroeder, 2013], [Peterson, C., 2014], but has yet to include for NDT applications where it may be necessary to further evaluate the reliability of these sensor electronics in the neutron beam.

Use multiple imagers – A single depth camera was used as a sensor to identify, locate, and track various parts. With only one camera the resulting data is not fully 3D, therefore more than half of an object's geometry is typically occluded. By adding a second depth camera, a more complete 3D view of the parts could be captured. In order to do this, after collecting and transforming point cloud data, the point clouds would have to be concatenated together to form a single dataset containing all of the information from the sensor array.

Gripper mechanism – The two-finger gripper used in this work can be replaced with a three-finger concentric gripper resolving the potential problem of sample slip during rotation. Also, both gripper systems allow for the fingertips of the systems to be replaced. The tips from the manufacturer were used for this effort, but, as discussed above, new ones using more "transparent" materials could be fabricated.

Long-term failure rates – Even though neutron activation and other preliminary analysis suggests that robot survivability will not be an issue, it is necessary to complete a more comprehensive analysis of the reliability, survivability, and hardening requirements of the robot. The analysis above shows the system should perform in the proposed environments, but failures over longer periods should be examined to validate this effort

and determine what, if any, additional complexities should have been accounted for. It is recommended that individuals who consider this effort develop a system to document and record any system failures for future analysis. The issue of the robot having continued feasibility after prolonged periods of time needs to be addressed further. For example, if one were to let the robot sit for months or after moving it to a different location, would the robot still have the necessary repeatability? Even though it has been shown theoretically and experimentally that the robot can survive in certain radiation fields, more studies should be performed to quantify how long a robot can survive without any mechanical or electrical performance issues in high radiation fields. The system developed in this work can serve as a cost-effective platform for the future study of radiation effects in robots.

Further minimizing radiation damage - To further minimize radiation damage to the robot, the absolute encoders in the robot can be wired electrically outside of the radiation environment or can be shielded inside the robot. Developments to ensure compatibility with radiation levels may include identification and replacement of certain non-radiation tolerant components and removal of all electronics from the manipulator. Additional radiation testing is required to better estimate the tolerance of the robot. This can be accomplished in an irradiation facility that recreates the environmental conditions of expected use.

Testing at scale – The analysis above shows the system successfully scanning several parts, but future tests should include the robot scanning hundreds of parts to see if there are any potential issues with repeatability over an extended period of time.

Quantifying undesired motion - Future work with this system will include quantifying "wobble" or undesired motion in the location of the rotating axis in order to minimize the part's profile, resulting in fewer images needed for scans. The

implementation of force/torque sensing to find center of rotation of the part would also result in fewer images required for a successful scan. Along with force/torque sensing, x-ray and/or neutron images can determine the axis of rotation. This is important, because one needs to know where the axis of rotation on the robot is with respect to the camera/detector.

Motion planner that avoids radiation – The MCNP modeling component can also be used to inform a motion planner about the radiation field in the beam port. This would allow the radiation dose to the robot's microelectronics to be computed in simulation to determine how much reduction is possible by the use of motion planning techniques that aim to minimize radiological exposure. A radiation counter/detector could also be placed on the robot's EEF to physically characterize the radiation field. MCNP runs can also be used to determine the change in reflective intensity from the shielding as a function of shielding thickness.

Additional NDT techniques – It can be seen that the utilization of existing equipment combined with a robotic system may lend itself to additional inspection techniques. When comparing NDT to the application of a robotic system, one needs to look at the objectives of the equipment and the throughput of the parts in the facility. NDT facilities will have the ability to perform static radiography, in-motion radiography, and linear tomography with one installation. A dedicated computed tomography system would have a very difficult time matching these tests. The more parts that can be inspected with the robotic system will result in a quicker return on the investment.

Optimization problem – A non-linear programming optimization problem can be used to formulate the problem of automating NDT imaging systems correctly and formally. The idea is to minimize a function subject to certain criteria, which could include the ability for the robotic arm to reach the object, keep the dose that the robot

receives below a certain level, etc. What is minimized could be dosage, task time, etc. For example, if task time is minimized, dosage would become a criterion. Criteria should capture all definitions. Dosage or task time should be minimized without losing accuracy in part positioning. For example, a deviation of $< 0.1°$ can used as a criterion for minimum accuracy lost allowed. Assumptions would have to be made in order to solve the optimization problem.

Graphical User Interface – A GUI could be used as a means to visualize the radiographed part in real-time and communicate information with the system operator. This allows the operator to make decisions regarding the current robot or object state. A digital imager, like the Varian Panel or CCD camera used in this work, would have to be used to visualize the part in real-time. Having a GUI with a simple user display interface and simple control buttons showing the digital radiograph would be beneficial to the user. The GUI would allow the user to teleoperate the robot in 6 DoF (i.e. translation (x, y, and z) and rotation (Θ, Λ, and Σ)) about the EEF frame) by manually entering values into the GUI. Absolute or relative positions could be entered. If a value entered is out of the range of the robot, an error would alert the user. The GUI would also display a simulation of the robot with its current position updated in real-time. Figure below illustrates how the GUI may look. MoveIt [2013], which already provides a simple GUI control for EEF motions of a robot can be leveraged to include the necessary controls.
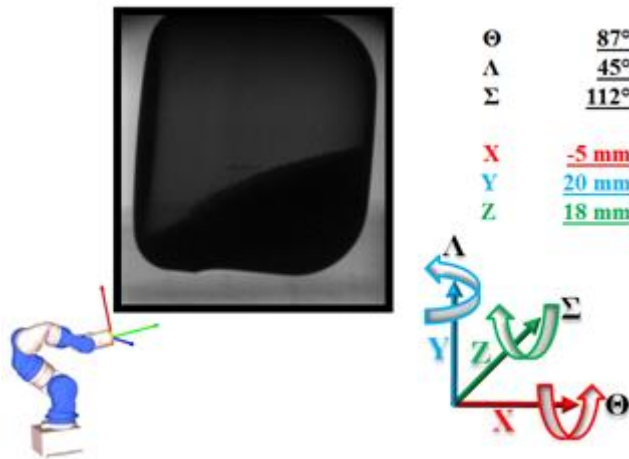
Figure 7-1. Example GUI for robotic radiography part positioning system.

CT code and robot link – A tightly linked feedback loop between the robot and CT code opens the door for additional imaging techniques and applications, improved radiograph quality, and reduced throughput time. For example, this system can achieve evenly spaced views around a sphere autonomously. Also, after an initial radiograph is acquired the CT code could communicate to the robot what additional views are needed to reduce error. This process can be iterated however many times are required to achieve an optimal radiograph or CT.

7.3 CONCLUDING REMARKS

The research presented in this document advanced NDT automation capabilities in nuclear environments. The major contributions of this work are:

- Integration between ROS and image acquisition devices. A Varian flat-panel was integrated using a python script and a CCD camera was integrated using MATLAB.
- ROS-compatible NDT code.
- Radiation damage model that quantifies the DPA and dose to the robot's exterior and interior components.

237

- The integration of an industrial robot with NDT imaging workspaces for autonomous radiography, CT, and other imaging applications.

These contributions lay the groundwork for efficient, safe, and feasible NDT automation. This work provides a strong foundation upon which UT NRG and LANL can continue to develop advanced automation capabilities that support x-ray and neutron imaging applications in DOE facilities. It also provides methods for the NDT community to further explore solutions for autonomous radiography, CT and other imaging applications.

APPENDIX A: U.T. AUSTIN TRIGA BEAM PORT 5 MCNP MODELS

A.1   BP5 COMPLETE MCNP INPUT FILE

This is the MCNP input deck of BP5 of the TRIGA MARK II research reactor at U.T. Austin modified to include a robotic manipulator and additional shielding for the robot. The original code was written by Cao in 2007.

```
1.  --------------- UT-TRIGA - BP5 Model - 6/26/2013 ---------------
2.  c
3.  c MCNP deck to simulate neutron/gamma dose rate
4.  c
5.  c ----------------------------------------------------------------
6.  c               Cell Card Specifications
7.  c ----------------------------------------------------------------
8.  c Cell Cards (cell #; material #; cell material density; geom; params)
9.     2   3 -1   (1 -2 -3 4 6 -300 97 ) #18 #17 imp:n=1 imp:p=1
10.    3   3 -1   (1 -2 -3 4 300 -25 308 ) imp:n=1 imp:p=1
11.    4   5 -2.35  (1 -2 -3 4 25 -26 31 ):(1 -2 -3 4 26 -27 32):
12.                 (1 -2 -3 4 27 -28 33 ):(1 -2 -3 4 28 -306 34 ):
13.                 (1 -2 -3 4 306 -29 34 ):(1 -2 -3 43 45 -30 ):
14.                 (1 -42 45 -30 4 -44 ) imp:n=1 imp:p=1
15.    97  5 -2.35  (1 -2 -3 4 39 29 -45 ) #33 imp:n=1 imp:p=1
16.    94  5 -2.35  (1 -2 -3 4 45 -30 ) #42 #43 #44 imp:n=1 imp:p=1
17.    95  5 -2.35     (1 -2 -3 4 30 -500 ) imp:n=2 imp:p=1
18.    5   1 -0.00115  (-52 56 -53 54 500 -55 ) #51 #52 #53 #54 #55 #56
19.        #57 #58 #800 #80 #81 #82 #85 #83 #84 #86 #87 #88 #89 #90 #6 #900
20.        #910 #914 #916 #918 #920 #922 #924 #926 imp:n=2 imp:p=1
21.    6   0 1 -2 -64 4 5 -51 imp:n=2 imp:p=1 $imaging plane, void
22.    7   0 ((-1 :2 :3 :-4 )-500 :-6 ):((52 :-56 :53 :-54 )500 :55) imp:n=0 imp:p=0
23. c Light-Tight Box and Tally
24.    80  1 -0.00115 (81 -82 83 -84 86 -85 ) #81 #82 #85 $Inner Box #84 #86 #87 #88 #89 #90
25.        imp:n=1 imp:p=1
26.    81  1 -0.00115  801 -808 -87 imp:n=1 imp:p=1 $MCP tally area
27.    82  1 -0.00115  83 -88 -89 imp:n=2 imp:p=1 $CCD tally area
28.    83  14 -1.64  813 -801 814 -804 86 -85 87 imp:n=1 imp:p=1 $ Boron flex
29.    84  0 -815 imp:n=1 imp:p=1 $tally sphere 1
30.    86  0 -816 imp:n=1 imp:p=1 $tally sphere 2
31.    87  0 -817 imp:n=1 imp:p=1 $tally sphere 3
32.    88  0 -818 imp:n=2 imp:p=1 $tally sphere 4
33.    89  0 -819 imp:n=1 imp:p=1 $tally sphere 5
34.    90  0 -820 imp:n=1 imp:p=1 $tally sphere 6
35.    800 2 -2.7  (801 -802 803 -804 806 -805 ) #80 #81 #82 #85 #84 #86
36.              #87 #88 #89 #90 imp:n=8 imp:p=1
37. c Shielding in Light-Tight Box
38.    85  9 -11.34  81 -82 811 -810 86 -85 812 imp:n=2 imp:p=1
39. c First collimor
40.    101 2 -2.7   301 -303 307 -308 imp:n=8 imp:p=1
```

```
41.    102 2 -2.7   302 -303 308 -310 imp:n=2 imp:p=1
42.    103 2 -2.7   300 -301 400 -308 imp:n=8 imp:p=1
43.    104 2 -2.7   301 -401 400 -307 imp:n=2 imp:p=1
44.    105 1 -0.00115   300 -401 -400 imp:n=1 imp:p=1
45.    107 2 -2.7   401 -403 406 -307 imp:n=2 imp:p=1
46.    108 7 -2.52   403 -404 406 -307 imp:n=1 imp:p=1
47.    109 2 -2.7   404 -405 406 -307 imp:n=1 imp:p=1
48.    110 1 -0.00115   401 -405 -406 imp:n=2 imp:p=1
49.    111 6 -7.8   405 -407 311 -307 imp:n=2 imp:p=1
50.    112 1 -0.00115   405 -407 -311 imp:n=1 imp:p=1
51.    113 6 -7.8   407 -408 409 -307 imp:n=2 imp:p=1
52.    114 4 -9.8   407 -408 -409 imp:n=1 imp:p=1
53.    115 10 -0.95   408 -410 311 -307 imp:n=2 imp:p=1
54.    116 1 -0.00115   408 -410 -311 imp:n=2 imp:p=1
55.    117 2 -2.7   410 -411 414 -307 imp:n=1 imp:p=1
56.    118 7 -2.52   411 -412 414 -307 imp:n=1 imp:p=1
57.    119 2 -2.7   412 -413 414 -307 imp:n=1 imp:p=1
58.    120 1 -0.00115   410 -413 -414 imp:n=2 imp:p=1
59.    121 9 -11.34   413 -415 312 -307 imp:n=1 imp:p=1
60.    122 1 -0.00115   413 -415 -312 imp:n=1 imp:p=1
61.    123 2 -2.7   415 -416 312 -307 imp:n=2 imp:p=1
62.    124 1 -0.00115   415 -416 -312 imp:n=1 imp:p=1
63.    125 1 -0.00115   416 -303 -307 imp:n=2 imp:p=1
64. c Middle Collimator
65.    201 2 -2.7   303 -452 451 -310 imp:n=1 imp:p=1
66.    202 7 -2.52   452 -453 451 -310 imp:n=2 imp:p=1
67.    203 2 -2.7   453 -304 451 -310 imp:n=1 imp:p=1
68.    204 1 -0.00115   303 -304 -451 imp:n=2 imp:p=1
69. c Last collimator
70.    301 2 -2.7   304 -305 312 -310 imp:n=1 imp:p=1
71.    302 2 -2.7   305 -454 312 -309 imp:n=1 imp:p=1
72.    303 1 -0.00115   304 -454 -312 imp:n=1 imp:p=1
73.    304 2 -2.7   305 -306 309 -310 imp:n=2 imp:p=1
74.    305 1 -0.00115   454 -455 -309 imp:n=1 imp:p=1
75.    306 2 -2.7   455 -456 312 -309 imp:n=2 imp:p=1
76.    307 1 -0.00115   455 -456 -312 imp:n=1 imp:p=1
77.    308 9 -11.34   456 -457 312 -309 imp:n=1 imp:p=1
78.    309 1 -0.00115   456 -457 -312 imp:n=1 imp:p=1
79.    310 2 -2.7   457 -458 461 -309 imp:n=1 imp:p=1
80.    311 7 -2.52   458 -459 461 -309 imp:n=2 imp:p=1
81.    312 2 -2.7   459 -460 461 -309 imp:n=2 imp:p=1
82.    313 1 -0.00115   457 -460 -461 imp:n=1 imp:p=1
83.    314 2 -2.7   460 -306 312 -309 imp:n=1 imp:p=1
84.    315 1 -0.00115   460 -306 -312 imp:n=2 imp:p=1
85.    320 12 -0.95   471 -306 310 -39 imp:n=1 imp:p=1 $Borated poly rings
86.    8    2 -2.7   -97 461 6 -300 imp:n=1 imp:p=1 $Through tube
87.    9    2 -2.7 -308 200 -201 imp:n=1 imp:p=1
88.    126 10 -3 -307 201 -202 imp:n=1 imp:p=1 $c10 beam scatter
89.    11   2 -2.7 -307 202 -203 imp:n=1 imp:p=1
90.    12   1 -0.00115 -307 203 -204 imp:n=1 imp:p=1
91.    13   2 -2.7 307 -308 201 -204 imp:n=1 imp:p=1
92.    14   1 -0.00115 308 -461 200 -204 imp:n=1 imp:p=1
93.    15   1 -0.00115 -461 204 -300 imp:n=1 imp:p=1
94.    16   1 -0.00115 6 -461 -200 imp:n=1 imp:p=1
95. c Core
96.    17   0 -93 -95 96 4 imp:n=2 imp:p=1
97.    18   10 -2.25 93 -94 -95 96 4 97 imp:n=1 imp:p=1
```

```
98.  c Stell Tube
99.   29  6 -7.8 25 -26 -31 36 imp:n=1 imp:p=1
100.        30  6 -7.8 26 -27 -32 37 imp:n=1 imp:p=1
101.        31  6 -7.8 27 -28 -33 38 imp:n=1 imp:p=1
102.        32  6 -7.8 28 -29 -34 39 imp:n=1 imp:p=1
103.        33  9 -11.34 29 -45 -47 imp:n=2 imp:p=1 $Lead gamma shutter(open position)
104.        42  9 -11.34 45 -30 -41 42 -43 44 46 imp:n=1 imp:p=1 $Lead filling cov
105.        43  6 -7.8 45 -30 40 -46 imp:n=1 imp:p=1
106.        44  1 -0.00115 45 -30 -40 imp:n=1 imp:p=1 $Air in center hole of shutter cover
107.        45  1 -0.00115 25 -26 -36 308 imp:n=1 imp:p=1
108.        46  1 -0.00115 26 -27 -37 308 imp:n=1 imp:p=1
109.        47  1 -0.00115 27 -302 -38 308 imp:n=1 imp:p=1
110.        48  1 -0.00115 302 -28 -38 310 imp:n=1 imp:p=1
111.        49  1 -0.00115 28 -471 310 -39 imp:n=1 imp:p=1
112.        50  1 -0.00115 306 -45 -39 imp:n=1 imp:p=1 $Air when gamma shutter open
113.     c Beam Shutter
114.        51  12 -0.95 500 -699 62 -63 67 -68 imp:n=1 imp:p=1 $Neutron shutter open
115.        52  12 -0.95 (500 -699 61 -62 -69 65 ):(500 -699 63 -64 -69 65 ):
116.                   (500 -699 62 -63 -66 65 ) imp:n=1 imp:p=1
117.     c Concrete Wall
118.        53  5 -2.35 56 -57 500 60 -59 -58 imp:n=1 imp:p=1 $wall No.1
119.        54  5 -2.35 56 -57 500 -53 -55 70 imp:n=1 imp:p=1 $ wall No.2
120.        55  5 -2.35 56 -57 71 -72 -73 74 imp:n=1 imp:p=1 $wall No.3
121.        56  5 -2.35 56 -57 -76 74 72 -75 imp:n=1 imp:p=1 $wall No.4
122.        57  5 -2.35 56 -57 77 -78 75 -55 imp:n=1 imp:p=1 $wall No.5
123.        58  5 -2.35 56 -57 79 -55 78 -70 imp:n=1 imp:p=1 $wall No.6
124.     c Simulated Part to be Radiographed
125.        900 2 -2.7 -900 imp:n=1 imp:p=1 $Simulated sample (sphere of Al)
126.     c Tallying Spheres (Robot)
127.     c  901 12 -0.95 -901 imp:n=2 imp:p=1 $Sphere for tallying
128.     c  902 12 -0.95 -902 imp:n=2 imp:p=1
129.     c  903 12 -0.95 -903 imp:n=2 imp:p=1
130.     c  904 12 -0.95 -904 imp:n=2 imp:p=1
131.     c  905 12 -0.95 -905 imp:n=2 imp:p=1
132.     c  906 12 -0.95 -906 imp:n=2 imp:p=1
133.     c  907 12 -0.95 -907 imp:n=2 imp:p=1
134.     c  908 12 -0.95 -908 imp:n=2 imp:p=1
135.     c  909 12 -0.95 -909 imp:n=2 imp:p=1
136.        910 12 -0.95 -910 912 -911 imp:n=2 imp:p=1 $Base
137.        914 12 -0.95 -914 911 -913 imp:n=2 imp:p=1 $Link 1
138.        916 12 -0.95 -916 913 -915 imp:n=2 imp:p=1 $Link 2
139.        918 12 -0.95 -918 915 -917 imp:n=2 imp:p=1 $Link 3
140.        920 12 -0.95 -920 921 -919 imp:n=2 imp:p=1 $Link 4
141.        922 12 -0.95 -922 923 -921 imp:n=2 imp:p=1 $Link 5
142.        924 12 -0.95 -924 925 -923 imp:n=2 imp:p=1 $Link 6
143.     c Table for Robot
144.        926 15 -7.8 -926 imp:n=1 imp:p=1
145.
146.        c ----------------------------------------------------------------
147.        c              Surface Card Specifications
148.        c ----------------------------------------------------------------
149.        c Surface cards (surface #; surface mneomic; numbers that describe the surface)
150.        c Beginning of Surfaces for Cube Boundary
151.        1 pz -50 $Problem top boundary
152.        2 pz 50 $Problem bottom boundary
153.        3 py 114.99 $Problem back boundary
154.        4 py -50
```

```
155.          5 px 532 $Imaging plane left boundary
156.          51 px 533 $Imaging plane right boundary
157.          6 px -62.2 $Problem left boundary
158.          52 pz 154.33 $bp#5 cave top boundary
159.          53 py 180 $bp#5 cave back boundary
160.          54 py -330 $bp#5 cave front boundary
161.          55 px 1000 $bp#5 cave right boundary
162.          56 pz -95.67 $bp#5 cave bottom boundary
163.          57 pz 104.33 $Top of concrete wall, 2 meters high
164.          58 px 578.55 $Right of wall No.2
165.          59 py -120 $Back of wall No.2
166.          60 py -180 $Front of wall No.2
167.          70 py 100 $Front of wall No.1
168.          71 px 587 $Left of wall No.6
169.          72 px 636 $Right end of wall No.6
170.          73 py -246 $Back of wall No.6
171.          74 py -300 $Front of wall No.6
172.          75 px 715 $Right of wall No.5
173.          76 py -100 $Back o fwall No.5
174.          77 py -240 $Front of wall No.3
175.          78 py -162 $back of wall No.3
176.          79 px 950 $Left of wall No.4
177.       c End of Surface for Cube Boundary
178.       c   101 pz -2
179.       c   102 pz 2
180.       c   104 py -1
181.       c   103 py 1
182.       c   105 px 499
183.       c   106 px 499.3
184.       c   13 c/x 0 0 0.05
185.       c   14 c/x 0 1 0.2
186.       c   15 c/x 0 -1 0.1
187.       c First Collimator
188.          300 px 101.7
189.          301 px 106.8
190.          302 px 185.5
191.          303 px 189.4
192.          304 px 190
193.          305 px 192.5
194.          306 px 311.9
195.          307 cx 6.35
196.          308 cx 6.985
197.          309 cx 12.73
198.          310 cx 13.65
199.          311 kx 186.82 0.00155 -1
200.          312 kx 110.62 0.00155 1
201.          400 cx 3.35
202.          401 px 109.34
203.       c   402 kx 96.99986 0.508 1
204.          403 px 109.51
205.          404 px 109.91
206.          405 px 110.1
207.          406 cx 2.63
208.          407 px 117.22
209.          408 px 120.14
210.          409 cx 3.24
211.          410 px 148.08
```

```
212.          411 px 148.25
213.          412 px 148.65
214.          413 px 148.82
215.          414 cx 1
216.          415 px 153.8
217.          416 px 156.34
218.     c Beam Scatterer
219.          200 px 1.905
220.          201 px 2.54 $Start beam scatter
221.          202 px 9.525 $End beam scatter
222.          203 px 10.16
223.          204 px 43.18
224.     c Middle Collimator
225.          451 cx 2.71
226.          452 px 189.5
227.          453 px 189.9
228.     c Last Collimator
229.          454 px 193.8
230.          455 px 299.9
231.          456 px 302.4
232.          457 px 307.5
233.          458 px 307.7
234.          459 px 308.1
235.          460 px 308.2
236.          461 cx 7.6
237.          471 px 291.6
238.     c Stell Tube
239.          25 px 105.6 $Water / concrete
240.          26 px 122.7 $1
241.          27 px 167.2 $2
242.          28 px 251.1 $3
243.          29 px 319.8 $4
244.          30 px 340.6
245.          31 cx 8.3001
246.          32 cx 10.7
247.          33 cx 15.7
248.          34 cx 19.9
249.          36 cx 7.6001
250.          37 cx 10.1
251.          38 cx 15.1
252.          39 cx 19.3
253.          40 cx 19.4
254.          41 pz 22.54
255.          42 pz -36.51
256.          43 py 114.99
257.          44 py -29.79
258.          45 px 335.52
259.          46 cx 20.35
260.          47 c/x 43.54 0 22.225
261.     c  48 c/x 43.54 0 23.18
262.     c Core and Reflector
263.          93 c/z 0 -35.3 27 $Core
264.          94 c/z 0 -35.3 53 $Reflector
265.          95 pz 19.05 $Top core and reflector
266.          96 pz -19.05 $Bottom core and reflector
267.          97 cx 8.3 $1st Al tube
268.     c  99 px 62.2 $Right end Al tube
```

243

```
269.        c Steel Plate, Lead Plate, and Gamma Shutter
270.          500 px 341.55
271.        c  501 py 114.99
272.        c  502 py -37.41
273.        c  503 pz 30.2
274.        c  504 pz -44.1
275.        c  505 cx 19.41
276.        c Neutron Beam Shutter
277.          61 py -60.96
278.          62 py -22.86 $Neutron shutter block left
279.          63 py 22.86 $Neutron shutter block right
280.          64 py 60.96
281.          65 pz -68.23
282.          66 pz -19.97
283.          67 pz 20 $Neutron shutter block bottom
284.          68 pz 68.23 $Neutron shutter block top
285.          69 pz 51.7
286.          699 px 362.19 $End of neutron shutter
287.        c  698 pz 28.26 $To use when neutron shutter close
288.        c Light-Tight Box
289.          801 px 500
290.          81 px 500.635
291.          82 px 530.48
292.          802 px 531.12
293.          83 py -86
294.          803 py -86.635
295.          84 py 15.24
296.          804 py 15.875
297.          85 pz 12.7
298.          805 pz 13.34
299.          86 pz -15.24
300.          806 pz -15.875
301.        c Tally
302.          87 cx 2.711 $Tally for dose
303.        c  807 px 501 $Front surface for tally or MCP area
304.          808 px 503 $End surface for tally or MCP area
305.          88 py -65 $Right surface for CCD
306.          89 c/y 515 0 5 $CCD
307.          815  s  515.57  0  0  1  $Tally sphere 1
308.          816  s  515.57  -20  0  1  $Tally sphere 2
309.          817  s  515.57 -45 0  1  $Tally sphere 3
310.          818  s  505  -45  0  1  $Tally sphere 4
311.          819  s  505  -70  0  1  $Tally sphere 5
312.          820  s  525  -70  0  1  $Tally sphere 6
313.        c Light-Tight Box Shielding
314.          810 py -35
315.          811 py -40.08
316.          812 c/y 515 0 3.175 $Hole in lead shieding
317.          813 px 499.365 $Front of boron flex
318.          814 py -55 $Right of boron flex
319.        c Simulated Part to be Radiographed
320.          900 sx 480 2 $Simulated sample
321.        c Tallying Spheres (Robot)
322.        c  901 s 480 56 -60.5 8 $Surface for tallying
323.        c  902 s 480 56 -44.5 8
324.        c  903 s 480 56 -28.5 8
325.        c  904 s 480 56 -12.5 8
```

244

```
326.    c  905 s 480 56 0 4.5
327.    c  906 s 480 47 0 4.5
328.    c  907 s 480 38 0 4.5
329.    c  908 s 480 29 0 4.5
330.    c  909 s 480 20 0 4.5
331.       910 c/z 480 56 10
332.       911 pz -51
333.       912 pz -64
334.       913 pz -36.3
335.       914 c/z 480 56 8
336.       915 pz -21.6
337.       916 c/z 480 56 8
338.       917 pz -5.4
339.       918 c/z 480 56 8
340.       919 py 56
341.       920 c/y 480 0 5.4
342.       921 py 40
343.       922 c/y 480 0 5.4
344.       923 py 23
345.       924 c/y 480 0 5.4
346.       925 py 6
347.    c Table Surface
348.       926 rpp 455 505 31 81 -69 -64
349.
350.    c ----------------------------------------------------------------
351.    c                 Data Card Specifications
352.    c ----------------------------------------------------------------
353.       mode n p $Specifies what particles might be created and tracked
354.    c Materials Cards (material name and #; atomic number followed by atomic mass; nuclide fra
    ction)
355.    c Air
356.       m1  8016          -0.23
357.           7014          -0.77
358.    c Al
359.       m2  13027         -0.9685
360.           26000.50c     -0.0070
361.           29000.50c     -0.0025
362.           14000.60c     -0.0060
363.           12000.66c     -0.0110
364.           24000.50c     -0.0035
365.           25055         -0.0015
366.    c Water
367.       m3  1001          0.66667
368.           8016          0.33333
369.       mt3 lwtr.60t $294K cme
370.    c Bi
371.       m4  83209.50c      1
372.    c Concrete 2.35
373.       m5  1001.50c       0.104
374.           8016.50c       0.583
375.           11023.51c      0.014
376.           12000.51c      0.002
377.           13027.50c      0.032
378.           14000.51c      0.211
379.           16032.51c      0.001
380.           19000.51c      0.01
381.           20000.51c      0.039
```

```
382.            26000.55c      0.004
383.      c Iron
384.        m6  26000.55c    1
385.      c B4C
386.        m7  5010         0.1584
387.            5011         0.6416
388.            6012.50      0.2
389.      c Lead
390.        m9  82000.42c     -1
391.      c Graphite (Carbon)
392.        m10 6000         1
393.        mt10 grph.60t                      $ 294K cme
394.      c Borated Poly (0.95)
395.        m12 5010.50c      -0.00916
396.            5011.50c      -0.04084
397.            6000.50c      -0.8135
398.            1001.50c      -0.1365
399.      c Boron/Flex, 1.64 g/cm^3
400.        m14 1001.50c       0.5378
401.            5010.50c       0.0976
402.            5011.50c       0.03645
403.        mt14   smeth.01t$1wtr.60t
404.      c Stainless Steel (Structural) type 304
405.        m15 26000.50c     -0.6785
406.            6000         -0.0080
407.            14000.60c     -0.0100
408.            24000.50c     -0.1800
409.            28000.50c     -0.0980
410.            25055        -0.0180
411.            15031        -0.0045
412.            16000.66c     -0.0030
413.      c Human
414.        m16 8016.50c      -0.762
415.            6012.50c      -0.111
416.            1001.50c      -0.101
417.            7014.50c      -0.026
418.      c Source Definition
419.      c Source Location: Close to Beam Exit
420.        sdef sur=45 erg=d1 tme=0 wgt=1 par=1 pos=335.52 0 0 rad=d2 dir=d3
421.        si1 h 1e-10 1e-8 1e-7 4e-7 1e-6 1e-5 1e-4 1e-3 1e-2 1e-1 1 20
422.        sp1 d 0 1.43e-6 3.45e-5 7.15e-6 1.16e-6 2.90e-6 2.57e-6 3.25e-6
423.                        2.66e-6 4.32e-6 6.16e-6 6.78e-6 $Spectrum with moderator
424.        si2 19.3
425.        si3 h 0 0.9992 1.0
426.        sp3 d 0 0.0001 0.9999
427.      c Number of Particles to Run
428.        nps 1E+5 $Number of particle histories
429.      c  fir5:n 532.1 0 0 0 335.52 0 0 0 0 0 $Neutron radiography tally
430.      c  fs5 -2.5  9i 2.5 $Radiograph vertical resolution
431.      c  c5 -2. 9i 2. $Radiograph horizontal resolution
432.        prdmp 0 0 1
433.      c Photon dose over a cell
434.        f34:p 81 82 900 910 914 916 918 920 922 924
435.        fc34 Photon Tally for Calculation of Photon Dose (Kerma)
436.        de34 1.00E-02 3.00E-02 5.00E-02 7.00E-02 1.00E-01 1.50E-01
437.             2.00E-01 2.50E-01 3.00E-01 0.35 0.4 0.45 0.5 0.55 0.6
438.             0.65 0.7 0.8 1.0 1.4 1.8 2.2 2.6 2.8 3.25 3.75 4.25 4.75
```

```
439.         5.0 5.25 5.75 6.25 6.75 7.5 9.0 11.0 13.0 15.0 $Dose energy
440.      df34 3.96E-06 5.82E-07 2.90E-07 2.58E-07 2.83E-07 3.79E-07
441.           5.01E-07 6.31E-07 7.59E-07 8.78E-07 9.85E-07 1.08E-06
442.           1.17E-06 1.27E-06 1.36E-06 1.44E-06 1.52E-06 1.68E-06
443.           1.98E-06 2.51E-06 2.99E-06 3.42E-06 3.82E-06 4.01E-06
444.           4.41E-06 4.83E-06 5.23E-06 5.60E-06 5.80E-06 6.01E-06
445.           6.37E-06 6.74E-06 7.11E-06 7.66E-06 8.77E-06 1.03E-05
446.           1.18E-05 1.33E-05 $Dose function
447.     c Neutron fluxes
448.      f14:n 81 82 900 910 914 916 918 920 922 924
449.      fc14 Neutron Flux Tally
450.      e14     1.000E-11 5.000E-09 1.000E-08 1.500E-08 2.000E-08 2.500E-08
451.              3.000E-08 3.500E-08 4.200E-08 5.000E-08 5.800E-08 6.700E-08
452.              8.000E-08 1.000E-07 1.520E-07 2.510E-07 4.140E-07 6.830E-07
453.              1.125E-06 1.855E-06 3.059E-06 5.040E-06 8.315E-06 1.371E-05
454.              2.260E-05 3.727E-05 6.144E-05 1.013E-04 1.670E-04 2.754E-04
455.              4.540E-04 7.485E-04 1.234E-03 2.035E-03 2.404E-03 2.840E-03
456.              3.355E-03 5.531E-03 9.119E-03 1.503E-02 1.989E-02 2.554E-02
457.              4.087E-02 6.738E-02 1.111E-01 1.832E-01 3.020E-01 3.887E-01
458.              4.979E-01 6.392E-01 8.208E-01 1.108 1.353 1.737
459.              2.231 2.865 3.678 4.965 6.065 10.0
460.              14.91 16.90 20.00 25.00 T
461.     c Neutron energy deposited/g averaged over a cell
462.      f106:n 900
463.      f116:n 910
464.      f126:n 914
465.      f136:n 916
466.      f146:n 918
467.      f156:n 920
468.      f166:n 922
469.      f176:n 924
```

A.2   BP5 SIMPLIFIED INPUT FILE

This is the simplified MCNP input deck of BP5 of the TRIGA MARK II research reactor at U.T. Austin. It defines a radiation-damage model for a robot exposed to neutron radiation from BP5 and can be used to determine DPA rates in the robot.

```
1.  DPA Robot
2.  c Defines a radiation-damage model for a robot exposed to
3.  c neutron radiation from TRIGA beamport 5.
4.  c
5.  c Cell Cards
6.  c ==========
7.  1   1 -0.001205 -102  203 IMP:N=1 $ air inside walls
8.  2   2 -2.300000 -101  102 IMP:N=1 $ concrete walls
9.  3   3 -2.690000 -201  202 IMP:N=1 $ outer layer of robot
10. 4   4 -2.764047 -202      IMP:N=1 $ inner layer of robot
11. 5   5 -1.000000  201 -203 IMP:N=1 $ robot shield
12. c 5   1 -0.001205  201 -203 IMP:N=1 $ robot shield (air = no shield)
13. 999 0           101       IMP:N=0 $ graveyard
14.
```

```
15. c Surface Cards
16. c =============
17. c Outer surfaces of walls, floor, ceiling
18. 101 RPP -300.0 300.0 -165.0 165.0 -110.0 110.0
19. c Inner surfaces of walls, floor, ceiling
20. 102 RPP -300.0 299.6 -164.6 164.6 -70.0 70.0
21. c Outer surface of robot
22. 201 RCC 0.0 0.0 -35.0 0.0 0.0 70.0 8.0
23. c Inner surface of robot
24. 202 RCC 0.0 0.0 -35.0 0.0 0.0 70.0 4.0
25. c Outer surface of robot shield
26. 203 RCC 0.0 0.0 -35.0 0.0 0.0 70.0 11.372
27.
28. c Data Cards
29. c ==========
30. c  --- Material Cards
31. M1    6000 -0.000124  $ Air for void region
32.       7014 -0.755268  $ rho = 0.001205 g/cc
33.       8016 -0.231781  $ Taken from PNNL-15870
34.      18000 -0.012827
35. M2    1001 -0.010000  $ Regular concrete for walls and floor
36.       8016 -0.532000  $ rho = 2.300000 g/cc
37.      11023 -0.029000  $ Taken from PNNL-15870
38.      13027 -0.034000
39.      14000 -0.337000
40.      20000 -0.044000
41.      26000 -0.014000
42. M3   29063 -0.027668  $ AC4C-T6 Al Alloy for robot exterior
43.      29065 -0.012332  $ rho = 2.690000 g/cc
44.      14028 -0.064100
45.      14029 -0.003246
46.      14030 -0.002155
47.      12000 -0.400000
48.      26054 -0.010521
49.      26056 -0.165157
50.      26057 -0.003814
51.      26058 -0.000508
52.      25055 -0.040000
53.      24050 -0.008690
54.      24052 -0.167578
55.      24053 -0.019002
56.      24054 -0.004730
57.      13027 -0.921900
58. M4    1001 -0.019149  $ Robot internals composition
59.       6000 -0.137684  $ rho = 2.764047 g/cc
60.       7014 -0.270883
61.       8016 -0.161070
62.      14028 -0.092330
63.      14029 -0.004670
64.      14030 -0.003100
65.      17000 -0.056726
66.      18000 -0.004489
67.      26054 -0.005845
68.      26056 -0.091754
69.      26057 -0.002119
70.      26058 -0.000282
71.      28058 -0.068077
```

248

```
72.       28060 -0.026233
73.       28061 -0.001140
74.       28062 -0.003634
75.       28064 -0.000926
76.       29063 -0.034585
77.       29065 -0.015415
78. M5     1001 -0.125355  $ borated polyethylene shield for robot
79.        5010 -0.100000  $ rho = 1.000000
80.        6000 -0.774645  $ from PNNL-15870
81. M6    13027 -1.000000  $ pure aluminum for tally
82. M7    14028 -0.922300  $ pure silicon for tally
83.       14029 -0.046700
84.       14030 -0.031000
85. M8    26054 -0.058450  $ pure iron for tally
86.       26056 -0.917540
87.       26057 -0.021190
88.       26058 -0.002820
89. M9    29063 -0.691700  $ pure copper for tally
90.       29065 -0.308300
91. M10   28058 -0.680770  $ pure nickel for tally
92.       28060 -0.262330
93.       28061 -0.011400
94.       28062 -0.036340
95.       28064 -0.009260
96. c
97. c --- Source cards
98. MODE N
99. NPS 1000000
100.        talnp
101.        prdmp 0 0 1
102.        c TRIGA BP5 source distribution
103.        sdef erg=d1 tme=0 wgt=1 par=1 pos=-300 0 0 rad=d2 dir=d3
104.             ext=0 axs=1 0 0 vec=1 0 0
105.        si1 h 1e-10 1e-8 1e-7 4e-7 1e-6 1e-5 1e-4 1e-3 1e-2 1e-1 1 20
106.        sp1 d 0 1.43e-6 3.45e-5 7.15e-6 1.16e-6 2.90e-6 2.57e-6 3.25e-6
107.             2.66e-6 4.32e-6 6.16e-6 6.78e-6
108.        si2 19.3
109.        si3 h 0 0.9992 1.0
110.        sp3 d 0 0.0001 0.9999
111.        c
112.        c --- Tallies
113.        F14:N 3
114.        FM14 (1 6 444)
115.        FC14 Al Shell Damage
116.        F24:N 3
117.        FM24 (1 7 444)
118.        FC24 Si Shell Damage
119.        F34:N 3
120.        FM34 (1 8 444)
121.        FC34 Fe Shell Damage
122.        F44:N 4
123.        FM44 (1 7 444)
124.        FC44 Si Inner Damage
125.        F54:N 4
126.        FM54 (1 8 444)
127.        FC54 Fe Inner Damage
128.        F64:N 4
```

249

```
129.        FM64 (1 9 444)
130.        FC64 Cu Inner Damage
131.        F74:N 4
132.        FM74 (1 10 444)
133.        FC74 Ni Inner Damage
134.        c MESH TALLIES
135.        c ============
136.        c Mesh tallies are used to visualize energy deposition throughout the
137.        c  volumes of the problem.
138.        c Since the default cylindrical mesh tally is about the z-axis, no
139.        c  transformation card is required.
140.        c
141.        c XY
142.        FMESH104:N GEOM=xyz ORIGIN= -250 -40 -50
143.                      IMESH= 250 IINTS= 99 $x
144.                      JMESH= 40 JINTS= 99  $y
145.                      KMESH= 50 KINTS= 1   $z
146.        c ZX
147.        FMESH204:N GEOM=xyz ORIGIN= -250 -60 -40
148.                      IMESH= 250 IINTS= 99 $x
149.                      JMESH= 60 JINTS= 1   $y
150.                      KMESH= 40 KINTS= 99   $z
151.        c YZ
152.        FMESH304:N GEOM=xyz ORIGIN= -250 -30 -30
153.                      IMESH= 250 IINTS= 1 $x
154.                      JMESH= 30 JINTS= 99  $y
155.                      KMESH= 30 KINTS= 99   $z
156.        c
157.        FM104 (630720 3 444)
158.        FM204 (630720 3 444)
159.        FM304 (630720 3 444)
```

APPENDIX B: ROS CODES FOR NDT APPLICATIONS

B.1 CT

This ROS program was written in C++ and was used for the motion control of the

robotic part positing system for CT applications.

```cpp
1.   #include <ros/ros.h>
2.   #include <ros/package.h>
3.   #include <moveit/move_group_interface/move_group.h>
4.   #include <geometric_shapes/shape_operations.h>
5.   #include <moveit/robot_state/conversions.h>
6.   #include <workcell_interface/workcell_interface.h>
7.   #include <std_msgs/Int8.h>
8.   #include <assembly/tool_status.h>
9.   #include <manipulator_xml_functions/src/manipulator_xml_functions.cpp>
10.  #include <fstream>
11.  #include "std_msgs/String.h"
12.
13.  manip_xml_func::GraspMap grasp_map;
14.  manip_xml_func::PoseMap tool_storage;
15.  assembly::tool_status tool_state;
16.
17.  bool assembly_init();
18.
19.  const double PI = 4.0*atan(1.0);
20.
21.  int main(int argc, char** argv)
22.  {
23.      if(argc < 3)
24.      {
25.          std::cout << "Too few arguments to radiography app. Usage: assembly_main bool  use_gripper
     _interface, double ct_increment" << std::endl;
26.          return false;
27.      }
28.
29.      ros::init(argc, argv, "ctScan");
30.      ros::NodeHandle n;
31.
32.      ros::Publisher status_pub = n.advertise<std_msgs::Int8>("assembly_status", 10);
33.      ros::Publisher chatter_pub = n.advertise<std_msgs::String>("chatter", 1000);
34.      std_msgs::Int8 status;
35.      std_msgs::Bool stop;
36.      stop.data = true;
37.      status.data = 0;
38.      status_pub.publish(status);
39.
40.      trajectory_msgs::JointTrajectory dummy_traj;
41.      trajectory_msgs::JointTrajectoryPoint point;
42.      ros::Time start_time, time_last;
43.
44.      ros::AsyncSpinner spinner(1);
```

```cpp
45.     spinner.start();
46.
47.     //Set up workcell interface
48.     WorkcellInterface workcell("sia5d");
49.     workcell.Init(n, atoi(argv[1]), "set_changer", "set_gripper");
50.
51.     double ct_increment = atof(argv[2])*PI/180;;
52.
53.     //set up joint jogging.
54.     dummy_traj.joint_names = workcell.arm->getJoints();
55.     point.positions = workcell.arm->getCurrentJointValues();
56.     dummy_traj.points.push_back(point);
57.
58.     ros::Subscriber cancel_sub = n.subscribe("assembly/safe_stop", 1, &WorkcellInterface::SafeStop
    , &workcell);
59.
60.     ros::Publisher streaming_pub = n.advertise<trajectory_msgs::JointTrajectory>("joint_command",
    10);
61.
62.     //Call init function to get application stuff set up.
63.     if (!assembly_init() )
64.         return 1; // failure
65.
66.     //Set the tolerance that is used for reaching the goal
67.     workcell.arm->setGoalTolerance(0.00000001);
68.
69.     //Get the tool.
70.     if(!workcell.tool_equipped){
71.         if(!workcell.EquipTool("gripper", grasp_map["gripper"]))
72.         {
73.             ROS_INFO("Unable to perform pick maneuver.");
74.             status.data = -1;
75.             status_pub.publish(status);
76.             workcell.SafeStop(stop);
77.             //workcell.GenerateReport("tool_equip");
78.             return 0;
79.         }
80.     }
81.     ros::Duration(0.5).sleep();
82.
83.     //Get the part.
84.     if(!workcell.Pick("pin_tool", grasp_map["pin_tool"]))
85.     {
86.         ROS_INFO("Unable to perform pick maneuver.");
87.         status.data = -1;
88.         status_pub.publish(status);
89.         workcell.SafeStop(stop);
90.         workcell.GenerateReport("hemi_pick");
91.         return 0;
92.     }
93.
94.     //Perform CT Scan
95.     workcell.UpdateRobotState();
96.
97.     sleep(1);
98.
99.     std::cout << "Moving Joint 7 to -180 degrees." << std::endl;
```

```
100.            double theta_i = -180 * (PI/180); //-180 degrees
101.
102.            workcell.arm->setJointValueTarget("joint_t", theta_i);
103.            if(!workcell.arm->move())
104.            {
105.                ROS_INFO("Failure during move to folded pose.");
106.                status.data = -1;
107.                status_pub.publish(status);
108.                workcell.SafeStop(stop);
109.                workcell.GenerateReport("robot_folded");
110.                return 0;
111.            }
112.            sleep(2);
113.            //CT Scan
114.            std::cout << "Performing CT Scan from -180 to 180 degrees" << std::endl;
115.            int num_points = 4;
116.            double radians = -PI;//radians
117.            double sub_delta = ct_increment/num_points;
118.            point.velocities.resize(7);
119.            point.velocities.at(6) = 0.6; //We're going for about 0.6 rad/s.
120.            double dt = sub_delta/point.velocities.at(6);
121.            std::vector<double> joints(7);
122.
123.            std::cout << "Acquire first image. Press 'Enter' when done to continue" << std::endl;

124.            std::cin.ignore();
125.
126.            while(radians < PI)
127.            {
128.                std::cout << "radians: " << radians << std::endl;
129.                start_time = ros::Time::now();
130.                joints = workcell.arm->getCurrentJointValues();
131.                std::cout << "current joint value: " << joints.at(6) * (180/PI) << std::endl; //de
grees
132.                radians = radians + ct_increment;
133.                //Everything below here is new for small joint deltas:////////////////////////////
134.                //Jog joint 7 to 'radians'...
135.                //We'll divide the move into 4 points, and stream them at
136.                joints = workcell.arm->getCurrentJointValues();
137.                for(unsigned int i=0; i<num_points; i++)
138.                {
139.                    point.positions.at(6) = joints.at(6)+i*sub_delta;
140.                    point.time_from_start = ros::Duration(i*dt);
141.                    dummy_traj.points.at(0) = point;
142.                    streaming_pub.publish(dummy_traj);
143.                }
144.                point.positions.at(6) = radians;
145.                point.time_from_start = ros::Duration(num_points*dt);
146.                dummy_traj.points.at(0) = point;
147.                streaming_pub.publish(dummy_traj);
148.                sleep(2);
149.                /**
150.                * This is a message object. You stuff it with data, and then publish it.
151.                */
152.                std_msgs::String msg;
153.
154.                std::stringstream ss;
```

```
155.            ss << "acquire image ";
156.            msg.data = ss.str();
157.            /**
158.             * The publish() function is how you send messages. The parameter
159.             * is the message object. The type of this object must agree with the type
160.             * given as a template parameter to the advertise<>() call, as was done
161.             * in the constructor above.
162.             */
163.            chatter_pub.publish(msg);
164.
165.            ros::spinOnce();
166.
167.            ROS_INFO("%s", msg.data.c_str());
168.
169.
170.            ros::Duration(1.0+1.25*point.time_from_start.toSec()).sleep();
171.        }
172.        joints = workcell.arm->getCurrentJointValues();
173.        std::cout << "current joint value: " << joints.at(6) * (180/PI) << std::endl; //degree
    s
174.        sleep(2);
175.    }
176.    status.data = 1;
177.    status_pub.publish(status);
178.
179.    sleep(2.0);
180.    spinner.stop();
181.    return 0;
182.
183.    bool assembly_init()
184.    {
185.
186.        std::string ros_package_path = ros::package::getPath("assembly");
187.        if (ros_package_path.empty()) {
188.            ROS_FATAL("Package path not found");
189.            return false;
190.        }
191.
192.        //Set up grasp map from XML file
193.        std::string file_name = "assembly_main_grasps.xml";
194.        std::string file_path = ros_package_path + "/data/" + file_name;
195.        if ( !manip_xml_func::LoadGraspsXML(file_path.c_str(), grasp_map) )
196.            return false;
197.
198.        //Set up tool storage pose map from text file
199.        file_name = "assembly_main_poses";
200.        file_path = ros_package_path + "/data/" + file_name;
201.        if ( !manip_xml_func::LoadPosesTextFile(file_path.c_str(), tool_storage) )
202.            return false;
203.
204.        return true;
205.    }
```

B.2   HELICAL SCAN

This ROS program was written in C++ and was used for the motion control of the

robotic part positing system for helical scans.

```cpp
1.  #include <ros/ros.h>
2.  #include <ros/package.h>
3.  #include <moveit/move_group_interface/move_group.h>
4.  #include <geometric_shapes/shape_operations.h>
5.  #include <moveit/robot_state/conversions.h>
6.  #include <workcell_interface/workcell_interface.h>
7.  #include <std_msgs/Int8.h>
8.  #include <assembly/tool_status.h>
9.  #include <manipulator_xml_functions/src/manipulator_xml_functions.cpp>
10. #include <fstream>
11. #include "std_msgs/String.h"
12.
13. manip_xml_func::GraspMap grasp_map;
14. manip_xml_func::PoseMap tool_storage;
15. assembly::tool_status tool_state;
16.
17. bool assembly_init();
18.
19. const double PI = 4.0*atan(1.0);
20.
21. // Rotate a geometry_msgs::Pose about some axis by some angle
22. geometry_msgs::Pose Rotate_Pose(geometry_msgs::Pose starting_pose, std::string direction, double angle)
23. {
24.     tf::Matrix3x3 m;
25.     if(direction == "x")
26.     {
27.         m.setValue(1, 0, 0, 0, cos(angle), -sin(angle), 0, sin(angle), cos(angle));
28.     }
29.     else if (direction == "y")
30.     {
31.         m.setValue(cos(angle), 0, sin(angle), 0, 1, 0, -sin(angle), 0, cos(angle));
32.     }
33.     else if (direction == "z")
34.     {
35.         m.setValue(cos(angle), -sin(angle), 0, sin(angle), cos(angle), 0, 0, 0, 1);
36.     }
37.     tf::Vector3 starting_pose_pos(starting_pose.position.x, starting_pose.position.y, starting_pose.position.z);
38.     tf::Quaternion starting_pose_quat;
39.     tf::quaternionMsgToTF(starting_pose.orientation, starting_pose_quat);
40.     tf::Matrix3x3 starting_matrix(starting_pose_quat);
41.     tf::Matrix3x3 return_matrix = starting_matrix*m;
42.     tf::Transform return_tf(return_matrix, starting_pose_pos);
43.     geometry_msgs::Pose return_pose;
44.     tf::poseTFToMsg(return_tf, return_pose);
45.
46.     return return_pose;
```

```cpp
47. }
48.
49. int main(int argc, char** argv)
50. {
51.     if(argc < 3)
52.     {
53.         std::cout << "Too few arguments to radiography app. Usage: assembly_main bool  use_gripper
    _interface, double ct_increment" << std::endl;
54.         return false;
55.     }
56.
57.     ros::init(argc, argv, "helicalScan");
58.     ros::NodeHandle n;
59.
60.     ros::Publisher status_pub = n.advertise<std_msgs::Int8>("assembly_status", 10);
61.     ros::Publisher chatter_pub = n.advertise<std_msgs::String>("chatter", 1000);
62.     std_msgs::Int8 status;
63.     std_msgs::Bool stop;
64.     stop.data = true;
65.     status.data = 0;
66.     status_pub.publish(status);
67.
68.     ros::AsyncSpinner spinner(1);
69.     spinner.start();
70.
71.     //Set up workcell interface
72.     WorkcellInterface workcell("sia5d");
73.     workcell.Init(n, atoi(argv[1]), "set_changer", "set_gripper");
74.
75.     ros::Subscriber cancel_sub = n.subscribe("assembly/safe_stop", 1, &WorkcellInterface::SafeStop
    , &workcell);
76.
77.     ros::Publisher streaming_pub = n.advertise<trajectory_msgs::JointTrajectory>("joint_command",
    10);
78.
79.     //Call init function to get application stuff set up.
80.     if (!assembly_init() )
81.         return 1; // failure
82.
83.     //Set the tolerance that is used for reaching the goal
84.     workcell.arm->setGoalTolerance(0.00000001);
85.
86.     //Get the tool.
87.     if(!workcell.tool_equipped){
88.         if(!workcell.EquipTool("gripper", grasp_map["gripper"]))
89.         {
90.             ROS_INFO("Unable to perform pick maneuver.");
91.             status.data = -1;
92.             status_pub.publish(status);
93.             workcell.SafeStop(stop);
94.             //workcell.GenerateReport("tool_equip");
95.             return 0;
96.         }
97.     }
98.     ros::Duration(0.5).sleep();
99.
100.             //Get the hemishell.
```

```
101.          if(!workcell.Pick("pin_tool", grasp_map["pin_tool"]))
102.          {
103.              ROS_INFO("Unable to perform pick maneuver.");
104.              status.data = -1;
105.              status_pub.publish(status);
106.              workcell.SafeStop(stop);
107.              workcell.GenerateReport("hemi_pick");
108.              return 0;
109.          }
110.
111.          //Start Helical Scan
112.          double jointTol = 0;
113.          double orienTol = 0;
114.          double posTol = 0;
115.          jointTol = workcell.arm->getGoalJointTolerance();
116.          std::cout << "jointTol " << jointTol << std::endl;
117.          orienTol = workcell.arm->getGoalOrientationTolerance();
118.          std::cout << "orienTol " << orienTol << std::endl;
119.          posTol = workcell.arm->getGoalPositionTolerance();
120.          std::cout << "posTol " << posTol << std::endl;
121.
122.
123.          std::cout << "Moving to beam position." << std::endl;
124.          std::vector<double> joints_folded;
125.          for(unsigned int i=0; i<7; i++)
126.          {
127.              joints_folded.push_back(0.0);
128.          }
129.          joints_folded.at(0) = -6.52479 * (PI/180);
130.          joints_folded.at(1) = 27.5724 * (PI/180);
131.          joints_folded.at(2) = -17.0917 * (PI/180);
132.          joints_folded.at(3) = -52.6552 * (PI/180);
133.          joints_folded.at(4) = 21.7508 * (PI/180);
134.          joints_folded.at(5) = 82.8236 * (PI/180);
135.          joints_folded.at(6) = PI;
136.
137.          workcell.arm->setJointValueTarget(joints_folded);
138.          if(!workcell.arm->move())
139.          {
140.              ROS_INFO("Failure during move to folded pose.");
141.              status.data = -1;
142.              status_pub.publish(status);
143.              workcell.SafeStop(stop);
144.              workcell.GenerateReport("robot_folded");
145.              return 0;
146.          }
147.
148.          int counter = 0;
149.          double phi=0;
150.          std::cout << "Enter rotation desired in degrees." << std::endl;
151.          std::cin >> phi;
152.
153.          double translate=0;
154.          std::cout << "Translate EEF by ____ mm at each step?" << std::endl;
155.          std::cin >> translate;
156.          translate = translate / 1000;
157.
```

```cpp
158.            std::vector<double> joints = workcell.arm->getCurrentJointValues();
159.            geometry_msgs::PoseStamped pose = workcell.arm->getCurrentPose("link_t");
160.            int value = 0;
161.
162.            while(phi * (counter +1) <= 360)
163.            {
164.                std::cout << "phi *counter+1 * pi/180 in degrees = " << phi * (counter +1) << std::
      endl;
165.                pose.pose = Rotate_Pose(pose.pose, "x", (phi * (PI/180)) );
166.                pose.pose.position.x = pose.pose.position.x-translate;
167.
168.                sleep(1);
169.
170.                double x, y, z = 0;
171.                char axisChoice;
172.
173.                geometry_msgs::PoseStamped pose_link = workcell.arm->getCurrentPose("link_t");
174.                std::cout << "Cartesian pose of x-
      direction link_t (word frame) (meters):" << std::endl;
175.                std::cout << pose_link.pose.position.x << std::endl; //quaternion
176.                std::cout << "Acquire first image. Press 'x' when done to continue" << std::endl;
177.                std::cin >> axisChoice;
178.
179.                if( axisChoice == 'x' )
180.                {
181.                    //do nothing
182.                }
183.                else
184.                {
185.                    std::cout << "You did not enter x." << std::endl;
186.                    return 0;
187.                }
188.
189.                if(!workcell.MoveArmCartesian(pose.pose))
190.                {
191.                    ROS_INFO("Unable to perform Cartesian-interpolated move.");
192.                    return 0;
193.                }
194.                else
195.                {
196.                }
197.
198.                sleep(1);
199.
200.                counter ++;
201.            }
202.
203.            status.data = 1;
204.            status_pub.publish(status);
205.
206.            sleep(2.0);
207.            spinner.stop();
208.            return 0;
209.        }
210.
211.        bool assembly_init()
212.        {
```

```
213.
214.        std::string ros_package_path = ros::package::getPath("assembly");
215.        if (ros_package_path.empty()) {
216.            ROS_FATAL("Package path not found");
217.            return false;
218.        }
219.
220.        //Set up grasp map from XML file
221.        std::string file_name = "assembly_main_grasps.xml";
222.        std::string file_path = ros_package_path + "/data/" + file_name;
223.        if ( !manip_xml_func::LoadGraspsXML(file_path.c_str(), grasp_map) )
224.            return false;
225.
226.        //Set up tool storage pose map from text file
227.        file_name = "assembly_main_poses";
228.        file_path = ros_package_path + "/data/" + file_name;
229.        if ( !manip_xml_func::LoadPosesTextFile(file_path.c_str(), tool_storage) )
230.            return false;
231.
232.        return true;
233.    }
```

B.3 REAL-TIME VISION SYSTEM

The following C++ and python code were used for the object localization and tracking system.

ar_kinect.cpp (modified from https://github.com/mikeferguson/ar_kinect)

```
1.  /*
2.   *  Multi Marker Pose Estimation using ARToolkit & Kinect
3.   *  Copyright (C) 2010, CCNY Robotics Lab, 2011 ILS Robotics Lab
4.   *  Ivan Dryanovski <ivan.dryanovski@gmail.com>
5.   *  William Morris <morris@ee.ccny.cuny.edu>
6.   *  Gautier Dumonteil <gautier.dumonteil@gmail.com>
7.   *  http://robotics.ccny.cuny.edu
8.   *
9.   *  Michael Ferguson <ferguson@cs.albany.edu>
10.  *  http://robotics.ils.albany.edu
11.  *
12.  *  This program is free software: you can redistribute it and/or modify
13.  *  it under the terms of the GNU General Public License as published by
14.  *  the Free Software Foundation, either version 3 of the License, or
15.  *  (at your option) any later version.
16.  *
17.  *  This program is distributed in the hope that it will be useful,
18.  *  but WITHOUT ANY WARRANTY; without even the implied warranty of
19.  *  MERCHANTABILITY or FITNESS FOR A PARTICULAR PURPOSE.  See the
20.  *  GNU General Public License for more details.
21.  *
22.  *  You should have received a copy of the GNU General Public License
23.  *  along with this program.  If not, see <http://www.gnu.org/licenses/>.
24.  */
```

```
25.
26. #include <math.h>
27. #include "ar_kinect/ar_kinect.h"
28. #include "ar_kinect/object.h"
29.
30. int main (int argc, char **argv)
31. {
32.    ros::init (argc, argv, "ar_kinect");
33.    ros::NodeHandle n;
34.    ar_pose::ARPublisher ar_kinect (n);
35.    ros::spin ();
36.    return 0;
37. }
38.
39. namespace ar_pose
40. {
41.    tf::Transform tfFromEigen(Eigen::Matrix4f trans)
42.    {
43.      tf::Matrix3x3 btm;
44.      btm.setValue(trans(0,0),trans(0,1),trans(0,2),
45.                   trans(1,0),trans(1,1),trans(1,2),
46.                   trans(2,0),trans(2,1),trans(2,2));
47.      tf::Transform ret;
48.      ret.setOrigin(tf::Vector3(trans(0,3),trans(1,3),trans(2,3)));
49.      ret.setBasis(btm);
50.      return ret;
51.    }
52.
53.    pcl::PointXYZRGB makeRGBPoint( float x, float y, float z )
54.    {
55.      pcl::PointXYZRGB p;
56.      p.x = x;
57.      p.y = y;
58.      p.z = z;
59.      return p;
60.    }
61.
62.    ARPublisher::ARPublisher (ros::NodeHandle & n):n_ (n), configured_(false)
63.    {
64.      std::string path;
65.      std::string package_path = ros::package::getPath (ROS_PACKAGE_NAME);
66.      ros::NodeHandle n_param ("~");
67.      XmlRpc::XmlRpcValue xml_marker_center;
68.
69.      // **** get parameters
70.
71.      if (!n_param.getParam ("publish_tf", publishTf_))
72.        publishTf_ = true;
73.      ROS_INFO ("\tPublish transforms: %d", publishTf_);
74.
75.      if (!n_param.getParam ("publish_visual_markers", publishVisualMarkers_))
76.        publishVisualMarkers_ = true;
77.      ROS_INFO ("\tPublish visual markers: %d", publishVisualMarkers_);
78.
79.      if (!n_param.getParam ("threshold", threshold_))
80.        threshold_ = 100;
81.      ROS_INFO ("\tThreshold: %d", threshold_);
```

```
82.
83.    if (!n_param.getParam ("marker_pattern_list", path)){
84.       sprintf(pattern_filename_, "%s/data/objects_kinect", package_path.c_str());
85.    }else{
86.       sprintf(pattern_filename_, "%s", path.c_str());
87.    }
88.    ROS_INFO ("Marker Pattern Filename: %s", pattern_filename_);
89.
90.    if (!n_param.getParam ("marker_data_directory", path)){
91.       sprintf(data_directory_, "%s", package_path.c_str());
92.    }else{
93.       sprintf(data_directory_, "%s", path.c_str());
94.    }
95.    ROS_INFO ("Marker Data Directory: %s", data_directory_);
96.
97.    // **** subscribe
98.
99.    configured_ = false;
100.        cloud_sub_ = n_.subscribe(cloudTopic_, 1, &ARPublisher::getTransformationCallback, thi
   s);
101.
102.        // **** advertise
103.
104.        arMarkerPub_ = n_.advertise < ar_pose::ARMarkers > ("ar_pose_markers",0);
105.        if(publishVisualMarkers_)
106.        {
107.            rvizMarkerPub_ = n_.advertise < visualization_msgs::Marker > ("visualization_marke
   r", 0);
108.        }
109.    }
110.
111.        ARPublisher::~ARPublisher (void)
112.        {
113.          arVideoCapStop ();
114.          arVideoClose ();
115.        }
116.
117.        /*
118.         * Setup artoolkit
119.         */
120.        void ARPublisher::arInit ()
121.        {
122.          arInitCparam (&cam_param_);
123.          ROS_INFO ("*** Camera Parameter ***");
124.          arParamDisp (&cam_param_);
125.
126.          // load in the object data - trained markers and associated bitmap files
127.          if ((object = ar_object::read_ObjData (pattern_filename_, data_directory_, &objectnum)
   ) == NULL)
128.             ROS_BREAK ();
129.          ROS_DEBUG ("Objectfile num = %d", objectnum);
130.
131.          sz_ = cvSize (cam_param_.xsize, cam_param_.ysize);
132.          capture_ = cvCreateImage (sz_, IPL_DEPTH_8U, 4);
133.          configured_ = true;
134.        }
135.
```
261

```
136.          /*
137.           * One and only one callback, now takes cloud, does everything else needed.
138.           */
139.          void ARPublisher::getTransformationCallback (const sensor_msgs::PointCloud2ConstPtr & ms
    g)
140.          {
141.            sensor_msgs::ImagePtr image_msg(new sensor_msgs::Image);
142.            ARUint8 *dataPtr;
143.            ARMarkerInfo *marker_info;
144.            int marker_num;
145.            int i, k, j;
146.
147.            /* do we need to initialize? */
148.            if(!configured_)
149.            {
150.              if(msg->width == 0 || msg->height == 0)
151.              {
152.                ROS_ERROR ("Deformed cloud! Size = %d, %d.", msg->width, msg->height);
153.                return;
154.              }
155.
156.              cam_param_.xsize = msg->width;
157.              cam_param_.ysize = msg->height;
158.
159.              cam_param_.dist_factor[0] = msg-
    >width/2;          // x0 = cX from openCV calibration
160.              cam_param_.dist_factor[1] = msg-
    >height/2;         // y0 = cY from openCV calibration
161.              cam_param_.dist_factor[2] = 0;                        // f = -
    100*k1 from CV. Note, we had to do mm^2 to m^2, hence 10^8->10^2
162.              cam_param_.dist_factor[3] = 1.0;                      // scale factor, should probably b
    e >1, but who cares...
163.
164.              arInit ();
165.            }
166.
167.            /* convert cloud to PCL & PCLPointCloud2 */
168.            PointCloud cloud;
169.            pcl::PCLPointCloud2 cloud_2;
170.            pcl_conversions::toPCL(*msg, cloud_2);
171.            pcl::fromPCLPointCloud2(cloud_2, cloud);
172.
173.            /* get an OpenCV image from the cloud */
174.            pcl::PCLImage pcl_image;
175.            pcl::toPCLPointCloud2(cloud_2, pcl_image);
176.            pcl_conversions::moveFromPCL(pcl_image, *image_msg);
177.
178.            cv_bridge::CvImagePtr cv_ptr;
179.            try
180.            {
181.                cv_ptr = cv_bridge::toCvCopy(image_msg, sensor_msgs::image_encodings::BGR8);
182.            }
183.            catch (cv_bridge::Exception& e)
184.            {
185.                ROS_ERROR ("Could not convert from '%s' to 'bgr8'.", image_msg-
    >encoding.c_str ());
186.            }
```

262

```
187.            dataPtr = (ARUint8 *) cv_ptr->image.ptr();
188.
189.            /* detect the markers in the video frame */
190.            if (arDetectMarkerLite (dataPtr, threshold_, &marker_info, &marker_num) < 0)
191.            {
192.              argCleanup ();
193.              return;
194.            }
195.
196.            arPoseMarkers_.markers.clear ();
197.            /* check for known patterns */
198.            for (i = 0; i < objectnum; i++)
199.            {
200.              k = -1;
201.              for (j = 0; j < marker_num; j++)
202.              {
203.                if (object[i].id == marker_info[j].id)
204.                {
205.                  if (k == -1)
206.                    k = j;
207.                  else                    // make sure you have the best pattern (highest confidence
      factor)
208.                    if (marker_info[k].cf < marker_info[j].cf)
209.                      k = j;
210.                }
211.              }
212.              if (k == -1)
213.              {
214.                object[i].visible = 0;
215.                continue;
216.              }
217.
218.              /* create a cloud for marker corners */
219.              int d = marker_info[k].dir;
220.              PointCloud marker;
221.              marker.push_back( cloud.at( (int)marker_info[k].vertex[(4-
      d)%4][0], (int)marker_info[k].vertex[(4-d)%4][1] ) ); // upper left
222.              marker.push_back( cloud.at( (int)marker_info[k].vertex[(5-
      d)%4][0], (int)marker_info[k].vertex[(5-d)%4][1] ) ); // upper right
223.              marker.push_back( cloud.at( (int)marker_info[k].vertex[(6-
      d)%4][0], (int)marker_info[k].vertex[(6-d)%4][1] ) ); // lower right
224.              marker.push_back( cloud.at( (int)marker_info[k].vertex[(7-
      d)%4][0], (int)marker_info[k].vertex[(7-d)%4][1] ) );
225.
226.              /* create an ideal cloud */
227.              double w = object[i].marker_width;
228.              PointCloud ideal;
229.              ideal.push_back( makeRGBPoint(-w/2,w/2,0) );
230.              ideal.push_back( makeRGBPoint(w/2,w/2,0) );
231.              ideal.push_back( makeRGBPoint(w/2,-w/2,0) );
232.              ideal.push_back( makeRGBPoint(-w/2,-w/2,0) );
233.
234.              /* get transformation */
235.              Eigen::Matrix4f t;
236.              TransformationEstimationSVD obj;
237.              obj.estimateRigidTransformation( marker, ideal, t );
238.
```

```
239.
240.            /* get final transformation */
241.            tf::Transform transform = tfFromEigen(t.inverse());
242.
243.            // any(transform == nan)
244.            tf::Matrix3x3  m = transform.getBasis();
245.            tf::Vector3    p = transform.getOrigin();
246.            bool invalid = false;
247.            for(int i=0; i < 3; i++)
248.              for(int j=0; j < 3; j++)
249.                invalid = (invalid || isnan(m[i][j]) || fabs(m[i][j]) > 1.0);
250.
251.            for(int i=0; i < 3; i++)
252.                invalid = (invalid || isnan(p[i]));
253.
254.            if(invalid)
255.              continue;
256.
257.            /* publish the marker */
258.            ar_pose::ARMarker ar_pose_marker;
259.            ar_pose_marker.header.frame_id = msg->header.frame_id;
260.            ar_pose_marker.header.stamp = msg->header.stamp;
261.            ar_pose_marker.id = object[i].id;
262.
263.            ar_pose_marker.pose.pose.position.x = transform.getOrigin().getX();
264.            ar_pose_marker.pose.pose.position.y = transform.getOrigin().getY();
265.            ar_pose_marker.pose.pose.position.z = transform.getOrigin().getZ();
266.
267.            ar_pose_marker.pose.pose.orientation.x = transform.getRotation().getAxis().getX();
268.            ar_pose_marker.pose.pose.orientation.y = transform.getRotation().getAxis().getY();
269.            ar_pose_marker.pose.pose.orientation.z = transform.getRotation().getAxis().getZ();
270.            ar_pose_marker.pose.pose.orientation.w = transform.getRotation().getW();
271.
272.            ar_pose_marker.confidence = marker_info->cf;
273.            arPoseMarkers_.markers.push_back (ar_pose_marker);
274.
275.            /* publish transform */
276.            if (publishTf_)
277.            {
278.              broadcaster_.sendTransform(tf::StampedTransform(transform, msg->header.stamp, msg-
    >header.frame_id, object[i].name));
279.            }
280.
281.            /* publish visual marker */
282.
283.            if (publishVisualMarkers_)
284.            {
285.              tf::Vector3 markerOrigin (0, 0, 0.25 * object[i].marker_width * AR_TO_ROS);
286.              tf::Transform m (tf::Quaternion::getIdentity (), markerOrigin);
287.              tf::Transform markerPose = transform * m; // marker pose in the camera frame
288.
289.              tf::poseTFToMsg (markerPose, rvizMarker_.pose);
290.
291.              rvizMarker_.header.frame_id = msg->header.frame_id;
292.              rvizMarker_.header.stamp = msg->header.stamp;
293.              rvizMarker_.id = object[i].id;
294.
```

```
295.              switch (i)
296.              {
297.                case 0:
298.              rvizMarker_.scale.x = 0.15;// * object[i].marker_width * AR_TO_ROS;
299.              rvizMarker_.scale.y = 0.15;// * object[i].marker_width * AR_TO_ROS;
300.              rvizMarker_.scale.z = 0.15;// * object[i].marker_width * AR_TO_ROS;
301.              rvizMarker_.ns = "basic_shapes";
302.              rvizMarker_.type = visualization_msgs::Marker::SPHERE;
303.              rvizMarker_.action = visualization_msgs::Marker::ADD;
304.                rvizMarker_.color.r = 0.0f;
305.                rvizMarker_.color.g = 0.0f;
306.                rvizMarker_.color.b = 1.0f;
307.                rvizMarker_.color.a = 1.0;
308.                break;
309.                case 1:
310.              rvizMarker_.scale.x = 0.15;// * object[i].marker_width * AR_TO_ROS;
311.              rvizMarker_.scale.y = 0.15;// * object[i].marker_width * AR_TO_ROS;
312.              rvizMarker_.scale.z = 0.15;// * object[i].marker_width * AR_TO_ROS;
313.              rvizMarker_.ns = "basic_shapes";
314.              rvizMarker_.type = visualization_msgs::Marker::SPHERE;
315.              rvizMarker_.action = visualization_msgs::Marker::ADD;
316.                rvizMarker_.color.r = 1.0f;
317.                rvizMarker_.color.g = 0.0f;
318.                rvizMarker_.color.b = 0.0f;
319.                rvizMarker_.color.a = 1.0;
320.                break;
321.                default:
322.              rvizMarker_.scale.x = 0.15;// * object[i].marker_width * AR_TO_ROS;
323.              rvizMarker_.scale.y = 0.15;// * object[i].marker_width * AR_TO_ROS;
324.              rvizMarker_.scale.z = 0.15;//* object[i].marker_width * AR_TO_ROS;
325.              rvizMarker_.ns = "basic_shapes";
326.              rvizMarker_.type = visualization_msgs::Marker::SPHERE;
327.              rvizMarker_.action = visualization_msgs::Marker::ADD;
328.                rvizMarker_.color.r = 0.0f;
329.                rvizMarker_.color.g = 1.0f;
330.                rvizMarker_.color.b = 0.0f;
331.                rvizMarker_.color.a = 1.0;
332.              }
333.              rvizMarker_.lifetime = ros::Duration ();
334.
335.              rvizMarkerPub_.publish (rvizMarker_);
336.              ROS_DEBUG ("Published visual marker");
337.            }
338.          }
339.        arMarkerPub_.publish (arPoseMarkers_);
340.        ROS_DEBUG ("Published ar_multi markers");
341.        }
342.
343.      }                                 // end namespace ar_pose
```

bell_yellow_listener.py

```
1.  #!/usr/bin/env python
```

```python
2.    import roslib; roslib.load_manifest('kinect_bell_ver01')
3.    import rospy
4.    from std_msgs.msg import String
5.    import ar_pose
6.    from ar_pose.msg import ARMarker
7.    from ar_pose.msg import ARMarkers
8.    from kinect_bell_ver01.msg._YellowLightMessage import YellowLightMessage
9.    import pygame
10.   import time
11.   import math
12.
13.   def callback(data):
14.       yellow_light_pub = rospy.Publisher('yellow_light_topic', YellowLightMessage)
15.
16.       yellow_light_on_off = YellowLightMessage()
17.       yellow_light_on_off = 'off'
18.
19.       r = rospy.Rate(1)
20.       if data.markers:
21.           if len(data.markers) >= 2:
22.
23.               print 'range(0, len(data.markers) = '
24.               print range(0, len(data.markers))
25.               position = []
26.               for i_length in range(0, len(data.markers)):
27.                   # collect marker positions into list position
28.                   print 'Marker %i position is (%.3f, %.3f, %.3f)' % (i_length, data.markers[i_lengt
      h].pose.pose.position.x, data.markers[i_length].pose.pose.position.y, data.markers[i_length].pose.
      pose.position.z)
29.
30.                   position.append([data.markers[i_length].pose.pose.position.x, data.markers[i_lengt
      h].pose.pose.position.y, data.markers[i_length].pose.pose.position.z])
31.
32.               distance = []
33.               h_index = -1
34.               for i_length in range(0, len(data.markers)):
35.                   for j_length in range(i_length + 1, len(data.markers)):
36.                       # calculate distances between each marker
37.
38.                       h_index = h_index + 1
39.
40.                       distance.append(math.sqrt(math.pow((position[i_length][0] -
      position[j_length][0]),2) + math.pow((position[i_length][1] -
      position[j_length][1]),2) + math.pow((position[i_length][2] - position[j_length][2]),2)))
41.
42.               for i_length in range(0, len(distance)):
43.                   print 'distance = %.3f' % distance[i_length]
44.                   if distance[i_length] < .30:
45.                       if distance[i_length] > .2:
46.                           # determine if markers are within caution range
47.                           yellow_light_on_off = 'on'
48.
49.               yellow_light_pub.publish(yellow_light_on_off)
50.               r.sleep()
51.
52.   def listener():
53.
```

```
54.     # in ROS, nodes are unique named. If two nodes with the same
55.     # node are launched, the previous one is kicked off. The
56.     # anonymous=True flag means that rospy will choose a unique
57.     # name for our 'listener' node so that multiple listeners can
58.     # run simultaenously.
59.     rospy.init_node('listener_yellow', anonymous=True)
60.
61.     rospy.Subscriber("ar_pose_markers", ARMarkers, callback)
62.
63.     # spin() simply keeps python from exiting until this node is stopped
64.     rospy.spin()
65.
66. if __name__ == '__main__':
67.     listener()
```

yellow_light_listener.py

```
1.  #!/usr/bin/env python
2.  import rospy
3.  from std_msgs.msg import String
4.  from kinect_bell_ver01.msg._YellowLightMessage import YellowLightMessage
5.  import pygame
6.  import time
7.
8.  def callback(data):
9.      #rospy.loginfo(rospy.get_caller_id()+"I heard %s",data.data)
10.     #print '''yellow light: %s''' % data
11.
12.     if data.on_off_state == 'on':
13.         print '*** YELLOW LIGHT WARNING!!! ***'
14.         pygame.mixer.music.load('Homer.ogg')
15.         pygame.mixer.music.play(1)        # Plays six times, not five!
16.         time.sleep(1)
17.
18.
19.
20. def listener():
21.
22.     # in ROS, nodes are unique named. If two nodes with the same
23.     # node are launched, the previous one is kicked off. The
24.     # anonymous=True flag means that rospy will choose a unique
25.     # name for our 'listener' node so that multiple listeners can
26.     # run simultaenously.
27.     rospy.init_node('yellow_light_listener', anonymous=True)
28.
29.     rospy.Subscriber("yellow_light_topic", YellowLightMessage, callback)
30.
31.     # spin() simply keeps python from exiting until this node is stopped
32.     rospy.spin()
33.
34. if __name__ == '__main__':
35.     pygame.mixer.init()
36.     listener()
```

APPENDIX C: ROS REAL-TIME VISION SYSTEM TUTORIAL

The following tutorial describes how to utilize the object localization and tracking system used in this dissertation using the ROS system developed as part of this work.

Preliminaries

Before proceeding, make sure you are using a computer that has ROS installed, as well as the openni_camera, openni_launch, ar_tools, and ar_kinect packages. ROS Hydro was used for this work. To do this, from a terminal:

```
sudo apt-get install ros-hydro-openni-camera ros-hydro openni-launch
git clone https://github.com/mikeferguson/ar_kinect
git clone https://github.com/LucidOne/ar_tools
```

Refer to http://wiki.ros.org/openni_launch for setting up rviz. Then make sure that the ROS directory of your local ROS workspace is listed in the ROS_PACKAGE_PATH variable of ~/.bashrc. Your ~/.bashrc file should have some lines that look like this:

```
export ROS_PACKAGE_PATH=:$ROS_PACKAGE_PATH:~/ros_workspace
export ROS_WORKSPACE=~/ros_workspace
```

You will need to make sure that the ROS package management tools can find the ar_tools and ar_kinect packages, and that the packages have been built. From a terminal:

```
roscd ar_tools
rosmake ar_tools
roscd ar_kinect
rosmake ar_kinect
```

Testing

Verify that the Kinect is plugged in. From a terminal:

```
roscore
roslaunch openni_launch openni.launch
roslaunch ar_kinect ar_kinect.launch
rosrun rviz rviz
```

268

In rviz: add the TF, Maker, and Camera. Note that all ROS nodes run as their own processes so you will need to do each of the above from a different terminal.

Details

To show the published topic of ar_kinect, from a terminal:

```
rostopic echo ar_pose_markers
```

The accuracy of the Xbox 360 Kinect is ~ 3 cm. The outputted position is relative from the Kinect's camera_rgb_optical_frame. The camera_rgb_optical_frame's x-axis is red, y-axis is green, and z-axis is blue.

APPENDIX D: ROS IMAGING APPLICATION COMMUNICATION C++ EXAMPLE

```cpp
1.  //ROS imaging cpp file
2.
3.  void acquireCallback(const std_msgs::String::ConstPtr& msg)
4.  {
5.    ROS_INFO("I heard: [%s]", msg->data.c_str());
6.  }
7.
8.  int main (int argc, char **argv)
9.  {
10.   ros::init (argc, argv, "imaging_app");
11.   ros::NodeHandle n;
12.   ros::Publisher acquire_image_pub = n.advertise<std_msgs::String>("acquire_image", 1000);

13.   ros::spin ();
14.   return 0;
15. }
16.
17. // While application is running
18. // Move robot
19.
20. // After motion is complete
21. // Publish message to acquire image
22. /**
23.     * This is a message object. You stuff it with data, and then publish it.
24.     */
25.     std_msgs::String msg;
26.
27.     std::stringstream ss;
28.     ss << "acquire image ";
29.     msg.data = ss.str();
30.     /**
31.      * The publish() function is how you send messages. The parameter
32.      * is the message object. The type of this object must agree with the type
33.      * given as a template parameter to the advertise<>() call, as was done
34.      * in the constructor above.
35.      */
36.     Acquire_image_pub.publish(msg);
37.
38.     ros::spinOnce();
39.
40.     ROS_INFO("%s", msg.data.c_str());
41.
42. // Subscribe to Varian python script or CCD camera MATLAB script to tell when panel or cam
    era has finished acquiring image
43. /**
44.      * The subscribe() call is how you tell ROS that you want to receive messages
45.      * on a given topic.  This invokes a call to the ROS
46.      * master node, which keeps a registry of who is publishing and who
47.      * is subscribing.  Messages are passed to a callback function, here
48.      * called acquireCallback.  subscribe() returns a Subscriber object that you
49.      * must hold on to until you want to unsubscribe.  When all copies of the Subscriber
50.      * object go out of scope, this callback will automatically be unsubscribed from
```

```
51.    * this topic.
52.    *
53.    * The second parameter to the subscribe() function is the size of the message
54.    * queue.  If messages are arriving faster than they are being processed, this
55.    * is the number of messages that will be buffered up before beginning to throw
56.    * away the oldest ones.
57.    */
58.    ros::Subscriber sub = n.subscribe("image_acquire_on_off", 1000, acquireCallback);
59. if (image_acquire_on_off == on)
60. // do not continue - Image acquisition is running }
61. else if (image_acquire_on_off = off)
62. // continue - Image acquisition has finished }
63.
64.    /**
65.     * ros::spin() will enter a loop, pumping callbacks.  With this version, all
66.     * callbacks will be called from within this thread (the main one).  ros::spin()
67.     * will exit when Ctrl-C is pressed, or the node is shutdown by the master.
68.     */
69.    ros::spin();
```

APPENDIX E: ROS – FLAT PANEL DETECTOR COMMUNICATION PYTHON EXAMPLE

```python
1.  #!/usr/bin/env python
2.  import roslib; roslib.load_manifest('varian_panel_ver01')
3.  import rospy
4.  from std_msgs.msg import String
5.  from image_acquire_ver01.msg._ImageAcquireMessage import ImageAcquireMessage
6.  import wx
7.  from ctypes import *
8.  import numpy
9.  import time
10.
11. def callback(data):
12.     rospy.loginfo(rospy.get_caller_id() + "I heard %s", data.data)
13.
14. # Publish to ROS master node when image/radiograph has been acquired
15. def talker():
16.     image_acquire_pub = rospy.Publisher('image_acquire_topic', ImageAcquireMessage, queue_
    size=10)
17.     rospy.init_node('talker', anonymous=True)
18.     image_acquire_on_off = ImageAcquireMessage()
19.     image_acquire_on_off = 'off' # Image acquisition is not running
20.     rate = rospy.Rate(10) # 10hz
21.
22.     if #Varian panel is acquiring image
23.         # Start publishing image_acquire_on_off
24.         image_acquire_on_off = 'on' # Image acquisition is running
25.
26.     image_acquire_pub.publish(image_acquire_on_off)
27.     rate.sleep()
28.
29. if __name__ == '__main__':
30.     try:
31.         talker()
32.     except rospy.ROSInterruptException:
33.         pass
34.
35. # Listen to ROS when image is to be acquired
36. def listener():
37.
38.     # In ROS, nodes are uniquely named. If two nodes with the same
39.     # node are launched, the previous one is kicked off. The
40.     # anonymous=True flag means that rospy will choose a unique
41.     # name for our 'listener' node so that multiple listeners can
42.     # run simultaneously.
43.     rospy.init_node('listener_image_acquisition', anonymous=True)
44.
45.     rospy.Subscriber("acquire_image", String, callback)
46.
47.     # spin() simply keeps python from exiting until this node is stopped
48.     rospy.spin()
49.
50. if __name__ == '__main__':
51.     listener()
```

APPENDIX F: ROS – CCD CAMERA COMMUNICATION MATLAB EXAMPLE

```matlab
function ROS_Camera
    % Connect to the IP address of the ROS PC
    rosinit('128.165.230.152',11311)

        keepLooking = true;

        % Create publisher to ROS master node when image/radiograph has been acquired
        image_acquire_pub = rospublisher('/image_acquire_on_off','std_msgs/String');
        msg = rosmessage(image_acquire_pub);
        msg.Data = 'off';
        if % CCD camera is acquiring image
            msg.Data = 'on';
        else % do nothing - CCD camera is acquiring image

        send(image_acquire_pub,msg);

        % Create subscriber and call function to acquire image
        sub = rossubscriber('/image_acquire_on_off', @camera_acquire)
        % Receive messages
        while keepLooking
            msg = sub.receive();
        end

    % Acquire image function
    function camera_acquire(src,msg)
        % Acquire image
        disp([char(msg.Data()), sprintf('\n Message received: %s', datestr(now))]);
    end
end
```

References

Abfalterer, W. P., et al. "Measurement of Neutron Total Cross Sections up to 560 MeV." *Physical Review C* 63.044608 (2001): 1-19.

Agile Planet, ed. "Kinematix." *Agile Planet*. 10 June 2013. <http://www.agileplanet.com/technology/kinematix>.

Allied Vision. *Prosilica GE 680*,2015 .

ANDOR, ed. "iXonEM+." *ANDOR Technology* , 2008. 23 July 2015.

ANSI/RIA R15.05-1. *American National Standard for Industrial Robots and Robot Systems - Point-to-Point and Static Performance Characteristics*,1990. .

Applied Scintillation Technologies, ed. "SECUREX ND." *AST*. , 2014. 23 July 2015. <http://appli-47688-001.dvs.demon.net/products/securex-nd>.

Arduino, ed. "Arduino Uno." *Arduino*. , 2015. 23 July 2015. <https://www.arduino.cc/en/Main/arduinoBoardUno>.

ASTM E262. "Standard Test Method for Determining Thermal Neutron Reaction Rates and Thermal Neutron Fluence Rates by Radioactivation Techniques." *ASTM E262-08*, 2008. .

ASTM E545. "Standard Test Method for Determining Image Quality in Direct Thermal Neutron Radiographic Examination." *ASTM E545-05* , 2005. .

Avery, G. E. "Radiation Hardening." *Military Electronics, Countermeasures* 74 (1979)

Berger, H. *Nondestructive Testing Standards: A Review*. Astm Intl, 1977.

Bosserman, Daniel W. "The Future of NDT: Radiography Meets Robotics." *Quality Magazine*. , 27 Aug. 2007. 7 June 2013. <http://www.qualitymag.com/articles/84931-the-future-of-ndt-radiography-meets-robotics>.

Bruce, M. B., and M. V. Davis. *Radiation Effects on Organic Materials in Nuclear Power Plants*. Rept. no. NP-2129. Atlanta: Georgia Institute of Technology, 1981.

Bucky, G. Method and Apparatus for Projecting Roentgen Images. Patent 1,164,987. 1915.

Burdea, G. C., S. M. Dunn, and G. Levy. "Evaluation of Robot-Based Registration for Subtraction Radiography." *Medical Image Analysis* 3.3 (1999): 265-74.

Cao, L. "Development of a High Spatial Resolution Neutron Imaging System." Diss. U of Texas at Austin, 2007.

Chamberlain, D. A., R. Edney, and G. Bleakley. "Robotic Handling of Gamma-Ray Sources in Site Radiography of Steel Storage Tanks." *13th International*

Symposium on Automation and Robotics in Construction and Mining (1996): 653-62.

Chitta, S., I. A. Sucan, and S. Cousins. "MoveIt! [ROS Topics]." *IEEE Robot. Automat. Mag.* 19.1 (2012): 18-19.

Decreton, M., S. Coenen, and J. D. Geeter. "Implementing Radiation Hardened Sensors for Computer Aided Teleoperation in a Nuclear Environment." *IEEE Industrial Electronics* (1997): 278-84.

Department of Energy. *Environmental Restoration and Waste Management Robotics Technology Development Program Robotics 5-Year Plan*. Washington: DOE/CE-0007T, Vol. 1-3, 1990.

Dhillon, B. S., A. R. Fashandi, and K. L. Liu. "Robot Systems Reliability and Safety: A Review." Journal of Quality in Maintenance Engineering 8.3 (2002): 170-212.

Edwards, S., and C. Lewis. "ROS-Industrial - Applying the Robot Operating System (ROS) to Industrial Applications." *ICRA/ROSCon* (2012)

Egnatuk, Christine M. "Radioargon Production at The University of Texas at Austin." Diss. U of Texas at Austin, 2012.

El-Guebaly, L. "Overview of ARIES-RS Neutronics and Radiation Shielding: Key Issues and Main Conclusions." *Fusion Engineering and Design* 38.1-2 (1997): 139-58.

Fleetwood, D. W., P. V. Dressendorfer, and D. C. Turpin. "A Reevaluation of Worst-Case Postirradiation Response for Hardened MOS Transistors." *IEEE Trans. Nucl. Sci.* 34 (1987)

General Electric. *Industrial Radiography Image Forming Techniques*. : General Electric Company, 2007.

Graham, J., et al. "Neutron Fux Characterization Techniques for Radiation Effects Studies." *J Radioanal Nucl Chem* (2012): 503-07.

Grillo, A., et al. "Radiation Hardness Measurements on MAXIM Full Custom Bipolar Processes C-Pi and CB2." *SCIPP* 96.34 (1996)

Hashem, J. "Automating X-Ray and Neutron Non-Destructive Testing Applications." *Proc. of the ANS Winter Mtg.* (2013)

Hashem, Joseph, Brian O'Neil, and Mitch Pryor. "Integrating Fixed and Flexible Solutions for Glovebox Automation." *Proceeding of the 3rd International Topical Meeting on Robotics and Remote Systems, Knoxville, TN* (2011)

Hashem, Joseph A. "The Requirements and Implementation of Dynamically-Deployed Robotic Systems for Use in Confined, Hazardous Environments." MS thesis. U of Texas at Austin, 2012.

Heinisch, H. L., et al. "Displacement Damage in Silicon Carbide Irradiated in Fission Reactors." *Journal of Nuclear Materials* 35.29 (2004): 175-81.

Heitmann, T., and W. Montfrooij. "Practical Neutron Scattering at a Steady State Source." *Mizzou Media* (2012)

Holmes-Siedle, A., and L. Adams. *Handbook of Radiation Effects*. Oxford: Oxford UP, 1993.

Hopkins, D. N. "Determination of the Linear Attenuation Coefficients and Buildup Factors of MCP-96 Alloy for Use in Tissue Compensation and Radiation Protection." Diss. Ball State U, 2010.

Hoshikawa, A., et al. "Automatic Sample Changer for IBARAKI Materials Design Diffractometer (iMATERIA)." *Journal of Physics: Conf. Series* 251.1 (2010)

Houssay, L. P. "Robotics and Radiation Hardening in the Nuclear Industry." Diss. U of Florida, 2000.

Hughes, H., T. P. Ma, and P. V. Dressendorfer. *Ionizing Radiation Effects in MOS Devices and Circuits*. New York: J. Wiley and Sons, 1989.

Hunter, J. "X-Ray Radiography and Computed Tomography Capabilities at AET-6." *LANL* (2012)

Idaho National Laboratory. "MOOSE Simulation Environment." INL Fact Sheets. , 23 Nov. 2015. <http://www4vip.inl.gov/research/moose-applications/>.

ISO 9283. "Manipulating Industrial Robots — Performance Criteria and Related Test Methods." *International Standards Organization* (1998)

Jimenez, E. S. "High Performance Graphics Processor Based Computed Tomography Reconstruction Algorithms for Nuclear and Other Large Scale Applications." *Sandia Report SAND2013-8059* (2013)

Kak, Avinash C., and Malcolm Slaney. *Principles of Computerized Tomographic Imaging*. New York: IEEE Press, 1988.

Kershaw, K., et al. "Remote Inspection, Measurement and Handling for Maintenance and Operation at CERN." *International Journal of Advanced Robotic Systems* 10.382 (2013)

Keyser, Ronald M. *Performance and Characteristics of a Low-Background Germanium Well Detector for Low-Energy Gamma-ray Nuclides*. Ed. Peter Warwick. : RSC Publishing, 2011.

King, R. T., A. Jostson, and K. Farrell. "Neutron Irradiation Damage in a Precipitation-Hardened Aluminum Alloy." *ASTM Special Technical Publication* (1973): 165-83.

Kinova, ed. "JACO Research Edition." *Kinova Robotics*. , 2012. 7 June 2013. <http://kinovarobotics.com/>.

Kippen, K. E., et al. "LANSCE Focus: Particles in Motion." *LA-UR-14-26511* (2014)

Lacerda, A. H., and K. F. Schoenberg. "Building the Foundation for New Capabilities." *LANSCE Activity Report* 2012:

Lambrechts, P., M. Boerlage, and M. Steinbuch. "Trajectory Planning and Feedfoward Design for High Performance Motion Systems." *Proceedings of the American Control Conf.* 5 (2004)

Landauer, ed. "Dosimeter for X, Gamma, Beta, and Neutron Radiation." *Luxel+.* , 2005. 19 Mar. 2014. <http://www.landauer.com/uploadedFiles/Healthcare_and_Education/Products/Dosimeters/LuxelSpecifications.en-US.pdf>.

LANL. "Long-Range Infrastructure Development Plan." Los Alamos. Sept. 2013. Speech.

Laux, Rick. "Theoretical Application of Dual Robotic Systems for Radiographic Tomography." *Materials Evaluation* May 2013: 513-16.

Lehmann, E. H., et al. "Neutron Imaging - Detector Options in Progress." 12th Int. Workshop on Radiation Imaging Detectors (2010)

Lehmann, E. H., et al. "How to Organize a Neutron Imaging User Lab? 13 Years of Experience at PSI, CH." *Nucl. Instrum. Method* (2011): 1-5.

Lumelsky, V. J., and E. Cheung. "Real-Time Collision Avoidance in Teleoperated Whole-Sensitive Robot Arm Manipulators." *IEEE Trans. Systems, Man and Cybernetics* 53 (1993): 194-203.

Maier-Hein, L., et al. "Human vs. Robot Operator Error in a Needle-Based Navigation System for Percutaneous Liver Interventions." Proc. SPIE, Medical Imaging: Visualization, Image-Guided Procedures, and Modeling 7261 (2009)

Markowicz, A. A. *Handbook of X-ray Spectrometry*. New York: Marcel Dekker, 1993.

MathWorks, ed. "Robotics System Toolbox." *MathWorks*. , 2015. 23 July 2015. <http://www.mathworks.com/products/robotics/>.

Matlab. "Image Processing Toolbox User's Guide." *MathWorks*, 2015.

Meieran, H. B. "International Overview." *Remote Techniques for Nuclear Plant* (1993)

Messenger, G. C. "Radiation Hardening." *AccessScience*. : McGraw-Hill Education, 2014.

Miclea, C., et al. "Effect of Neutron Irradiation on Some Piezoelectric Properties of PZT Type Ceramics." *J. Phys. IV France* 128 (2005): 115-20.

Mitutoyo. *ABSOLUTE Solar Digimatic Indicator 543-502*, 2015.

Moll, M., I. Sucan, and L. Kavraki. "The Open Motion Planning Library." *IEEE Robotics and Automation Magazine* Dec. 2012:

Molnár, Z. Wigner Course. *Neutron Activation Analysis*. 31 Mar. 2014.
        <http://www.reak.bme.hu/Wigner_Course/WignerManuals/Budapest/NEUTRON
        _ACTIVATION_ANALYSIS.htm>.

Morris, C. L., et al. "Charged Particle Radiography." Reports on Progress in Physics 76.4
        (2013)

Niekum, S., et al. "Learning Grounded Finite-State Representations from Unstructured
        Demonstrations." *International Journal of Robotics Research* 34.2 (2015): 131-
        57.

Nieves, E. E-mail interview. 25 July 2013.

Nof, Shimon Y., ed. *Handbook of Industrial Robotics*. 2nd ed: Wiley, 1999.

Olander, D. R. *Fundamental Aspects of Nuclear Reactor Elements*. : US Dept of Energy,
        1975.

O'Neil, Brian. "Object Recognition and Pose Estimation for Manipulation in Nuclear
        Material Handling Activities." Diss. U of Texas at Austin, 2013.

Packan, N. H. "Fluence and Flux Dependence of Void Formation in Pure Aluminum."
        Journal of Nuclear Materials 40.1 (1971): 1-16.

Patel, R. V., and F. Shadpey. Control of Redundant Robot Manipulators: Theory and
        Experiments. Germany: Springer, 2005.

Paffett, M. "Designing a Container for Safe, Long-Term Storage." *Actinide Research
        Quarterly* 2004: 1-32.

Pelowitz, D. B. *MCNPX User's Manual Ver. 2.7.0*. Rel. LA-CP-11-00438. Los Alamos
        National Laboratory, 2011. CD-ROM.

Peterson, C., M. Pryor, and S. Landsberger. "Evaluating Automation for Material
        Reduction in Gloveboxes Using Plutonium Surrogates." *Embedded Topical
        Meeting on Decommissioning and Remote Systems* (2014): 143-46.

Peterson, K. D., J. R. Gordon, and J. D. Jones. "A Gantry Robot System for Remote
        Handling of 3013 Inner and Outer Cans." *Embedded Topical Meeting on
        Decommissioning and Remote Systems 2014, Held at the American Nuclear
        Society 2014 Annual Meeting* (2014)

Prakash, R. *Nondestructive Testing Techniques*. : New Age Science, 2009.

Quigley, M., et al. "ROS: an Open-Source Robot Operating System." *International
        Conference on Robotics and Automation* (2009)

Radcal. "Ion Chambers." *Radcal*. , 2012. 2 Sept. 2015. <http://www.radcal.com/ion-
        chambers#10x5-series>.

Révaya, Z., et al. "Construction and Characterization of the Redesigned PGAA Facility at The University of Texas at Austin." *Nuclear Instruments and Methods in Physics Research* 577 (2007): 611-18.

Reillo, E. "On the neutron transparency of various materials proposed for the AIDA enclosure." *CIEMAT* (2010)

Roentgen, W. C. "On a New Kind of Rays." *Nature* 53.274 (1896)

ROS, ed. "RViz Package Summary." *ROS.org*, 2 June 2014. 23 July 2015. <http://wiki.ros.org/rviz>.

 ROS.org. , 23 May 2013. 10 June 2013. <http://www.ros.org/wiki/>.

Rusu, R. "3D is Here: Point Cloud Library (PCL)." *International Conference on Robotics and Automation* (2011)

Schoenberg, K. F., and P. W. Lisowski. "LANSCE: A Key Facility for National Science and Defense." *Los Alamos Science* 2006: 2-17.

Schroeder, K. "A Black Box Model for Estimating Joint Torque in an Industrial Serial Manipulator." *Proc. 2013 ASME IDETC/CIE* (2013)

Shu, D., T. S. Toellner, and E. E. Alp. "High-Precision Positioning Mechanism Development at the Advanced Photon Source." *2nd International Workshop on Mechanical Engineering Design of Synchrotron Radiation Equipment and Instrumentation* (2002): 214-22.

Sias, F. R., and J. S. Tulenko. "Radiation-Hardened Microcomputers for Robotics and Teleoperated Systems." *Trans. of ANS* 69 (1993)

Silverman, P. M., et al. "Helical CT: Practical Considerations and Potential Pitfalls." *RadioGraphics* 15.1 (1995): 25-36.

Soete, D. *Neutron Activation Analysis*. New York City: Wiley Interscience, 1972.

Tao, WeiMin, et al. "Residual Vibration Analysis and Suppression for SCARA Robots in Semiconductor Manufacturing." *International Journal of Intelligent Control and Systems* 11.2 (2006): 97-105.

Teague, E. C., and C. Evans. *Patterns for Precision Instrument Design (Mechanical Aspects)*. Gaithersburg: National Institute for Standards and Technology, 1988.

Tremsin, A. S. "Non-Destructive Studies of Fuel Pellets by Resonance Absorption Radiography and Thermal Neutron Radiography." *Journal of Nuclear Materials* 440 (2013): 633-46.

UniWest, ed. "Uni-Versal Robotic Eddy Current Test Machine." *UniWest*. , 2011. 10 June 2013. <http://www.uniwest.com/Uni-Versal-Robotic-Eddy-Current-Test-Machine-P14.aspx>.

U.S.NRC. "Units of Radiation Dose." *United States Nuclear Regulatory Commission*. , 10 July 2014. 10 Aug. 2015. <http://www.nrc.gov/reading-rm/doc-collections/cfr/part020/part020-1004.html>.

Varian Imaging Products. *PaxScan 2520D/CL Amorphous Silicon Digital X-Ray Imager*. Palo Alto, CA: , 2011.

Vestrand, W. T. "The RAPTOR Experiment: A System for Monitoring the Optical Sky in Real Time." *Advanced Global Communications Technologies for Astronomy* (2002): 126-36.

VGStudio MAX. Volume Graphics GmbH, 2013. CD-ROM.

Was, G. S. *Fundamentals of Radiation Materials Science*. Berlin: Springer, 2007.

Washington University in St. Louis. Radiation Safety Manual for Use of Radioactive Materials. ALARA Program, 2014.

Wasserman, S. R., et al. "Rapid-Access, High-Throughput Synchroton Cyrstallography for Drug Discovery." *Trends in Pharmacological Sciences* 33.5 (2012): 261-67.

WISE Uranium Project. Neutron Activation Calculator, 2012. 26 Mar. 2014. <http://www.wise-uranium.org/rnac.html>.

Wyllie, K. "Radiation Hardness Assurance." *CERN*. , 13 Nov. 2014. 23 July 2015. <http://lhcb-elec.web.cern.ch/lhcb-elec/html/radiation_hardness.htm>.

Yaskawa. SAI5D, 2012. 26 Mar. 2014. <http://www.motoman.com/datasheets/SIA5D.pdf>.

YouTube. *Using Neutrons to Study Advanced Nuclear Fuel at Los Alamos*. *YouTube*. , 5 June 2014. 27 July 2015. <https://www.youtube.com/watch?v=w4QhJEX6DiQ>.

Zinkle, S. "Impact of Radiation Damage on Materials for Nuclear Energy Systems." EFRC Summer School on Defects, Deformation and Damage in Structural Materials. Knoxville. June 2012. Speech.

Ziock, H. J., et al. "Temperature Dependence of the Radiation Induced Change of Depletion Voltage in Silicon Pin Detectors." *Nucl. Instrum. Meth.* 342 (1994)

Vita

Joseph Anthony Hashem was born in Round Rock, TX in 1987, the son of Abraham and Susan Hashem. He received the Bachelor of Science degree in Mechanical Engineering with Honors in the Liberal Arts from Southern Methodist University. While earning his degree, Joseph completed internships at the Los Alamos Neutron Science Center where his research efforts focused on analyzing prompt fission neutron spectra. Joseph entered the graduate school at The University of Texas at Austin in 2010 studying nuclear engineering and robotics. He earned his master's degree at UT in Mechanical Engineering in 2013. Joseph currently resides in Santa Fe, NM and works at LANL.

Permanent email: hashem.joey@gmail.com

This dissertation was typed by the author.